Measurements of the Double-Spin Asymmetry A_1 on Helium-3: Toward a Precise Measurement of the Neutron A_1

by

Diana Marwick Seymour Parno

A dissertation submitted in partial fulfillment of the requirements
for the degree of

Doctor of Philosophy

in the Department of Physics

Carnegie Mellon University

April 2011

Abstract

The spin structure of protons and neutrons has been an open question for nearly twenty-five years, after surprising experimental results disproved the simple model in which valence quarks were responsible for nearly 100% of the nucleon spin. Diverse theoretical approaches have been brought to bear on the problem, but a shortage of precise data – especially on neutron spin structure – has prevented a thorough understanding.

Experiment E06-014, conducted in Hall A of Jefferson Laboratory in 2009, presented an opportunity to add to the world data set for the neutron in the poorly covered valence-quark region. Jefferson Laboratory's highly polarized electron beam, combined with Hall A's facilities for a high-density, highly polarized ^{3}He target, allowed a high-luminosity double-polarized experiment, while the large acceptance of the BigBite spectrometer gave coverage over a wide kinematic range: $0.15 < x < 0.95$. In this work, we present the analysis of a portion of the E06-014 data, measured with an incident beam energy of 4.74 GeV and spanning $1.5 < Q^2 < 5.5$ (GeV/c)^2. From these data, we extract the longitudinal asymmetry in virtual photon-nucleon scattering, A_1, on the ^{3}He nucleus. Combined with the remaining E06-014 data, this will form the basis of a measurement of the neutron asymmetry A_1^n that will extend the kinematic range of the data available to test models of spin-dependent parton distributions in the nucleon.

Acknowledgments

No one in this age can earn a physics PhD based solely on her own work and study; the making of a doctor, like the making of a modern particle-physics experiment, requires the goodwill and support of many. In my own life and studies, I have been profoundly blessed by the presence of my family, friends, and colleagues. It is traditional to thank these wonderful people in these pages, as though words were enough. They aren't, but they are a start.

My parents, Christine Marwick and Richard Seymour, brought me up to have both a deep curiosity about the world and the work ethic I needed to answer my own questions. The love of language my mother gave me made writing this dissertation far less painful than it might have been; my father urged me to take my first voluntary science course and then kindly refrained from saying "I told you so" at the sudden fascination with physics that resulted. My not-so-little brother, Matthew, kept me honest with everything I did.

The love and support of my extended family has been invaluable. My grandparents, Bob and Dolores Marwick, generously funded my undergraduate education. They and my aunts, uncles, and assorted cousins, scattered around the continent, taught me that I could find something of home wherever I am. To Rob and Ann Marwick, Mike and Monica Marwick, Lorrie Marwick and Guy Marsh, Nancy and Don DeMuth, and Josephine Marwick, thank you for the delicious meals, the fascinating conversations and your willingness to talk physics. To my beloved cousins, thank you for everything. Growing up, I was also lucky to enjoy the love of many people who weren't family only by a technicality: my thanks go also to the Simses and the Sklovers. And thanks are also due to my new extended family, the Gordons and the Parnos, who have gracefully adapted to a marked increase in physics-related holiday conversation ever since they welcomed me to their lives.

Excellent teachers, in high school and in college, gave me the grounding I needed for my work in graduate school. At Woodrow Wilson High School, John Glaze and Irving Stern gave me such a strong grounding in calculus and computer science that I rely on my memories of their lessons each day. Art Siebens taught me how to approach an experiment with a song in my heart. At Harvard College, Howard Georgi made the Leverett House dining hall a haven every Wednesday night for young physics students beset by problem sets. Melissa Franklin made sure I took the classes I needed in something approximating the right order. Tom Hayes and Mara Prentiss taught me careful lab techniques. George Brandenburg first showed me just how cool particle physics could be, and Masahiro Morii gave me the strength and inspiration to soldier through.

The other skills a physicist needs – persistence, curiosity, and above all a sense of humor – I owe in part to my dear friends from high school and college. I want to take this opportunity to express my especial gratitude to Alanna Sklover, Cynthia Correa, Chia-Jung Tsay, Esther Bisker, Lesley Chin, Paul Fili, Maribel Hernandez, Maggie Morgan, Nicole Nitsche, Tatiana Rodriguez, Shashank Sinha, Lynette Winslow, and Brent Yorgey for company, foosball, problem sets, and general good friendship.

I was extraordinarily fortunate to be given several research opportunities at a young age; these set me on my path to this dissertation. When I was only a high-school junior, Brian Mason, Bill Hartkopf and Gary Wycoff kindly welcomed me into the Double Star group at the U.S. Naval

Observatory, giving me a taste for research that carried me into college and beyond. In college, I had my first glimpse of nuclear physics spending a summer at Michigan State University, where I was privileged to work with Betty Tsang and Giuseppe Verde; during a summer at Harvard College, in Gerald Gabrielse's lab and with the particular guidance of Dan Farkas, I learned to see an experiment through, from AutoCAD design to optics-table implementation. At Los Alamos National Laboratory, Israel Owens introduced me to nonlinear optics and computer modeling.

It is in graduate school, of course, that physicists are made, and I have been blessed at Carnegie Mellon University. I could not ask for a more supportive or exciting department in which to spend seven years of graduate school. Joining the Medium Energy Group was one of the best decisions I have ever made. Curtis Meyer, Reinhard Schumacher, and Brian Quinn are inspiring scientists and excellent colleagues. Gary Wilkin makes the whole group tick. And I am profoundly indebted to my advisor, Gregg Franklin, who always made sure I knew what I was doing (or how to find out), and who gave me the freedom to explore the projects that interested me most. His concept of an ice-cream-based feedback system enlivened trips to Jefferson Lab, and his patience and flexibility made this dissertation – completed thousands of miles from Carnegie Mellon – possible.

At Carnegie Mellon, I spent several years with the world's best officemates: Mike McCracken and Kei Moriya. Thank you for the ROOT tricks, YouTube videos, and everything else. I want to offer special thanks to Biplab Dey, with whom I shared an office for about five weeks, for welcoming me so warmly despite the chaos I brought. The other grad students and postdocs in the group filled my spare hours (especially lunch hours) with fun and companionship, especially Megan Friend, Ryan Dickson, Fatiha Benmokhtar, Matt Bellis, Seamus Riordan, Yves Van Haarlem, Brian Vernarsky, Will Levine, Dao Ho, Naomi Jarvis, Mike Williams, and Zeb Krahn. Michelle Ntampaka, Eric Evarts, and Nishtha Srivastava made lunch in the grad lounge a joy. I would also very much like to thank Mike Abd-El-Malek, Bonnie Bogovich, Erin Coningsby, Kim Dickson, Scott Garriss, Rebecca Kirzner, Jon and Kathleen McCune, Jim Newsome, Bertin Ntampaka, and Ahren and Casey Studer for welcoming me into their homes and lives over the last several years. I thank Leonard Kisslinger for giving me a taste of theoretical research.

A great deal of my graduate-school career was spent in Newport News, at Jefferson Lab, and I am deeply grateful for the help and friendship of the staff and users there. In particular, I'd like to thank Sirish Nanda, in whose Compton laser lab I spent six happy months; Bob Michaels, whose DAQ support was invaluable; Alexandre Camsonne and Vince Sulkosky, who between them know just about everything; and Brad Sawatzky, analysis coordinator for E06-014, whose 4 a.m. accesses to the Hall are a major reason we have such a good data set to work with, and whose guidance made our analysis faster and better. Botao Jia, Ellie Long, Saori Pastore, Wouter Deconinck, Mark Dalton, Dustin McNulty, Abdurahim Rakhman, David Flay, Matt Posik, and Yawei Zhang were wonderful people to share it all with. The E06-010 grad students and postdocs – Kalyan Allada, Chiranjib Dutta, Jin Huang, Joe Katich, Xin Qian, Yi Qiang and Yi Zhang– put in uncountable hours making sure that E06-014 would run as planned and teaching me the Hall A apparatus, DAQ and analyzer. The HAPPEX collaboration, especially Paul Souder, Kent Paschke, and Krishna Kumar, helped us drive the Compton polarimeter to heights no one had thought it could reach. Xiaodong Jiang and Zein-Eddine Meziani always had time for my questions. My committee members – Betsy Beise and the professors of the Medium Energy Group – vastly improved this document.

I am more grateful to all these people than I can possibly say, but I find myself particularly tongue-tied when it comes to one man: my husband, Bryan Parno. In sickness and in health, for well-behaved data sets and mysterious bugs, he has anchored my life and lit it too. He has patiently taught me new programming languages and new tricks. He has shown me new places, shared with me new ideas, and introduced me to a new family. He has borne without complaint my long absences for long experiments, and the long hours of work that come before and after. I do better physics for a brighter future because of his love.

for Bryan
because of everything

Contents

List of Figures

List of Tables

Chapter 1

Introduction: Describing the Nucleon

One of the driving inspirations of physics research has always been to understand matter: what it's made of, how it interacts with other matter, and how tiny building blocks combine to form stars, planets, people, and everything else that is encountered in everyday life. Nucleons – protons and neutrons, the building blocks of the nucleus – are vital components of large-scale matter, but they are simple to name and complicated to understand.

In this chapter, we will lay out a framework for describing and exploring nucleonic structure in the context of Quantum Chromodynamics. Section 1.1 enumerates the parts of the nucleon and describes an enduring mystery about its spin structure. In Section 1.2, we introduce experimental methods for investigating nucleon structure, especially through electron scattering. In Section 1.3, meanwhile, we give a detailed discussion of unpolarized and polarized structure functions, which are indispensable tools for organizing and interpreting experimental results. With this groundwork laid, we will then be ready to explore the longitudinal spin asymmetry A_1 – which will drive the remainder of this dissertation – in Chapter 2.

1.1 What Are Nucleons Made of?

The building block of macroscopic matter is the atom, which is composed of a positively charged nucleus and the negatively charged (and far less massive) electrons that orbit it. The nucleus is in turn made up of nucleons – positively charged protons and electrically neutral neutrons – held together by the strong force described by **Q**uantum **C**hromo**d**ynamics (QCD). In the Standard Model, electrons are fundamental particles in the lepton family, but nucleons have internal structure. One of the great outstanding challenges of nonperturbative QCD is determining how a nucleon's constituents – quarks, antiquarks, and gluons – contribute to its observable characteristics; in this section, we set the stage for the mystery.

1.1.1 Quarks, Gluons, and Antiquarks

In the simplest model, protons and neutrons are each made up of three light quarks. Quarks are fundamental particles with spin 1/2 and come in six flavors – up, down, charm, strange, top, and bottom – of which up and down are the lightest. An up quark u has charge $+2/3$ while a down quark d has charge $-1/3$; a proton (charge $+1$) can thus be made up of two ups and a down, uud, while a neutron (charge 0) is made up of two downs and an up, udd. These three partons are termed *valence quarks*.

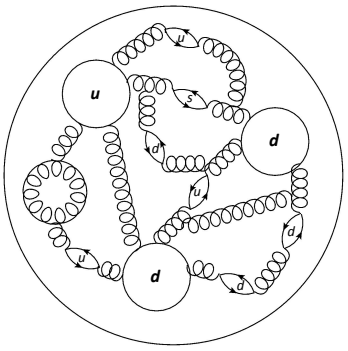

Figure 1.1: A representation of the internal structure of the neutron: valence quarks, sea quarks, and gluons, interacting with each other primarily through the strong force. This figure, as well as the Feynman diagrams that appear later in this work, was generated using Jaxodraw [1].

Each quark carries a color charge, which leads naturally to the term *Quantum Chromodynamics* for the theory of the force between these color charges. There are three possible color charges, conventionally labeled red, blue, and green, and each has a corresponding opposite charge (anti-red, anti-blue, or anti-green). The three valence quarks are bound by the strong force in a color singlet state, so that the nucleon as a whole is colorless.

The strong force is carried by *gluons*, massless spin-1 bosons which themselves carry color and anti-color. The quarks within a nucleon constantly exchange gluons, and gluons within the nucleon interact with each other, as well. As our understanding of the nucleon has grown more sophisticated, we have moved beyond the simplest model and realized that the gluonic contribution to nucleon structure must not be neglected.

The third component of nucleon structure is the *sea* of quark-antiquark pairs, appearing in pair production and disappearing in annihilation processes throughout the nucleon. Lighter particles are more likely to appear here, so the sea is dominated by the lightest quarks: $u\bar{u}$ and $d\bar{d}$ pairs. Strange quark-antiquark pairs ($s\bar{s}$) are believed to contribute to the behavior of the nucleon, but heavier pairs – $c\bar{c}$, $b\bar{b}$, and $t\bar{t}$ – occur with negligible probability.

Three valence quarks, uncountable gluons, and a sea of quarks and their antimatter partners: these are what nucleons are made of (Figure 1.1). Yet, as particle physicists were reminded in the 1980s, making a parts list is a far easier task than understanding precisely how they go together.

1.1.2 The Nucleon Spin Crisis

Precise measurements of nucleon substructure pose a significant experimental challenge, as we will explore in more detail in Section 1.2 (and, indeed, in the remainder of this dissertation). Historically, this has been especially true for experiments exploring aspects of nucleon structure that are dependent on spin – the intrinsic angular momentum carried by elementary particles, hadrons, and atomic nuclei. Such experiments require either spin-polarized particle beams or spin-polarized targets – or both – and the technology needed to perform precise measurements in these areas lagged theoretical predictions by years.

In the late 1970s and early 1980s, the E-80 [2, 3] and E-130 [4, 5] experiments at SLAC used a polarized electron beam, directed at a polarized proton target, to begin exploring the proton spin structure. These early measurements, with relatively low precision by modern standards and in a limited kinematic range, seemed to support the simple model that nearly all of the proton spin was carried by the spins of its valence quarks, and that other possible sources of angular momentum could be ignored. In 1988, however, this picture was shattered when the **E**uropean **M**uon **C**ollaboration (EMC), conducting polarized-muon-beam experiments at CERN, announced new results [6, 7]. The

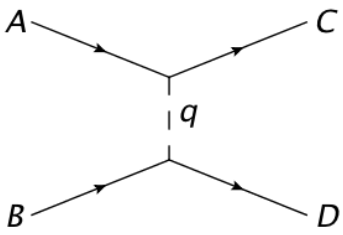

Figure 1.2: A generic Feynman diagram showing $AB \rightarrow CD$ scattering through exchange of a single boson (dashed line).

combination of the EMC and SLAC data showed that the quarks inside the proton (valence and sea together) contributed only about $12 \pm 17\%$ of the proton's total spin of 1/2 [7]. The predicted Ellis-Jaffe sum rule [8] was violated, the simple relativistic quark model was overturned, and the "proton spin crisis" had begun. The title of one 1988 paper [9] plaintively asked, "Where, oh where is the proton spin?"

Yet the proton spin crisis was also a spin opportunity, giving rise to a wide variety of new theories (several of which we will discuss in Section 2.3) and clever experiments. Spin contributions from gluons and orbital angular momentum could no longer be assumed to be negligible, which led to a more complete basic formulation for the total nucleon spin S_z^N

$$S_z^N = S_z^q + L_z^q + S_z^g + L_z^g = \frac{1}{2} \tag{1.1}$$

where $S_z^{q(g)}$ represents the z-axis projection of the quark (gluon) spin and $L_z^{q(g)}$ the z-axis projection of the quark (gluon) orbital angular momentum. Our present, and not wholly satisfactory, understanding [10] is that about $30 - 35\%$ of the nucleon spin comes from the spins of its quarks (with the valence quark contribution partially canceled by the sea quark contribution), while the total contribution J_z^g from gluons appears too small to account for the missing proton spin. This leaves the quark orbital angular momentum L_z^q; direct measurements of this quantity are not currently possible, but measurements of transverse quark motion provide some indirect access. This dissertation represents efforts toward filling in one more piece of the nucleon spin puzzle.

1.2 How to Experiment on a Nucleon

A typical nucleus has a diameter on the order of 2 to 15 femtometers (1 fm = 10^{-15} m = 1 fermi). A nucleon is smaller still: the proton has a **r**oot-**m**ean-**s**quare (RMS) charge radius of about 0.877 fm [11]. Conventional imaging techniques, such as optical microscopes or X-rays, cannot resolve objects on such a tiny scale. In this section, we will discuss a variety of methods used to explore nucleon structure, and introduce the formalism necessary to understand and interpret these explorations.

1.2.1 An Introduction to the Physics of Scattering

Fundamentally, the science of physics is the science of the interactions of forces and matter. Scattering interactions – in which some force deflects a particle from its straight-line trajectory – are a crucial tool for this study. Figure 1.2 shows a convenient way of describing a scattering event between two particles, mediated by the exchange of a force-carrying boson. Particles A and B, with four-momenta p_A and p_B, respectively, exchange a boson with four-momentum q; the final state of the system is composed of particles C and D, whose four-momenta are, respectively, p_C and p_D.

A scattering event $AB \rightarrow CD$ might be mediated by any of the four fundamental forces (or some combination of them); in practice, however, the gravitational force can be neglected in particle-particle interactions. By studying such interactions – how often they occur, the particles that are produced, the angles, momenta and energies involved – physicists can probe both the structure of the particles involved and the precise nature of their interactions. Different types of probes, and different types of targets, allow better access to various observables.

In explorations of nucleon spin structure, scattering probes may be divided into two broad categories. Hadron-hadron scattering – particularly nucleon-nucleon scattering – is one fruitful method. At Brookhaven National Laboratory's **R**elativistic **H**eavy **I**on **C**ollider (RHIC), for example, two beams of protons (either polarized or unpolarized) can be accelerated in opposite directions and brought together in a head-on collision. When the scattering interaction involves a large transfer of momentum, the mathematical description of the process can be *factorized* into contributions from long-distance and short-distance interactions [12, 13]. The short-distance contribution comes from hard interactions between quarks, anti-quarks, and gluons in the colliding protons, and can be calculated from first principles in the framework of QCD perturbation theory. Information about nucleon structure and parton distributions, meanwhile, can be extracted from the long-distance contributions to the interaction. By combining measurements of more than a dozen contributing processes, from pion production to the annihilation of a quark in one hadron with an antiquark in the other (the Drell-Yan process [14]), experimenters can isolate the spin contributions of quarks, anti-quarks, and even gluons.

The second major category of probes into nucleon spin structure is lepton scattering. In this process, a relativistic, charged lepton – generally an electron or a muon – exchanges a virtual photon or a virtual Z boson with a target nucleon. One great advantage of lepton-nucleon scattering as a probe of nucleon structure is that one vertex of the interaction – at which the lepton emits or absorbs a virtual boson and goes on its way – can be described solely by **Q**uantum **E**lectro**d**ynamics (QED) for photon exchange (or by electroweak theory for Z exchange), simplifying the interaction.

At the Thomas Jefferson National Accelerator Facility (Jefferson Lab), where the work of this dissertation took place, electrons are accelerated to energies of up to 6 GeV before striking a fixed target; electron scattering is thus the primary probe available at this institution. With this in mind, we will focus on electron scattering in the rest of this discussion, but the results are applicable to muon scattering as well.

Figure 1.3 shows the lowest-order electron-nucleon scattering interaction. Here, the incoming electron has four-momentum $k = (E, \vec{k})$, while the incoming nucleon has four-momentum $p = (E_p, \vec{p})$. They interact when the electron emits a virtual photon, with four-momentum q, that is absorbed by the nucleon. If the reaction is inelastic, then the nucleon breaks up into N distinct particles, each with final momentum p'_i; if the proton is left intact, then there is only one particle, with momentum p', in the final hadronic state. The scattered electron, meanwhile, has momentum k'. Electron scattering results are usually discussed in terms of five relativistically invariant quantities – ν, y, Q^2, W, and x – formed from these four-momenta, which characterize the interaction.

At each vertex of the process shown in Figure 1.3, the total four-momentum is conserved. We can therefore express q in terms of the initial and final four-momenta of the electron, k and k' respectively

$$q \equiv k - k' = \left(E - E', \vec{k} - \vec{k'}\right) = (E - E', \vec{q}) \tag{1.2}$$

where ν is defined as

$$\nu \equiv \frac{p \cdot q}{M_N} \tag{1.3}$$

and M_N is the mass of the nucleon. In the target rest frame, $p = (M_N, \vec{0})$ and we thus have $\nu = E - E'$, the electron *energy loss*. In the same way, the invariant quantity y is identified in the nucleon rest frame as the *fractional energy loss*

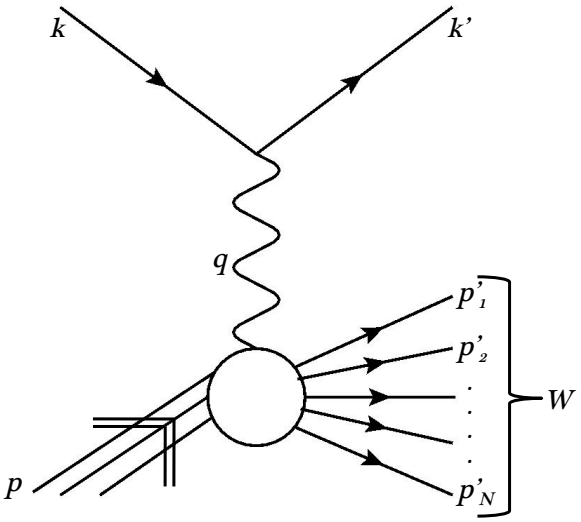

Figure 1.3: The lowest-order inclusive electron-nucleon scattering interaction, en → eX.

$$y \equiv \frac{p \cdot q}{p \cdot k} = \frac{E - E'}{E} \text{ in the nucleon rest frame.} \tag{1.4}$$

When $q^2 \neq 0$, the photon exchanged between the electron and the nucleon is off its mass shell and need not behave like a real photon: it is a *virtual photon*, effectively carrying borrowed energy for a short time in obedience to the Heisenberg uncertainty principle [15]. In practice, since $q^2 < 0$ for a virtual photon, it is convenient to define a positive expression Q^2 for the four-momentum transfer (or virtuality of the exchanged photon)

$$Q^2 \equiv -q^2 = 2EE'(1 - \cos\theta) \text{ in the nucleon rest frame} \tag{1.5}$$

where θ is the electron's scattering angle in the laboratory frame.

On the hadronic side of the interaction in Figure 1.3, there could be one outgoing particle (if the electron simply imparts some momentum to the nucleon without breaking it up) or many. In exclusive scattering, we measure both the scattered electron and outgoing particles from the hadron vertex; we may then exclude from our analysis any reaction channels without the particular outgoing particle or particles we have chosen to measure.

In inclusive electron-nucleon scattering, en → eX, only the scattered electron is measured; the final hadronic state X could be any of the multiparticle states that are possible with a given energy transfer. We define the invariant mass W of this unmeasured hadronic system

$$W^2 \equiv (p + q)^2 = M_N^2 + 2M_N\nu - Q^2. \tag{1.6}$$

The Bjorken x variable completes our set of useful, relativistically invariant kinematic variables:

$$x \equiv \frac{Q^2}{2p \cdot q} = \frac{Q^2}{2M_N\nu} \tag{1.7}$$

x has its simplest physical interpretation in the *infinite momentum frame*, in which the nucleon is traveling with a very large momentum compared to its mass. It can be shown that, in this frame, x is the fraction of the nucleon momentum carried by the quark that interacts with the virtual photon [15].

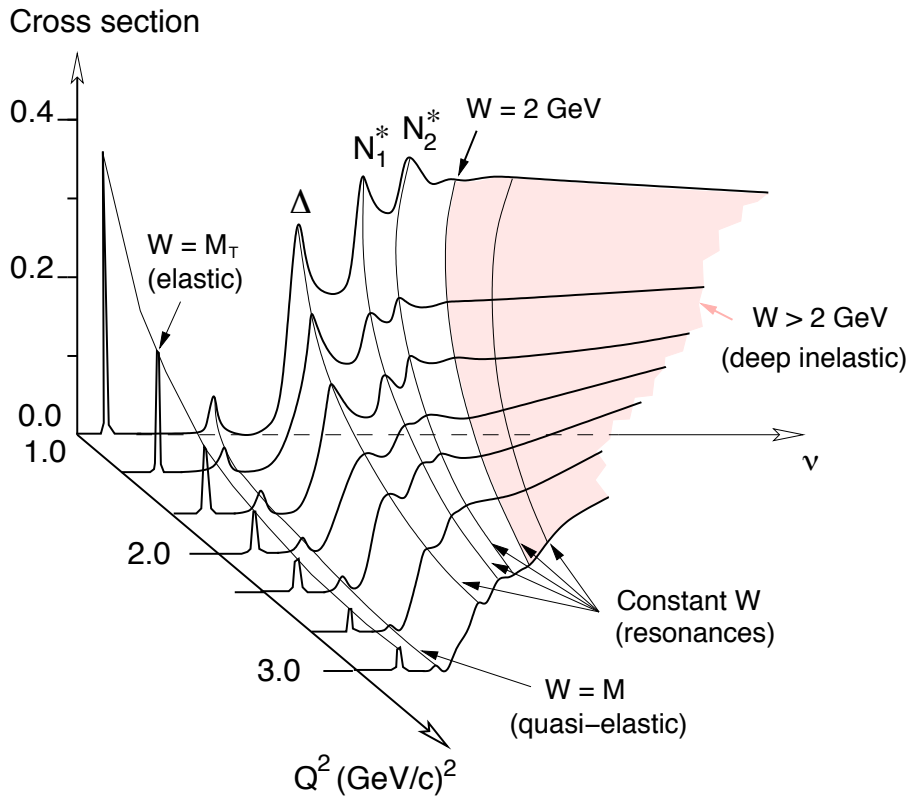

Figure 1.4: Schematic representation of cross section, in arbitrary units, as a function of Q^2 and ν for inclusive scattering of an electron from a light nucleus. For the first, "elastic", peak, W is calculated based on the momentum of the target nucleus; for the other peaks, the nucleon momentum is used. Reproduced from Zheng [16].

The intrinsic strength of a scattering reaction determines its *cross section*, which is proportional to the reaction rate and has units of area. Typically denoted σ, the cross section gives the probability of an interaction by defining the effective target area for that process. It is a formulation that does not rely on specific experimental parameters, such as the density of particles in the target or the intensity of the beam, allowing us to separate these details from our description of the basic underlying physics of the interaction. In the scattering of an electron from a nucleus via exchange of a single photon, the cross section σ shows strong dependence on Q^2 and ν, as illustrated in Figure 1.4.

The shape of the cross-section spectrum in Figure 1.4 suggests that we can think of Q^2 and ν as defining several different regimes of electron-nucleus scattering, each with different dynamics. It is helpful at this point to note that Q^2 effectively defines the spatial resolution of the virtual photon as a probe into the nuclear structure, in the same way that the frequency of a real photon used in a X-ray imager or a microscope defines the spatial resolution of the image.

The leftmost peak in Figure 1.4 corresponds to *elastic scattering* on the nucleus, which is at rest in the laboratory frame ($\vec{p} = 0$). For these values of four-momentum transfer Q^2 and energy transfer ν, the target nucleus has a high probability of remaining intact, in which case it scatters as a coherent whole with mass M_T and a momentum transfer spread across its constituent nucleons.

In *quasi-elastic scattering*, the excitation energy exceeds the nuclear binding energy and the probe "sees" quasi-free nucleons within. The electron scatters elastically from a single nucleon, either a proton or a neutron, and its target escapes the nucleus. The quasi-elastic peak is broader than the

elastic peak because the target nucleon, unlike its nucleus, is *not* at rest in the laboratory frame; instead, it has Fermi motion within the nucleus (which can be considered a Fermi gas) and has a momentum of up to about 250 MeV/c [17].

For $1.2 < W < 2.0$ GeV/c^2 – the *resonance* region – we begin to probe the substructure of the target nucleon itself. Absorption of the virtual photon excites the nucleon into a resonance, an unstable bound state. The lowest nucleon resonance is the $\Delta(1232)$ (in this notation, 1232 MeV/c^2 is its mass). Higher-mass resonances (such as the $N_1^*(1440)$ and $N_2^*(1520)$) often blur together in inclusive measurements.

Finally, for $W > 2$ GeV/c^2 and $Q^2 > 1$ (GeV/c)^2, we enter the *deep inelastic scattering* (DIS) region, in which we access partons – the constituents of the nucleon. Figure 1.4 shows a relatively smooth cross-section spectrum in this regime, which arises because – instead of a few possible resonances – we now have a variety of possible multiparticle states, accessible with a wide range of four-momentum transfers.

1.2.2 Scattering Formalism

We have introduced the scope and scale of electron-nucleon scattering, including a set of observables that give excellent access to the dynamics of these interactions. We will now develop a formal description of this type of scattering, following in the footsteps of Anselmino *et al.* [18].

Let us consider the differential cross section $d^2\sigma/d\Omega dE'$, which gives us the relative likelihood of detecting the scattered electron in the solid angle $d\Omega$ and in the energy range $(E', E + dE')$. Let the incident electron have four-momentum k and spin s and the scattered electron have four-momentum k' and spin s'. The incident nucleon has mass M, four-momentum p and spin S. In inclusive scattering, we detect the scattered electron but not the final hadronic state; we can thus ignore final-state interactions on the hadron side, so we cannot include information about their spins or momenta in our description of the interaction. We can, however, exercise some control over the initial state (k, s) and (p, S) through careful experimental design.

It is algebraically convenient to use tensor notation to represent the dynamics at each vertex of the interaction. The lepton vertex – that is, the upper vertex of Figure 1.3 – can be represented by the tensor $L_{\mu\nu}$, while the lower (hadron) vertex is represented by the tensor $W^{\mu\nu}$. This gives a deceptively simple form for the differential cross section

$$\frac{d^2\sigma}{d\Omega dE'} = \frac{\alpha^2}{2Mq^4}\frac{E'}{E}L_{\mu\nu}W^{\mu\nu} \tag{1.8}$$

where we have used α to represent the fine structure constant, $\alpha = e^2/4\epsilon_0\pi\hbar c$.

The leptonic tensor $L_{\mu\nu}$ is well understood from quantum electrodynamics and can be expressed in terms of the Dirac γ matrices, the electron Dirac spinor u, and $\bar{u} = u^\dagger\gamma^0$

$$L_{\mu\nu}\left(k, s; k', s'\right) = \left[\bar{u}(k', s')\gamma_\mu u(k, s)\right]^* \left[\bar{u}(k', s')\gamma_\nu u(k, s)\right]. \tag{1.9}$$

It is useful to divide $L_{\mu\nu}$ into four parts, two that are symmetric (S) under an interchange of the indices μ and ν and two that are antisymmetric (A) under the same interchange, giving us

$$L_{\mu\nu}\left(k, s; k', s'\right) = L_{\mu\nu}^{(S)}\left(k; k'\right) + iL_{\mu\nu}^{(A)}\left(k, s; k'\right) + L_{\mu\nu}^{\prime(S)}\left(k, s; k', s'\right) + iL_{\mu\nu}^{\prime(A)}\left(k; k', s'\right). \tag{1.10}$$

The unpolarized leptonic tensor, $2L_{\mu\nu}^{(S)}$, is obtained by summing $L_{\mu\nu}\left(k, s; k', s'\right)$ over the final spin states s' and averaging over the incident spin states s'.

The hadronic tensor $W^{\mu\nu}$ contains information about the structure of the target as well as QED and is consequently far less well understood. In order to simplify the problem of understanding $W^{\mu\nu}$, we can represent it as a linear combination of tensors that are symmetric and antisymmetric under μ, ν exchange, as we did for $L_{\mu\nu}$:

$$W_{\mu\nu}\left(q;p,S\right)=W_{\mu\nu}^{(S)}\left(q;p\right)+iW_{\mu\nu}^{(A)}\left(q;p,S\right). \tag{1.11}$$

Application of conservation laws at the hadron vertex allows us to derive general expressions for the symmetric and antisymmetric parts of $W^{\mu\nu}$.

$$W_{\mu\nu}^{(S)}\left(q;p\right)=2M\left(-g_{\mu\nu}+\frac{q_\mu q_\nu}{q^2}\right)W_1\left(p\cdot q,Q^2\right)+\frac{2}{M}\left(p_\mu-\frac{p\cdot q}{q^2}q_\mu\right)\left(p_\nu-\frac{p\cdot q}{q^2}q_\nu\right)W_2\left(p\cdot q,Q^2\right) \tag{1.12}$$

$$W_{\mu\nu}^{(A)}\left(q;p,S\right)=2\epsilon_{\mu\nu\alpha\beta}q^\alpha\left[M^2S^\beta G_1\left(p\cdot q,Q^2\right)+\left((p\cdot q)S^\beta-(S\cdot q)p^\beta\right)G_2\left(p\cdot q,Q^2\right)\right] \tag{1.13}$$

where the metric tensor $g_{\mu\nu}$ is given by

$$\begin{pmatrix}1&0&0&0\\0&-1&0&0\\0&0&-1&0\\0&0&0&-1\end{pmatrix} \tag{1.14}$$

and $\epsilon_{\mu\nu\alpha\beta}$ is 1 if $\mu\nu\alpha\beta$ is an even permutation of 0123, -1 if it is an odd permutation, and 0 if any two or more indices are the same.

In Equations 1.12 and 1.13, we have introduced four *structure functions*: $W_1\left(p\cdot q,Q^2\right)$ and $W_2\left(p\cdot q,Q^2\right)$ for the symmetric part, and $G_1\left(p\cdot q,Q^2\right)$ and $G_2\left(p\cdot q,Q^2\right)$ for the antisymmetric part. We will consider these functions in greater depth in Section 1.3. For now, they serve as useful tools that, in the words of Halzen and Martin [15], "parametrize our total ignorance of the form of the current at the [hadron] end of the propagator."

We can then combine the leptonic and hadronic tensors to obtain the full equation for the differential cross section. Terms that multiply tensors with opposite symmetry vanish in the sum over μ and ν, so we are left with

$$\frac{d^2\sigma}{d\Omega dE'}=\frac{\alpha^2}{2Mq^4}\frac{E'}{E}\left[L_{\mu\nu}^{(S)}W^{\mu\nu(S)}+L_{\mu\nu}^{\prime(S)}(s,s')W^{\mu\nu(S)}-L_{\mu\nu}^{(A)}(s)W^{\mu\nu(A)}(S)-L_{\mu\nu}^{\prime(A)}(s')W^{\mu\nu(A)}(S)\right]. \tag{1.15}$$

In principle, each tensor product in Equation 1.15 is a measurable quantity, so that one might conduct a series of experiments investigating $W^{\mu\nu(S)}$ and $W^{\mu\nu(A)}$ by varying the initial and final particle spins and measuring the cross sections. For example, we can single out the $L_{\mu\nu}^{(S)}W^{\mu\nu(S)}$ term by averaging over initial spins and summing over final spins, thus measuring the unpolarized cross section:

$$\frac{d^2\sigma^{unpol}}{d\Omega dE'}\left(k,p;k'\right)=\frac{\alpha^2}{Mq^4}\frac{E'}{E}L_{\mu\nu}^{(S)}W^{\mu\nu(S)}. \tag{1.16}$$

Alternatively, we might measure the cross section for both target-nucleon spin states. The difference between these cross sections, summed over the final electron spins, would then give us access to the $L_{\mu\nu}^{\prime(A)}W^{\mu\nu(A)}$ term:

$$\sum_{s\prime}\left[\frac{d^2\sigma}{d\Omega dE'}\left(k,s,p,-S;k',s'\right)-\frac{d^2\sigma}{d\Omega dE'}\left(k,s,p,S;k',s'\right)\right]=\frac{2\alpha^2}{Mq^4}\frac{E'}{E}L_{\mu\nu}^{(A)}W^{\mu\nu(A)}. \tag{1.17}$$

In practice, of course, it is usually simpler to control the spin s of the incident electron than it is to measure the scattered electron's spin s', which constrains experimental investigations of the hadronic tensor.

1.3 Nucleon Structure Functions: An Overview

Suppose that we were scattering relativistic electrons from a point-like, spin-$\frac{1}{2}$ nucleon that was infinitely heavy, with a charge of $+1e$; conservation of energy would dictate that $E = E'$. In this situation, we could replace the expression in Equation 1.16 with the much simpler, unpolarized Mott cross section:

$$\left(\frac{d\sigma}{d\Omega}\right)_{\text{Mott}} = \frac{\alpha^2 \cos^2 \frac{\theta}{2}}{4E^2 \sin^4 \frac{\theta}{2}} \tag{1.18}$$

where θ is the electron scattering angle in the laboratory frame. Since a real nucleon has structure and finite mass, we cannot make that replacement, but we can use the Mott cross section to simplify Equation 1.16, both algebraically and conceptually

$$\frac{d^2\sigma^{unpol}}{d\Omega dE'} = \left(\frac{d\sigma}{d\Omega}\right)_{\text{Mott}} \left[W_2(\nu, Q^2) + 2W_1(\nu, Q^2) \tan^2\left(\frac{\theta}{2}\right)\right] \tag{1.19}$$

where we have expressed W_1 and W_2 as functions of $\nu = p \cdot q/M$ rather than as functions of $p \cdot q$.

The form of Equation 1.19 makes clear that the inelastic structure functions $W_1(\nu, Q^2)$ and $W_2(\nu, Q^2)$ parameterize the manner in which the target nucleon's behavior deviates from that of a static particle. In their dependence on Q^2, they also parameterize its structure, *i.e.* the way in which it is different from a point particle. This, indeed, is why they bear the name *structure functions*. In this section, we will explore the use of structure functions to understand electron-nucleon scattering, in both the unpolarized case (where we have averaged over the initial particle spins) and the polarized case. Finally, in Section 1.3.3, we will examine physical interpretations of these useful quantities.

1.3.1 Unpolarized Structure Functions

By convention, the unpolarized structure functions $F_1(x, Q^2)$ and $F_2(x, Q^2)$ are commonly used in place of the structure functions $W_1(\nu, Q^2)$ and $W_2(\nu, Q^2)$ that we defined in Section 1.2.2. The two pairs of structure functions are very closely related

$$F_1(x, Q^2) = MW_1(\nu, Q^2) \tag{1.20}$$

$$F_2(x, Q^2) = \nu W_2(\nu, Q^2) \tag{1.21}$$

where the target nucleon has mass M. This convention reflects the experimental fact of Bjorken scaling (see Section 1.3.3.1): in the Bjorken limit of large Q^2, large ν, and fixed x, F_1 and F_2 lose most of their dependence on Q^2 and can be approximated as functions of x alone. Indeed, as we will see in Section 1.3.3.1, there exists a simple relationship between the two structure functions in that limit.

In our new notation, Equation 1.16 becomes

$$\frac{d^2\sigma^{unpol}}{d\Omega dE'} = \left(\frac{d\sigma}{d\Omega}\right)_{\text{Mott}} \left[\frac{1}{\nu} F_2(x, Q^2) + \frac{2}{M} F_1(x, Q^2) \tan^2\left(\frac{\theta}{2}\right)\right]. \tag{1.22}$$

Let us digress briefly from our discussion of pure electron-nucleon scattering to address a possible ambiguity in scattering experiments with a nuclear target. If the nucleus has mass number A, there are two competing conventions for the definition of F_1 and F_2. The definitions we have given in Equations 1.20 and 1.21 are the unpolarized structure functions over the nucleus. The alternative convention defines per-nucleon unpolarized structure functions $F_1' = F_1/A$ and $F_2' = F_2/A$. In this dissertation, we use the first convention, defining our structure functions over the nucleus rather than per nucleon.

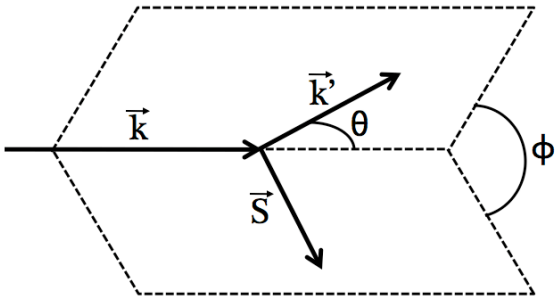

Figure 1.5: Scattering $(\hat{k}, \hat{k}')$ and polarization $(\hat{k}, \hat{S})$ planes.

1.3.2 Polarized Structure Functions

The measurement of the structure functions $F_1(x, Q^2)$ and $F_2(x, Q^2)$ through Equation 1.22 gives access to the symmetric part $W^{\mu\nu(S)}$ of the hadronic tensor. Recall from Equation 1.13 that the anti-symmetric part, $W^{\mu\nu(A)}$, is also expressed in terms of structure functions: $G_1(\nu, Q^2)$ and $G_2(\nu, Q^2)$.

As we found with $W_1(\nu, Q^2)$ and $W_2(\nu, Q^2)$ in Section 1.3.1, it is convenient to replace $G_1(\nu, Q^2)$ and $G_2(\nu, Q^2)$ with polarized structure functions that, to a first approximation, lose their Q^2-dependence in the Bjorken limit. These polarized structure functions, $g_1(x, Q^2)$ and $g_2(x, Q^2)$, are defined in terms of G_1 and G_2

$$g_1(x, Q^2) = M^2 \nu G_1(\nu, Q^2) \tag{1.23}$$

$$g_2(x, Q^2) = M\nu^2 G_2(\nu, Q^2). \tag{1.24}$$

Let us imagine an experiment with longitudinally polarized electrons – that is, electrons with spin parallel ($\uparrow$) or antiparallel ($\downarrow$) to their direction of motion – incident on a polarized nucleon target; the subject of this dissertation is just such an experiment. If we flip the target nucleon polarization, $S \to -S$, what difference will we measure in the differential cross section? Anselmino *et al.* [18] give a general description. Consider an arbitrary nucleon spin direction

$$S^\mu = (0, \hat{S}). \tag{1.25}$$

Meanwhile, the longitudinally polarized electron has spin

$$s^\mu_\uparrow = -s^\mu_\downarrow = \frac{1}{m}(E, \vec{k}) \tag{1.26}$$

where we recall that $\vec{k}$ is the three-momentum of the initial electron and E is its energy.

Now we could flip the spin of the target nucleon and find the difference in cross sections between the two cases; keeping the target spin the same, while flipping the spin of the initial electron, would give the same result. The difference in cross sections is given by [18]

$$\frac{d^2\sigma^{\uparrow,S}}{d\Omega dE'} - \frac{d^2\sigma^{\uparrow,-S}}{d\Omega dE'} = -\frac{4\alpha^2}{Q^2}\frac{E'}{E}\left[\frac{(\vec{k}' \cdot \hat{S} + \vec{k} \cdot \hat{S})}{M\nu} g_1(x, Q^2) + \frac{2(E\vec{k}' \cdot \hat{S} - E'\vec{k} \cdot \hat{S})}{M\nu^2} g_2(x, Q^2)\right]. \tag{1.27}$$

As before, E' is the energy of the scattered electron and $\vec{k}'$ is its three-momentum.

We are primarily concerned here with two special cases: longitudinal and transverse nucleon polarization, defined relative to the electron momentum. We will take the longitudinal case first. In

this terminology, a longitudinally polarized nucleon target has a spin either parallel ($\Uparrow$) or antiparallel ($\Downarrow$) to the incoming electron's longitudinal spin. We will take the parallel spin to be the positive variant of S; we thus have

$$\vec{k} \cdot \hat{S} = |\vec{k}| = E \tag{1.28}$$

$$\vec{k}' \cdot \hat{S} = E' \cos\theta \tag{1.29}$$

where we have neglected the electron mass, and where θ is the electron scattering angle in the laboratory frame, as defined in Figure 1.5. If we apply these results to Equation 1.27 and use the definition of Q^2 from Equation 1.5, we obtain the full expression for the longitudinal cross-section difference

$$\frac{d^2\sigma^{\downarrow\Uparrow}}{d\Omega dE'} - \frac{d^2\sigma^{\uparrow\Uparrow}}{d\Omega dE'} = \frac{4\alpha^2}{Q^2}\frac{E'}{E}\left[\frac{E + E'\cos\theta}{M\nu} g_1(x, Q^2) - \frac{Q^2}{M\nu^2} g_2(x, Q^2)\right]. \tag{1.30}$$

Meanwhile, a transversely polarized nucleon target has a spin perpendicular to the incident electron's momentum direction; the two senses of the nucleon spin are denoted $\Rightarrow$ and $\Leftarrow$. Our dot products may then be evaluated as

$$\vec{k} \cdot \hat{S} = 0 \tag{1.31}$$

$$\vec{k}' \cdot \hat{S} = E'\hat{k}' \cdot \hat{S} = E' \sin\theta \cos\phi \tag{1.32}$$

where ϕ is the angle between the polarization plane defined by $(\hat{k}, \hat{S})$ and the scattering plane defined by $(\hat{k}, \hat{k}')$, as shown in Figure 1.5. Inserting our results into Equation 1.27, we find the relationship between differential cross sections of the two transverse target polarizations

$$\frac{d^2\sigma^{\downarrow\Rightarrow}}{d\Omega dE'} - \frac{d^2\sigma^{\uparrow\Rightarrow}}{d\Omega dE'} = \frac{4\alpha^2}{Q^2}\frac{E'^2}{E}\sin\theta\cos\phi\left(\frac{g_1(x, Q^2)}{M\nu} + \frac{2E g_2(x, Q^2)}{M\nu^2}\right). \tag{1.33}$$

We see that the magnitude of the difference between cross sections is maximized when $\phi = 0$ or when $\phi = \pi$, the two cases when $\hat{S}$ lies on the scattering plane.

In practice, performing two complete, independent cross-section measurements and then taking their difference is an unnecessarily difficult and time-consuming way to investigate $g_1(x, Q^2)$ and $g_2(x, Q^2)$. It is simpler to study the structure functions by measuring *asymmetries*, in which many experimental limitations and sources of error cancel each other out. Let us adopt $d\sigma$ as shorthand for the differential cross section $d^2\sigma/d\Omega dE'$; we will represent the unpolarized differential cross section as $\bar{\sigma}$. We can then define a longitudinal spin-spin asymmetry $A_\parallel$ between cases where the nucleon and electron spins are parallel and antiparallel to each other

$$A_\parallel \equiv \frac{d\sigma^{\downarrow\Uparrow} - d\sigma^{\uparrow\Uparrow}}{d\sigma^{\downarrow\Uparrow} + d\sigma^{\uparrow\Uparrow}} = \frac{d\sigma^{\downarrow\Uparrow} - d\sigma^{\uparrow\Uparrow}}{2\bar{\sigma}}. \tag{1.34}$$

In the case of a transversely polarized nucleon target, we can define an analogous transverse spin-spin asymmetry $A_\perp$:

$$A_\perp \equiv \frac{d\sigma^{\downarrow\Rightarrow} - d\sigma^{\uparrow\Rightarrow}}{d\sigma^{\downarrow\Rightarrow} + d\sigma^{\uparrow\Rightarrow}} = \frac{d\sigma^{\downarrow\Rightarrow} - d\sigma^{\uparrow\Rightarrow}}{2\bar{\sigma}}. \tag{1.35}$$

Here, $\Rightarrow$ denotes a target spin in the scattering plane, perpendicular to the incident electron momentum and pointing toward the side of the beamline where scattered electrons are detected.

The denominators of the spin-spin asymmetries $A_\parallel$ and $A_\perp$ are the same: each is equal to $2\bar{\sigma}$, twice the unpolarized differential cross section. Their numerators are given by Equations 1.30 and 1.33, respectively.

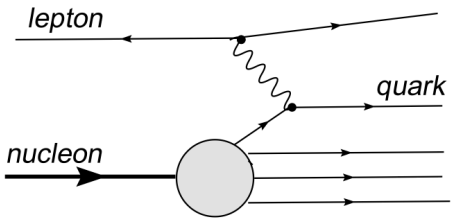

Figure 1.6: Deep inelastic scattering as scattering from a single quark, reproduced from Kuhn *et al.* [10].

Through these three measured quantities – $A_\parallel$, $A_\perp$, and $\bar{\sigma}$ – we may thus gain experimental access to the structure functions $F_1(x, Q^2)$, $F_2(x, Q^2)$, $g_1(x, Q^2)$, and $g_2(x, Q^2)$ [19].

1.3.3 Interpretation

We have seen that the unpolarized structure functions $F_1(x, Q^2)$ and $F_2(x, Q^2)$ (Section 1.3.1) and polarized structure functions $g_1(x, Q^2)$ and $g_2(x, Q^2)$ (Section 1.3.2) are useful algebraic tools in describing electron-nucleon scattering. These functions are more than means to simplify complicated equations, however: they are of great physical interest in and of themselves for the description they give of nucleon structure. In this section, we will discuss the physical interpretation of these structure functions, setting the stage for more focused investigations.

1.3.3.1 Bjorken Scaling

When we examine an object with a finite size – be it a cell, an atom, or a nucleon – our measurement will always depend on the spatial resolution of our probe. For experiments involving scattering through single-photon exchange, this means that our observables will depend on Q^2, the four-momentum transferred in the interaction.

Suppose that we increase the spatial resolution of our probe into nucleon structure. As we saw in Section 1.2.1, as Q^2 increases, we can start to think of inelastic electron-nucleon scattering as elastic electron-quark scattering: the electron is effectively interacting with a single "free", spin-$\frac{1}{2}$ quark inside the nucleon (Figure 1.6). Since quarks are point-like objects, further increases in spatial resolution will have no effect, and the behavior of the scattering interaction will lose its Q^2 dependence.

This phenomenon, known as Bjorken scaling, was first predicted by Bjorken and Paschos in 1969 [20]. It applies in the Bjorken limit of infinite energy and four-momentum transfer

$$Q^2 \to \infty \text{ and } \nu \to \infty \text{ with fixed } x = \frac{Q^2}{2M\nu}. \tag{1.36}$$

In this limit, the structure functions are independent of Q^2, so we can write them as $F_1(x)$, $F_2(x)$, $g_1(x)$, and $g_2(x)$, and the relationship between $F_1(x)$ and $F_2(x)$ is given by the Callan-Gross relation [21]:

$$F_2(x) = 2xF_1(x). \tag{1.37}$$

The scaling behavior of the structure functions is not exact, however. Scaling violation arises from the fact that single-photon exchange is only the simplest process through which an electron can interact with hadronic matter; higher-order processes obeying different dynamics also contribute to cross sections. Figure 1.7 shows the Feynman diagrams for two such processes, in which either the

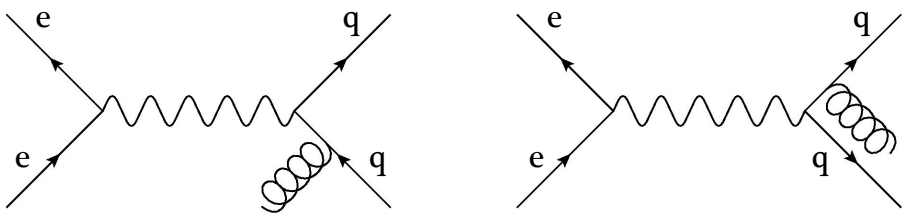

Figure 1.7: Lowest-order Feynman diagrams for gluon radiation in electron-quark scattering, complicating the simple picture of single-photon exchange.

incident quark or the scattered quark emits a hard gluon. Adding these radiative corrections to the simple picture of Figure 1.3 violates one of the underlying assumptions of Bjorken scaling – that the quarks' transverse momenta are negligible in the frame where the nucleon has a large longitudinal momentum – and gives the cross section a logarithmic evolution with Q^2.

Figure 1.8 shows the measured Q^2 evolution of the proton structure function $F_2^p(x, Q^2)$ for a range of fixed x values that spans four orders of magnitude. Bjorken scaling is approximately satisfied at $x \approx 0.1$, but scaling violation is clear at low and high values of x. Once the size of a structure function has been measured for some high Q^2 at a given value of x, its Q^2 evolution can be calculated from QCD.

1.3.3.2 The Quark-Parton Model

The approximate obedience of the nucleon structure functions to Bjorken scaling is strong evidence for the *quark-parton model*, in which a nucleon is composed of pointlike constituents that do not interact with each other and each carry a fraction x of the total momentum. These *partons* are identified with quarks, and we can neglect their interactions in the limit of small spatial resolution (large Q^2) because QCD predicts that they are asymptotically free at small distances.

In this picture, the cross section for lepton-nucleon deep inelastic scattering can then be modeled as the weighted sum of the cross sections for lepton scattering from each individual quark, with the weights computed according to the quark number densities.

Let us first consider the unpolarized case, in which we average over the possible spin states $\uparrow$ and $\downarrow$ of the parton. We define the unpolarized parton distribution function (PDF) $q_i(x)$ as the sum of the number densities for the two spin states

$$q_i(x) = q_i^{\uparrow}(x) + q_i^{\downarrow}(x). \tag{1.38}$$

In the Bjorken limit, $q_i(x)$ is simply the probability that the nucleon's i^{th} quark has momentum fraction x. (We can account for scaling violation by extending this notation to include Q^2 dependence: $q_i(x, Q^2)$ is the probability that the nucleon's i^{th} quark, when probed with a spatial resolution of Q^2, is found to have momentum fraction x.)

This simple parton model predicts that, in the Bjorken limit, the unpolarized structure functions satisfy

$$F_1(x) = \frac{1}{2}\sum_i e_i^2 q(x) = \frac{1}{2}\sum_i e_i^2 \left[q_i^{\uparrow}(x) + q_i^{\downarrow}(x)\right] \tag{1.39}$$

and

$$F_2(x) = x\sum_i e_i^2 q(x) = x\sum_i e_i^2 \left[q_i^{\uparrow}(x) + q_i^{\downarrow}(x)\right] \tag{1.40}$$

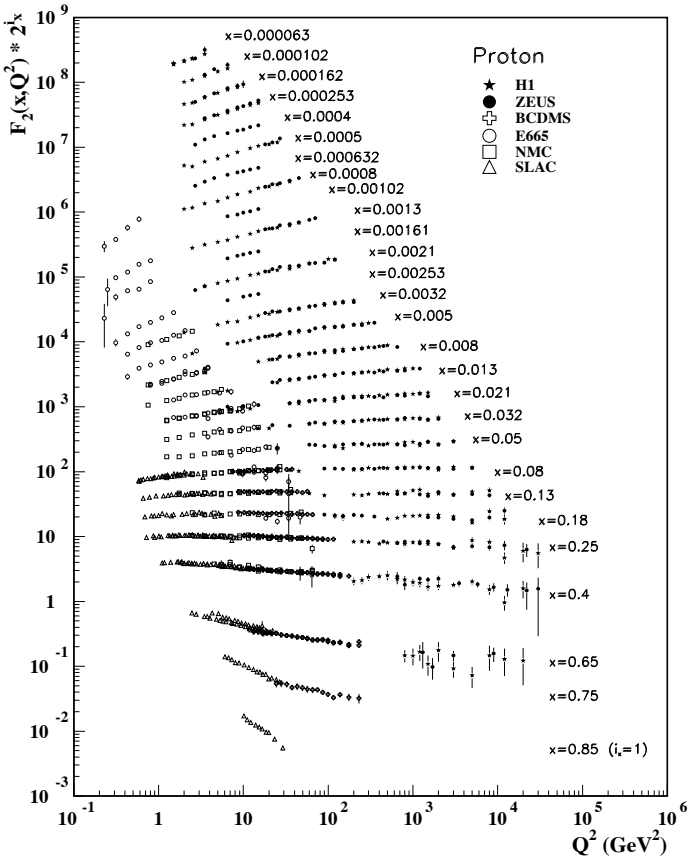

Figure 1.8: Scaling violation in the proton structure function F_2^p, reproduced from Nakamura *et al.* [11]. In order to provide visual separation between the data sets for different bins of fixed x, the F_2^p value has been multiplied by 2^{i_x}, where $1 \leq i_x \leq 28$ is the number of the x bin. H1 and ZEUS data points are from positron-proton collider experiments. The remaining data points are from lepton scattering on a fixed proton target; SLAC used an electron probe, while BCDMS, E665 and NMC used a muon probe.

where e_i is the electric charge of the i^{th} quark, which enters into the equations because the quark-virtual photon coupling is electromagnetic.

To predict the polarized nucleon structure functions in this model, we must introduce the polarized PDF $\Delta q_i(x)$

$$\Delta q_i(x) = q_i^{\uparrow}(x) - q_i^{\downarrow}(x). \tag{1.41}$$

The sign of $\Delta q_i(x)$ is set by letting $\uparrow(\downarrow)$ denote a quark spin (anti)parallel to the nucleon spin [18].

The polarized structure function $g_1(x)$ is then directly analogous to its unpolarized counterpart $F_1(x)$

$$g_1(x) = \frac{1}{2}\sum_i e_i^2 \Delta q_i(x) = \frac{1}{2}\sum_i e_i^2 \left[q_i^{\uparrow}(x) - q_i^{\downarrow}(x)\right]. \tag{1.42}$$

This simple model, however, fails to produce a description of $g_2(x)$, in which the transverse spin of the quark (relative to the nucleon spin direction) becomes important. To compute g_2, we need to

understand the forces that bind the nucleon together, *i.e.* the interactions between gluons and the struck quark.

1.3.3.3 The Operator Product Expansion

To calculate deep-inelastic-scattering cross sections or structure functions at finite values of Q^2, it is useful to separate the non-perturbative parts of the equations from the perturbative parts. The standard method of achieving this goal is to use the **O**perator **P**roduct **E**xpansion (OPE), introduced in 1969 by Kenneth Wilson [22]. Let us consider the product of two local operators $\mathcal{O}_a(d)\mathcal{O}_b(0)$, separated by a distance d. As their separation distance approaches zero, the two operators are essentially located at the same point, and we can express their product as an expansion in local operators:

$$\lim_{d\to 0} \mathcal{O}_a(d)\mathcal{O}_b(0) = \sum_k c_{abk}(d)\mathcal{O}_k(0). \tag{1.43}$$

The Wilson coefficients $c_{abk}(d)$ may be calculated in perturbation theory, since non-perturbative effects in QCD act on a scale much larger than d [23]. Information about these effects is contained in the non-perturbative operators $\mathcal{O}_k(0)$, each of which makes a cross-section contribution of order $x^{-n}(Q/M)^{2-t}$. The term n in the exponent is the operator spin; t is its *twist*, defined as

$$t \equiv D - n = \text{dimension} \; - \; \text{spin}. \tag{1.44}$$

Leading-twist ($t = 2$) operators dominate the OPE at large values of Q^2, but higher-twist operators become more important as Q^2 is reduced – and the polarized structure function $g_2(x, Q^2)$ gives us access to those higher-twist terms. In 1977, Wandzura and Wilczek showed that this structure function can be expressed as the sum of a twist-2 term (the Wandzura-Wilczek term $g_2^{WW}(x, Q^2)$) and a twist-3 term that arises from quark-gluon correlations [24]. That is,

$$g_2(x, Q^2) = g_2^{WW}(x, Q^2) + \bar{g_2}(x, Q^2) \tag{1.45}$$

where $\bar{g_2}(x, Q^2)$ is the twist-3 term and $g_2^{WW}(x, Q^2)$ can be expressed entirely as a function of $g_1(x, Q^2)$

$$g_2^{WW}(x, Q^2) = -g_1(x, Q^2) + \int_x^1 \frac{g_1(y, Q^2)}{y} dy. \tag{1.46}$$

Since $g_2(x, Q^2)$ contributes at leading order to the observable $A_\perp$, and since knowledge of $g_1(x, Q^2)$ can be used make a clean distinction between its twist-2 and twist-3 elements, $g_2(x, Q^2)$ is an appealing probe into non-perturbative QCD at higher twist.

1.4 Outline of the Dissertation

In the remainder of this dissertation, we will motivate and describe the measurement of a virtual photon-nucleon asymmetry, $A_1(x, Q^2)$, which gives access to three structure functions – $F_1(x, Q^2)$, $g_1(x, Q^2)$, and $g_2(x, Q^2)$. When measured on both the proton and the neutron, $A_1(x, Q^2)$ can also be used to untangle the polarized and unpolarized parton distribution functions, testing theoretical solutions to the nucleon spin puzzle. We will explore the theory and implications of this asymmetry, as well as previous measurements, in Chapter 2. Chapter 3 describes the source of our data, Experiment E06-014, which ran in Hall A of Jefferson Lab in February and March of 2009.

The measurement of any double-spin asymmetry requires understanding the polarizations both of the lepton beam and of the nucleon target; in Chapter 4, we describe Hall A's electron beam

polarimetry apparatus and discuss the final determination of the electron beam polarization. Chapter 5 contains a detailed discussion of the BigBite spectrometer, which took data for the asymmetry measurements, and its calibration. The specifics of our data analysis procedures are described in Chapter 6, and we report and discuss our preliminary results in Chapter 7.

Chapter 2

A_1^n: Measurements and Models

As we saw in Chapter 1, much theoretical and experimental effort has been devoted to teasing apart the problem of nucleon structure. By separating out the many different aspects of the problem, physicists have been able to make great progress on the puzzle, piece by piece.

In this dissertation, our piece of the puzzle concerns the virtual photon-nucleon asymmetries A_1 and A_2. In Section 2.1, we will define these asymmetries and discuss their physical interpretation, including how proton and neutron measurements can be combined to give insights into the nucleon spin puzzle. In Section 2.2, we survey previous measurements to summarize the current experimental status of these quantities. Finally, Section 2.3 is a survey of attempts to model A_1 theoretically. Having studied these asymmetries for the proton and the neutron, we will then turn our attention in Chapter 3 and beyond to a new measurement of A_1 on the ^{3}He nucleus and ultimately on the neutron.

2.1 The Spin Asymmetries A_1 and A_2

In electron scattering from a nucleon, the electron and nucleon exchange a virtual photon with four-momentum q. All three particles in this interaction have spin, and the relative spin direction of each affects the probability of the scattering interaction.

Consider the hadronic vertex of the interaction, where the nucleon (with four-momentum p) absorbs the virtual photon. Unlike a real photon, a virtual photon can be polarized in either a transverse or longitudinal direction relative to its momentum $\vec{q}$: it has three available polarization states rather than just two. What is the likelihood of the nucleon absorbing such a virtual photon? Answering this question requires a careful treatment of the flux factor, which is the number density of the incident virtual photons per unit time and is thus a necessary ingredient in the cross-section formula. While real photons have a flux factor $4M\nu$, the virtual-photon flux factor is arbitrary [15]. We choose a laboratory-frame flux factor $4M\left(\nu - Q^2/2M\right)$ in accordance with the Hand convention [25]. We can then express the laboratory cross section for electron-nucleon scattering in terms of two virtual photon-nucleon cross sections, one (σ_T) for transversely polarized virtual photons and one (σ_L) for longitudinally polarized virtual photons

$$\frac{d\sigma}{dE'd\Omega} = \Gamma(\sigma_T + \epsilon\sigma_L) \tag{2.1}$$

where

$$\Gamma = \frac{\alpha\left(\nu - Q^2/2M\right)}{2\pi^2 Q^2}\frac{E'}{E}\frac{1}{1-\epsilon} \tag{2.2}$$

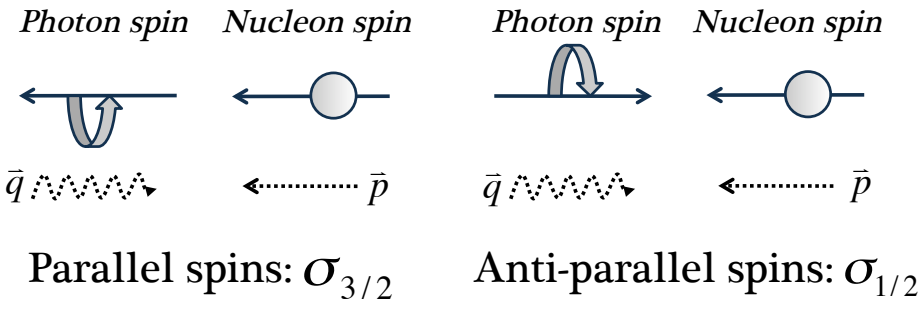

Figure 2.1: Definition of virtual photon-nucleon cross sections $\sigma_{3/2}$ and $\sigma_{1/2}$.

and ϵ, the ratio of the virtual photon's longitudinal polarization to its transverse polarization, is given by

$$\frac{1}{\epsilon} = 1 + 2\left(1 + \frac{Q^2}{\nu^2}\right)\tan^2\frac{\theta}{2}. \tag{2.3}$$

The virtual photon-nucleon cross sections σ_T and σ_L, like the unpolarized structure functions F_1 and F_2, encode information about the hadronic vertex. We can thus express one set of functions in terms of the other set [15]

$$\sigma_T \equiv \frac{4\pi^2\alpha}{\nu - Q^2/2M}\frac{1}{M}F_1(\nu, Q^2) \tag{2.4}$$

$$\sigma_L \equiv \frac{4\pi^2\alpha}{\nu - Q^2/2M}\left[\left(1 + \frac{\nu^2}{Q^2}\right)\frac{1}{\nu}F_2(\nu, Q^2) - \frac{1}{M}F_1(\nu, Q^2)\right]. \tag{2.5}$$

This notation allows us to express a relationship between F_1 and F_2

$$F_1(x, Q^2) = \frac{F_2(x, Q^2)\left(1 + \frac{(2Mx)^2}{Q^2}\right)}{2x\left(1 + \frac{\sigma_L(x,Q^2)}{\sigma_T(x,Q^2)}\right)}. \tag{2.6}$$

Combining this relationship with the Callan-Gross relation (Equation 1.37) allows one to deduce that σ_L vanishes in the Bjorken limit.

Let us suppose that the nucleon is longitudinally polarized and the virtual photon is circularly polarized (that is, it has a rotating transverse polarization), with helicity ± 1. Figure 2.1 shows the two possible spin configurations at this vertex. If the virtual photon and the nucleon have parallel spins, we denote the cross section of the interaction as $\sigma_{3/2}$; if their spins are antiparallel, the cross section is $\sigma_{1/2}$. The subscript of the cross sections represents the total spin projection along the direction of the virtual photon momentum, $\vec{q}$ [26, 16].

This helicity decomposition of the virtual photon absorption cross section allows us to ask how changing the polarization of the virtual photon affects the scattering interaction as a whole.

2.1.1 Definitions of A_1 and A_2

We begin by defining the longitudinal asymmetry, A_1, as the asymmetry between the two cross sections defined in Figure 2.1

$$A_1(x, Q^2) \equiv \frac{\sigma_{1/2} - \sigma_{3/2}}{\sigma_{1/2} + \sigma_{3/2}}. \tag{2.7}$$

A second virtual photon asymmetry, A_2, arises from interference between the longitudinal and transverse virtual photon-nucleon amplitudes. Consider the transition from the initial state $|H,h\rangle$, where the virtual photon has helicity H and the nucleon has helicity h, to a final state $|X\rangle$ that is not observed. We can express the interference cross section σ_{LT} in terms of the transitions between these states [27]

$$\sigma_{LT} = 2\mathrm{Re}\sum_X \langle +\frac{1}{2}, +1|X\rangle\langle -\frac{1}{2}, 0|X\rangle. \tag{2.8}$$

A_2 is then the fraction of the total cross section due to this interference term

$$A_2(x,Q^2) \equiv \frac{2\sigma_{LT}}{\sigma_{1/2}+\sigma_{3/2}}. \tag{2.9}$$

and σ_{LT} may also be expressed in terms of g_1 and g_2 [28]

$$\sigma_{LT} = \frac{4\pi^2\alpha}{M_N(\nu - Q^2/2M)}\frac{\sqrt{Q^2}}{\nu}\left(g_1(x,Q^2)+g_2(x,Q^2)\right) \tag{2.10}$$

Here, M_N is the nucleon mass and α is the fine structure constant.

A_2 is bounded [27] by a function of A_1 and the virtual photon absorption cross sections σ_L and σ_T that we defined in Equations 2.4 and 2.5:

$$|A_2| \leq \sqrt{\frac{\sigma_L}{2\sigma_T}(1+A_1)} \tag{2.11}$$

We can relate A_1 and A_2 to three of the four nucleon structure functions, both unpolarized (F_1) and polarized (g_1 and g_2). To simplify the algebra, it is both convenient and customary to define the ratio γ^2

$$\gamma^2 \equiv \frac{Q^2}{\nu^2} = \frac{(2M_N x)^2}{Q^2}. \tag{2.12}$$

It is then possible to derive the relationships

$$A_1(x,Q^2) = \frac{g_1(x,Q^2) - \gamma^2 g_2(x,Q^2)}{F_1(x,Q^2)} \tag{2.13}$$

$$A_2(x,Q^2) = \frac{\gamma\left[g_1(x,Q^2)+g_2(x,Q^2)\right]}{F_1(x,Q^2)}. \tag{2.14}$$

These equations can be combined to relate our virtual photon asymmetries A_1 and A_2 to the ratio of g_1 and F_1

$$A_1(x,Q^2) + \gamma A_2(x,Q^2) = (1+\gamma^2)\frac{g_1(x,Q^2)}{F_1(x,Q^2)}. \tag{2.15}$$

We can see from Equation 2.12 that $\gamma^2 \to 0$ as $Q^2 \to \infty$. Equation 2.13 then reduces to

$$A_1(x,Q^2) \approx \frac{g_1(x,Q^2)}{F_1(x,Q^2)} \text{ for large } Q^2 \tag{2.16}$$

Equation 2.16 is also supported by a simple physical argument [29]. Let us go back to the picture of our virtual photon as circularly polarized with its helicity parallel or antiparallel to the quark spin. If their spins are antiparallel, the quark may absorb the virtual photon and flip its helicity in the process. If their spins are parallel, however, this absorption is forbidden: the total projection of

the quark and virtual-photon spin onto the momentum axis is 3/2, but the quark is only a spin-1/2 particle.

If the virtual photon's helicity is parallel to the nucleon spin's projection onto its momentum axis (the $\sigma_{3/2}$ case), then it may only be absorbed by a quark whose spin is antiparallel to the spin of the nucleon on that axis. If $q^{\downarrow}(x)$ represents the distribution function of such quarks, then we have

$$\sigma_{3/2} \sim \sum e_i^2 q_i^{\downarrow}(x). \tag{2.17}$$

Now consider a virtual photon whose spin is antiparallel to the projection of the nucleon spin (the $\sigma_{1/2}$ case). By an analogous argument, it may only be absorbed by a quark whose spin is parallel to the spin of the nucleon

$$\sigma_{1/2} \sim \sum e_i^2 q_i^{\uparrow}(x). \tag{2.18}$$

We may then express A_1 as

$$A_1(x) \sim \frac{\sum e_i^2 \left(q_i^{\uparrow}(x) - q_i^{\downarrow}(x)\right)}{\sum e_i^2 \left(q_i^{\uparrow}(x) + q_i^{\downarrow}(x)\right)} = \frac{\sum e_i^2 \Delta q_i(x)}{\sum e_i^2 q_i(x)} = \frac{g_1(x)}{F_1(x)} \tag{2.19}$$

where we have used the quark-model expressions for $F_1(x)$ and $g_1(x)$, as given by Equations 1.39 and 1.42.

To leading order, $F_1(x, Q^2)$ and $g_1(x, Q^2)$ evolve with Q^2 in the same way, so their Q^2 evolutions partially cancel in Equation 2.16, leaving A_1 with little dependence on Q^2. Experimental data support this observation for both the proton and the neutron, as shown in Figure 2.2. This behavior helps make A_1 an appealing probe into the x dependence of nucleon spin structure.

2.1.2 Measuring A_1 and A_2 with a Polarized Electron Beam

We have defined A_1 and A_2 based on the orientation of the virtual photon spin relative to the nucleon spin. In practice, however, it is generally far simpler to align the spin of the incident electron either parallel or perpendicular to the nucleon spin. Knowing the electron spin and the kinematics of the interaction, we can then recover the effective polarization of the virtual photons.

Our task, then, is to find expressions for the virtual photon-nucleon asymmetries A_1 and A_2 in terms of the experimental electron-nucleon asymmetries $A_{\parallel}$ and $A_{\perp}$, defined in Equations 1.34 and 1.35. These latter two asymmetries depend on all four structure functions – F_1, F_2, g_1, and g_2 – which complicates comparison with theory. Fortunately, we can eliminate F_2 from the final linear combination of $A_{\parallel}$ and $A_{\perp}$ through use of the variable $R(x, Q^2)$, the ratio of the longitudinal to transverse virtual photoabsorption cross sections, which has been measured in earlier experiments [31]:

$$R \equiv \frac{\sigma_L}{\sigma_T} = \frac{F_2}{2xF_1}\left(1 + \frac{4M^2x^2}{Q^2}\right) - 1. \tag{2.20}$$

With R encapsulating our dependence on F_2, we may express the ratios g_1/F_1 and g_2/F_1 in terms of the parallel and perpendicular electron-nucleon asymmetries [32]

$$\frac{g_1}{F_1} = \frac{1}{d'}\left(A_{\parallel} + \tan\frac{\theta}{2} A_{\perp}\right) \tag{2.21}$$

$$\frac{g_2}{F_1} = \frac{y}{2d'}\left(\frac{E + E'\cos\theta}{E'\sin\theta} A_{\parallel} - A_{\perp}\right) \tag{2.22}$$

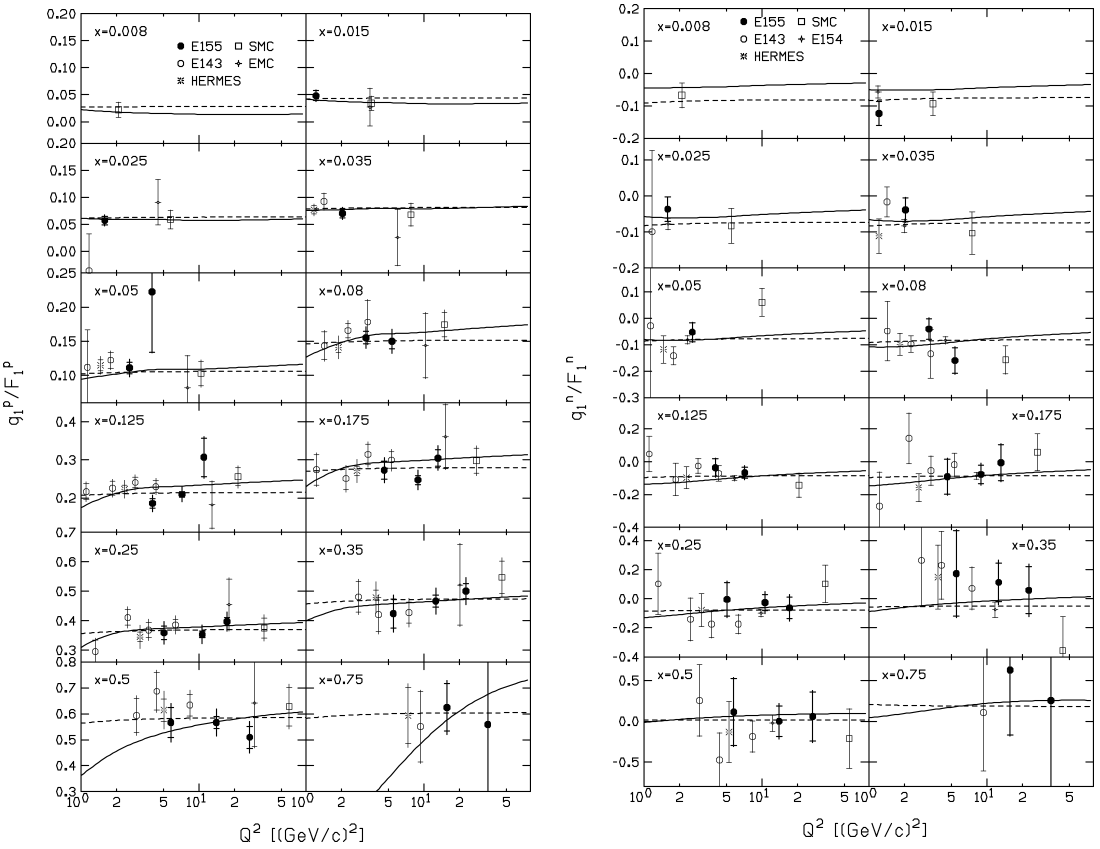

(a) (b)

Figure 2.2: Q^2 evolution of g_1/F_1 ratio for the proton (a) and for the neutron (b), reproduced from Anthony *et al.* [30].

where $y = \nu/E$ and

$$d' = \frac{(1-\epsilon)(2-y)}{y(1+\epsilon R)}. \tag{2.23}$$

With some algebra (see, for example, Melnitchouk *et al.* [32]), we may then obtain

$$A_{\parallel} = D\,(A_1 + \eta A_2) \tag{2.24}$$

$$A_{\perp} = d\,(A_2 - \xi A_1) \tag{2.25}$$

where we have used the kinematic variables

$$D = \frac{E - \epsilon E'}{E(1+\epsilon R)} \tag{2.26}$$

$$\eta = \frac{\epsilon\sqrt{Q^2}}{E - \epsilon E'} \tag{2.27}$$

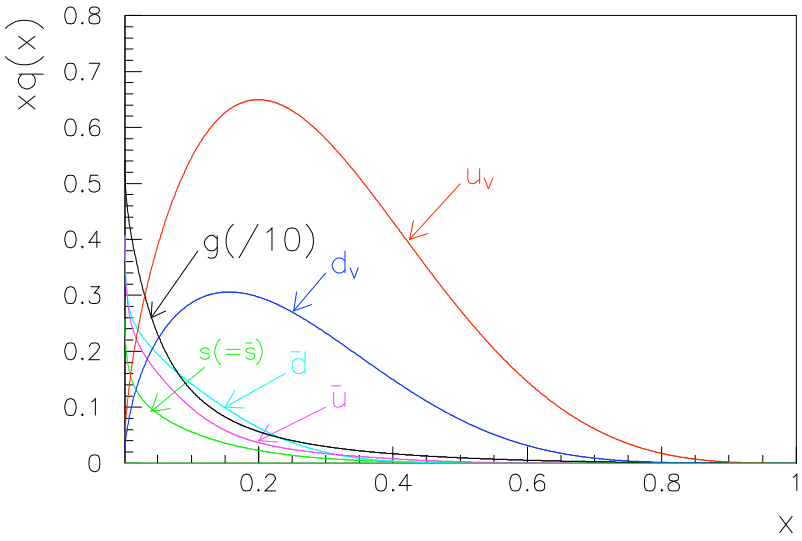

Figure 2.3: Proton parton distribution functions at $Q^2 = 5$ (GeV/c)^2. The PDFs marked u_V and d_V correspond to valence up and down quarks, respectively. Sea quark distributions are denoted $\bar{u}$ (up sea quarks), $\bar{d}$ (down sea quarks), or $s/\bar{s}$ (strange sea quarks). The gluon distribution, divided by 10 to give it the same scale as the others, is denoted g. This figure is reproduced from Zheng [16] and derived from global fits performed by Pumplin *et al.* [33].

$$d = D\sqrt{\frac{2\epsilon}{1+\epsilon}} \tag{2.28}$$

$$\xi = \eta\frac{1+\epsilon}{2\epsilon}. \tag{2.29}$$

Equations 2.24 and 2.25 give us, in turn,

$$A_1 = \frac{1}{D\,(1+\eta\xi)}A_{\parallel} - \frac{\eta}{d\,(1+\eta\xi)}A_{\perp} \tag{2.30}$$

$$A_2 = \frac{\xi}{D\,(1+\eta\xi)}A_{\parallel} + \frac{1}{d\,(1+\eta\xi)}A_{\perp} \tag{2.31}$$

which allow the direct computation of A_1 and A_2 from asymmetries measured in deep inelastic electron-nucleon scattering.

2.1.3 A_1 for the Proton and the Neutron: Flavor Decomposition

In Section 1.1.1, we described the partons that make up the nucleon: valence quarks (up and down), sea quarks and antiquarks (up, down and strange), and gluons. The parton distribution functions (PDFs) $q(x, Q^2)$ allow us to refine this picture by giving the probability of finding a particular parton, carrying a momentum fraction x, with a probe of inverse-squared spatial resolution Q^2.

Figure 2.3 shows the x evolution of proton PDFs at a fixed value of Q^2. We see that gluons and sea quarks dominate at low x, while the valence u and d quarks dominate at high x. This region, accessible through deep inelastic scattering, is often called the valence quark region. The dominance of valence quarks makes this a relatively simple region to model theoretically; perturbative QCD

may be used to predict structure functions, asymmetries and PDFs in the valence quark region, but not at lower values of x.

The unpolarized PDFs $q(x)$ are insensitive to spin; polarized PDFs, defined in Equation 1.41 as $\Delta q_i(x) = q_i^{\uparrow}(x) - q_i^{\downarrow}(x)$, incorporate spin information. If we assume isospin symmetry, we can combine data for the proton and the neutron to perform a flavor decomposition, separating out the behavior of different types of quarks.

For measurements in the valence quark region, we can ignore the contributions of strange quarks. Let $q(x)$ and $\Delta q(x)$ be proton PDFs. We can then combine Equations 1.39 and 1.42 to extract the ratio of g_1^p to F_1^p in terms of PDFs

$$\frac{g_1^p}{F_1^p} = \frac{4\Delta u(x) + \Delta d(x) + 4\Delta\bar{u}(x) + \Delta\bar{d}(x)}{4u(x) + d(x) + 4\bar{u}(x) + \bar{d}(x)}. \tag{2.32}$$

By isospin symmetry, the ratio for the neutron is the same, but with the proton PDFs $u(x)$ and $d(x)$ interchanged

$$\frac{g_1^n}{F_1^n} = \frac{\Delta u(x) + 4\Delta d(x) + \Delta\bar{u}(x) + 4\Delta\bar{d}(x)}{u(x) + 4d(x) + \bar{u}(x) + 4\bar{d}(x)}. \tag{2.33}$$

With a little algebra, we can combine Equations 2.32 and 2.33 to find the ratio of polarized PDFs to unpolarized PDFs for both u and d quarks. We obtain

$$\frac{\Delta u + \Delta\bar{u}}{u + \bar{u}} = \frac{4}{15}\frac{g_1^p}{F_1^p}\left(4 + \frac{d + \bar{d}}{u + \bar{u}}\right) - \frac{1}{15}\frac{g_1^n}{F_1^n}\left(1 + 4\frac{d + \bar{d}}{u + \bar{u}}\right). \tag{2.34}$$

$$\frac{\Delta d + \Delta\bar{d}}{d + \bar{d}} = \frac{4}{15}\frac{g_1^n}{F_1^n}\left(4 + \frac{u + \bar{u}}{d + \bar{d}}\right) - \frac{1}{15}\frac{g_1^p}{F_1^p}\left(1 + 4\frac{u + \bar{u}}{d + \bar{d}}\right). \tag{2.35}$$

Equations 2.34 and 2.35 are often presented in a simplified form, using the variable R^{du} to represent the ratio of down-quark PDFs to up-quark PDFs

$$R^{du} \equiv \frac{d + \bar{d}}{u + \bar{u}}. \tag{2.36}$$

As shown in Figure 2.3, the antiquark distributions $\bar{u}$ and $\bar{d}$ approach zero for $x > 0.3$, so that $R^{du} = (d + \bar{d}/(u + \bar{u}) \approx d/u$. This ratio may be extracted from existing data on protons and deuterons using electrons or neutrinos as probes. In the former case, data going to higher x is available, at the expense of increased dependence on nuclear models [34]. Figure 2.4 shows the evolution in x of $d/u \approx R^{du}$.

We see that combining measurements of g_1/F_1 on the proton with measurements of g_1/F_1 on the neutron allows us to compute the flavor-decomposed quark helicity distributions of Equations 2.34 and 2.35, when combined with existing data on R^{du}. These g_1/F_1 ratios are approximately equal to A_1 at large values of Q^2, but this approximation is not generally needed, since the asymmetry A_2 may be measured with the same data and g_1/F_1 is given exactly by a linear combination of A_1 and A_2 (Equation 2.15).

Equations 2.34 and 2.35 give PDF ratios $(\Delta q + \Delta\bar{q})/(q + \bar{q})$ for all quarks – valence and sea – but theoretical predictions are often given only for valence quark distributions $\Delta q/q$. A comparison of experiment to theory thus requires calculating how much these two ratios differ. Following the work of Zheng [36], we will show this calculation for generic quark PDFs q, for which either d or u may be substituted.

The antiquark content $\bar{q}$ of a nucleon is, by definition, part of the sea; the quark content is divided between valence quarks and sea quarks. If we write the valence quark distribution as q_V and the sea quark distribution as $q_S = \bar{q}$, then we may rewrite $q + \bar{q}$ as $q_V + q_S + \bar{q} = q_V + 2\bar{q}$. Doing the same thing for $\Delta q + \Delta\bar{q} = \Delta q_V + 2\Delta\bar{q}$ gives us

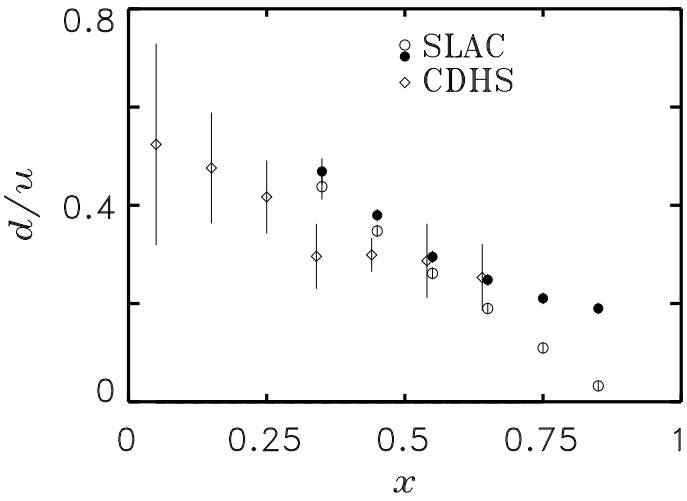

Figure 2.4: d/u ratio as a function of x, reproduced from Melnitchouk and Thomas [34]. Circles represent SLAC proton and deuteron data; open circles incorporate an on-shell deuteron model, while solid circles use an off-shell model. Neutrino-beam measurements from the CDHS collaboration [35], which are insensitive to nuclear effects, are shown as open diamonds.

$$\frac{\Delta q + \Delta\bar{q}}{q + \bar{q}} = \frac{\Delta q_V + 2\Delta\bar{q}}{q_V + 2\bar{q}}. \tag{2.37}$$

If we wish to extract the polarized-to-unpolarized PDF ratio for valence quarks alone, we must find a relationship between the quantity in Equation 2.37 and the valence-quark quantity $\Delta q_V/q_V$. We can accomplish this by finding the multiplicative factors that will transform one into the other:

$$\frac{\Delta q_V}{q_V} = \frac{\Delta q_V + 2\Delta\bar{q}}{q_V + 2\bar{q}} \cdot \frac{q_V + 2\bar{q}}{q_V} \cdot \frac{\Delta q_V}{\Delta q_V + 2\Delta\bar{q}} \tag{2.38}$$

Regrouping these factors simplifies the algebra

$$\frac{\Delta q_V}{q_V} = \frac{\Delta q_V + 2\Delta\bar{q}}{q_V + 2\bar{q}} \cdot \left(1 + \frac{2\bar{q}}{q_V}\right) \cdot \left(1 + \frac{2\Delta\bar{q}}{\Delta q_V}\right)^{-1}. \tag{2.39}$$

We now multiply the final fraction by $q_V/q_V = 1$ and multiply both sides of the equation by the resulting final term, $\left(1 + \frac{2\Delta\bar{q}}{q_V} \cdot \frac{q_V}{\Delta q_V}\right)^{-1}$.

$$\frac{\Delta q_V}{q_V} + \frac{2\Delta\bar{q}}{q_V} = \frac{\Delta q_V + 2\Delta\bar{q}}{q_V + 2\bar{q}} \cdot \left(1 + \frac{2\bar{q}}{q_V}\right). \tag{2.40}$$

Finally, we substitute the more familiar form $(\Delta q + \Delta\bar{q})/(q + \bar{q})$ back in

$$\frac{\Delta q_V}{q_V} = \frac{\Delta q + \Delta\bar{q}}{q + \bar{q}} \cdot \left(1 + \frac{2\bar{q}}{q_V}\right) - \frac{2\Delta\bar{q}}{q_V}. \tag{2.41}$$

In order to compute $\Delta q/q$ from measurements of g_1/F_1 using Equation 2.41, we use the measured nucleon structure function ratios to extract $(\Delta q + \Delta\bar{q})/(q + \bar{q})$ according to Equations 2.34 and 2.35, and then use fits to world data to estimate the sea-quark corrections $2\bar{q}/q_V$ and $2\Delta\bar{q}/q_V$. We can also use Equation 2.41 to find the error on $\Delta q/q$

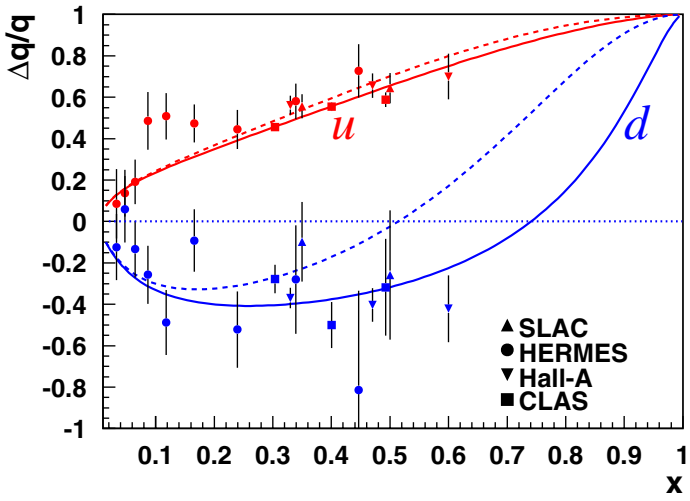

Figure 2.5: Quark helicity distributions as functions of x, reproduced from Avakian *et al.* [37] The dashed curves represent a prediction from by Leader *et al.* [38], while the solid curves give Avakian *et al.*'s prediction incorporating quark orbital angular momentum [37]. Circles represent data from HERMES [39]; triangles pointing up show SLAC data [40]; triangles pointing up correspond to data from Hall A of Jefferson Lab [41]; and squares show CLAS data [42].

$$\delta\left(\frac{\Delta q_V}{q_V}\right)^2 = \left(\frac{\delta(q_V)}{q_V}\right)^2 \left[2\bar{q}\frac{\Delta q + \Delta\bar{q}}{q+\bar{q}} - 2\Delta\bar{q}\right]^2 + \left(\frac{\delta(2\bar{q})}{q_V}\right)^2 \left(\frac{\Delta q + \Delta\bar{q}}{q+\bar{q}}\right)^2 + \left(\frac{\delta(2\Delta\bar{q})}{q_V}\right)^2 + \left[\delta\left(\frac{\Delta q + \Delta\bar{q}}{q+\bar{q}}\right)\right]^2 \left(1 + \frac{2\bar{q}}{q_V}\right)^2. \tag{2.42}$$

The same procedure may also be used to estimate the error on $(\Delta q + \Delta\bar{q})/(q+\bar{q})$ due to our neglect of strange-quark contributions [16]. We find

$$\frac{\Delta u + \Delta\bar{u}}{u+\bar{u}} = \left(\frac{\Delta u + \Delta\bar{u}}{u+\bar{u}}\right)_{s,\bar{s}=0} + \frac{s+\bar{s}}{u}\left[\frac{4}{15}\frac{g_1^p}{F_1^p} - \frac{1}{15}\frac{g_1^n}{F_1^n} - \frac{1}{5}\frac{\Delta s + \Delta\bar{s}}{s+\bar{s}}\right] \tag{2.43}$$

$$\frac{\Delta d + \Delta\bar{d}}{d+\bar{d}} = \left(\frac{\Delta d + \Delta\bar{d}}{d+\bar{d}}\right)_{s,\bar{s}=0} + \frac{s+\bar{s}}{d}\left[\frac{4}{15}\frac{g_1^n}{F_1^n} - \frac{1}{15}\frac{g_1^p}{F_1^p} - \frac{1}{5}\frac{\Delta s + \Delta\bar{s}}{s+\bar{s}}\right]. \tag{2.44}$$

The error may be bounded without the use of polarized strange-quark PDFs by applying the positivity constraints $|\Delta s/s| \leq 1$ and $|\Delta\bar{s}/\bar{s}| \leq 1$.

As we will see in Section 2.3.3, perturbative QCD predicts that both of the valence quark PDF ratios $\Delta u/u$ and $\Delta d/d$ approach 1 in the limit of $x \to 1$; that is, in a nucleon with spin 1/2, $q^\uparrow$ must dominate over $q^\downarrow$ at large x [37]. Figure 2.5 shows recent experimental data for $\Delta u/u$ (in red) and for $\Delta d/d$ (in blue). Although the measured behavior of $\Delta u/u$ is consistent with this prediction, $\Delta d/d$ shows no sign of approaching 1 in the x range where it has been measured. In this range, these results imply that up quark spins are generally parallel to the nucleon spin, while down quark spins are generally antiparallel, and quark orbital momentum makes a significant contribution to nucleon spin even in the valence quark region. Precise measurements of A_1^n at high x have the potential to test these results.

2.2 Measurements of A_1^n and A_1^p in the Valence Region

Theoretical interest in nucleon spin structure and spin structure functions substantially antedated physicists' ability to explore these areas experimentally. James Bjorken first described Bjorken scaling and proposed a polarized electroproduction sum rule in 1969 [20]; it was not until the late 1970s, at SLAC, that the first results came out from doubly-polarized experiments [2, 3], and not until the late 1980s that proton spin was discovered to be an unsolved problem [9]. The deep inelastic scattering region, or valence region, has long been of special interest due to the simplicity of the PDFs there, but increases in luminosity and x coverage have posed serious challenges.

Figure 2.6 displays the current world data on A_1^p and A_1^n in the deep inelastic scattering region, while Figure 2.7 shows world data on two polarized nuclear targets: deuterium (A_1^d) and ^{3}He ($A_1^{^3\mathrm{He}}$). Data points at different Q^2 values are plotted together, since, to leading order, A_1 does not vary with Q^2 in this kinematic range. In the following sections, we will briefly review the experiments that have produced these measurements over the past two decades; the DIS structure function database hosted at Durham University [43] is an invaluable resource. Once we know what the data look like, we will be better placed to consider the theoretical predictions to follow in Section 2.3.

2.2.1 Experiments at CERN

CERN, the **E**uropean Organization (formerly **C**ouncil) for **N**uclear **R**esearch, is an accelerator facility on the French-Swiss border. Among its many long-running and successful physics programs are a series of experiments probing the nucleon spin structure functions via inclusive and semi-inclusive deep inelastic scattering with naturally polarized muons from the M2 beamline of the **S**uper **P**roton **S**ynchrotron, or SPS. Accelerated protons strike a beryllium target, releasing pions and kaons, which then decay into muons; to an extent dependent on the muon and hadron energies, the forward-going muons are longitudinally polarized due to parity violation in the hadron decays [44].

EMC We will begin our experimental survey in the 1980s with the **E**uropean **M**uon **C**ollaboration (EMC), the first experiment to produce a precise measurement of A_1 on the proton. (We neglect 1970s results from the SLAC experiments E-80 and E-130, which have very large error bars compared to more modern data.) The muons were incident on a pair of target cells, separated by a 22-cm gap and filled with cryogenically cooled beads of solid ammonia. In each cell, the free protons in the ammonia were polarized by dynamic nuclear polarization [45], which involves doping the mixture with unpaired electrons. These paramagnetic radicals are polarized by a magnetic field and then transfer their polarization to neighboring protons on irradiation with a microwave field near their paramagnetic resonance. Protons in the two cells were polarized in opposite directions, so that an asymmetry could be formed in the count rates from each cell; once the background from the ^{14}N nuclei is subtracted, the result is a doubly-polarized measurement on the proton by itself. The resulting A_1^p measurement covered an x range of 0.01 to 0.70 and a Q^2 range from 3.5 to 29.5 $(\mathrm{GeV/c})^2$ [7].

SMC After EMC ended, the M2 polarized-muon beamline was upgraded and was inherited by the **S**pin **M**uon **C**ollaboration (SMC), which measured asymmetries and spin structure functions using both a polarized proton target and a polarized deuteron target. As in the EMC experiment, SMC used twin target cells, kept at opposite polarization and exposed to the muon beam simultaneously. Three types of target material were used during SMC: chips of irradiated ammonia ice, beads of butanol (C_4H_9OH) doped with a paramagnetic complex, and similarly doped beads of deuterated butanol (C_4D_9OH)[1]. The two butanol targets served as fairly clean polarized proton and deuteron

[1]The irradiation of the ammonia and the doping of the butanol were necessary for the process of dynamic nuclear polarization.

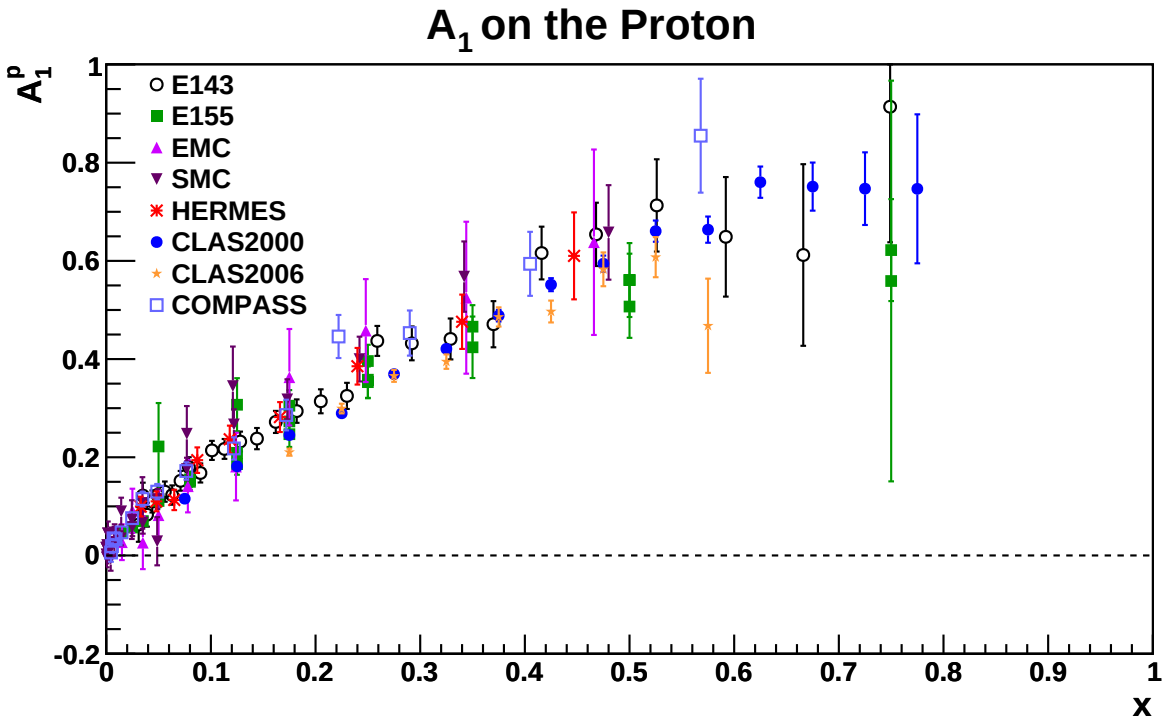

(a) Proton results

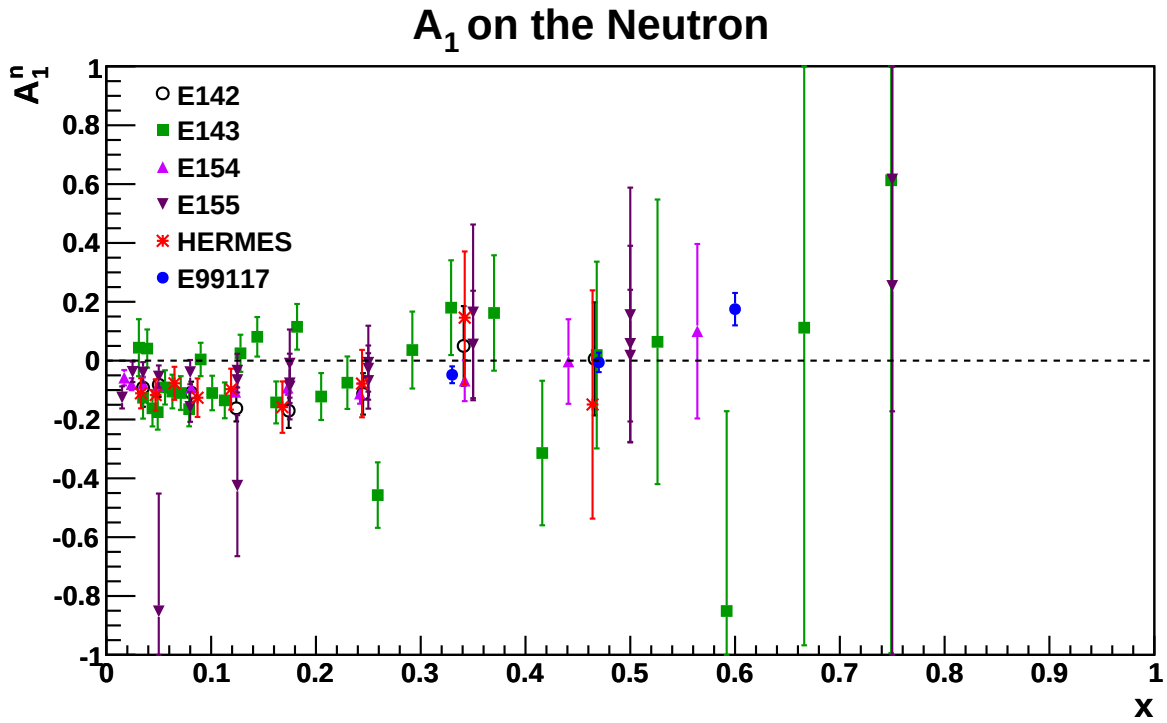

(b) Neutron results

Figure 2.6: World deep-inelastic-scattering data for A_1^p (a) and A_1^n (b). The experiments are described in the text.

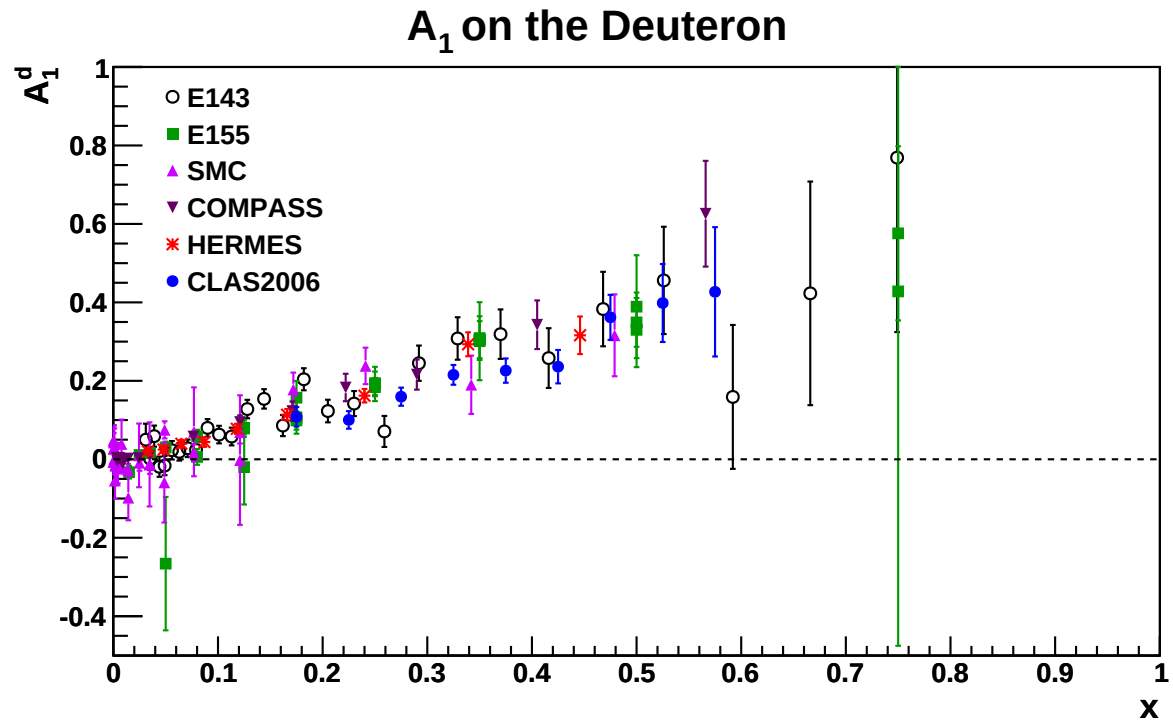

(a) Deuteron results

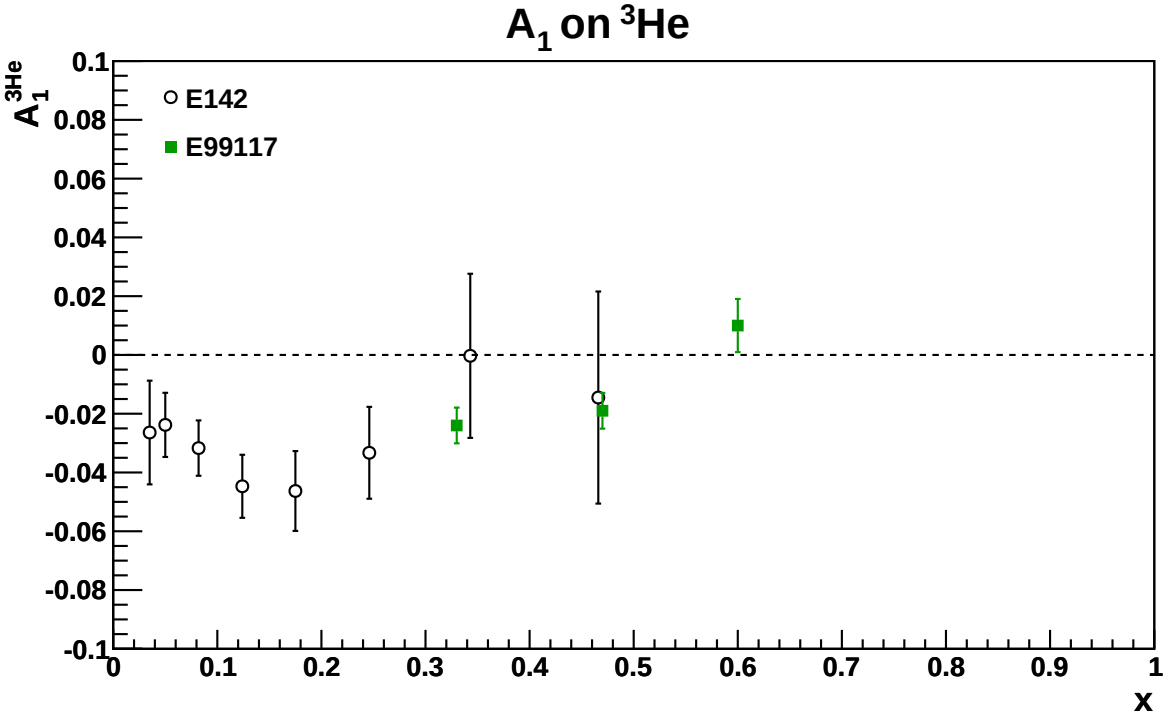

(b) ^{3}He results

Figure 2.7: World deep-inelastic-scattering data for A_1^d (a) and $A_1^{^3\mathrm{He}}$ (b). The experiments are described in the text.

targets, since the most common isotopes of carbon and oxygen have spinless nuclei [46]. To reduce background, the standard inclusive measurement (in which the scattered muon is the only final-state particle detected) was combined with a semi-inclusive measurement, in which the final-state muon was detected in coincidence with at least one final-state hadron. The results were measurements of A_1^p and A_1^d over a range of $0.0008 < x < 0.7$ and $0.2 < Q^2 < 100$ (GeV/c)^2 [47].

COMPASS At present, the M2 beamline is occupied by the **Co**mmon **M**uon-**P**roton **A**pparatus for **S**tructure and **S**pectroscopy, or COMPASS. Like its predecessors, COMPASS uses a two-cell polarized target, each cell with opposite polarization, so that it may simultaneously record data from each spin configuration. A two-stage spectrometer, constructed around two dipole magnets, offers a large acceptance in momentum and angle. Like SMC, COMPASS takes data with both inclusive and semi-inclusive triggers; data analysis for the two modes is handled separately and then combined for the final physics result.

From 2002 to 2004, COMPASS used deuterated lithium (^{6}LiD) as an effective polarized deuteron target; this choice was motivated by the material's high radiation resistance and by the fact that the ^{6}Li nucleus may be approximated as a deuteron and a spin-0 ^{4}He nucleus. In 2007, solid ammonia, of the same type used during SMC, was used as a polarized proton target. In both cases, target polarization was achieved using dynamic nuclear polarization [48]. To date, the experiment has published A_1 on the deuteron [49] in the range $0.004 < x < 0.07$ and $1 < Q^2 < 100$ (GeV/c)^2, and A_1 on the proton [50] in the range $0.004 < x < 0.7$ and $1.10 < Q^2 < 62.1$ (GeV/c)^2.

2.2.2 Experiments at SLAC

The SLAC National Accelerator Laboratory is a facility in Palo Alto, California, that began operating in the late 1960s as a linear accelerator capable of accelerating both electrons and positrons; it is now used as a coherent X-ray source. While many of SLAC's most famous experiments used colliding beams of electrons and positrons, the facility also had a vibrant fixed-target program, which included several precision measurements of A_1. These experiments took advantage of SLAC's ability to produce a polarized electron beam by illuminating a strained GaAs photocathode with circularly polarized laser light; this is essentially the same mechanism by which Jefferson Lab produces its polarized electron beam, and will be described in detail in Section 3.2.1.

E142 SLAC experiment E142, which ran at End Station A in 1992, was the first experiment to use ^{3}He gas as an effective polarized neutron target, a usage that is possible because the nuclear spin of 1/2 is carried by the neutron some 87% of the time (Section 3.3.3). The target was polarized using a method called spin-exchange optical pumping, which (with a few modifications) is used in the experiment that is the subject of this work; the technique is described in detail in Section 3.3.3.1. E142 collected data in two single-arm spectrometers in order to maximize the kinematic reach of the experiment, so that A_1 was measured both for the ^{3}He nucleus and for the neutron (after the application of nuclear corrections) in the range $0.03 < x < 0.60$ and $1.1 < Q^2 < 5.5$ (GeV/c)^2 [51].

E143 E143, which also ran at End Station A in the early 1990s, used frozen single-cell ^{15}N ammonia targets polarized via dynamic nuclear polarization. One target used ammonia molecules with normal hydrogen content ($^{15}NH_3$); the other used deuterated ammonia ($^{15}ND_3$). Electron beam irradiation introduced the paramagnetic radicals necessary for the polarization process. The spectrometer setup was nearly identical to E142's, but the magnets were held at higher fields and the hodoscopes were altered to allow for higher rates. A_1^p and A_1^d could be measured fairly directly on their respective targets; the experiment also extracted A_1^n by combining their proton and deuteron data [26]. The kinematic range covered was $0.031 < x < 0.749$ and $1.27 < Q^2 < 9.52$ (GeV/c)^2.

E154 E154 built on the success of E143 to achieve a reduction in error on A_1^n, as well as an extension of the covered range to lower values of x. Electrons at a single energy (48.3 GeV) were incident on a ^{3}He target polarized by spin-exchange optical pumping. Inclusive events were measured in two new single-arm spectrometers. The resulting measurements covered a kinematic range of $0.014 < x < 0.7$ and $1.2 < Q^2 < 15.0$ (GeV/c)^2 [52].

E155 E155 took E154's two single-arm spectrometers and added a third in order to increase the experiment's Q^2 range. The polarized electron beam ran at a single energy of 48.3 GeV and two dynamically nuclear-polarized targets were used. For proton measurements, the target contained frozen ammonia, as for E143; deuteron measurements used a sample of ^{6}LiD, which would later also be used in the COMPASS experiment at CERN. On the latter target, g_1^d/F_1^d – approximately equal to A_1^d in this region – was measured in the range $0.015 < x < 0.75$ and $1.22 < Q^2 < 34.79$ (GeV/c)^2 [53]. Proton and deuteron data were combined to measure g_1^p/F_1^p and g_1^n/F_1^n for the same kinematic range [30].

2.2.3 HERMES Experiment at DESY

The **D**eutches **E**lektronen **Sy**nchrotron, DESY, is a German institution for particle physics research with locations in Hamburg and in Zeuthen. Historically, the Hamburg site has been home to several accelerators, and it was at the **H**adron-**E**lectron **R**ing **A**ccelerator (HERA), which was active between 1992 and 2007, where measurements of A_1 took place. HERA consisted of two parallel accelerators, one for protons and one for either electrons or positrons; the lepton beam polarizes itself over time via the Sokolov-Ternov mechanism, whereby the probability of a spin-flipping synchrotron emission changes depending on the orientation of the electron spin relative to the magnetic guiding field [54]. Over time, this slight asymmetry gives rise to a transversely polarized lepton beam.

The HERMES experiment (**HERA Me**asurement of **S**pin) ran in HERA's East Hall. Magnetic spin rotators just upstream of the hall rotated the transverse beam polarization into longitudinal polarization; downstream of the experiment, a Compton polarimeter measured the longitudinal polarization before another spin rotator returned the polarization to a transverse direction. HERMES ran primarily with positron beams, but also took some data with electrons. The targets, polarized hydrogen and polarized deuterium, were produced using an **A**tomic **B**eam **S**ource (ABS), wherein neutral atoms were formed into beams and passed through a Stern-Gerlach-type device that selected atomic hyperfine states with the desired nuclear polarization. A target storage cell, fed by the ABS, increased the density by a factor of 100. The experiment used a single, large-acceptance spectrometer with the ability to detect coincidences between scattered leptons and hadrons, allowing semi-inclusive measurements. Inclusive measurements of A_1^p covered a kinematic range of $0.033 < \langle x \rangle < 0.44$ and $1.22 < \langle Q^2 \rangle < 9.18$ (GeV/c)^2, where $\langle x \rangle$ and $\langle Q^2 \rangle$ are averages in each bin; the A_1^d inclusive measurement covered nearly the same range, but with a maximum $\langle Q^2 \rangle$ value of 9.16 (GeV/c)^2 [39].

2.2.4 Experiments at Jefferson Laboratory

Jefferson Laboratory, the site of the experiment with which this work is concerned, is the home of an electron accelerator in Newport News, Virginia. Longitudinally polarized electrons, produced from a photocathode illuminated by circularly polarized light (Section 3.2.1) may be accelerated to energies of up to 6 GeV in the CEBAF accelerator (**C**ontinuous **E**lectron **B**eam **A**ccelerator **F**acility). Fixed-target experiments may be performed simultaneously in three experimental halls, each with a different basic configuration.

E99-117 To date, the highest-precision available measurements of A_1^n are from experiment E99-117, which took inclusive data in Hall A using twin High-Resolution Spectrometers (Section 3.3.5),

operated independently and at the same scattering angles in order to double the statistics. The effective polarized neutron target was ^{3}He gas contained in a glass cell and polarized via spin-exchange optical pumping; the system was quite similar to that described in Section 3.3.3. A_1^n was measured at three kinematic points: $x = 0.33$, 0.47 and 0.60 and $Q^2 = 2.7$, 3.5 and 4.8 (GeV/c)^2 [41].

CLAS In Hall B, most experiments are built around the **CEBAF L**arge **A**cceptance **S**pectrometer (CLAS), an approximately spherical detector that surrounds the target with multiple detection layers (including wire chambers, Čerenkov counters, and lead-glass calorimeters) [55]. Glass cylinders housed the ammonia-ice beads (either NH_3 or ND_3), longitudinally polarized via dynamic nuclear polarization [56]. In the deep-inelastic scattering regime, deuteron and proton measurements of A_1, from the EG1 experiment, have been published for a range of $0.175 < \langle x \rangle < 0.575$ and $1.01 < Q^2 < 4.16$ (GeV/c)^2 [42]. Additional A_1^p data from the EG2000 experiment, labeled "CLAS2000" in Figure 2.6(a), are available for $0.075 < x < 0.775$ at $Q^2 = 2$ (GeV/c)^2 [57, 58].

Planned A_1^n Measurements after Upgrade Jefferson Laboratory is in the final stages of planning for an accelerator upgrade, which will increase the maximum beam energy after five passes through the accelerator to 11 GeV while adding a fourth experimental hall (Hall D) that will take 12-GeV beam after five and a half passes through the accelerator. Two experiments have been approved to make precision measurements of A_1^n at high values of x. The E12-06-122 experiment [59] is tentatively scheduled to serve as Hall A's commissioning experiment after the upgrade; it will use the BigBite spectrometer (Section 3.3.4) to measure the asymmetry, while one of the high-resolution spectrometers provides corroborating data. The polarized ^{3}He target will be designed along similar lines to the one used during E99-117 and E06-014 (the subject of this dissertation), and a kinematic range of $0.32 < x < 0.71$ and $3.0 < Q^2 < 8.4$ (GeV/c)^2 is planned.

In Hall C, experiment E12-10-101 [60] plans to take data with the High-Momentum and Super-High-Momentum Spectrometers, the latter of which is a new spectrometer under development for the upgrade, and a polarized ^{3}He target similar to that of E12-06-122. The inclusive measurement of A_1^n will cover the kinematic range of $0.3 < x < 0.77$ and $3 < Q^2 < 10$ (GeV/c)^2, complementing the planned Hall A measurement while providing an independent check.

2.3 Models of A_1^n

A wide variety of theoretical approaches have been applied to the problem of nucleon spin structure. Some match the available data fairly well; some include parameters which must be fixed by fits to the available data; and some, while not congruent with the available data, nonetheless help guide insights into the problem. Here, we will take a brief and necessarily incomplete tour of the theoretical models of the past few decades, with special attention to those making direct predictions of the asymmetry A_1^n.

2.3.1 Unbroken SU(6) Symmetry

The simplest model of nucleon structure is the non-relativistic constituent quark model, in which the three constituent quarks of the nucleon obey an unbroken SU(6) symmetry in both the constituent quark basis and the current quark basis. The nucleon spin and isospin are both equal to 1/2 and we assume that the system has no orbital angular momentum. Consider a neutron that is polarized in the positive z direction. Its wave function is then given by [61, 62]

$$\begin{aligned} |n^\uparrow\rangle = \frac{1}{\sqrt{18}}(&2|d^\uparrow u^\downarrow d^\uparrow\rangle + 2|d^\uparrow d^\uparrow u^\downarrow\rangle + 2|u^\downarrow d^\uparrow d^\uparrow\rangle - |d^\uparrow d^\downarrow u^\uparrow\rangle - |d^\uparrow u^\uparrow d^\downarrow\rangle - |d^\downarrow u^\uparrow d^\uparrow\rangle \\ &- |u^\uparrow d^\downarrow d^\uparrow\rangle - |u^\uparrow d^\uparrow d^\downarrow\rangle - |d^\downarrow d^\uparrow u^\uparrow\rangle). \end{aligned} \tag{2.45}$$

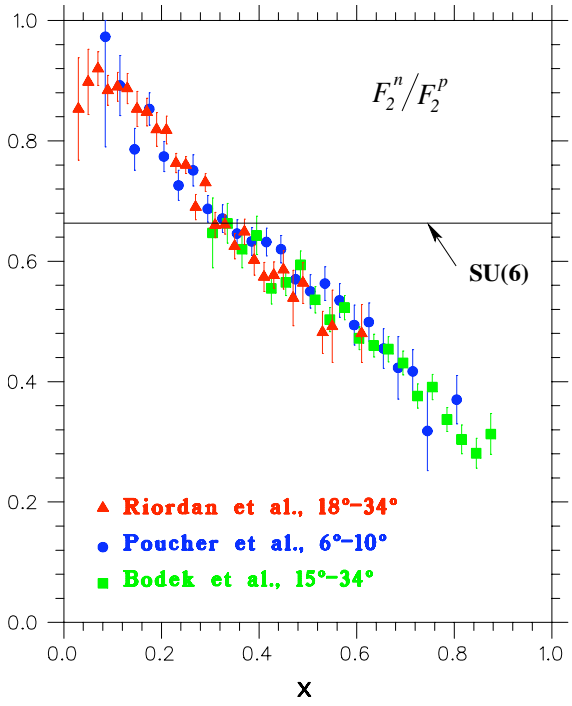

Figure 2.8: SLAC measurements of $F_2^n/F_2^p = R^{np}$ as a function of x; the angles in the legend are electron scattering angles. The measurements were performed by Bodek *et al.* [63], Poucher *et al.* [64], and Riordan *et al.* [65]. The prediction that $R^{np} = 2/3$, which arises from an assumption of exact SU(6) symmetry, is shown as a solid horizontal line. Figure reproduced from Zheng [16].

The equivalent wave function for the proton, $|p^{\uparrow}\rangle$, is given by Equation 2.45 with the u and d quark labels interchanged.

What would this mean for A_1^p and A_1^n? Close [62] works through the implications in detail. By extracting the total probability of finding each quark in a given spin state from Equation 2.45, and by making certain assumptions about the virtual photon absorption cross section for the nucleon (*e.g.* that they are equal to the sum of the virtual photon absorption cross sections for the three constituent quarks), one can derive the predictions

$$A_1^p = \frac{5}{9} \tag{2.46}$$

$$A_1^n = 0. \tag{2.47}$$

SU(6) symmetry, however, was soon shown to be broken. If we let $q(x)$ represent a proton parton distribution function, as we did in Section 2.1.3, then we can use Equation 1.40 to write the ratio of the neutron F_2 structure function to the proton F_2 structure function in the valence region:

$$R^{np} \equiv \frac{F_2^n}{F_2^p} = \frac{u(x) + 4d(x)}{4u(x) + d(x)}. \tag{2.48}$$

If exact SU(6) symmetry held for the nucleon, then the valence quark distributions should have the same shape, giving $u(x) = 2d(x)$. We can then simplify Equation 2.48 to give the prediction

$$R^{np} = \frac{2}{3}. \tag{2.49}$$

As Figure 2.8 shows, when R^{np} was measured at SLAC in the 1970s, it was found to deviate quite dramatically from the prediction of exact SU(6) symmetry. SU(6) symmetry is broken [66, 67]; we must turn to more complicated models to predict A_1^n and A_1^p.

2.3.2 SU(6) Symmetry Breaking via Hyperfine Interactions

The fact of SU(6) symmetry breaking, in and of itself, may be exploited to make predictions of polarized PDFs and A_1 if we assume that the mechanism is color hyperfine interactions, mediated by one-gluon exchange between each quark pair (i, j) [68, 69]. By analogy to electromagnetic interactions between two magnetic dipoles, such an interaction may be expressed as

$$H_{hyp}^{ij} = A_{ij}\left[\frac{8\pi}{3}\vec{S}_i\cdot\vec{S}_j\delta^3(\vec{r}_{ij}) + \frac{1}{r_{ij}^3}\left(3(\vec{S}_i\cdot\hat{r}_{ij})(\vec{S}_j\cdot\hat{r}_{ij}) - \vec{S}_i\cdot\vec{S}_j\right)\right]. \tag{2.50}$$

In this notation, $\vec{S}_i$ is the spin of the i^{th} quark; $\vec{r}_{ij}$ gives the relative position of the i^{th} and j^{th} quarks; and A_{ij} is set by the quark masses and the interaction strength. To lowest order, $A_{ij} = 2\alpha_s/3m_im_j$.

What does this say about nucleon structure? To zeroth-order, nucleons are S-wave particles, so to first order we may ignore all of Equation 2.50 save the Fermi contact term, $\vec{S}_i\cdot\vec{S}_j\delta^3(\vec{r}_{ij})$. In the rest frame of the nucleon, this term raises the energy of quark pairs (*diquarks*) with $S = 1$, while lowering the energy of diquarks with $S = 0$ [70].

In the valence region, this hyperfine perturbation of the constituent quark model may be used to make predictions. Consider the region of large x, where the struck quark carries most of the nucleon energy; the spectator diquark is in a low-energy state, which implies that it has $S = 0$. The nucleon spin must then be entirely carried by the struck quark, giving us

$$\lim_{x\to 1} A_1 = 1. \tag{2.51}$$

Further precision may be obtained through parameterization of the quark distribution functions. First, the basic SU(6) model is extended to allow relativistic motion of the constituent quarks. This relativistic motion quenches the quark spin; we may describe this as a probability $c_A(x)/2$ for a spin flip (i.e. a spin-up quark flipping to a spin-down state, or vice versa). Then two rough parameterizations are applied [70]

$$\frac{d(x)}{u(x)} = \kappa(1-x) \text{ for } x\to 1 \text{ and } 0.5 < \kappa < 0.6 \tag{2.52}$$

$$c_A(x) = nx(1-x)^n. \tag{2.53}$$

Equation 2.52 is chosen so that $d(x)/u(x)$ vanishes for large x; this is required by the model, since these are proton PDFs. In the SU(6) wavefunction, a pair of identical quarks is in a spin-1 state [69]. The up quarks have a higher energy, on average, than the down quarks, so that there is a much higher probability of finding an up quark at high x than a down quark. Equation 2.53 also satisfies fundamental requirements of the model: $c_A(x)$ must vanish at very low x and very high x, and for $2 < n < 4$ the equation provides the necessary degree of relativistic quenching.

Figure 2.9 shows the resulting predictions for A_1^p and A_1^n; the shaded band gives the region defined by all possible combinations of κ and n. The theory also predicts

$$\lim_{x\to 1}\frac{F_2^n}{F_2^p} = \frac{1}{4} \tag{2.54}$$

in agreement with the experimental data shown in Figure 2.8.

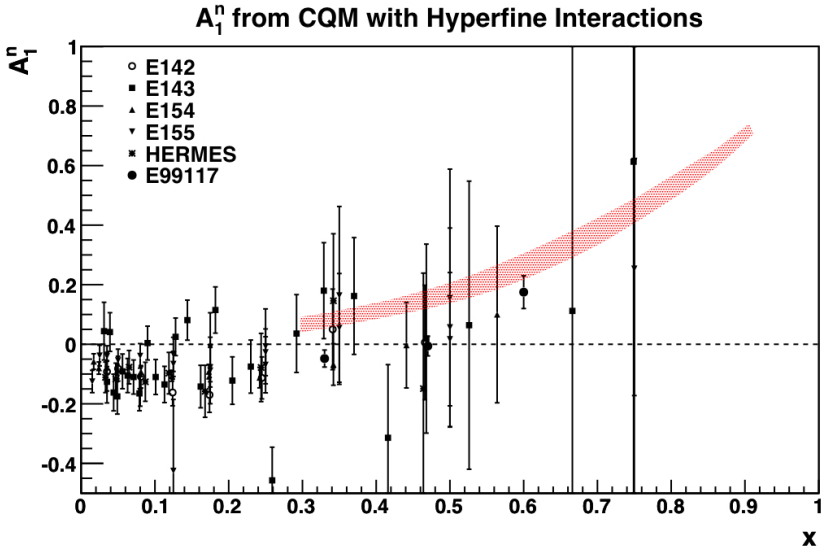

Figure 2.9: Predictions of A_1^n from constituent quark model, compared to world data. The dashed line on the x-axis marks $A_1^n = 0$, the prediction from unbroken SU(6) symmetry. The shaded red band shows the range of A_1^n values allowed in a model where SU(6) symmetry is broken by hyperfine interactions between quarks [70]. We have made use of parameterizations compiled by X. Zheng [71].

2.3.3 Perturbative QCD

At large x, the theoretical picture is simplified. When a single quark is carrying nearly all of the nucleon momentum, it has a large invariant mass, and its effective couplings to gluons are small. The problem may then be treated perturbatively. With a few additional assumptions, one can make predictions for A_1 and for the polarized-to-unpolarized PDF ratios.

2.3.3.1 Hadron Helicity Conservation

The simplest initial assumption is that made by Farrar and Jackson [72, 73] in the very early days of perturbative QCD: that the quarks' orbital angular momentum is zero. From this starting point, they argue that the low-momentum pair of spectator quarks have their spins anti-aligned; the configuration in which the spectator quarks have parallel spins is suppressed by a relative factor of $(1-x)^2$. As $x \to 1$, then, it is the struck quark that must carry the helicity of the nucleon as a whole.

This requirement of *hadron helicity conservation* leads to the absolute prediction that A_1 goes to 1 as x approaches 1; in the same limit, $R^{np} \to 3/7$. At lower values of x, the model may be used to guide parameterizations of the data for deep inelastic scattering. In 1995, Brodsky, Burkardt, and Schmidt performed a fit to the data set that was then available (namely the results of E142 at SLAC and SMC at CERN), requiring helicity conservation at large x [74]. They thus obtained a parameterization of polarized and unpolarized parton densities in this model; the parameterization is known by their initials, BBS. Three years later, Leader, Sidorov, and Stamenov [38] expanded on this work by including a model for Q^2 evolution and by fitting to direct measurements of A_1 (rather than to derived measurements of g_1). The resulting parameterizations, both BBS and LSS(BBS), are shown in Figure 2.10.

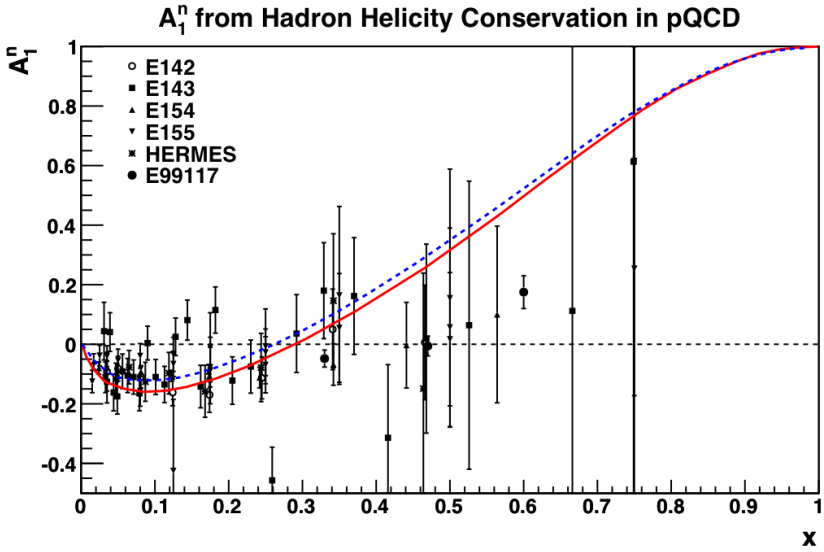

Figure 2.10: Predictions of A_1^n from perturbative QCD with the requirement of hadron helicity conservation. The solid red line is the BBS parameterization [74] to early experiments; the dashed blue line shows the LSS(BBS) extension of the BBS parameterization [38]. We have made use of parameterizations compiled by X. Zheng [71].

2.3.3.2 Quark Orbital Angular Momentum

What if the quark orbital angular momentum is *not* zero? In that case, angular momentum transfer between the helicity of the struck quark and the orbital angular momentum would negate the underlying assumptions of hadron helicity conservation. To further complicate the picture, most data for polarized deep inelastic scattering were not taken at particularly high values of Q^2 and W^2. In parameterizations of unpolarized data, this *preasymptotic region* and its non-negligible $1/Q^2$ terms may be neglected; for the polarized data, where insufficient data exist in the asymptotic region, a more complicated picture is necessary. Leader *et al.* recently gave a useful summary of the pitfalls inherent in parameterizations of polarized deep inelastic scattering data [75].

To address this pair of issues, Leader, Sidorov, and Stamenov have made a practice of performing fits to the world data at both leading order and next-to-leading order, without imposing the constraint of hadron helicity conservation. Figure 2.11 shows the parameterization of the g_1^n/F_1^n data for three Q^2 values from their 2007 fit [76]; these are the most recent predictions of g_1^n/F_1^n for which the $1/Q^2$ terms (target-mass and higher-twist corrections) have been taken into account. For the most recent parameterization [78], these corrections have been taken into account in the calculation of polarized parton densities, but have not yet been extended to the calculation of g_1^n; the final result is expected to be quite similar to the plotted parameterization [77]. (In this approach, only g_1 is predicted; F_1 is extracted from phenomenological parameterizations of F_2 [79] and R [80].)

In 2007, Avakian *et al.* developed a perturbative QCD model that explicitly includes Fock states with nonzero quark orbital angular momentum [37]. These states enhance the helicity-flip amplitudes logarithmically. At large x, the "positive helicity state," for which the quark spin is aligned with the nucleon spin, scales as $(1-x)^3$; the negative helicity state, for which the quark and nucleon spins are anti-aligned, now scales as $(1-x)^5 \log^2(1-x)$. Using an extension of the BBS parameterization, they fit this predicted behavior to the available data. As we saw in Figure 2.5, this has a dramatic effect on the polarized PDF ratio $\Delta d/d$; the red curve in Figure 2.11 shows the resulting prediction of A_1^n.

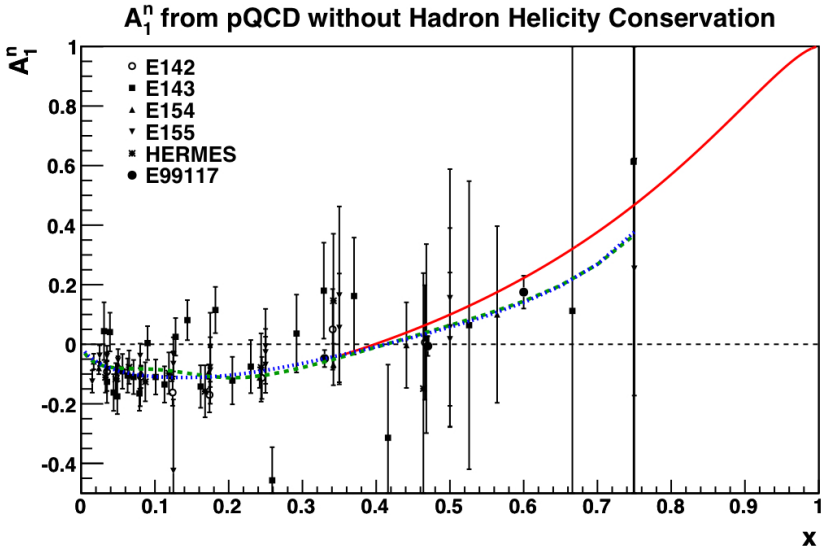

Figure 2.11: Predictions of A_1^n from perturbative QCD, allowing quark orbital angular momentum. The solid red line is the parameterization by Avakian *et al.* [37], who fit the data with a theory including explicit orbital angular momentum. The remaining curves are parameterizations by Leader, Sidorov, and Stamenov [76, 77], using next-to-leading-order QCD without requiring hadron helicity conservation. Each curve is for a constant Q^2 value: 2.5 $(\mathrm{GeV/c})^2$ (dotted blue line) and 10 $(\mathrm{GeV/c})^2$ (dashed green line).

2.3.4 Statistical Model of the Nucleon

In a statistical-mechanical model [81], the nucleon may be regarded as a gas composed of massless partons: quarks, antiquarks, and gluons. Suppose that these partons are in equilibrium in some volume of a finite size; let $\bar{x}$ represent their universal temperature, and X_{0p} their thermodynamical potential. At given input energy scale, the helicity-dependent portions $p^h(x)$ of the parton distribution functions $p(x)$ may then be expressed as being proportional to the thermodynamic distribution

$$p^h(x) \propto \left(e^{\left(x - X_{0p}^h\right)/\bar{x}} \pm 1\right)^{-1}. \tag{2.55}$$

Quarks and antiquarks obey Fermi-Dirac statistics and take the plus sign; gluons follow a Bose-Einstein distribution and take the minus sign. The total parton distribution also includes a diffractive term, which is helicity-independent and does not feature in predictions of A_1. As a whole, the approach is motivated by its use of a relatively small number of free parameters (eight) [82].

The chiral nature of QCD leads to two properties of the thermodynamical potential. First, the potential of a quark with helicity h is the opposite of the potential of an antiquark with helicity $-h$. Second, the gluon thermodynamical potential is 0. Meanwhile, DIS data leads to further conclusions; for example, the relative dominance of $u(x)$ over $d(x)$ implies that the total potential of u quarks is greater than the total potential of d quarks. These conclusions eventually lead to a prediction [83] that, at $Q^2 = 4$ $(\mathrm{GeV/c})^2$,

$$\lim_{x \to 1} A_1 \sim 0.6 \frac{\Delta u(x)}{u(x)}. \tag{2.56}$$

Other statistical approaches to nucleon structure exist; in 1994, for example, a statistical-mechanical extension of the MIT bag model (Section 2.3.8) was used to compute the unpolarized

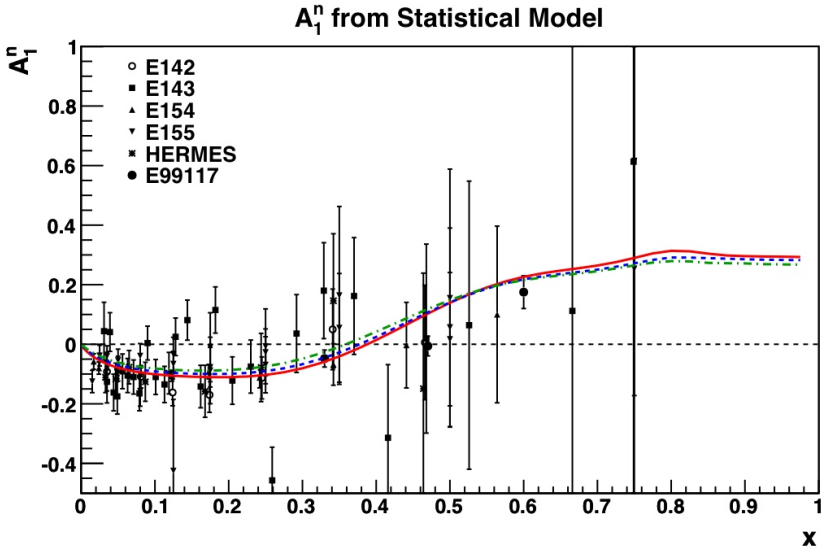

Figure 2.12: Predictions of A_1^n from statistical model [82]. Each curve represents predictions with a constant value of Q^2: 4 (GeV/c)^2 (solid red line), 10 (GeV/c)^2 (dashed blue line), and 100 (GeV/c)^2 (dash-dotted green line). We have made use of parameterizations compiled by X. Zheng [71].

structure functions of the proton, but the results failed to agree with experiment [84]. Bhalerao *et al.* [85, 86] had better success with a model wherein calculations are performed in the nucleon rest frame and eventually boosted to the infinite-momentum frame; they also make explicit corrections for the finite size of the nucleon. Measured values of polarized and unpolarized PDFs for the proton and neutron are used to constrain the model.

Figure 2.12 shows predictions of A_1 from Bourrely *et al.* [83] for three values of Q^2.

2.3.5 Quark-Hadron Duality

In the early 1970s, Elliot Bloom and Fred Gilman [87, 88] observed a curious relationship between measurements of nucleon structure in two very different kinematics: the deep inelastic scattering regime and the resonance region (see Figure 1.4). The dynamics in these two kinematic regions are quite different; in the resonance region, the electron is seen as scattering from a cluster of quarks and gluons, all of which interact with each other and respond in a correlated way, while deep-inelastic scattering sees the electron scattering from an essentially free, pointlike quark. Yet, if the unpolarized structure function F_2 is measured in both regions, we see

$$\int_{x_1(W_1,Q^2)}^{x_2(W_2,Q^2)} dx F_2^{res}(x,Q^2) = \int_{x_1}^{x_2} dx F_2^{DIS}(x,Q^2). \tag{2.57}$$

Here, F_2^{res} represents the measurement of F_2 in the resonance region, at relatively low Q^2. F_2^{DIS}, meanwhile, is F_2 as measured through deep inelastic scattering, evolved to the same low Q^2. The integral may be performed over the resonance region as a whole, in which case Equation 2.57 describes *global duality*; alternatively, *local duality* holds when Equation 2.57 is true for integrals over a single resonance. Figure 2.13 shows a portion of the initial evidence for quark-hadron duality; data in the resonance region oscillate around the scaling curve, but follow the curve on average [32]. This implies a profound relationship between the two scattering regimes: as Bloom and Gilman expressed it in their original paper [87], "the resonances are not a separate entity but are an intrinsic part of

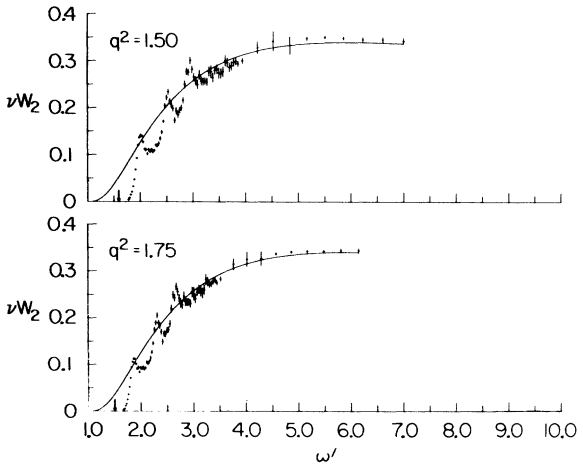

Figure 2.13: Initial evidence for quark-hadron duality. The value of F_2 is plotted as a function of the scaling variable $\omega' = 1 + W^2/Q^2$. For each Q^2 value in GeV, measurements in the resonance region (at low ω') are compared to the solid curve, a smooth fit of measurements in the Bjorken scaling region. Reproduced from Bloom and Gilman [88].

the scaling behavior of" F_2.

The high luminosity available over the last ten years has allowed precise tests of local and global quark-hadron duality. Data from Jefferson Lab's Hall C showed 10% agreement with global duality for the unpolarized structure functions for Q^2 values as low as 0.5 $(\mathrm{GeV/c})^2$; local duality also holds for each of the three most prominent resonances [89]. Extending these tests to spin structure, experiments at DESY [90] and Jefferson Lab's Hall B [42, 91] have found that global quark-hadron duality is satisfied for proton and deuteron polarized structure functions, down to $Q^2 = 1.7$ $(\mathrm{GeV/c})^2$ – but these same polarized structure functions violate local duality up to the highest Q^2 value covered by the experiment, 5.0 $(\mathrm{GeV/c})^2$ [91]. A similar test for the polarized structure function g_1 of the neutron and the ^{3}He nucleus, conducted in Jefferson Lab's Hall A, found that global duality held down to $Q^2 = 1.8$ $(\mathrm{GeV/c})^2$ [92].

If we assume that local duality holds true, then electromagnetic form factors measured in elastic scattering at large Q^2 can be used to predict the behavior of structure functions as $x \to 1$ in the deep inelastic scattering regime, and vice versa [93]. This method is model-independent, as local duality is a phenomenological observation, and the result is consistent with the perturbative-QCD prediction that $A_1 \to 1$ as $x \to 1$.

The underlying mechanism of quark-hadron duality is not well understood, although theorists have seen some success by expressing the finite-energy sum rules in terms of the moments of the structure functions, which naturally mix contributions from all scattering regimes and lead to duality as long as scaling violations were not too large [95]. By combining the observed fact of quark-hadron duality with various mechanisms for SU(6) symmetry breaking, however, it is possible to make some fairly detailed predictions [96]. Depending on the model by which the SU(6) symmetry is broken, some types of resonances (e.g. states with spin 3/2) will be suppressed at large x. In each case, relative strengths for the resonances may be found by requiring the model to reproduce local duality, leading to predictions of A_1 and other functions. Figure 2.14 shows the results of this analysis for three scenarios: the suppression of spin-3/2 resonances at large x, the suppression of transitions with helicity 3/2, and the suppression of resonances with symmetric wave functions.

After Jefferson Lab's 12-GeV upgrade, one of the planned A_1^n experiments will further test duality by comparing resonance and deep-inelastic-scattering measurements of g_1^n in the range $0.45 \leq x \leq 0.77$ [60].

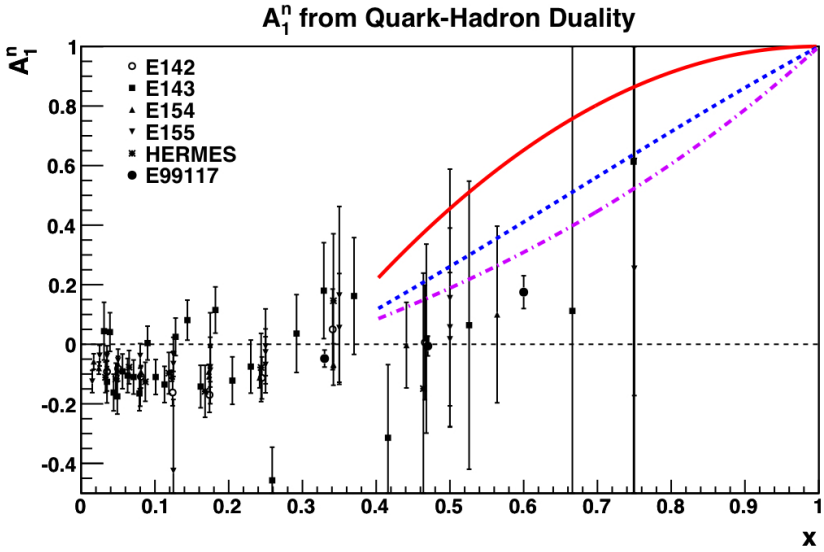

Figure 2.14: Predictions of A_1^n from quark-hadron duality, assuming suppression of: transitions with helicity 3/2 (solid red line), resonances with spin 3/2 (dashed blue line), and resonances with symmetric wave functions (dash-dotted purple line) [93, 94].

2.3.6 Chiral Soliton Model

The chiral soliton model is a promising non-perturbative means of studying and predicting the behavior of nucleons; Diakonov and Petrov provide a useful introduction to this approach [97]. The key theoretical basis of the model is **S**pontaneous **C**hiral **S**ymmetry **B**reaking, or SCSB, which is held to dominate the physics of nucleons.

Consider the QCD Lagrangian formulated with some number N_f of massless flavors. One of the features of this Lagrangian is a global symmetry under $U(N_f) \times U(N_f)$ rotations of the full Dirac spinors of left- and right-handed quark fields. This *chiral* symmetry allows the mixing of states with different parities (through axial $U(N_f)$ rotations), so that we would expect to see a parity degeneracy in each set of states with otherwise identical quantum numbers if the symmetry were exact. Yet we know that this symmetry is not exact; the bare masses of even the light quarks ($m_u \approx 2$ MeV and $m_d \approx 4.5$ MeV [11]) break chiral symmetry explicitly. Yet these masses are far too small to explain the observed splitting between states with the same quantum numbers except for parity; for example, the mass difference between the nucleon and its parity partner, the N(1535), is nearly 600 MeV! This discrepancy implies that chiral symmetry is broken both spontaneously and strongly; the associated order parameter, the *chiral condensate*, is on the order of a few hundred MeV, large enough to be a significant effect in the dynamics of the nucleon.

It is then useful to work in a generalized SU(N_c) group where there is an arbitrary number of colors N_c (as opposed to the real world, which has $N_c = 3$). If N_c is arbitrarily large, then $1/N_c$ may be used as an expansion parameter. At low energies, the chiral soliton model reduces the nucleon to a collection of weakly interacting mesons and glueballs, binding together the valence quarks. Despite this non-intuitive basis, the model has resulted in some startlingly accurate predictions; for example, the relationship between mass splittings in the baryon decuplet and the baryon octet, predicted by this method, fits the observed data to better than 1% [98].

Within these broad parameters, there are a variety of chiral soliton models. The **N**ambu-**J**ona-**L**asinio (NJL) model [99, 100], based on a local four-fermion interaction with U(1)×SU(2)$_L$×SU(2)$_R$ chiral symmetry, is a popular choice for studies of nucleon structure functions [101, 102, 103] be-

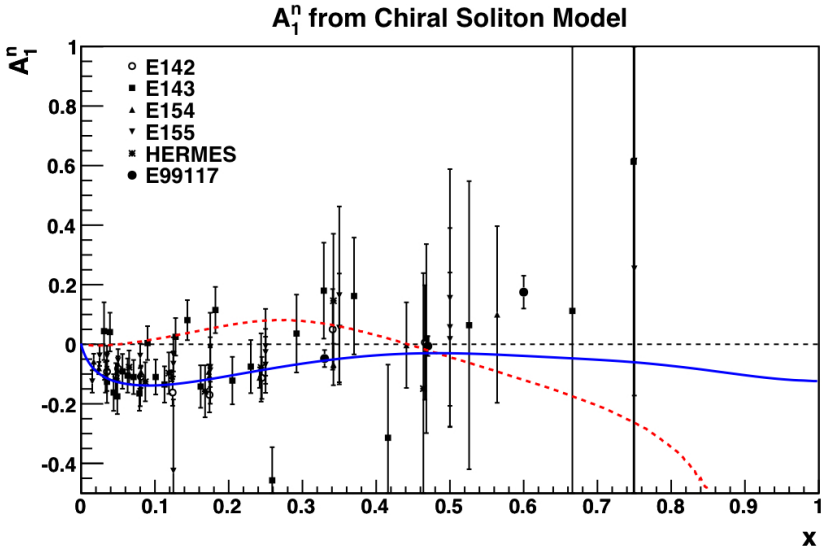

Figure 2.15: Predictions of A_1^n from chiral soliton models. The red dashed line is a prediction from the NJL model [101, 102]; the blue solid line is a prediction from an SU(3)-based model [104, 105]. We have made use of parameterizations compiled by X. Zheng [71].

cause it uses quark degrees of freedom to describe the hadronic currents, which simplifies the calculation [103]. An alternative approach [97] begins from the assumption that SCSB is caused by instantons, nonperturbative gluon-field fluctuations which allow delocalization of quark wave functions. This approach has the advantage that the model preserves the original $\mathrm{SU}_L(N_f)\times\ \mathrm{SU}_R(N_f)$ symmetry of the QCD Lagrangian (although it does explicitly break the axial $U_A(1)$ symmetry). This second approach has recently been extended to three quark flavors and used to make predictions about nucleon structure functions [104, 105].

Figure 2.15 shows the ratio g_1^n/F_1^n as predicted by these two approaches to the chiral soliton model. These predictions do not incorporate any fit to world data.

2.3.7 Instanton Model

Let us return briefly to the concept of *instantons*, the nonperturbative gluon-field fluctuations we described as a possible source of chiral symmetry breaking in Section 2.3.6. At any moment, the collection of instantons may be regarded as binding quarks at zero energy [97]. Delocalization occurs when quarks tunnel between instantons, and quarks flip their helicity in the zero-mode form of this interaction. This mechanism would tend to depolarize quarks by transferring their polarization to gluons and quark-antiquark pairs within the nucleon.

In an effort to explain the proton spin puzzle, Nikolai Kochelev used the instanton liquid model for the QCD vacuum to estimate the effect of instanton-induced processes on the polarized proton structure function g_1^p [106]. The resulting contribution is negative and quite large at low x, but approaches 0 as $x \to 1$, giving a possible explanation to the spin puzzle and suggesting that A_1^p is negative [41]. Unfortunately, it is not straightforward to apply this model to the neutron, as the theory is extremely sensitive to the precise mechanics of SU(6) symmetry breaking in the valence-quark distribution functions. If the instanton contribution to g_1^n is analogous to that for the proton, which is by no means clear, this model could imply that A_1^n is negative at high x, but the prediction that $A_1^p < 0$ is clearly at odds with the data.

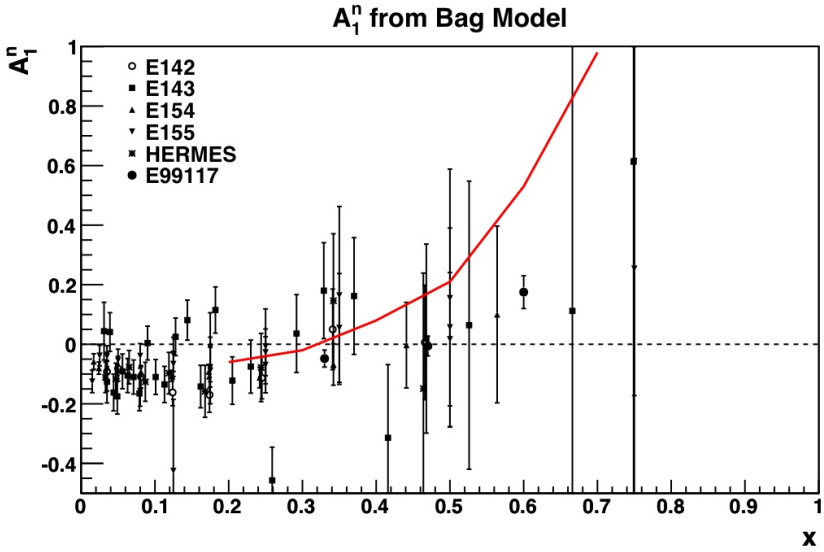

Figure 2.16: Prediction of A_1^n from bag model [107], including hyperfine effects but excluding corrections due to the pion cloud. We have made use of parameterizations compiled by X. Zheng [71].

2.3.8 Bag Model

The MIT bag model [108], proposed in 1975 by a quintet of physicists from the Massachusetts Institute of Technology, treats the hadron as a "finite region of space" in which strong fields are confined. Inside this region – the *bag* – massless quarks move quasi-freely and relativistically, but they are confined to the bag by boundary conditions; outside the bag, they are infinitely massive.

In the most basic formulation of the bag model, each quark moves in its own orbital and the quarks do not interact with each other. In later refinements of the model, this simplification was addressed by allowing certain types of interactions. Schreiber, Signal and Thomas, for example, obtained a prediction of $2xg_1/F_2$ for the proton by beginning with the three-dimensional MIT bag model, modifying the wave functions to bring them into momentum space, and introducing one-gluon exchange (that is, a color hyperfine interaction) between the quarks [109]. In the Bjorken limit, where the Callan-Gross relation is expected to hold, this quantity is equal to g_1/F_1 and thus to A_1.

One-gluon exchange is not the only spin-dependent effect of importance in models of the nucleon; as we saw in Sections 2.3.6 and 2.3.7, nonperturbative instanton interactions must also be considered. More general spin-dependent interactions may be included in the bag model by means of an explicit symmetry-breaking parameter, which again enables predictions of $2xg_1/F_2$ for both the proton and the neutron [110].

A failing of the basic MIT bag model is the fact that chiral symmetry is explicitly broken on the surface of the bag. This problem is addressed by the *cloudy bag model* [111, 112], wherein a meson cloud couples to the quarks at the bag's surface. This meson cloud may be assumed to be composed primarily of pions; since other mesons have higher mass, any corrections due to their presence will be smaller than the adjustments due to pions [113].

Reasoning in the cloudy bag model, Tony Thomas has argued that the proton spin puzzle has been solved [114] – or, at least, that experiment and theory are now in agreement that approximately 35% of the proton spin is carried by its valence quarks. The theoretical side of the solution hinges on the relativistic treatment of the valence quarks, intrinsic to the original MIT bag model; the prediction that the pion cloud (whose role is constrained by lattice QCD) has net spin opposite to

the net spin of the *bare* nucleon (that is, the nucleon undressed with pions); and the inclusion of one-gluon exchange, which further reduces the valence quark spin.

Boros and Thomas have published predictions of the polarized structure function g_1 for the proton in this model, with and without pion corrections [107]. As part of the same work, they also predicted values for A_1^n, with hyperfine interactions [115] but without pion corrections [116], as shown in Figure 2.16.

Chapter 3

The E06-014 Experiment

The data presented in this dissertation were taken during Experiment E06-014 at the Thomas Jefferson National Accelerator Facility (Jefferson Lab) in Newport News, Virginia. The measurement of A_1^n was not a primary goal of this experiment, but the data set was, happily, able to accommodate more than one interesting physics measurement. In this chapter, we describe E06-014 in detail, from motivation to apparatus to execution. In Section 3.1, we will give a brief introduction to the driving physics goal of E06-014, summarize the experimental setup, and describe the actual course of data-taking. Section 3.2 describes CEBAF, the electron accelerator at Jefferson Lab. In Section 3.3, we give a detailed discussion of most of the hardware in Hall A, the experimental hall where E06-014 took place; the hall's two polarimeters, however, are the subject of Chapter 4, and spectrometer calibrations will be described in Chapter 5. Our analysis software system – a vital component of any modern accelerator experiment – is described in Section 3.4. Finally, in Section 3.5, we briefly summarize the course of the actual experimental run.

3.1 Overview of Experiment E06-014

Experiment E06-014, also known as the d_2^n experiment, ran in Hall A of Jefferson Lab from February 7 to March 17, 2009. Its purpose was to perform a precision measurement in the neutron system of the quantity d_2, which is formed from the polarized structure functions g_1 and g_2. Although this dissertation is primarily concerned with A_1 rather than d_2, it is worth a brief digression into the physics of d_2 in order to motivate the experimental choices of E06-014.

d_2 is a function of Q^2 and is defined as follows

$$d_2\left(Q^2\right) \equiv \int_0^1 x^2 \left[2g_1\left(x, Q^2\right) + 3g_2\left(x, Q^2\right)\right] dx. \tag{3.1}$$

Through its dependence on g_2, d_2 is sensitive to quark-gluon correlations and other high twist processes (see Section 1.3.3.3). Indeed, if we separate g_2 into a twist-2 piece g_2^{WW} (the Wandzura-Wilczek term of Equation 1.46) and a higher-twist piece $\bar{g}_2$, we see that d_2 is solely determined by higher-twist dynamics

$$d_2 = \int_0^1 x^2 \bar{g}_2(x, Q^2) dx. \tag{3.2}$$

In the operator product expansion (Section 1.3.3.3), we can express d_2 as a twist-3 matrix element. Let $F_{\alpha\beta}$ refer to the gluon field operators and g refer to the QCD coupling constant. S^μ is the proton spin and P^μ its momentum. If we define

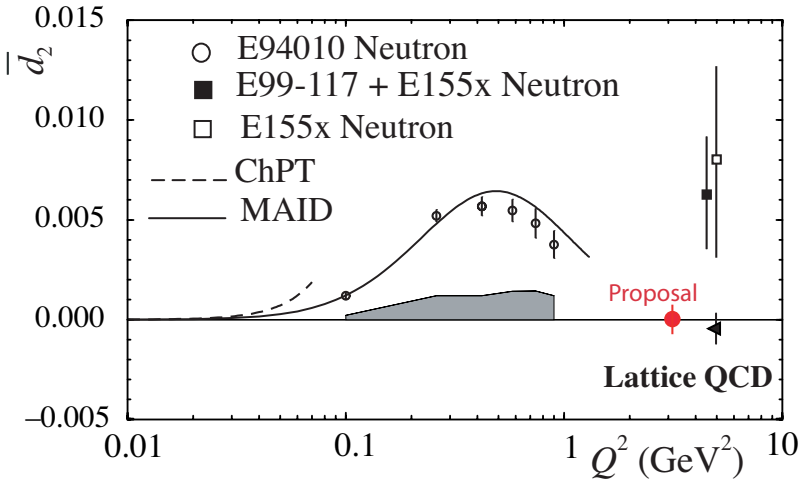

Figure 3.1: Projected error bar on E06-014 measurement of $\bar{d}_2^n$ at $\langle Q^2 \rangle = 3$ GeV^2, compared to a lattice QCD prediction [118], the results of Jefferson Lab experiments E94-010 [119] and E99-117 [41], and the results of SLAC experiment E155X [120]. The quantity $\bar{d}_2^n$ is equal to d_2^n with the elastic contribution ($x = 1$) subtracted from the integral. The solid line shows the results of a MAID calculation [28]; the dashed line is from a chiral perturbation theory calculation at low Q^2 [121]. This figure is reproduced from the E06-014 proposal [122].

$$\bar{F}^{\mu\nu} \equiv \frac{1}{2}\epsilon^{\mu\nu\alpha\beta}F_{\alpha\beta} \tag{3.3}$$

then we may represent d_2 as

$$d_2 S^{[\mu}P^{\{\nu]}P^{\lambda\}} = \frac{1}{8}\sum_q \langle P,S|\bar{\psi}_q g \bar{F}^{\{\mu\nu}\gamma^{\lambda\}}\psi_q|P,S\rangle \tag{3.4}$$

where the brackets $\{...\}$ denote symmetrization of indices and the brackets $[...]$ denote antisymmetrization [117], so that the left-hand side of Equation 3.4 is symmetric under ν, λ interchange and antisymmetric under μ, ν interchange.

Equation 3.4 sets the stage for one of the two main physical interpretations of d_2^n. Since both the strong force and the electromagnetic force conserve parity, we can pursue an analogy between color fields and electromagnetic fields: in the rest frame of a polarized nucleon, the color magnetic field $\vec{B}$ is along the nucleon polarization direction, while the color electric field $\vec{E}$ is perpendicular to it. We can then define the color polarizabilities of the nucleon, χ_B and χ_E, in the nucleon rest frame

$$\langle P,S|\hat{O}_{B,E}|P,S\rangle = \chi_{B,E} 2M_N^2 \vec{S} \tag{3.5}$$

where M_N is the mass of the nucleon and the color singlet operators are defined by $\hat{O}_B \equiv j_a^0 \vec{B}_a$ and $\hat{O}_E \equiv \vec{j}_a \times \vec{E}_a$, where we have expressed the quark current as $j_a^\mu = -g\bar{\psi}\gamma^\mu t_a \psi$ [123] and $t_a = \lambda_a/2$ is a generator of SU(3), with λ_a a Gell-Mann matrix.

By combining Equations 3.4 and 3.5, we obtain [124]

$$d_2 = \frac{1}{4}\left(2\chi_B + \chi_E\right). \tag{3.6}$$

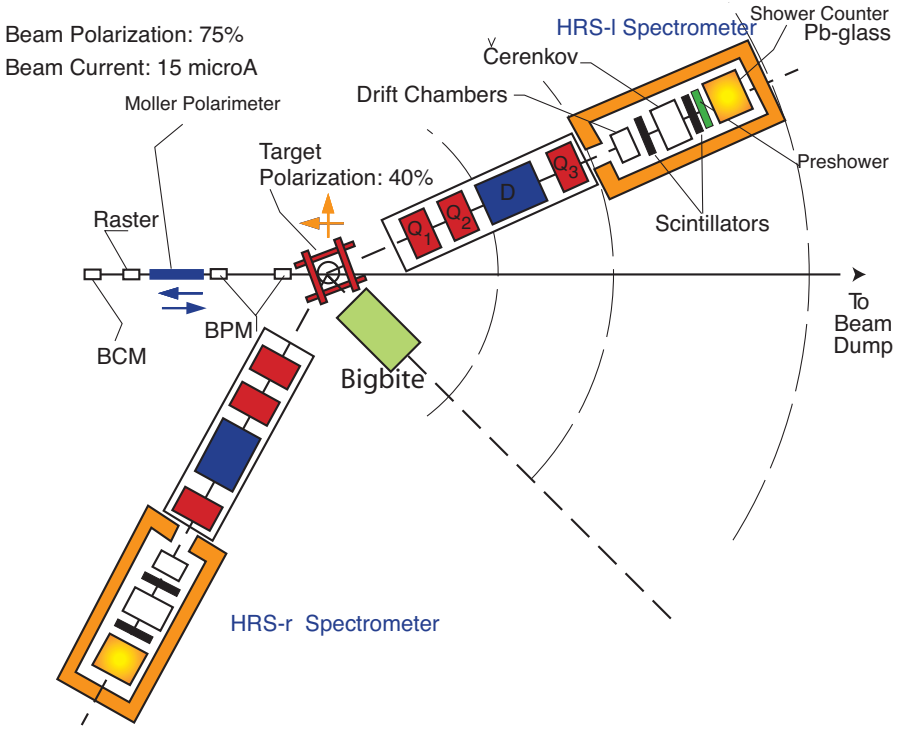

Figure 3.2: Hall A spectrometer placement during E06-014, reproduced from the E06-014 proposal [122].

In the words of Filippone and Ji [117], we see that "d_2 measures the response of the color electric and magnetic fields to the polarization of the nucleon." Meanwhile, if we consider a nucleon with transverse spin relative to the incident electron momentum, d_2 measures the mean color magnetic field $\vec{B}$ in the direction of its transverse spin [125].

Conventionally, polarizability refers not just to an alignment of spins, but to the distortion of a charge distribution from its usual shape in the presence of an external field. As the Q^2 of an interaction increases, we can still speak of the nucleon as being spin-aligned, but the correlators are local and it is no longer deformed in shape; it is then increasingly less appropriate to speak in terms of "polarizability" [124]. At high values of Q^2, we have

$$d_2 = \frac{-1}{M_N^2} F^y(0) \tag{3.7}$$

which gives us the second physical interpretation of d_2: at time $t = 0$, immediately after a quark inside the nucleon has been struck by a virtual photon, d_2 is proportional to the ensemble-averaged transverse force on the struck quark [124].

The quantity d_2 may be measured on either the proton (d_2^p) or the neutron (d_2^n). Like A_1, it has been calculated for both nucleons using a variety of models and methods, from QCD sum rules [125] to the chiral-quark soliton model [126] to lattice QCD [118]. A lack of precise data at large x values dominates error bars on the world data. By improving statistics in this region, E06-014 was designed to improve the statistical error bar on d_2^n by a factor of almost four [122], as shown in Figure 3.1.

3.1.1 Measurement Strategy

In order to achieve this fourfold statistical error reduction, E06-014 was designed to take data entirely in the **d**eep **i**nelastic **s**cattering (DIS) region, in the range $0.2 < x < 0.7$ and 2 $(\mathrm{GeV/c})^2 < Q^2 < 6$ $(\mathrm{GeV/c})^2$. It took data for six weeks in Hall A, the largest of Jefferson Lab's three experimental halls and ran with 15μA of polarized electrons incident on a fixed, polarized ^{3}He target (Section 3.3.3). Since a free neutron has an average lifetime of only about 14.75 minutes [11], a free-neutron fixed target is impractical; further, spin-polarizing neutral particles imposes an additional layer of complexity. A ^{3}He target makes an excellent proxy, however, as the polarization of the ^{3}He nucleus is carried by the neutron with a probability of approximately 87% [127].

The experiment used two of the hall's three large spectrometers: BigBite (Section 3.3.4) and the **L**eft **H**igh-**R**esolution **S**pectrometer (LHRS) (Section 3.3.5). Each spectrometer was placed at an angle of 45° relative to the beamline and operated in a single-arm mode, configured to detect electrons. BigBite – chosen for its large acceptance and ability to handle high counting rates – took data for measurements of the double spin asymmetries $A_\parallel$ and $A_\perp$. The LHRS, with lower noise and a better-understood efficiency, took data for a measurement of the unpolarized total cross section σ_0. The asymmetry measurements were made possible by the fast (30 Hz) flipping of the electron beam helicity, and by periodic changes to the polarization direction of the ^{3}He target.

These three measured quantities – σ_0, $A_\parallel$ and $A_\perp$ – can be combined with the kinematic variables defined in Section 1.2.1 to form an expression for d_2^n

$$d_2^n = \int_0^1 \frac{MQ^2}{4\alpha^2} \frac{x^2y^2}{(1-y)(2-y)} \sigma_0 \left[\left(3\frac{1+(1-y)\cos\theta}{(1-y)\sin\theta} + \frac{4}{y}\tan(\theta/2) \right) A_\perp + \left(\frac{4}{y} - 3 \right) A_\parallel \right] dx \quad (3.8)$$

where M is the neutron mass and θ is the electron scattering angle in the laboratory frame. Expressing d_2^n in terms of the direct experimental observables (cross section and asymmetry) simplified the problem of optimizing the statistical error on d_2^n (rather than on the structure function g_2): since $A_\perp$ contributes the most to this error, the majority of running time was spent with the target polarized transverse to the electron beam.

Figure 3.2 shows the layout of the spectrometers on the floor of Hall A. The right HRS position was chosen so as to leave enough space for the BigBite spectrometer; it was not used for E06-014 data.

3.1.2 Kinematic Settings

Figure 3.3 shows the planned kinematic coverage of the experiment. In order to report results with a constant Q^2 over a wide x range, the decision was made to measure two Q^2 points at each x value and interpolate. The experiment therefore took data with two electron beam energies: 4.7 GeV and 5.9 GeV. A single BigBite magnetic field setting covered the entire kinematic range; the LHRS, with a much smaller acceptance, required twenty magnet settings, ten at each beam energy, to achieve the same coverage. These are the bands of different colors in Figure 3.3.

Due to time constraints, the experiment took data for only fifteen out of the twenty planned LHRS magnet settings. Tables 3.1 and 3.2 list the final kinematic settings for the two beam energies, with corresponding x and Q^2 values.

3.2 CEBAF

The Continuous Electron Beam Accelerator Facility (CEBAF) [130], Jefferson Lab's source of accelerated, polarized electrons, is a superconducting radiofrequency accelerator. Figure 3.4 is an aerial view of the site, showing CEBAF's racetrack shape in the background and the domed experimental halls in the foreground. CEBAF can deliver simultaneous beam of varying energy to all

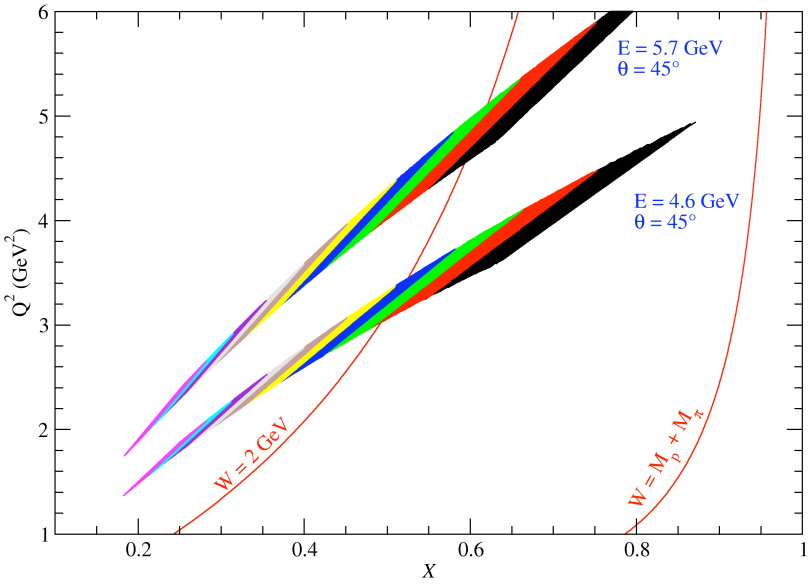

Figure 3.3: Planned E06-014 kinematic coverage, reproduced from readiness review [128]. Each band gives the kinematic range at a constant spectrometer angle and beam energy. The width of each band is set by BigBite's horizontal angular acceptance; the colored bins within each band represent the ten LHRS central-momentum settings that were planned for each beam energy.

three halls. The lowest possible operating energy is about 0.6 GeV, while the highest approaches 6 GeV. Table 3.3 gives selected operating parameters for the accelerator. In the following sections, we will describe the beam source, the accelerator itself, and the delivery of accelerated beam to the experimental halls.

3.2.1 Polarized Electron Source

Experimental programs in the three halls demand highly polarized electron beams that can be delivered simultaneously to three end stations, each of which may require different beam energies and different currents. (In particular, currents in Hall B are up to 10^5 times lower than currents in the other two halls.) To achieve these goals, the beam in each hall is made up of bunches with a repetition rate of 499 MHz, the third harmonic of the 1497-MHz fundamental frequency of the accelerator. The beams for the three halls are interleaved together [130]; thus, the properties of a given bunch in the accelerator are shared with the electrons three bunches ahead and three bunches behind, but not with the bunches immediately preceding and following.

The source of the polarized electron beam is a photocathode that emits electrons when illuminated by a pulsed laser at a certain energy; the laser's pulse rate sets the bunch repetition rate of the beam. The photocathode is made of strained superlattice gallium arsenide (GaAs), a descendant of photoemission gun technology that dates from 1976 [131]. When the photocathode absorbs a photon of the right energy, an electron is excited into the conduction band; in the presence of a large external electric field, it then diffuses to the surface and escapes to the vacuum outside. It is the energy-level structure of GaAs that allows us to produce polarized electrons with a circularly polarized laser beam [132].

Figure 3.5(a) shows the energy levels for bulk GaAs. The lowest level in the conduction band, with its minimum marked Γ_6 in the diagram, has s-type symmetry. The top levels of the valence band, their maxima marked Γ_7 and Γ_8, have p-type symmetry; the energy gap between them is due

Momentum Setting (GeV/c)	x	Q^2 (GeV/c)^2
0.60	0.208	2.07
0.90	0.331	3.11
1.13	0.436	3.89
1.20	0.470	4.14
1.27	0.505	4.38
1.34	0.541	4.62
1.42	0.584	4.89
1.51	0.633	5.21
1.60	0.685	5.52
1.70	0.745	5.87

Table 3.1: LHRS kinematic settings during E06-014 for a beam energy of 5.89 GeV.

Momentum Setting (GeV/c)	x	Q^2 (GeV/c)^2
0.60	0.214	1.66
0.80	0.300	2.22
1.42	0.633	3.93
1.51	0.692	4.18
1.60	0.754	4.43

Table 3.2: LHRS kinematic settings during E06-014 for a beam energy of 4.73 GeV.

Repetition rate	499 MHz/hall
Transverse RMS beam size	$\sim$ 80 μm
RMS bunch length	300 fs/90 μm
Energy spread	2.5×10^{-5}
Average cavity accelerating gradient	7.5 MV/m
RF power per cavity	$<$ 3.5 kW
Average cavity Q_0	4.0×10^9
Cavity operating temperature	2.08 K
Beam power	$<$ 1 MW
Beam loss	$<$ 1 μA
Beam current	1-150 μA (Halls A and C) 1-100 nA (Hall B)

Table 3.3: Selected operating parameters for CEBAF [130].

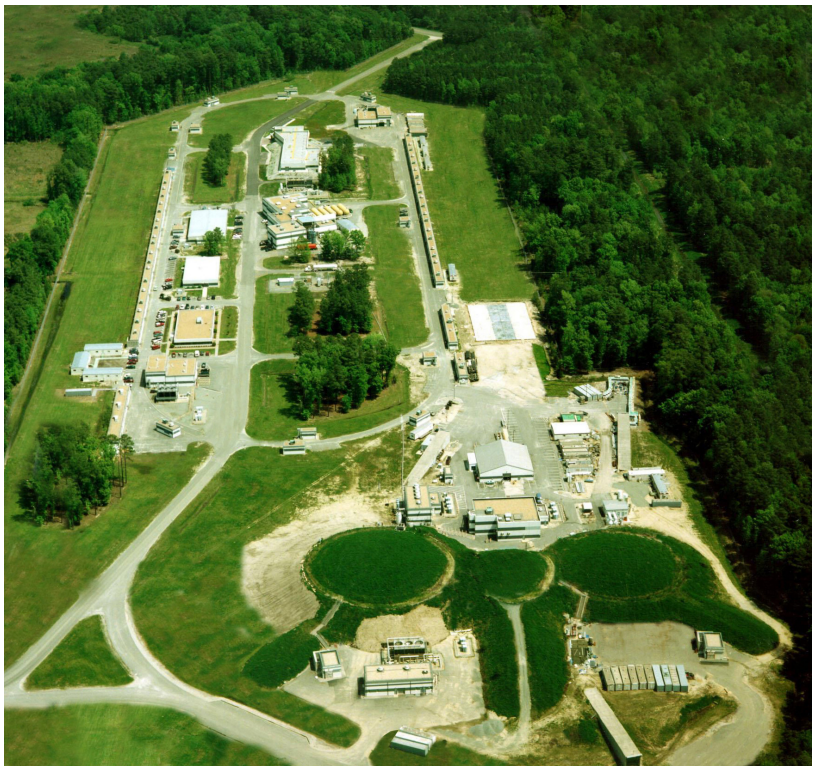

Figure 3.4: Aerial view of Jefferson Lab accelerator site, taken in 2001. The racetrack shape of the underground accelerator is reflected in the support buildings and roads visible in the upper left. The round, grass-covered hills over the three experimental halls can be seen in the lower right; Hall A is the leftmost of the three halls. This photograph was submitted by Shannan Kyte to the Jefferson Lab Picture Exchange [129].

to spin-orbit coupling, but Γ_8 is two-fold degenerate, taking contributions from both the light hole band (lh, $m_j = \pm 1/2$) and the heavy hole band (hh, $m_j = \pm 3/2$). Suppose that we illuminate the crystal with left-circularly polarized light (σ^-) whose photon energy is larger than the band gap energy E_g, but less than $E_g + \Delta_{SO}$. Since the photons have helicity -1, only two transitions are possible for the electrons they excite: $m_j = 3/2 \rightarrow m_j = 1/2$, and $m_j = 1/2 \rightarrow m_j = -1/2$. The first transition is three times more likely than the second, so the final population of electrons will have three times as many positive-helicity electrons as negative-helicity electrons.

The polarization P of an electron beam is defined as an asymmetry between the number of electrons in each helicity state

$$P = \frac{N_+ - N_-}{N_+ + N_-}. \tag{3.9}$$

This gives the electron beam from a bulk-GaAs photocathode a maximum polarization of 50%, as shown at the right of Figure 3.5(a). For illumination with right-circularly polarized light, which has helicity $+1$, we can work through an analogous derivation to find that the resulting electron beam is 50% polarized in the opposite direction.

In the 1990s, this performance was improved dramatically by the introduction of strained GaAs photocathodes [133]. These photocathodes typically consist of a layer of GaAs grown on top of a layer of GaAsP. The lattice spacing of the pure GaAs layer shrinks slightly to meet the lattice

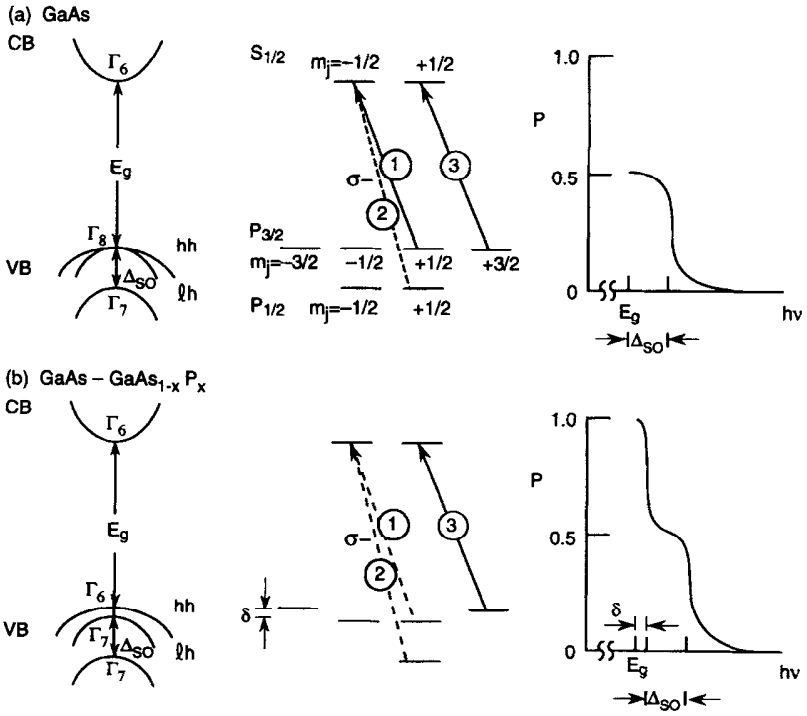

Figure 3.5: Energy levels for bulk (a) and strained (b) GaAs, reproduced from Alley *et al.* [132]. At left is the minority carrier energy E as a function of momentum k, showing the conduction band at the top and the valence band at the bottom. In the center, transitions between energy levels are shown for absorption of a left-circularly polarized photon; dashed-line transitions may be avoided through a careful choice of photon energy, and numbers in circles indicate the relative transition probabilities (*i.e.* the transition marked *3* is three times as likely as the one marked *1*). At right is the polarization of the excited electrons as a function of photon energy.

spacing of the GaAsP layer, and the resulting strain breaks the degeneracy of the light hole and heavy hole bands. Figure 3.5(b) shows the resulting level diagrams. It is now possible to choose a photon energy so that only one transition is possible from the valence band to the conduction band; in principle, this could result in an arbitrarily well-polarized electron beam.

In practice, however, electron beams generated from this method showed a maximum polarization of about 80%. Investigation showed that this was partly due to the fact that the pure GaAs layers in these photocathodes were too thick (about 100 nm) to experience uniform strain throughout their volume. The solution was to form a strained superlattice, formed of multiple pairs of GaAs and GaAsP layers, thin enough to avoid strain relaxation [134]. Jefferson Lab's strained superlattice photocathode consists of 14 layer pairs with a total depth of 100 nm [135].

Strained superlattice technology has one additional appealing feature: the 780-nm photons required to excite the photocathode can be produced by frequency-doubling commercially available, fiber-based 1560-nm lasers. These require far less maintenance than the mode-locked Ti-Sapphire lasers that drove the 850-nm transitions of the older, single-strained-layer photocathodes [136]. Furthermore, lasers, amplifiers and fibers at a wavelength of 1560 nm are relatively cheap, since this wavelength is common in the telecommunications industry.

Each of the three halls has its own dedicated laser system: a 1560-nm seed laser, an ErYb-doped fiber amplifier, and a periodically poled lithium niobate (PPLN) crystal used to double the photon frequency via second harmonic generation [137]. Each laser is gain-switched so that it pulses at a rate

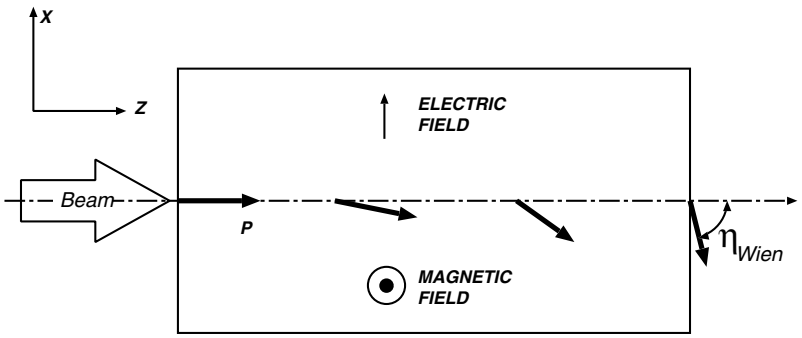

Figure 3.6: Schematic of a Wien filter for an electric field and spin rotation in the horizontal plane. Reproduced from Grames *et al.* [139].

of 499 MHz, 120° out of phase with the others. With beam splitters, polarizers, and dichroic mirrors, the three laser beamlines are eventually directed along a single axis, so that all three lasers illuminate the same photocathode. Along this common beamline, a Pockels cell operates as a quarter-wave plate, converting the linearly polarized 580-nm beams into circularly polarized beams; fast helicity flipping (right circular to left circular, and vice versa) is made possible by flipping the sign of the Pockels cell voltage.

Just before entering the Pockels cell that will give it circular polarization, the linearly polarized 780-nm light passes through another Pockels cell whose voltage, changing according to the same fast-helicity-flipping sequence, is set to vary the intensity of the laser light in order to minimize the helicity-correlated charge asymmetry of the beam. This cell is part of a feedback loop that includes the Hall A beam current monitors and a special data-acquisition system developed by the HAPPEX (Hall A Proton Parity Experiment) collaboration, and generally keeps the charge asymmetry below about 200 ppm. For additional control of helicity-correlated effects, an insertable half-wave plate (IHWP), made of mica, can be placed in the photon beamline, changing the helicity produced by a given Pockels cell voltage [138].

A constant, -100-kV electric field on the photocathode aids in electron extraction and gives the electrons an energy of 100 keV on their way into the injector. In this 100-keV beamline, a Wien filter [139] is used to rotate the electron spin direction without changing the central beam orbit. When configured with knowledge of spin precession in the accelerator and in the beamlines to the experimental halls, this allows the polarization direction to be optimized in the three halls. As shown in Figure 3.6, a Wien filter provides static electric and magnetic fields perpendicular to each other and to the electron velocity. The apparatus rotates the beam polarization through an angle η_{Wien} in the electric field plane; the size of the angle is largely determined by the size of the electric field integral. The magnetic field strength is chosen to satisfy $|E/B| = \beta$ (where $\beta = v/c$ is the electron velocity) so as to cancel the Lorentz force exerted on the beam by the electric field.

3.2.2 Accelerator

Polarized electrons from the electron source are accelerated to high speeds using superconducting radiofrequency (srf) technology. The basic unit of the accelerator is the accelerating cavity, two of which are shown in Figure 3.7. Each cavity is fashioned from pure niobium and contains five cells with an elliptical cup shape; they are kept at a temperature of 2.08 K, at which niobium is a superconductor, by liquid helium supplied by the Central Helium Liquefier (CHL). With the aid of its own 5 kW klystron, each cavity is driven by a 1497 MHz electromagnetic wave so that the wave crests can be aligned with the electron bunches, giving the cavities an average gradient of up to 7.5 MV/m. Each pair of five-cell cavities is sealed together in a single cryostat to make a cryounit; in

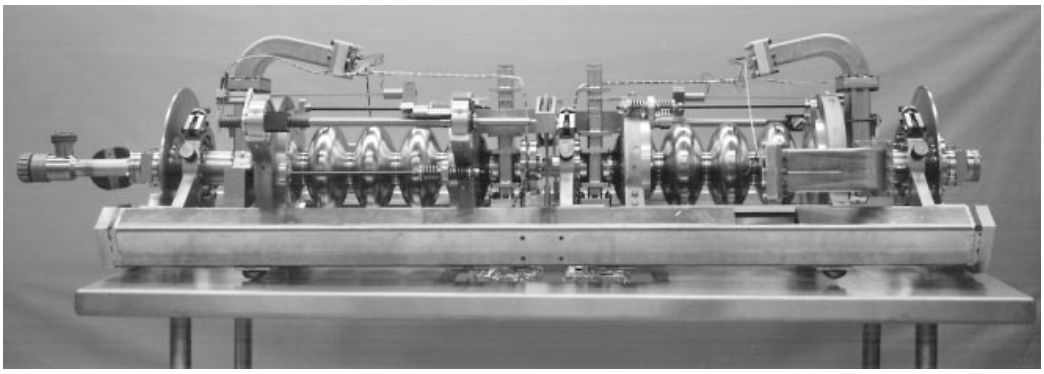

Figure 3.7: Pair of accelerating cavities, later installed in the CEBAF beamline. Each 50-cm cavity contains five cells. Four cavity pairs make up a cryomodule. Reproduced from Leemann *et al.* [130].

turn, four cryounits are joined to make an 8.25-meter cryomodule. Neighboring cryomodules are connected by warm beam pipes and steering magnets [130].

The basic layout of CEBAF is shown in Figure 3.8. At the injector, electrons from the source are accelerated from their initial energy of 100 keV to a final energy of 45 MeV; this is accomplished by passing them through two and a quarter cryomodules. From the injector, they enter the north linear accelerator segment, which consists of 20 consecutive cryomodules or 160 srf cavities. Early in Jefferson Lab's operational history, an electron passing through this linac would have experienced an energy gain of about 400 MeV, but an energy gain of 600 MeV is now commonplace.

After passing through the north linac, electrons are taken through a 180° bend by a series of quadrupole and dipole magnets in a recirculation arc with a radius of 80 meters. These magnets steer the beam into the south linac, antiparallel to the north linac but otherwise identical, where it gains another 600 MeV, and another recirculation arc completes the racetrack shape.

The experimental halls are located at the end of the south linac, but instead of going directly to these end stations, the beam may be recirculated through the pair of linacs up to four times, each time using a different set of recirculation arcs, for a total of up to five passes through the accelerator. RF separators and septum magnets allow particular bunch trains and energies to be extracted from the second recirculation arc and sent to the appropriate hall. With this combination of extraction tools, each hall may take a different beam energy, as long as they are all multiples of the one-pass beam energy, or any number of halls may simultaneously take beam at the maximum energy setting. A maximum total current of 150 μA may be divided arbitrarily among the three halls.

3.2.3 Beam Delivery to the Experimental Halls

Once the bunch train for Hall A's beam has been extracted from the end of the south linac, it must be bent through an angle of 37.5° to enter the hall [141]. This is primarily accomplished by the series of eight dipoles that, with support magnets (a quadrupole and a pair of steering magnets for each dipole), makes up the Hall A arc. (Similar systems handle beam delivery for the other two halls.) This system must not only deliver tightly specified beam to the target location, but must also meet additional specifications at certain points along the way; for example, 50 μm position stability is needed not only at the target, but also at the two beamline polarimeters.

Fast helicity flipping at the electron source (Section 3.2.1) is programmable according to experimental needs, but since the Pockels cell is on the common photon beamline, the same helicity structure is sent to all halls. During E06-014, the beam helicity followed the specifications engineered by the G^0 experiment in Hall C [142]. In this scheme, the electron beam is be subdivided into 1/30-second helicity *windows*, also known as *MPS*es for the **M**aster **P**ulse **S**ignals which mark

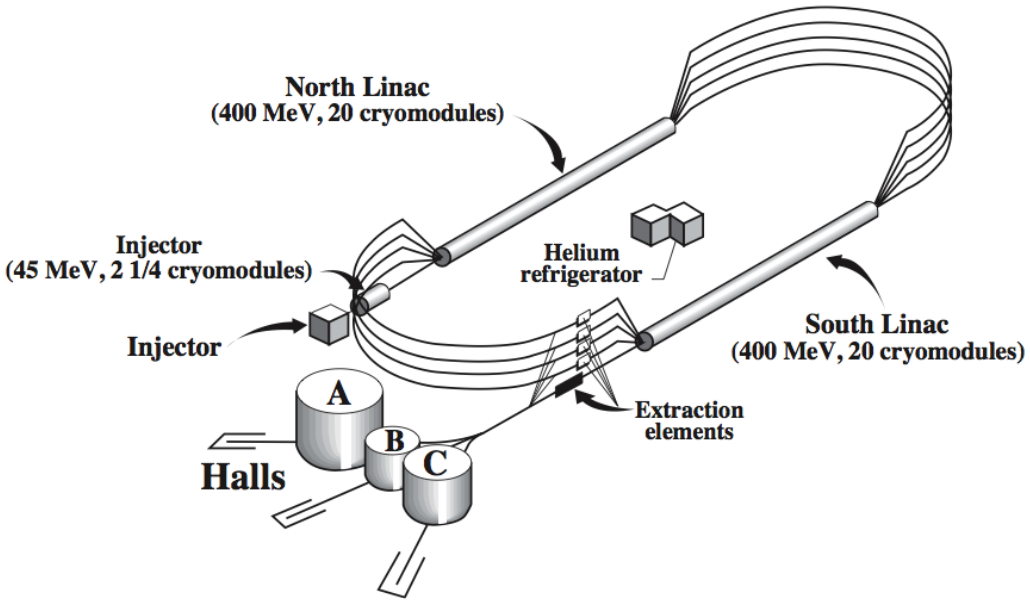

Figure 3.8: Schematic of CEBAF, reproduced from Alcorn *et al.* [140]. The electron beam originates at the injector and is accelerated to 45 MeV before entering the north linear accelerator. The electrons gain energy in each of the two linacs, and can be recirculated through the pair of linacs up to four times before being delivered to one of the three experimental halls.

their boundaries. During each window, the electron beam helicity has a well-defined nominal direction, either parallel (+) or antiparallel (−) to its momentum. (We will discuss determinations of the electron beam polarization – i.e. the degree to which "parallel" or "antiparallel" is an accurate description of the electrons' longitudinal spins – in Chapter 4.)

Sets of four consecutive helicity windows are arranged in one of two symmetric quartets: either $+--+$ or $-++-$. Each quartet comprises two consecutive helicity *pairs*; each pair includes both complementary helicity states. Once the helicity state of the first window in a quartet is decided (via a pseudorandom number-generation algorithm), the three subsequent helicity states are likewise uniquely determined. A signal indicating the helicity direction is sent in real time to the data-acquisition systems, as is a signal marking the beginning of a quartet. The MPS signal marks the beginning of a new helicity window, and gives a pulse regardless of whether or not the helicity is actually flipped. This pulse marks a possible transition; during it, the helicity of electrons in the hall is indeterminate.

Figure 3.9 shows the timing for the MPS, helicity signal, and quartet-initialization (QRT) signal. Many experiments, particularly those that are sensitive to very small helicity-correlated systematic effects, run with a delayed helicity signal, where information about a helicity window's polarization direction arrives several MPSes after the accelerated electrons do. (A typical delay is eight MPSes.) E06-014 declined this option and ran with a prompt helicity signal.

3.3 Hall A Hardware

E06-014 ran in Hall A, one of Jefferson Lab's three experimental halls. In this section, we describe the Hall-based apparatus that made the measurement possible, most of which is standard equipment with some modifications for our experiment.

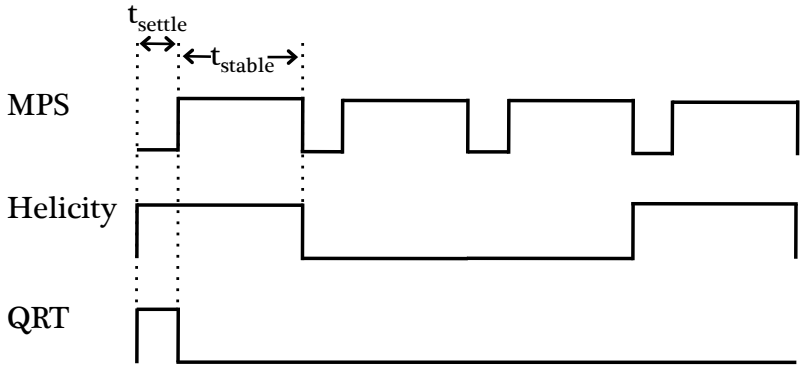

Figure 3.9: Timing for MPS, helicity and QRT signals in the G^0 scheme. The helicity signal shown is for a $+--+$ quartet; it would be inverted for a $-++-$ quartet, while the other signals would remain the same.

3.3.1 Coordinate Systems in Hall A

Two coordinate systems are in use to characterize the behavior of the electron beam as it travels along the Hall A beamline; additional coordinate systems are introduced once the beam strikes the target, so as to describe the paths of the scattered particles relative to the target and to the spectrometers. Here, we will define the various coordinate systems used in Hall A; over the remainder of this dissertation, we will refer back to these systems frequently.

Upstream of the target, the z axis is traditionally placed along the beamline, with increasing z in the downstream direction (toward the target). Two coordinate systems – the Accelerator system, used for beam steering, and the Hall A system, used for equipment surveys and for tracing the beam upstream of the target – define z thus, and denote the vertical axis as y (with positive y in the upward direction). As shown in Figure 3.10, however, the two systems differ in their definitions of the x axis. The Hall A coordinate system places positive x to beam left (when the system is viewed looking downstream); the Accelerator coordinate system, which is used in the definitions of EPICS variables, places positive x to beam right, and is thus a left-handed coordinate system [143]. The origin of the Hall A coordinate system is taken as the nominal center of the target cell, which is also the pivot point of the High-Resolution Spectrometers.

We can also define a *target coordinate system* for each spectrometer, so named because the origin is in the target (where the central ray of the spectrometer intersects with the z axis in the Hall A system). Here, the z axis points down the central ray of the spectrometer, away from the target and parallel to the floor. The x axis points downward (with gravity); note that the x_{tg} axis is vertical whereas the x_{Hall} axis is horizontal. The y axis, which is parallel to the floor, is defined so as to form a right-handed coordinate system: $\hat{y} = \hat{z} \times \hat{x}$. These systems are typically used when projecting tracks back to the target in order to determine momenta and scattering vertices.

Finally, each spectrometer has a set of *detector coordinates*, which simplify the problem of finding tracks in drift chambers and projecting these trajectories into other parts of the detector stack. For BigBite, the detector coordinate system has its origin in the center of the first multi-wire drift chamber plane. The z axis is the nominal direction of a particle traveling perpendicular to the wire plane; its angle relative to the Hall A $x-z$ plane is thus equal to the 10° pitch of the detector stack. The x axis, perpendicular to z, lies in the wire plane; positive x is downward, with gravity, since that is the magnetic dispersion direction. The y axis, also in the wire plane, is once again defined to form a right-handed coordinate system, so that positive y points roughly toward the beam dump [144].

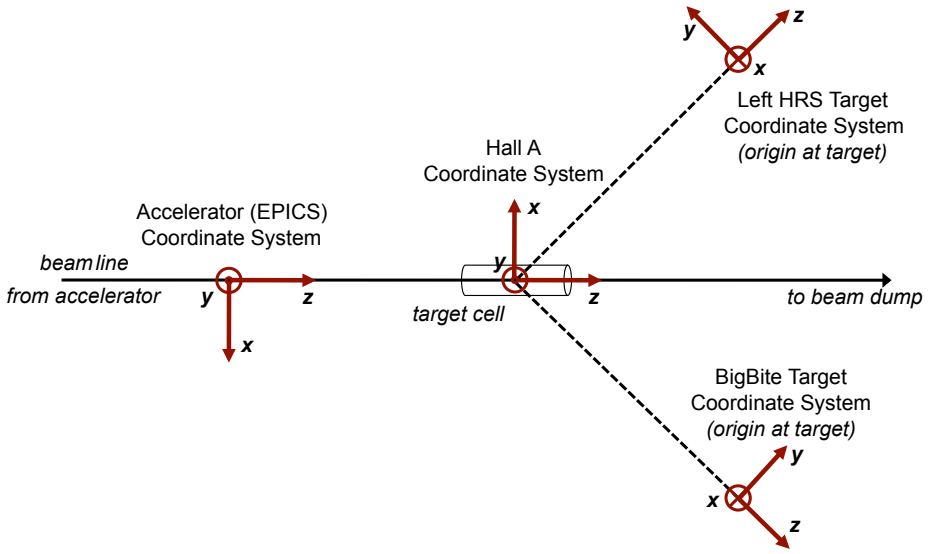

Figure 3.10: A schematic of four coordinate systems in common use in Hall A. Here, the beamline is seen from above, with the downstream direction toward the right of the figure.

3.3.2 Hall A Beamline

Upstream of the target, the Hall A beamline contains a variety of devices used to monitor various characteristics of the electron beam, several of which are shown in Figure 3.2. The Møller and Compton polarimeters measure the beam polarization; they will be discussed in Sections 4.2 and 4.3, respectively. (The Compton polarimeter, which is located in the tunnel leading to the Hall rather than in Hall A itself, is not shown in the figure.) Below, we describe our measurements of beam energy (Section 3.3.2.4), current and charge (Section 3.3.2.1), position (Section 3.3.2.2), and raster (Section 3.3.2.3).

3.3.2.1 Beam Current and Charge

E06-014 ran with beam currents of about 15 μA. Fluctuations around the current setpoint – as well as occasional beam trips, due to transient difficulties in the accelerator or in other halls – make it essential to monitor the actual beam current in real time.

For this purpose, Hall A's standard beamline equipment includes two resonant RF cavities, stainless-steel cylinders with a high ($\sim$ 3000) Q factor, which are tuned to the fundamental beam frequency of 1.497 GHz. These **B**eam **C**urrent **M**onitors (BCMs) are denoted *upstream (u)* and *downstream (d)*, based on their relative positions on the beamline. Each produces a voltage signal proportional to the measured current. This signal is fanned out into three copies, each of which is amplified by a different gain factor (1, 3, or 10) and sent to a VtoF converter. The resulting signals – three for each BCM, or six altogether – have frequencies proportional to the beam current and may be read out by scalers in the HRS and BigBite arms for a continuous measurement of both current and accumulated beam charge [140]. They are denoted u1, u3, u10, d1, d3, and d10, based on the originating BCM (**u**pstream or **d**ownstream) and gain factor.

In order to calibrate these readouts, it is necessary to take dedicated calibration runs, systematically stepping through several beam-current set points. There are two steps in this calibration process. First, at the injector, the OL02 resonant cavity is calibrated to the Faraday cup, a water-cooled copper beam dump that can be inserted into the injector beamline so as to collect all of the current [145]. No beam can be received downstream of the Faraday cup while it is in place, but the

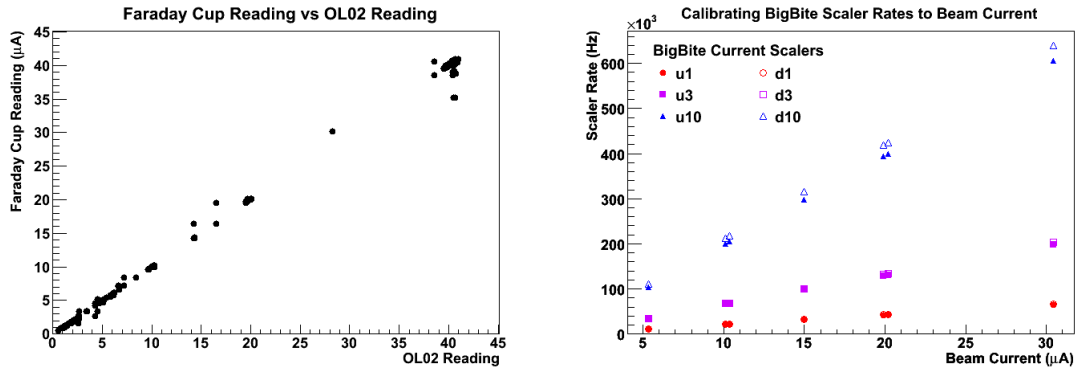

(a) (b)

Figure 3.11: Procedure for calibrating beam current measurements. (a): The relationship of the current reading of the OL02 cavity (at the injector) to the current measurement from the Faraday cup. (b): The relationship of the beam-current scaler rates (in the BigBite arm) to the beam current from the calibrated OL02 cavity reading.

injector cavity does not disturb the beam, so it is the OL02 injector cavity's current reading that is compared directly to the Hall A BCM readouts in the second step.

Figure 3.11(a) shows the OL02 current as a function of the absolute measurement taken by the Faraday Cup. With this information, we can plot the rate measured in each of the six beam-current scalers as a function of the beam current, derived from the OL02 readings during our calibration run (Figure 3.11(b)). From a linear fit to the scaler readouts between 5 and 30 μA, we can determine the slope of the line relating our scaler rates to the beam current: $\omega_n = \text{offset}_n + \text{slope}_n \cdot I$. The fit does not extend to zero because the BCM readouts are known to be nonlinear at low currents; instead, the offset (the scaler rate for zero current) is determined from a Gaussian fit to the scaler rates recorded over the course of five minutes with the beam off. Table 3.4 shows the calibration constants resulting from these fits. Over a given time interval, these values allow us to extract both the beam current I and the accumulated beam charge Q from the scaler rate ω_n of the nth beam-current signal, according to Equations 3.10 and 3.11.

$$I = \frac{\omega_n - \text{offset}_n}{\text{slope}_n} \tag{3.10}$$

$$Q = I \cdot t = \frac{t\,(\omega_n - \text{offset}_n)}{\text{slope}_n} \tag{3.11}$$

This calibration was performed with the scalers on the BigBite arm; the scalers on the Left HRS arm record the same signal, and yield consistent results. If we neglect errors in the clock rate, the error on the fit corresponds to a systematic error of about 0.03% on the beam current calculated from the u3 scaler rate.

3.3.2.2 Beam Position from the Beam Position Monitors

In order to make an accurate reconstruction of the momentum and vertex position of a given track, we need to know the position of the beam, in the plane transverse to the nominal beam direction (x and y in Hall A coordinates), at the location of the target. This position is affected by the beam's orbit in the accelerator, the settings of the Compton and Møller magnets, and the fast raster (Section 3.3.2.3). For slow beam position measurements (over a timescale of several tenths of a

Scaler	Slope (Hz/μA)	Offset (Hz)	Scaler	Slope (Hz/μA)	Offset (Hz)
u1	2101 ± 1	396	**d1**	2152 ± 1	154
u3	6480 ± 2	453	**d3**	6658 ± 3	133
u10	19731 ± 11	771	**d10**	21008 ± 10	293

Table 3.4: Calibration results for beam-current scalers, three upstream (u) and three downstream(d), with gain factors of 1, 3, and 10. Errors on the offsets are on the order of 10^{-2} Hz.

second), we rely on the two **B**eam **P**osition **M**onitors, four-antenna arrays placed 7.524 meters and 1.286 meters upstream of the target. By combining the positions measured by the two BPMs, we can determine the actual direction of the beam and extrapolate its position at the target.

Each BPM works via a comparison of the signals in an opposing pair of wire antennae. The channel offsets and their relative gain factors are combined to obtain position readings in the BPM coordinate system, which is a $\sim$45° counterclockwise rotation from the Accelerator coordinate system [143]. In order to interpret the readings from our BPMs, we must compute the transformation between the BPM readings and target coordinate system.

Typically, this transformation is determined using beam profiles from the harp wire scanners; one harp is located immediately downstream of each BPM. Unlike the BPMs, harp measurements are destructive, so the calibration requires a dedicated set of runs during the experiment. The measurements are conventionally performed in a "bull's-eye" configuration: a series of five data points with the beam positioned at different locations. Four points describe the corners of a 4-mm by 4-mm square, and the fifth data point measures the square's center near (0,0).

Unfortunately, in the months leading up to E06-014, slips in their encoders made the harp scans unreliable as absolute position measurements [146]. Instead, we calibrated the analog BPM readouts to the beam-position readouts in the EPICS data management system (Section 3.3.7.2), which are derived from the BPM signals. These EPICS readouts, which use the left-handed Accelerator coordinate system (Section 3.3.1), reflect the results of an earlier calibration using the harp wire scanners. This method allowed us to recover the coordinate system transformation from the earlier calibration, as a substitute for performing independent beam-position measurements with two types of equipment; we effectively reverse-engineered the EPICS calibration.

Using data from the bull's eye scan, we fit a Gaussian distribution to each measurement of x and y, EPICS and analog, and extracted the rotation and offset of the coordinate transformation from a fit to the mean readings at each location. Table 3.5 reports the results of this procedure, performed independently for each of the two BPMs in each of the two arms of the experiment; separating the BigBite and LHRS data-acquisition systems was necessary since each set of ADCs has its own pedestals, its own input scale, and its own sources of electronic noise.

The slow readout rate (roughly every five seconds) of the EPICS measurements meant that only a few dozen such measurements were available for some locations, leading to significant statistical error. We estimated the total error by computing the beam position at the target from each spectrometer's readouts and coordinate transformation, and then comparing these two measurements for each point in the bull's-eye scan. As shown in Figure 3.12, these results are consistent to within about 300 μm in the horizontal and about 400 μm in the vertical.

3.3.2.3 Beam Position from the Raster

In order to avoid damage to the thin glass cell of the production target, the beam must be rastered to have a relatively large rectangular cross section at the target; heating damage from an unrastered beam striking a small area of the target could easily rupture the cell. During E06-014, the beam was rastered to a size of 4×6 mm^2 using a fast (17-24 kHz) rastering system some 23 m upstream of the target [140]. By generating low-magnitude transverse magnetic fields at its position in the

BPM A	rot_{11}	rot_{12}	rot_{21}	rot_{22}	disp_1 (m)	disp_2 (m)
BigBite	-0.614348	0.658442	0.618053	0.669323	-0.00319424	0.000672374
Left HRS	-0.676324	0.69569	0.679527	0.706064	-0.000687716	0.000685615
BPM B	rot_{11}	rot_{12}	rot_{21}	rot_{22}	disp_1 (m)	disp_2 (m)
BigBite	-0.814325	0.556614	0.814739	0.56004	-0.0061156	0.0078037
Left HRS	-0.679278	0.675238	0.684226	0.674596	0.000349452	0.00134201

Table 3.5: Coordinate transformation for beam-position monitors A (top) and B (bottom), obtained from a fit to beam positions recorded in EPICS. The rot_{mn} values are elements of the two-by-two rotation matrix, while disp_i values correspond to the displacement vector between the two coordinate systems. These EPICS positions originate from the same BPMs, but reflect the results of an earlier calibration.

beamline, the rastering system is able to sweep the beam position at the target through deviations of up to several millimeters, in two independent directions transverse to the beam. The raster current is read out by a passive transformer – a Pearson probe – which allows a more-or-less instantaneous calculation of the beam position [143]. However, the calibration of raster current to beam position must then be redone every time the beam into the Hall is re-tuned, as a change of tune also changes the way in which the beam passes through the raster magnet and the optics between the raster and the target.

Although, for reasons of efficiency and safety, it is critically important for any experiment with a glass-cell target to employ the raster, most experiments are not so sensitive to beam position that the raster readouts must be used in their data analysis. E06-014 is no exception. In event reconstruction, the beam's position transverse to the beamline is needed primarily in order to determine the momentum of the scattered particle, and it is its vertical position – that is, its position along the spectrometer dispersion direction – that matters. In E06-014's experimental setup, then, the Left High-Resolution Spectrometer (Section 3.3.5) is naturally the detector most sensitive to position, due to its high momentum resolution. Consider this detector's first-order transport matrix, which takes the scattered particle's trajectory at its vertex and transforms it to a measured vertical position x (in meters) and angle θ at the focal plane

$$\begin{bmatrix} x \\ \theta \end{bmatrix}_{fp} = \begin{bmatrix} -2.18 & -0.198 & 11.9 \\ -0.10 & -0.469 & 1.967 \end{bmatrix} \begin{bmatrix} x_0 \\ \theta_0 \\ \delta p/p_c \end{bmatrix}. \tag{3.12}$$

The elements of the transport matrix are approximate values taken from a SNAKE simulation of the standard tune [147]. x_0 gives the vertical position in meters of the particle trajectory, assumed to be the vertical position of the beam itself at the target, immediately after scattering; θ_0 gives its vertical angle; and $\delta p/p_c = (p - p_c)/p_c$ gives the trajectory's fractional deviation from the central momentum setting p_c of the HRS. If we take the average height of the beam at the target to be 0, then x_0 is the size of the vertical deviation induced by the raster, and we can follow the matrix algebra through to estimate its effect on the reconstructed momentum

$$p = p_c + p_c\,(0.090x - 0.038\theta - 0.201x_0)\,. \tag{3.13}$$

If we were to erroneously assume $x_0 = 0$, the error in p would be approximately equal to $|0.201x_0p_c|$ [148]. For a vertical raster sweep of ± 2 mm and a maximum momentum setting of 1.70 GeV/c, such an assumption would introduce a maximum error of only 0.68 MeV/c into the momentum, a small effect compared to the experimental resolution. Accordingly, the effects of the raster will be neglected throughout the E06-014 analysis.

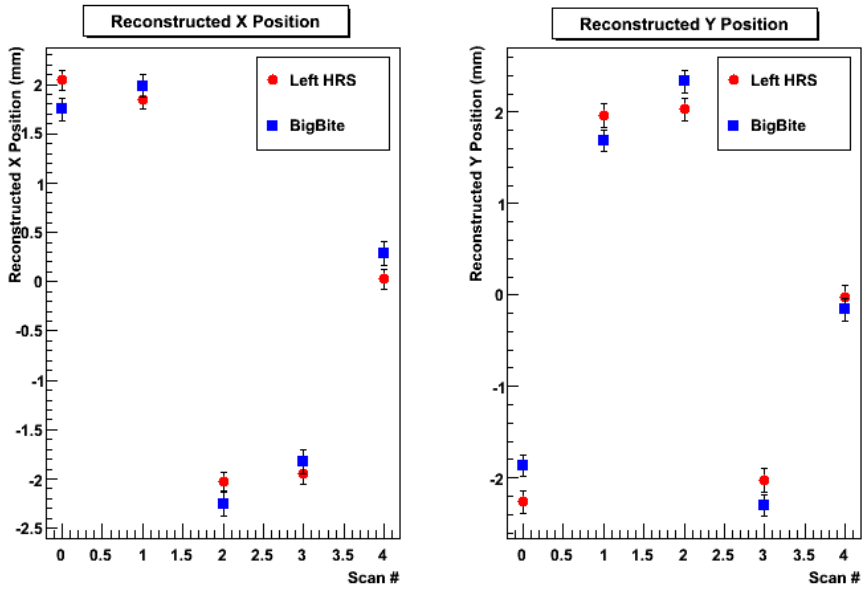

Figure 3.12: Reconstructed beam positions in BigBite and Left HRS during a bull's-eye scan.

3.3.2.4 Beam Energy

Accurate kinematic calculations require knowledge of the incoming electron beam energy. During E06-014, the beam energy was continuously monitored via the Tiefenback method [149], in which beam position measurements from the BPMs (Section 3.3.2.2) are combined with the field integral of the Hall A arc magnets to compute the energy of the beam as it enters the Hall.

The Tiefenback method is kept calibrated via comparisons to an absolute means of measuring the beam energy: an arc measurement (Figure 3.13). (A second absolute measurement method, relying on the angular distribution of scattered electrons and protons in H(e,$e'p$) scattering, is also available in Hall A, but was not used for E06-014 data.) In the arc section of the beamline – just before the portion properly considered the Hall A beamline – eight dipoles bend the beam through a nominal angle of 34.3°. Any deviation from this nominal bending angle is measured by the SuperHarps, pairs

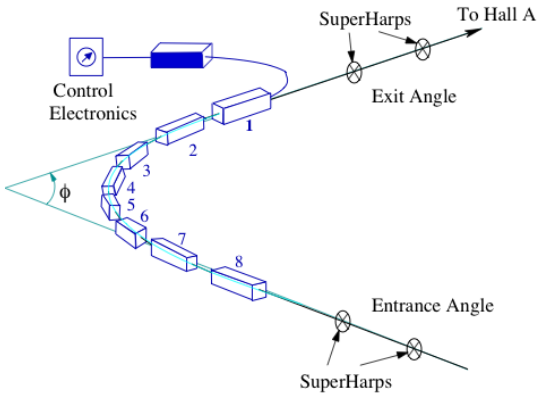

Figure 3.13: Schematic of an arc beam energy measurement, reproduced from Zheng [16].

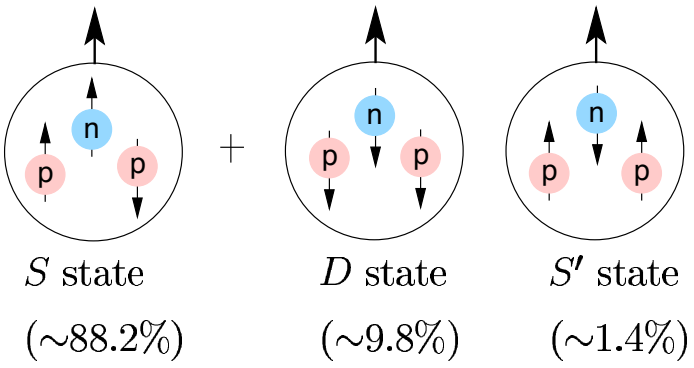

Figure 3.14: Nucleon polarization in ^{3}He, reproduced from Zheng [16]. The large arrow gives the spin direction of the nucleus, while the small arrows give the spin directions of the nucleons.

of wire scanners located both before and after the magnet suite. The actual bend angle through the arc is related to the beam momentum (and thus to its energy) by

$$p = k\frac{\int \vec{B}\cdot\vec{dl}}{\theta} \tag{3.14}$$

where $k = 0.299792/c$ GeV rad T^{-1} m^{-1} [140]. Simultaneously with the SuperHarp measurement of the actual bend angle, the magnetic field integral is measured using a ninth dipole, a reference magnet that is located outside the vacuum and is measured directly with a Hall probe. The total error on this measurement is about $\delta E/E = 2\times10^{-4}$ [150].

No independent arc measurements were taken during E06-014; instead, the experiment's confidence in the Tiefenback method rests on a measurement performed during E06-010, which compared the results of an arc measurement and of the Tiefenback method. The result of this measurement is shown in Table 3.6.

Arc Result (MeV)	**Tiefenback Result (MeV)**
$5889.4 \pm 0.5_{stat} \pm 1_{syst}$	$5891.3 \pm 2.5_{syst}$

Table 3.6: Results of near-simultaneous beam energy measurements on November 17, 2008, using the arc and Tiefenback methods [151].

3.3.3 Target

In the absence of a free, polarized neutron target, experimenters interested in neutron spin structure must make do with bombarding a polarized nuclear target and correcting for the presence of protons. The two most popular choices of nuclei for this purpose are deuterium, which has spin 1, and ^{3}He, which has spin 1/2. In deuterium, both the proton and the neutron spins are aligned with the nuclear spin, but large corrections for the proton contribution pose a significant source of uncertainty. In ^{3}He, the model dependence of the result is greatly reduced because the nucleus is in the S state with a probability of more than 88%, and in that state the proton spins cancel each other, leaving only a neutron contribution to the spin asymmetry. (Figure 3.14 shows the ^{3}He spin sub-states.) The effective neutron polarization in a perfectly polarized ^{3}He sample is about 87% [127].

E06-014 therefore used polarized ^{3}He gas, contained in a hand-blown glass cell, as an effective polarized neutron target. In this section, we will discuss how ^{3}He can be polarized and how that

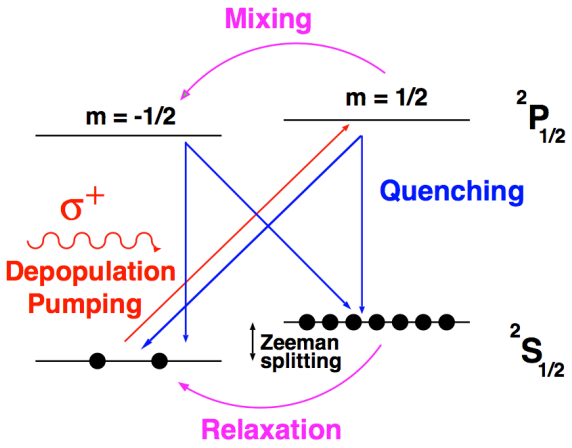

Figure 3.15: Optical pumping of alkali atoms with zero nuclear spin (*i.e.* neglecting hyperfine structure), using right-circularly polarized photons (σ^+). The atoms are in a magnetic holding field, which induces a Zeeman splitting. Reproduced from Kominis [152].

polarization can be measured; describe the production ^{3}He cell as well as the targets used for calibration; and detail the construction of the target apparatus.

3.3.3.1 Hybrid Spin-Exchange Optical Pumping

The ^{3}He target used during E06-014 is polarized with a three-stage process known as **h**ybrid **s**pin-**e**xchange **o**ptical **p**umping (HSEOP). In optical pumping, circularly polarized laser light is used to polarize the electrons in rubidium atoms, which then transfer their polarization to potassium atoms through spin-exchange collisions. Finally, the polarized potassium atoms undergo spin-exchange collisions with ^{3}He nuclei, in which polarization is transferred to the latter nuclei. It is the inclusion of this intermediate potassium stage that makes the process a hybrid. Spin exchange between rubidium and ^{3}He is far less efficient and may consequently be neglected.

In order to maintain a high polarization despite spin relaxation in the target gas mixture, the target must continuously undergo HSEOP. We will discuss each of the three stages of the process in turn.

Optical Pumping In its ground state, a ^{85}Rb atom has one valence electron, located in the $5^2S_{1/2}$ orbital[1]; it is the spin of this electron that is polarized via optical pumping. The first excited state, with orbital angular momentum $L = 1$, resolves into two sublevels due to spin-orbit coupling – $5^2P_{1/2}$ and $5^2P_{3/2}$ – where the subscript is given by $J = L \oplus S$. We neglect the $5^2P_{3/2}$ level for now and focus our attention on the energy levels with $J = 1/2$. Under the hyperfine interaction, which arises from coupling between J and the nuclear spin I, these levels each split into two more. These hyperfine levels have $F = 2$ and $F = 3$, where $F = I \oplus J$. In a magnetic field, each hyperfine level undergoes Zeeman splitting, resulting in a multiplet of $2F + 1$ levels labeled by the quantum number $m_F = -F, -F + 1, ..., F - 1, F$.

Although ^{85}Rb has a nuclear spin $I = 5/2$, let us first consider the simpler case of an alkali atom with $I = 0$ (Figure 3.15), so that we may neglect hyperfine structure. Suppose that we place

[1] In spectroscopic notation, atomic levels are denoted according to their quantum numbers: n (the principal quantum number), S (the total electron spin), L (giving the orbital angular momentum of electrons in the level) and J (the total electron angular momentum). These are reported in the format $n^{2S+1}L_J$, where the value of L is given by a letter; for historical reasons, S signifies $L = 0$, while P signifies $L = 1$.

this atom in a magnetic holding field, so as to induce a Zeeman splitting between the sublevels $m_J = \pm 1/2$, and then illuminate it with circularly polarized light (σ^+), propagating against the holding field direction, at a wavelength that excites the D_1 transition between the $5^2S_{1/2}$ and $5^2P_{1/2}$ states. Conservation of angular momentum dictates that such a photon can only be absorbed by an atom in a level with $m_J = -1/2$. In absorbing these photons, the atoms are excited to the $^2P_{3/2}$ level, shown by the red arrow in Figure 3.15. They then decay very quickly (on the order of 10^{-8} s [153]) to the ground state. Since the electron has $m_J = +1/2$ while in the P orbital (due to its absorption of the σ^+ photon), it has a 2/3 probability of decaying to an S-orbital state with $m_J = -1/2$ and a 1/3 probability of decaying to an S-orbital state with $m_J = +1/2$, indicated by the blue arrows in Figure 3.15.

This results in a decrease in the $m_J = -1/2$ population despite the higher probability of an electron ending a D_1 transition and decay with $m_J = -1/2$, since further D_1 transitions are excited only on $m_J = -1/2$ atoms rather than on $m_J = +1/2$ atoms. Continuous optical pumping thus polarizes the alkali atoms via depopulation: the population of atoms in the $m_J = -1/2$ state is steadily depleted, leaving more and more atoms in the $m_J = +1/2$ state. For optical pumping with left-circularly polarized photons (σ^- and $\Delta m_J = -1$), the process is inverted: it is the $m_J = +1/2$ state that is depopulated, leaving Rb atoms with $m_J = -1/2$.

For an atom with non-zero nuclear spin, like ^{85}Rb, the simple description of Figure 3.15 is no longer accurate: we must account for hyperfine splitting, so the Zeeman levels are described by m_F rather than by m_J. Optical pumping with σ^+ photons depopulates the levels with low m_F values in favor of those with high m_F values, one unit of angular momentum at a time. The optical pumping of atoms with $I \neq 0$ is thus slower than the analogous process for atoms with zero nuclear spin, as it takes the absorption of many photons for each atom to work its way up the multiplets, but the end result is quite similar: illumination with circularly polarized photons $\sigma^\pm$ will eventually produce a population of atoms mostly in the $m_F = \pm 3$ state [154].

Rb polarization may be reduced by several spin relaxation processes, which notably include thermal mixing between $5P_{1/2}$ and $5P_{3/2}$ states, and absorption of the unpolarized photons emitted when Rb atoms decay from a 5P state to a 5S state. The latter mechanism may be suppressed by the addition of a small amount of nitrogen gas, which quenches the radiative decay of Rb by allowing its excitation energy to be transferred in a collision with N_2 [152]. Meanwhile, continuous optical pumping mitigates Rb depolarization.

Rb-K Spin Exchange The potential $V(r)$ of an interaction between two $S_{1/2}$ atoms, Rb and K, depends on a spin-independent part $V_0(r)$ and a spin-dependent part $V_1(r)$

$$V(r) = V_0(r) + \vec{S}_{Rb} \cdot \vec{S}_K V_1(r) \tag{3.15}$$

where $\vec{S}_{Rb}$ is the spin of the rubidium atom and $\vec{S}_K$ is the spin of the potassium atom. This hyperfine, or spin-spin, interaction allows the spins of the two atoms to be interchanged in some percentage of interactions; this percentage is determined by the size of $V_1(r)$ relative to $V_0(r)$. Even when spin-exchange interactions are a small portion of the total, the polarization of one group of atoms may equilibrate with the other group in a matter of hours – especially when the first group is continuously re-polarized via optical pumping. The total spin of the interacting atomic pair is always conserved [155].

In the case of rubidium and potassium, the cross section of the spin-exchange process is about 2×10^{-14} cm^2. At a particle density of 10^{14} cm^{-3}, this corresponds to a spin-exchange rate of more than 100,000 per second, compared to a spin-relaxation rate of 500 per second [156].

K-^{3}He Spin Exchange ^{3}He may also undergo spin-exchange interactions, but its two valence electrons are in a spin-singlet state, so it is the nuclear spin that takes part through a Fermi-contact interaction [157, 158]. Inefficiencies arise primarily from spin relaxation, in which the electron spin

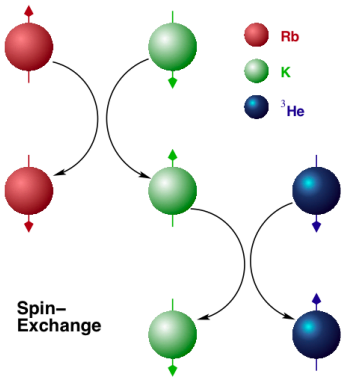

Figure 3.16: Two-step spin exchange, Rb→K→^{3}He, reproduced from Kolarkar [153]. For Rb and K, the valence electron spin is shown before and after the interaction; for ^{3}He, the nuclear spin is shown.

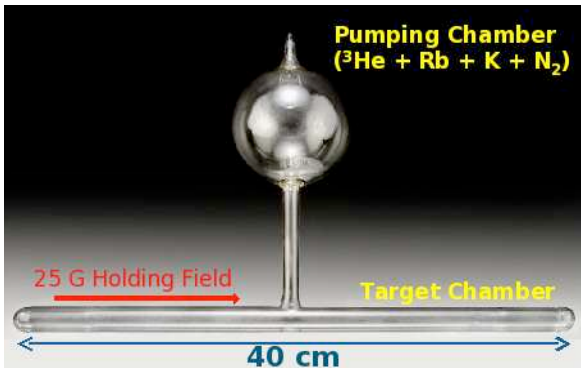

Figure 3.17: Polarized ^{3}He cell, reproduced from Kolarkar [153]. The glass sphere at the top of the photograph is the pumping chamber. A thin transfer tube connects it to the target chamber, which is oriented with its long axis along the beamline.

of the alkali metal couples to the rotational angular momentum of the pair of colliding atoms, rather than to the nuclear spin of the noble gas atom. In collisions involving ^{3}He, the spin relaxation cross section is dominated by the alkali metal's spin-orbit splitting, so that using a lighter alkali metal atom (*e.g.* potassium instead of rubidium) can greatly decrease the spin relaxation cross section and thereby increase the efficiency of spin exchange [159].

The parameter η_{SE}, the ratio of the spin transfer rate to ^{3}He nuclei to the spin relaxation rate by alkali metal atoms, forms a useful point of comparison. Measurements at common SEOP temperatures ($\sim$ 350 K) give η_{SE} as about 2% for Rb-^{3}He, but 25% for K-^{3}He [160]. There is a tremendous practical difference in efficiency between a Rb-^{3}He spin-exchange optical pumping process and a Rb-K-^{3}He hybrid spin-exchange optical pumping process (shown in Figure 3.16): typical hybrid reference cells at Jefferson Lab take about 3-5 hours to achieve maximum ^{3}He polarization, while pure Rb cells took about 15 hours [161]. A faster *spin-up time* both reduces overhead for spin rotations and improves the ability of continuous optical pumping to work against depolarization.

Figure 3.17 is a photograph of a typical polarized ^{3}He cell used in Hall A. The spherical pumping chamber[2] is where rubidium atoms are optically pumped, and where their polarization is transferred first to potassium atoms and then to ^{3}He nuclei. N_2 and ^{3}He atoms diffuse from the pumping chamber to the target chamber – where interactions with the electron beam take place – through the thin, cylindrical transfer tube; a thermal gradient along the transfer tube confines the alkali-metal atoms to the pumping chamber [162]. This gradient is sufficient to ensure that any Rb and K presence in the target chamber is negligible. The rate at which ^{3}He atoms diffuse between the target and pumping chambers is much greater than the rate at which ^{3}He atoms are polarized in the pumping chamber, so that the ^{3}He polarization is approximately equal in the two chambers [153].

3.3.3.2 Polarizing Apparatus for the E06-014 ^{3}He Target

Keeping a ^{3}He target polarized requires two major subsystems: a laser system to perform optical pumping of the target, and a holding field to keep the nuclear spins aligned in the correct direction.

Laser System E06-014 benefited from the installation of a new set of COMET lasers a few months prior to the experiment. These lasers had a linewidth of 0.2 nm, a factor of ten less than the linewidth of their predecessors (FAP lasers). This dramatically improved the optical pumping efficiency, since a narrower linewidth means that proportionately more photons excite the desired atomic transitions.

The three COMET lasers and most of their associated optics were sited aboveground, in a laser lab behind the counting house. Each diode laser produced 25 W of unpolarized, 795-nm light, which traveled through a 75-m optical fiber to reach the hall. Beams from the three fibers were combined into a single fiber using a 5-to-1 combiner, so that all three lasers could simultaneously deliver light to the target.

In order to give the beams the circular polarization required for optical pumping[3], the beam from the 5-to-1 combiner output was first passed through a polarizing beamsplitter, which separated it into two linearly polarized components. One of these components was passed twice through a quarter-wave plate, after which both components had the same linear polarization. Finally, passing each component of the beam through another quarter-wave plate converted their linear polarization to circular polarization, and the components were recombined, focused and aligned to illuminate the pumping chamber with a spot about 7.5 cm in diameter (the size of the chamber) [151]. Three independent optics lines, one each for longitudinal, transverse (horizontal), and vertical target polarization, were installed in the months before E06-014 and its sister experiment E06-010.

Holding Field Three pairs of Helmholtz coils, their positions and orientations shown in Figure 3.18, are capable of producing static magnetic fields in three orthogonal directions: longitudinal (along the beam line), transverse (horizontal and perpendicular to the beamline), and vertical (also perpendicular to the beamline). The vertical coil is the largest and completely surrounds the small and large coils. E06-014 used combinations of these coils to generate holding fields for spins in the longitudinal and transverse directions; a typical holding field is 25 G, which requires currents on the order of 7 A in each coil.

In addition to the Helmholtz coils, Figure 3.18 also shows the location of radiofrequency (RF) and pickup coils, which are necessary for measurements of the target chamber polarization (Section 3.3.3.3).

[2]The tapered tail at the top of the pumping chamber is the *pull-off* and provides access to the target for filling. It does not affect target performance outside of initial preparation and handling constraints [151].

[3]It is necessary to polarize the beam at the target, rather than at the laser output, because light traveling through polarization-maintaining optical fiber suffers higher attenuation than it would traveling through single-mode fiber. The 75-m single-mode optical fiber used in Hall A has a measured power loss of about 6% [151].

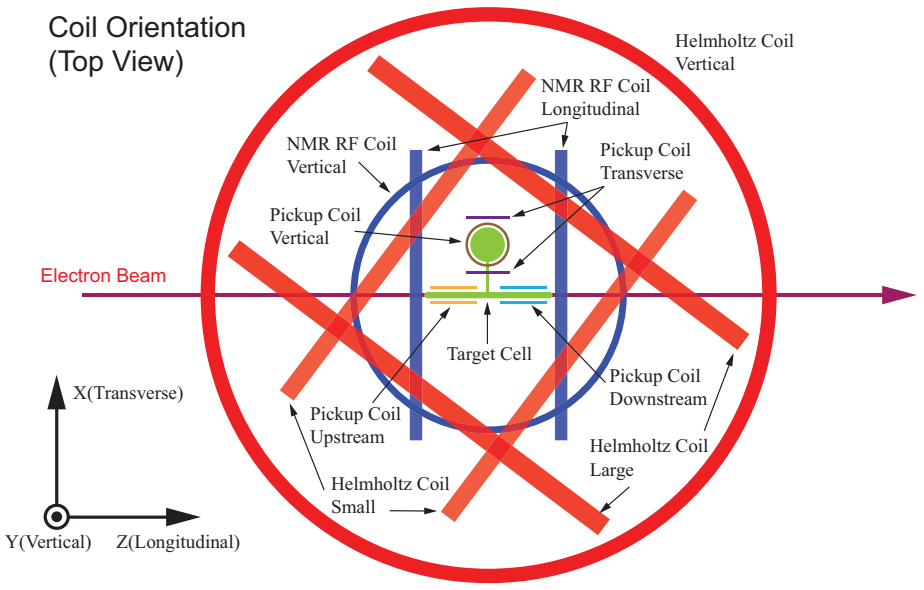

Figure 3.18: Top view of Helmholtz and RF coils for ^{3}He target, reproduced from Hall A general operations manual [141].

	Small coil	**Large coil**	**Vertical coil**
Inner diameter (m)	1.27	1.45	1.83
Number of turns	256	272	355
Resistance (Ω)	3	3	4.4

Table 3.7: Characteristics of Helmholtz coils for target holding field [151].

3.3.3.3 Target Polarization Measurements

The degree to which our ^{3}He target nuclei are polarized is an essential parameter in extracting a spin-spin asymmetry like A_1^n. In order to measure this polarization, the Hall A target is equipped with the means to perform both relative and absolute polarization measurements: EPR (electron paramagnetic resonance) measurements provide the absolute polarization in the pumping chamber, while NMR (nuclear magnetic resonance) measurements give relative values for the polarization in the target chamber. We will briefly describe both methods here; the results of these measurements for E06-014 running will be discussed in Section 5.1.2.

NMR In the phenomenon of nuclear magnetic resonance (NMR), the magnetic moments of nuclei in a constant magnetic field will precess when a radiofrequency (RF) magnetic field is applied in a perpendicular direction. By sweeping the frequency of this RF field through the resonant frequency of the ^{3}He nucleus, we can reverse the nuclear spin direction (*e.g.* from 90° to 270° relative to the electron momentum direction). The motion of the spins changes the flux through the pickup coils shown in Figure 3.18, inducing a radiofrequency electromotive force. Signals from the coils are combined, pre-amplified, and sent to a lock-in amplifier; the magnitude of this final signal is proportional to the ^{3}He polarization [163].

It is important to conduct NMR measurements in such a way that polarization is not degraded afterward. Accordingly, sweeps are performed using to the Adiabatic Fast Passage (AFP) technique,

which mandates a passage through the resonant frequency that is both faster than the spin relaxation time and slow enough to allow the nuclear spins to follow the sweep of the RF field.

The underlying principle of NMR can be explained in a classical framework [45]. Consider a nucleus with magnetic moment $\vec{M}$ in a constant magnetic holding field, $\vec{H}_0$. The nucleus experiences a torque $\vec{\tau}$

$$\vec{\tau} = \vec{M} \times \vec{H}_0. \tag{3.16}$$

Now, $\vec{M}$ may be expressed in terms of the nuclear spin $\vec{I}$ as $\vec{M} = \gamma\hbar\vec{I}$, where γ is the gyromagnetic ratio and $\hbar$ is the reduced Planck constant. Torque is defined as the rate of change of the angular momentum, so we may express it as $\vec{\tau} = \hbar d\vec{I}/dt$. Combining this information with Equation 3.16, we find an expression for the rate of change of the magnetic moment

$$\frac{d\vec{M}}{dt} = \gamma\vec{M} \times \vec{H}_0. \tag{3.17}$$

At this point, it is convenient to move from the laboratory reference frame to a rotating frame with angular velocity $\vec{\omega}$ relative to the lab, where ω is the frequency of the RF magnetic field we will later apply. Let $d\vec{M}'/dt'$ be the magnetic moment's rate of change in the new, rotating frame, while $d\vec{M}/dt$ is defined in the original laboratory frame. We can relate these two quantities by

$$\frac{d\vec{M}}{dt} = \frac{d\vec{M}'}{dt'} + \vec{\omega} \times \vec{M}. \tag{3.18}$$

Equations 3.17 and 3.18 combine to give an expression in the rotating frame for the motion of the magnetic moment

$$\frac{d\vec{M}'}{dt'} = \gamma\vec{M} \times \left(\vec{H}_0 + \frac{\vec{\omega}}{\gamma}\right). \tag{3.19}$$

A comparison to Equation 3.17 shows that the effective magnetic field in the rotating frame is given by $\vec{H}_0 + \vec{\omega}/\gamma$. We also see that, at the Larmor frequency $\omega_0 = \gamma|\vec{H}_0|$, $\vec{M}$ is a constant of the motion when the angular velocity of the rotating frame is antiparallel to the holding field $\vec{H}_0$, so that at this resonance frequency the magnetic moment no longer precesses about $\vec{H}_0$ in the rotating frame.

Let us set our rotating reference frame so that its sense of motion is parallel to the holding field in the direction defined by the unit vector $\hat{\imath}$, and apply an RF magnetic field H_{RF} in the perpendicular direction $\hat{\jmath}$. In this frame, the magnetic moment of the ^{3}He nucleus sees a constant effective magnetic field $\vec{H}_e$

$$\vec{H}_e = \left(H_0 + \frac{\omega}{\gamma}\right)\hat{\imath} + H_{RF}\hat{\jmath}. \tag{3.20}$$

The spin precession in this frame is about the axis defined by $\vec{H}_e$, which we can rotate either by sweeping the holding field H_0 through a range of magnitudes, or by sweeping the RF field H_{RF} through a range of frequencies. As long as we meet the conditions of Adiabatic Fast Passage, the nuclear spins, following $\vec{H}_e$, will rotate as well [163].

During E06-014, NMR-AFP measurements were taken approximately once every four hours. We used the frequency sweep method, taking the RF field from 77 kHz to 87 kHz and back at a rate of 5 kHz/sec. Figure 3.19 shows a typical lineshape, its signal amplitude h fit according to

$$h \propto \frac{\omega_1}{\sqrt{(\omega - \omega_0)^2 + \omega_1^2}} \tag{3.21}$$

where ω is the frequency of the RF field, ω_0 is the Larmor frequency, and ω_1 parameterizes $|H_{RF}|$ and the width of the signal spectrum [151].

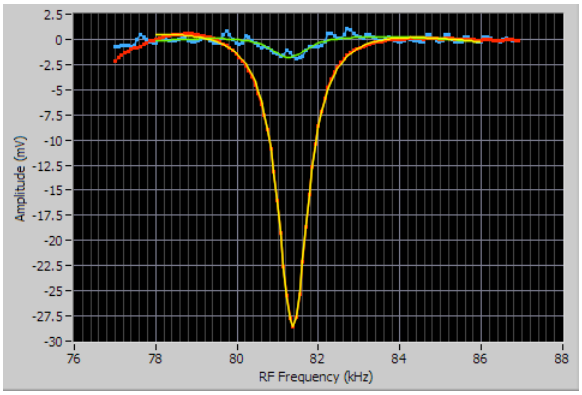

Figure 3.19: Typical signal from online analysis of a frequency-sweep NMR measurement. The red and orange curves are from the x-direction pickups; the y pickups (green and blue) were not used.

NMR provides only a relative determination of the target polarization, but NMR measurements taken during the experiment may be calibrated by comparison to NMR measurements of a sample with a known polarization. Water is typically used for this purpose, since its polarization under known conditions (temperature, pressure and magnetic field) may be calculated directly from statistical mechanics [163]. Water calibration measurements are performed on a water-filled target cell, under conditions as similar as possible to the original experiment.

EPR When ^{3}He is polarized, the aligned magnetic moments of the gas are responsible for a small magnetic field ($\sim$0.1 G) that either adds to or subtracts from the holding field, depending on the polarization direction [164]. An electron paramagnetic resonance (EPR) measurement determines the ^{3}He polarization by measuring the resulting frequency shift in the level transitions of alkali atoms.

As we discussed in Section 3.3.3.1, an external magnetic field induces a splitting between the $(2F+1)$ levels with the same total angular momentum F but different components m_F in the direction of the holding field. Transitions between these levels can be made through absorption or emission of a photon with the right frequency; for adjacent levels, this frequency is given by $\nu_0 = \gamma B_0$ where γ is the characteristic response of the alkali atom (0.466 MHz/G in the case of the rubidium ground state [153]). This would be the end of the story if our target were made solely of rubidium atoms, but it also contains potassium and ^{3}He. The small effective magnetic field ΔB due to ^{3}He magnetization and to spin exchange interactions between the species induces a shift $\Delta\nu$ in the rubidium transition frequency. The actual EPR frequency is then given by [165]

$$\nu_{EPR} = \nu_0 + \Delta\nu. \tag{3.22}$$

To measure the ^{3}He polarization, we must determine how much of the frequency shift is due to the ^{3}He spins. We do this by taking two EPR measurements: one in the initial ^{3}He spin state, and one after reversing the ^{3}He spins via a frequency sweep of an RF magnetic field under AFP conditions, exactly as is done during NMR measurements. The difference between the two measured EPR frequencies, $\Delta\nu_{EPR}$, is twice the frequency shift due to the ^{3}He magnetization and may be expressed as [165]

$$\Delta\nu_{EPR} = \frac{4\mu_0}{3}\frac{d\nu_{EPR}}{dB}\kappa_0\mu_{^3\mathrm{He}}n_{pc}P_{pc} \tag{3.23}$$

where μ_0 is the vacuum permeability, κ_0 is a temperature-dependent, species-specific enhancement factor, $\mu_{^3\mathrm{He}}$ is the magnetic moment of ^{3}He, n_{pc} is the ^{3}He number density in the pumping chamber,

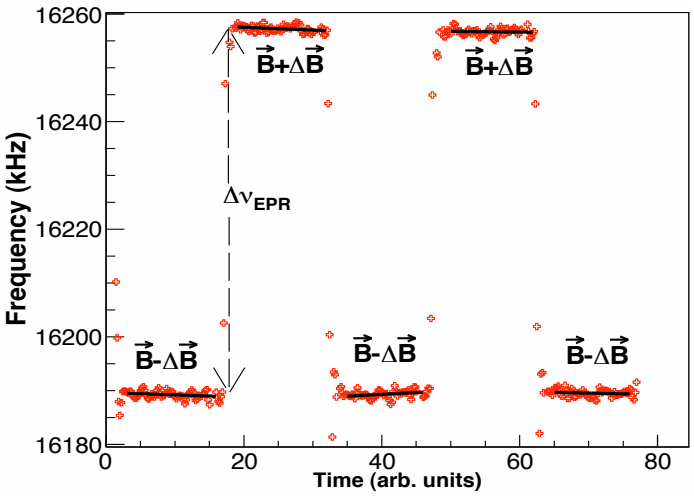

Figure 3.20: Typical spectrum from repeated EPR measurements, reproduced from Dutta [151] and showing measurements with ^{3}He spins antiparallel ($\vec{B} - \Delta\vec{B}$) and parallel ($\vec{B} + \Delta\vec{B}$) to the holding field $\vec{B}$.

and P_{pc} is the ^{3}He polarization in the pumping chamber. The derivative $d\nu_{EPR}/dB$ is calculated based on the evolution of the absolute EPR frequency in a magnetic field with changing field magnitude.

In normal target operations, the alkali-atom populations in the pumping chamber are highly polarized, so they do not absorb polarized light. To measure their energy splitting, we need a large number of level transitions, so we depolarize the alkali atoms by applying an additional RF field [16]. When the frequency of the RF field matches the potassium $m_F = -2 \rightarrow m_F = -1$ or $m_F = +2 \rightarrow m_F = +1$ level splitting (approximately 19 and 16 MHz, respectively, in a 25 G holding field [151]), the potassium atoms are depolarized, allowing spin-exchange interactions which then depolarize the rubidium atoms.

The partially depolarized rubidium population is now primed for optical pumping from the $S_{1/2}$ state to the $P_{1/2}$ state. Most such atoms decay directly back to $S_{1/2}$, emitting 795-nm light characteristic of the D1 transition. There is, however, thermal mixing between the $P_{1/2}$ and $P_{3/2}$ states, so we also observe the $P_{3/2} \rightarrow S_{1/2}$ decay – a D2 transition in which 780-nm light is emitted. When sweeping the frequency of the RF field over several hundred kHz in the right range, we can thus find the true level splitting of the potassium atoms by looking for an increase in D1 and D2 light, which heralds the potassium transition and the depolarization of rubidium. Repeating the procedure after an AFP ^{3}He spin reversal gives us the EPR frequency shift due to the helium polarization, which is on the order of tens of kHz [151].

In practice, an increase in D1 light is very difficult to measure, since the pumping chamber is awash in D1 light from optical pumping. We therefore find the EPR frequency by looking for an increase in D2 light, using two bandpass filters to dramatically reduce the amount of D1 light reaching the detection photodiode. Figure 3.20 shows a typical EPR spectrum resulting from numerous repeated frequency sweeps and AFP spin reversals.

3.3.3.4 E06-014 Targets

Although all production data were taken with a polarized ^{3}He target, E06-014 used three additional targets for various purposes, from beam tuning to optics calibration to determining a nitrogen dilution factor. These four targets were positioned on a target ladder, which could be moved vertically

Figure 3.21: Carbon foils of the optics target, with the production ^{3}He cell visible above. The photograph is from the Transversity Photo Diary [166].

over a range of 31.5 cm [141] in order to place the desired target in the path of the beam. This vertical motion was controlled remotely via EPICS (Section 3.3.7.2); each target move contributed a few minutes of dead time, since beam could not be delivered to the Hall unless the target ladder was stationary with an approved target in the beamline.

Empty Target The empty-target position corresponds to a hole in the target ladder, through which the beam passes with no obstructions. This position is primarily used during beam tuning and Møller polarization measurements, when beam excursions could cause severe damage to other target components.

Optics Target The optics target consists of seven carbon foils, shown in Figure 3.21, inline with a solid BeO target further upstream. The BeO foil serves as an alignment point when steering the beam, since the beam makes a bright spot on the foil that is plainly visible in the target camera. The carbon foils, meanwhile, are used to calibrate spectrometer optics: the thin, regularly spaced foils, each about 6.7 cm from its neighbor, allow precise tests of vertex reconstruction along the beamline direction.

Production ^{3}He Cell Polarized ^{3}He cells in Hall A are generally hand-blown from aluminosilicate glass (GE180) to the geometry shown in Figure 3.17. The cell used for E06-014 was named Samantha and was made by Mike Souza at Princeton University. The pumping chamber is about 7.6 cm in diameter; the target chamber is a cylinder that is 40 cm long and an average of 18.95 ± 0.54 mm in diameter. The long axis of the target chamber is placed along the beamline so that the pumping chamber and its transfer tube are to beam left and slightly above the bulk of the target; the transfer tube is at an angle of 42° from vertical. In Figure 3.21, part of the transfer tube is visible before disappearing into a steel mounting block above the target itself.

The pumping chamber was kept at a temperature of 230° C, ideal for optical pumping, by an oven above the target chamber and surrounding the pumping chamber. Compressed hot air, supplied by a compressor in the hall, passed through two heaters and then circulated through the oven before leaving in an exhaust pipe. A thermocouple measured the temperature of the air entering the oven and a resistive temperature device (RTD) measured the temperature of the air inside; through feedback electronics controlling one of the two heaters, the oven temperature was kept stable to within 2° C [151].

Table 3.8 gives glass thickness measurements [167] for the target chamber; these are used as inputs into energy-loss computations and radiative corrections.

Fiducial	Description	Position	Thickness (mm)
W1	Entrance window	-	0.121
A	Beam-right sidewall	2.5 cm from W1	1.563
B	Beam-right sidewall	12.5 cm from W1	1.556
C	Beam-right sidewall	20.3 cm from W1	1.75
D	Beam-right sidewall	25.4 cm from W1	1.70
E	Beam-right sidewall	35.6 cm from W1	1.70
W2	Exit window	-	0.125
F	Beam-left sidewall	2.5 cm from W2	1.70
G	Beam-left sidewall	11.4 cm from W2	1.67
H	Beam-left sidewall	19.1 cm from W2	1.671
I	Beam-left sidewall	26.7 cm from W2	1.614
J	Beam-left sidewall	35.6 cm from W2	1.678

Table 3.8: Glass thickness measurements for the ^{3}He production cell, Samantha [167]. From a vantage point above the target chamber, the fiducial points, which are all located at the same height as the cell's long axis, begin at W1 (the entrance window) and progress counter-clockwise around the cylinder.

Reference Cell A 40-cm glass tube serves as a reference cell; for E06-014, the name of this cell was GMA. Table 3.9 gives glass thickness measurements [167] for this cell. An automatic gas handling system allows the target operator to remotely vent the cell and refill it with H_2, ^{3}He, or N_2, depending on the needs of the experiment; the former two gases are typically used to provide elastic-scattering data for tests of momentum reconstruction, while the latter allows a calculation of the dilution factor due to nitrogen contamination in the polarized ^{3}He cell.

3.3.3.5 Target Enclosure

For safety reasons, the target ladder is surrounded by a roughly spherical target enclosure, shown in Figure 3.22. While in place, the fiber-glass cover confines light from the target laser, protecting workers in other parts of the hall. In the event of a target cell explosion, the enclosure contains the resulting radioactive contamination. The target enclosure has an additional benefit: it may be flushed with ^{4}He gas, which has a much larger radiation length than air and thus reduces the energy loss of scattered electrons leaving the target [141].

Upstream and downstream of the target, the electron beamlines, which are under vacuum, interface with the target enclosure through beryllium windows in the wall of the target enclosure. The window at the entrance to the target enclosure is 0.254 mm thick, enough to keep glass shards out of the beamline if the target cell explodes. (The window at the enclosure's exit is 0.508 mm thick.) Each window is also covered with 0.076 mm of aluminum foil on the enclosure side to keep it from being exposed to air.

3.3.4 BigBite Spectrometer

Experiment E06-014 consisted of two independent, single-arm measurements. The double-polarization asymmetries of interest for this dissertation were measured in the large-acceptance BigBite spectrometer, positioned at an angle of 45° to beam right. Meanwhile, the **L**eft **H**igh-**R**esolution **S**pectrometer (LHRS) – one of Hall A's twin high-resolution spectrometers – was positioned at an angle of 45° to beam left in order to measure the total unpolarized cross section at each kinematic point. (The **R**ight **HRS** was not used by the E06-014 collaboration; it was positioned at a large angle to beam right

Fiducial	Description	Position	Thickness (mm)
W1	Entrance window	-	0.129
A	Beam-right sidewall	2.5 cm from W1	1.806
B	Beam-right sidewall	12.5 cm from W1	1.692
C	Beam-right sidewall	20.3 cm from W1	1.738
D	Beam-right sidewall	23.4 cm from W1	1.75
E	Beam-right sidewall	36.4 cm from W1	1.731
W2	Exit window	-	0.134
F	Beam-left sidewall	3.0 cm from W2	1.716
G	Beam-left sidewall	9.0 cm from W2	1.68
H	Beam-left sidewall	20.0 cm from W2	1.637
I	Beam-left sidewall	28.4 cm from W2	1.657
J	Beam-left sidewall	37.4 cm from W2	1.7

Table 3.9: Glass thickness measurements for the reference cell, GMA [167]. From a vantage point above the cell, the fiducial points, which are all located at the same height as the cell's long axis, begin at W1 (the entrance window) and progress counter-clockwise around the cylinder.

and used for parasitic tests of an upcoming experiment's new data-acquisition system design [168].) We will describe the LHRS in Section 3.3.5. In this section, we will briefly discuss the elements of the spectrometer and its detector stack; a detailed discussion of the spectrometer calibrations will follow in Chapter 5.

As its name implies, BigBite was designed as a large-acceptance spectrometer, accepting particles with a wide range of angles and momenta. The heart of the spectrometer is the BigBite magnet, a non-focusing dipole magnet designed and built for use at NIKHEF before coming to Hall A. Its water-cooled coils are constructed of hollow copper piping; its yoke and polar pieces are made of low-carbon steel. The magnet's entrance face is perpendicular to the floor, while its exit face is tilted 5° from the perpendicular [169]. A lead sieve-slit [161] may be placed at the front face of the magnet to assist with the calibration of the magnet optics; detection elements are "stacked" horizontally, behind the magnet. Figure 3.23 shows an engineering drawing of the magnet and detector stack for Experiments E06-010 and E06-014; the magnet front was about 1.5 m from the target in both run periods, although E06-010 deployed it at a different angle from the beamline (30°). In its configuration for E06-014, the magnet had an angular acceptance of about 65 msr, with ±240 mrad of acceptance in the vertical and ±67 mrad of acceptance in the horizontal [122].

BigBite's magnetic field is horizontal, running parallel to the floor, and perpendicular to the momentum direction of a particle passing through the center of the magnet from the center of the target. The magnet's dispersion direction is thus vertical. Both negative- and positive-polarity settings are available; at negative polarity, a positively charged particle is bent down (toward the floor) and a negatively charged particle is bent up. At an operating current of 710 A, the field in the center of the magnet is about 1.2 T, near the operational maximum of this device. As the field mapping in Figure 3.24 shows, the magnetic field is approximately uniform over a distance of about 15 cm.

The BigBite detector stack is extremely adaptable, with components added, removed or repositioned for different experiments. Figure 3.25 gives a schematic of the detector layout for E06-010 and E06-014; we will now describe each element of the stack in detail.

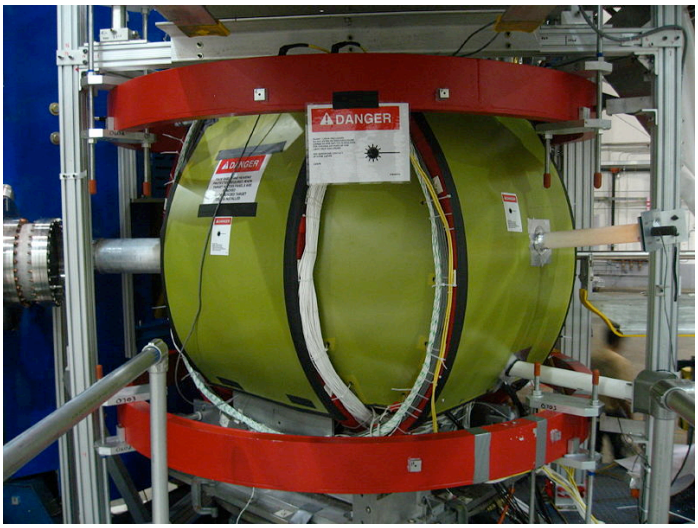

Figure 3.22: Target enclosure. Both of the vertical Helmholtz coils can be seen, as can one coil from each of the small and large Helmholtz pairs. The photograph is from the Transversity Photo Diary [166].

3.3.4.1 Multi-Wire Drift Chambers

Charged-particle trajectories in BigBite are reconstructed from measurements in three **M**ulti-**W**ire **D**rift **C**hambers (MWDCs) placed after the magnet. (The center of the first MWDC is the origin of the detector coordinate system.) Each chamber is filled with a 50-50 mixture of argon and ethane gas, bubbled through ethyl alcohol, a quenching agent, at 0° C [161], and contains three pairs of wire planes for a total of eighteen wire planes across all three chambers.

Each of these eighteen wire planes is perpendicular to the detector's nominal central ray (z) and is bounded by two cathode planes, one upstream and one downstream, six millimeters apart. Halfway between the cathode planes is a series of wires in which field wires and sense wires alternate; the sense wires have a one-centimeter spacing (Figure 3.26). The field wires and cathode planes are held at the same constant high voltage, producing a potential around the sense wires that is approximately symmetric (Figure 3.27).

When a charged particle passes through the MWDC, it ionizes the argon-ethane gas. Due to the difference in electrostatic potential between wires, charges freed in the ionization of the gas molecules tend to drift toward the closest wire; as these ionized particles gain energy from the electric field, they may ionize additional molecules in turn. The resulting avalanche produces an electrical signal in the sense wire. The signal is amplified and sent to a discriminator; if it passes the pre-set threshold, a hit is recorded in the **T**ime-to-**D**igital **C**onverter (TDC). Generally, a particle coming from the BigBite magnet will register only one hit in each plane. Later, in off-line analysis, these hits are combined in order to reconstruct the path that the particle took through the MWDCs.

Each wire chamber contains three pairs of wire planes, and each pair has a different orientation (Figure 3.28), an arrangement chosen to simplify the problem of reconstructing tracks in three dimensions. The wires in the two X planes run horizontally. U-plane wires are oriented at $+30°$ from horizontal, while V-plane wires are at an angle of $-30°$ to the horizontal, as shown in Figure 3.28. In each plane, there is a one-centimeter separation between wires; in each plane pair (X and X', U and U', and V and V') the wire patterns are offset from each other by 0.5 cm. The hit position in plane X', for example, thus allows the tracking algorithm to determine whether the particle passed to the left or to the right of the wire that registered a hit in plane X. The position resolution of the

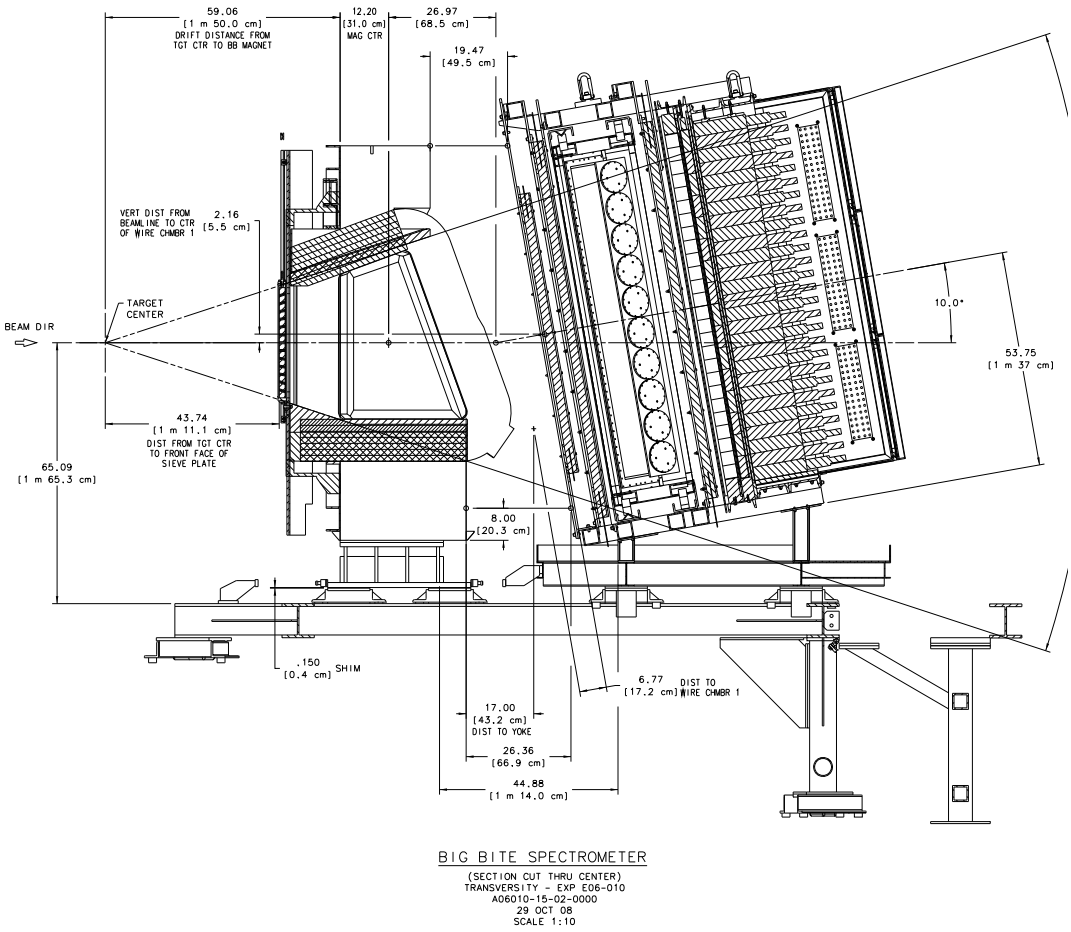

Figure 3.23: An engineering drawing of the BigBite spectrometer, configured for the E06-010 and E06-014 experiments in October 2008 - March 2009, reproduced from Qian [170].

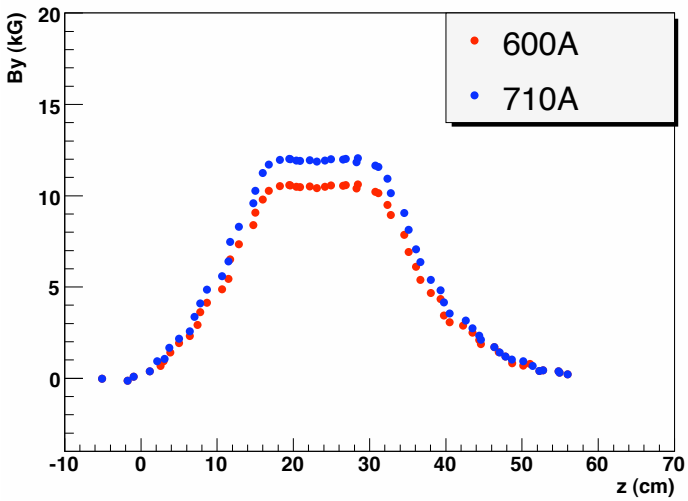

Figure 3.24: Partial field map of the BigBite magnet at two current settings, reproduced from Qian [170]. The current setting during E06-014 was 710 A (blue points). z is the direction of the central ray.

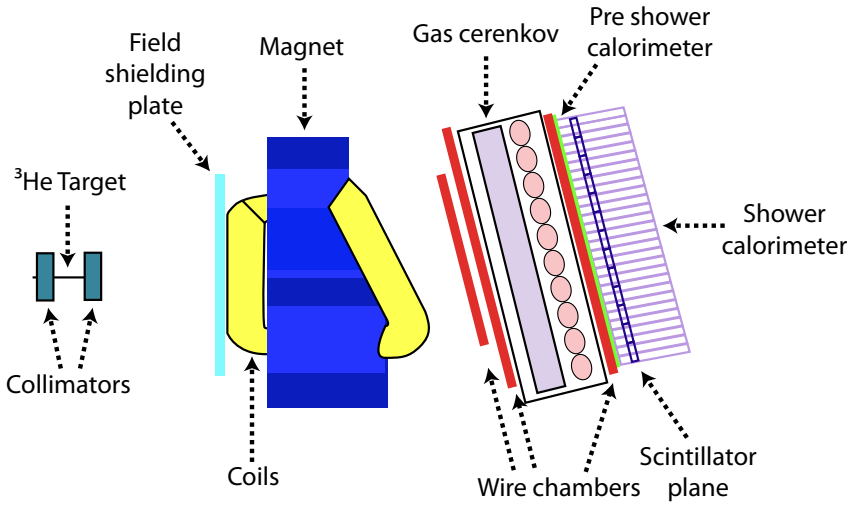

Figure 3.25: A schematic of the components of the BigBite spectrometer, and their arrangement during the experiments, reproduced from Qian [170].

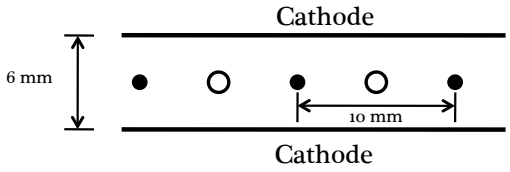

Figure 3.26: Schematic of a BigBite MWDC wire plane (side view).

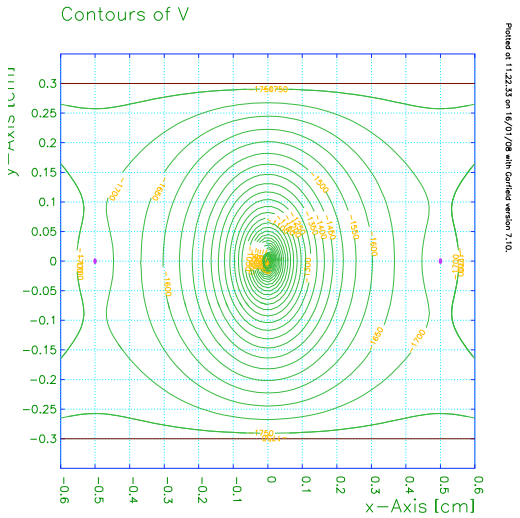

Figure 3.27: Equipotential lines around a sense wire in an MWDC wire plane, generated with GARFIELD for a previous experiment. Reproduced from Riordan [144].

resulting tracks is at the level of 0.3 mm or less.

In reconstructing a charged-particle trajectory, the straight-line tracking that the MWDCs make possible also allows us to reconstruct the particle's curved trajectory through the BigBite magnet, which in turn allows us to compute both the position of the initial scattering vertex (projected to the plane of the beam) and the momentum of the scattered particle. The extension of the trajectory recorded in the MWDCs back through the magnet and to the initial scattering vertex is the task of the optics software package.

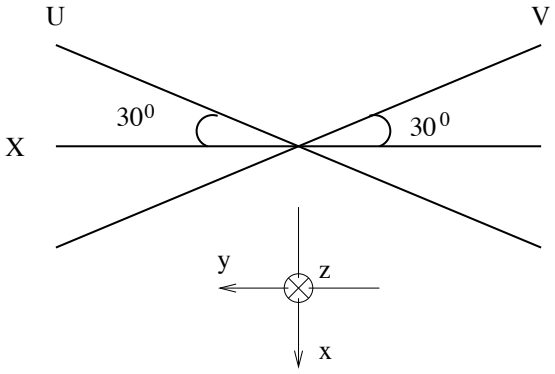

Figure 3.28: U, V, and X wire-plane orientations in BigBite multiwire drift chambers, reproduced from Allada [161].

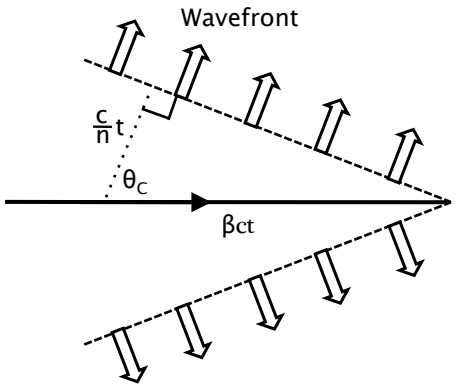

Figure 3.29: Čerenkov radiation.

3.3.4.2 Gas Čerenkov

The BigBite gas Čerenkov was a new element of the BigBite detector stack, commissioned during E06-014. Pion and proton rates were expected to be a factor of between ten and fifty higher than electron rates [171]. Running in single-arm mode, without the option of using coincidences with the LHRS to remove pions and protons from the sample, E06-014 used the gas Čerenkov to remove most pions and protons from the online BigBite trigger.

Čerenkov counters detect charged, high-energy particles that pass through a dielectric medium at velocities greater than the speed of light in the medium: c/n, where c is the speed of light in a vacuum and n is the refractive index of the medium. Such particles, traveling faster than the group velocity of light in the medium, generate something akin to a photonic shock wave by polarizing the atoms in their path. The resulting fields superimpose to form a conical wavefront, as shown in Figure 3.29. The opening angle θ_C of the cone is given by

$$\cos\theta_C = \frac{ct/n}{\beta ct} = \frac{1}{\beta n} \text{ for } \beta > \frac{1}{n} \tag{3.24}$$

where $\beta = v/c$ indicates the particle's speed [172].

The Čerenkov effect is sensitive to velocity rather than to momentum, making Čerenkov counters powerful particle-identification tools when used in conjunction with magnetic spectrometers. A π^- track in BigBite might look just like an e^- track in BigBite, with the same momentum and trajectory, but the heavier pion has a lower velocity. To produce Čerenkov radiation and trigger a Čerenkov counter, a pion must therefore have significantly higher momentum than an electron. We can calculate the momentum threshold for the Čerenkov effect by inserting the threshold condition, $\beta = 1/n$, into the relativistic expression for a particle's three momentum, $\vec{p} = mc\vec{\beta}/\sqrt{1-\beta^2}$ where m is the particle's mass. We obtain

$$\vec{p}_{thr} = \frac{mc}{\sqrt{n^2-1}}. \tag{3.25}$$

The BigBite gas Čerenkov is a threshold counter used as an electron tagger: pions need a much higher momentum than electrons to trigger the detector, and so are much less likely to produce a Čerenkov signal. The dielectric medium used in this detector is C_4F_8O gas at 1 atm of pressure. C_4F_8O, chosen for its commercial availability and ease of handling, has an index of refraction of $n = 1.00135$. The resulting momentum thresholds for electrons, positrons, pions and protons, computed according to Equation 3.25, are given in Table 3.10.

The detector is located between the front and back MWDC assemblies. Twenty spherical focusing mirrors are arranged in two columns of ten at the back of the Čerenkov tank. Each mirror is 31

Particle	Mass (MeV/c^2)	Momentum Threshold (MeV/c)
$e^{\pm}$	0.5110	9.831
$\pi^{\pm}$	139.6	2685
p	938.3	18050

Table 3.10: Momentum thresholds in BigBite gas Čerenkov. Particle masses are taken from the Particle Data Group's 2010 review [11].

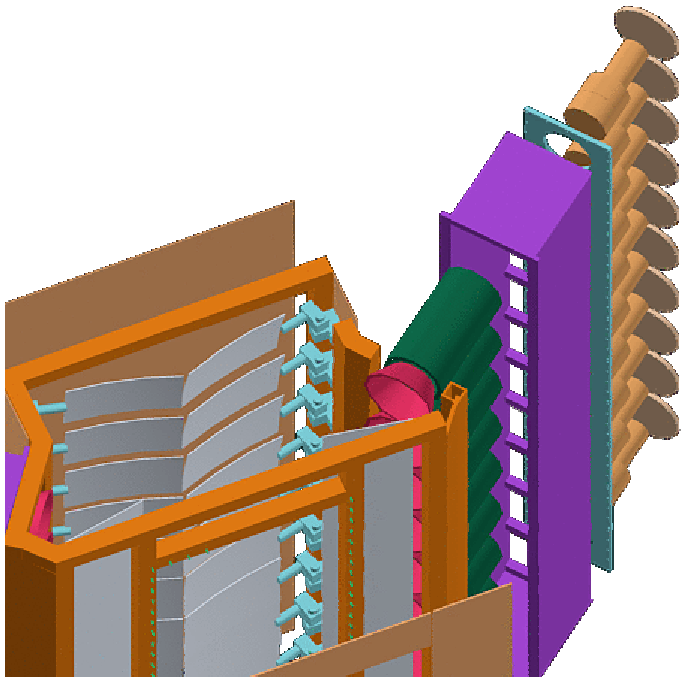

Figure 3.30: Exploded CAD diagram of the BigBite gas Čerenkov, showing mirrors in gray, Winston cones in pink, and PMTs inside green mu-metal shielding. Reproduced from Sawatzky [173].

cm wide and 21 cm tall, with a focal length of 58 cm and a radius of 116 cm. As high-velocity charged particles move through the tank, the resulting Čerenkov light strikes the spherical mirrors, each of which reflects light into one of the twenty PMTs. Reflected light from each spherical mirrors is redirected onto its PMT by a plane secondary mirror, 24 cm wide and 21 cm tall, at the front of the tank. To accommodate the wide momentum range of particles accepted by BigBite, a Winston cone [174] is fitted like a collar on each PMT, extending the diameter of its light collection area from five inches to eight inches [171]. Figure 3.30 shows the geometry of this apparatus.

T2, the primary trigger used for E06-014 production data, required a coincidence between a signal in the gas Čerenkov and a signal in the shower. The thresholds for each could be set independently to maximize electron acceptance while minimizing pion contamination.

3.3.4.3 Scintillator Plane

A scintillator plane, sandwiched between the preshower and shower calorimeters (Section 3.3.4.4), is available to provide timing information. When an ionizing particle moves through a scintillator, exciting its molecules, the material luminesces, and the resulting light can be measured in PMTs

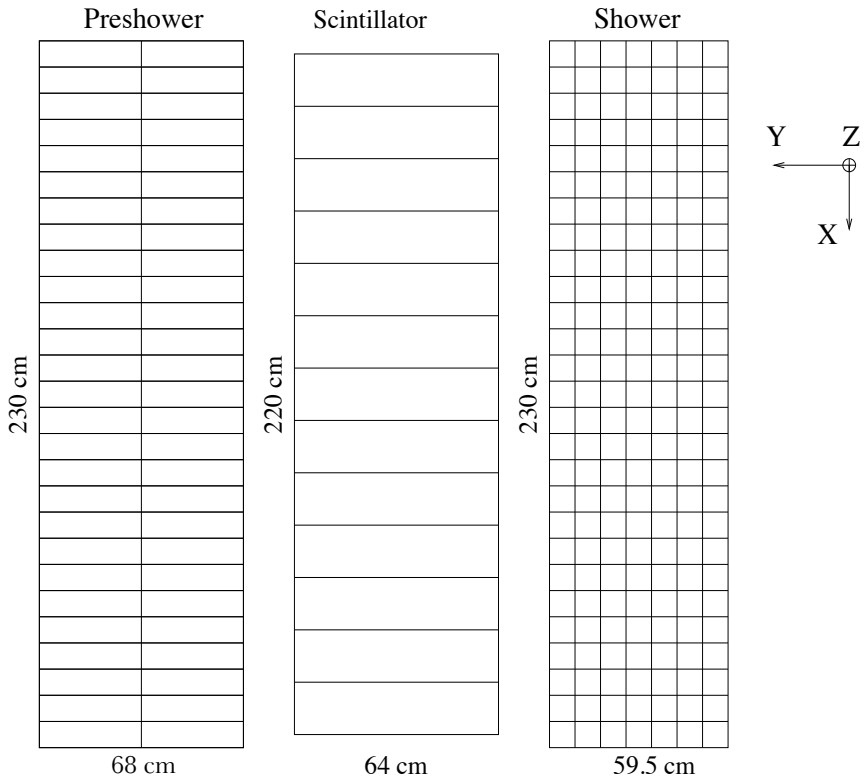

Figure 3.31: Transverse geometry of BigBite preshower, scintillator and shower detectors, adapted from Allada [161].

coupled to the scintillating material. In the present application, the great advantage of this method is its speed: the decay time of a scintillator can be as short as a few nanoseconds for some materials.

BigBite's scintillator plane is made up of thirteen $17 \times 64 \times 4$ cm^3 bars of plastic scintillator, arranged in a single column with the shortest (4 cm) dimension in the longitudinal direction, as shown in Figure 3.31. Its active area is thus 221×64 cm^2. Each bar is read out by a pair of PMTs, one on either side; the signal from each side, amplified by a factor of ten, goes to a discriminator and then to a TDC to record timing information [161]. This system is essential for coincidence experiments, which require precise comparisons of particle timing in each arm, but is not critical for single-arm experiments like E06-014.

3.3.4.4 Preshower and Shower

Further particle identification is provided by the preshower and shower calorimeters, which also contribute to the BigBite trigger (Section 3.3.6); the scintillator is sandwiched between these detectors. Both the preshower and shower detectors are arrays of lead-glass blocks measuring $8.5 \times 8.5 \times 34$ cm^3 [175]; the preshower uses TF-5 lead glass while the shower uses TF-2. Preshower blocks are oriented so that the long (34 cm) side is perpendicular to the trajectory of a particle passing through the center of the detector, while shower blocks are placed so that the long side is along that trajectory. The preshower thus has an active area of 229.5×68 cm^2, with its blocks arranged in two columns; the seven-column shower array has an active area of 229.5×59.5 cm^2. Both layers have 27 rows of blocks. A PMT mounted on each of these blocks produces a signal proportional to the energy deposited. Figure 3.31 shows the layout of the preshower, scintillator and shower arrays.

A high-energy electron, positron or photon passing through a lead-glass block will undergo pair-production and bremsstrahlung processes, generating additional electrons, positrons and photons with lower energies. These secondary shower particles undergo the same types of processes, resulting in an electromagnetic cascade in which much of the initial electron energy is deposited in the material. The cascade dissipates only when the particles resulting from the shower drop below an energy at which they can produce more shower particles, instead interacting with the medium via excitation and ionization.

In a material with radiation length X_0, the distance $t_{max} = x_{max}/X_0$ at which the maximum energy is deposited and the cascade begins to dissipate can be approximated as

$$t_{max} = \ln E_0/E_c - 0.5 \tag{3.26}$$

where E_c is the critical energy, below which the cascade begins to dissipate [11]. The critical energy for electrons in lead is about 7 MeV [176], with radiation lengths in lead glass on the order of a few centimeters, depending on the exact formulation of the material. The 8.5-cm longitudinal dimension of a preshower block represents about three radiation lengths of TF-5, while the 34-cm longitudinal dimension of a shower block is about thirteen radiation lengths of TF-2 [161].

Due to Coulomb scattering, an electromagnetic cascade also has a significant transverse size; we must consider the cross-section of a block that can contain the majority of the shower. In this, it is useful to define the Molière radius R_M

$$R_M = \frac{X_0 \cdot 21.2 \text{ MeV}}{E_c}. \tag{3.27}$$

On average, a cylinder with radius R_M contains 90% of the total deposited energy; a cylinder with radius $3.5R_M$ contains 99% [177]. In the transverse direction, the edge of a shower block is only about $1.6R_M$ from its center; for this reason, our analysis groups neighboring blocks into clusters, which catch more of the cascade.

At Jefferson Lab energies, a heavier particle – such as a muon or a pion – acts as a ***m**inimum **i**onizing **p**article* (MIP) in the lead-glass block, with a very different deposited-energy profile. Instead of producing a cascade, it loses small amounts of energy in successive ionization reactions. Energy loss by a MIP can be approximated as about 1.5 MeV per g/cm^2 traveled [178]. The TF-5 lead glass of the preshower has a density of 4.77 g/cm^3 [179], which means that, if nuclear interactions are neglected, a muon or pion is likely to deposit only about 60 MeV in the 8.5 cm of the preshower block and fewer than 300 MeV in the preshower and shower together, while an electron will deposit nearly all its energy in the two calorimeters. This discrepancy makes the preshower and shower calorimeters potent tools for differentiating electron tracks from pion background.

3.3.5 Left High-Resolution Spectrometer

The second arm of E06-014 is the LHRS, positioned at an angle of 45° to beam left and configured to detect electrons for the measurement of the total unpolarized cross section σ_0. Although the measurement of A_1 does not use LHRS data, we briefly describe the spectrometer here in order to gain a more complete sense of the experiment.

Figure 3.32 shows the size and configuration of an HRS relative to Hall A as a whole. The bulk of each HRS rests on a steel cradle that is supported by four bogies (wheeled carriages) riding on steel plates, so that the HRS can be rotated into position at the desired azimuthal angle; the maximum speed of the servomotor-driven system is 3° per minute [140]. Of course, they cannot be deployed to arbitrarily small angles ($< 12.5°$) as in Figure 3.32, lest they collide with each other, with the beam pipe downstream of the target, or with other Hall infrastructure. The spectrometer angle is measured from markings on the Hall floor and confirmed by surveyors.

The LHRS optics consist of a series of four magnets: two superconducting $\cos(2\theta)$ quadrupole magnets, a long superconducting dipole magnet, and a final superconducting $\cos(2\theta)$ quadrupole

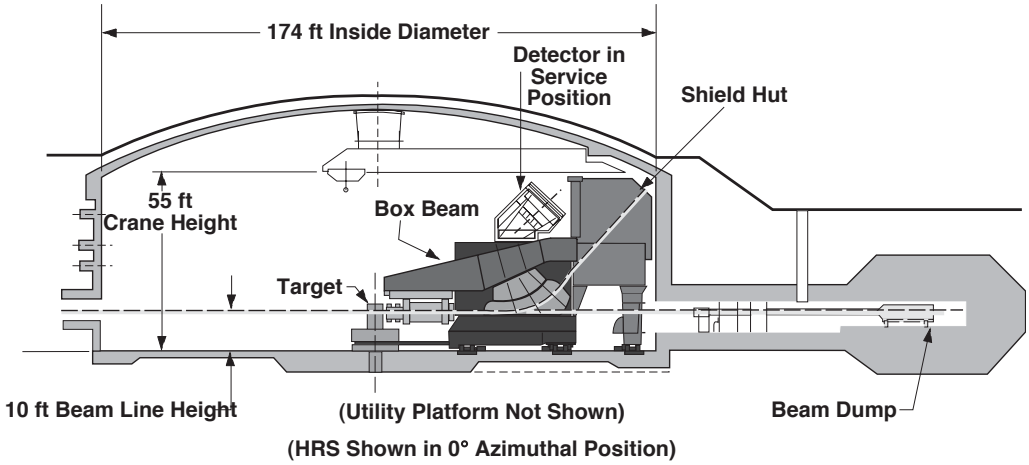

Figure 3.32: A schematic cross section of Hall A, showing a High-Resolution Spectrometer placed at the physically impossible, but conceptually simple, angle of 0° relative to the beamline. Reproduced from Alcorn *et al.* [140].

magnet (Figure 3.33). By adjusting the set currents for each magnet, experimenters can change the central momentum value in a range from 0.3 to 4.0 GeV/c. (The spectrometer accepts particle momenta within 4.5% of the central momentum setting.) The dispersion plane is vertical and the bending angle is 45°. The spectrometer's high designed momentum resolution (10^{-4}) and angular resolution (0.5 mrad in the horizontal and 1.0 mrad in the vertical) come at the price of a solid-angle acceptance of only 6 millisteradians [140].

Figure 3.34 shows the configuration of the LHRS detector stack during E06-010 and E06-014. The detectors, as well as their data acquisition systems, are located inside a concrete shield hut in order to reduce background radiation. For completeness, we will now briefly discuss each element of this detector stack, although LHRS data do not otherwise figure in this dissertation.

A particle emerging from the LHRS's magnets strikes the two **V**ertical **D**rift **C**hambers first. The VDCs work on the same principle as BigBite's MWDCs (Section 3.3.4.1), although certain details of the implementation are different. The two VDCs are filled with a 62-38 mixture of argon and ethane. Each chamber has two wire planes, one each in the u and v orientations (at angles of 45° relative to the dispersive and non-dispersive directions); unlike the BigBite wire chambers, the VDCs are not perpendicular to the nominal central ray but rather intersect it at an angle of 45°. The VDCs allow track reconstruction with a position resolution of 100 μm and an angular resolution of 0.5 mrad.

Next is the S1 scintillator plane, which is made up of six paddles of plastic scintillator (each with a PMT on either side) and forms part of the HRS trigger; we will describe the trigger in detail in Section 3.3.6. After this is an aerogel Čerenkov detector used by E06-010 to separate pions from kaons and protons, followed by a CO_2 gas Čerenkov detector used by both experiments to differentiate pions from electrons with 99% efficiency. The third and final Čerenkov detector in the LHRS stack is the **R**ing-**I**maging **Č**erenkov (RICH), a liquid C_6F_{14} detector that identified kaons for E06-010 but sat idle during E06-014 [170].

The LHRS Čerenkov trio is followed by the S2m scintillator plane, consisting of sixteen scintillator paddles (again, each has a PMT on each side). It is the S2m, positioned two meters downstream of the S1, that gives LHRS events their timing, and it is thus crucial for time-of-flight calculations.

The final elements in the LHRS detector stack are two layers of pion rejectors. Each layer is a 2×17 array of lead-glass shower blocks, each with dimensions 15 cm × 15 cm × 35 cm and each read

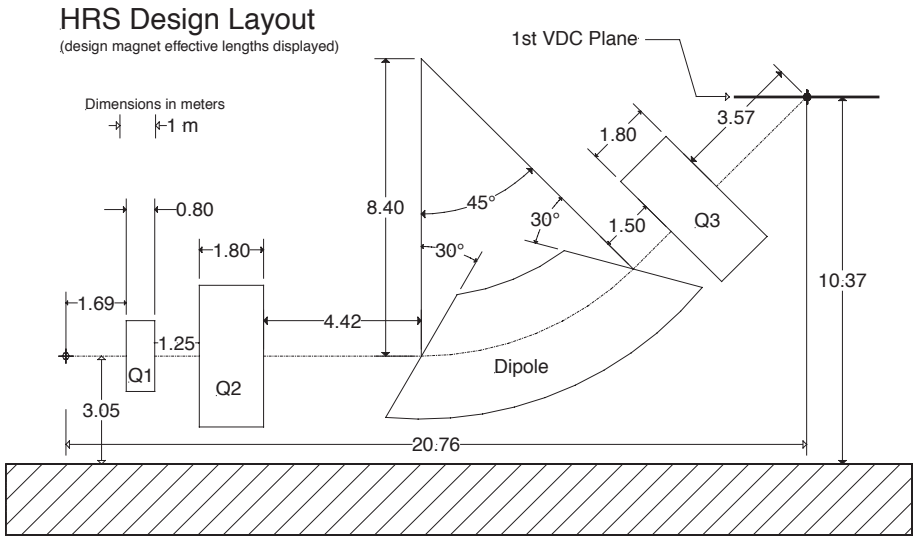

Figure 3.33: Configuration of dipole and quadrupole magnets within the LHRS, reproduced from Allada [161].

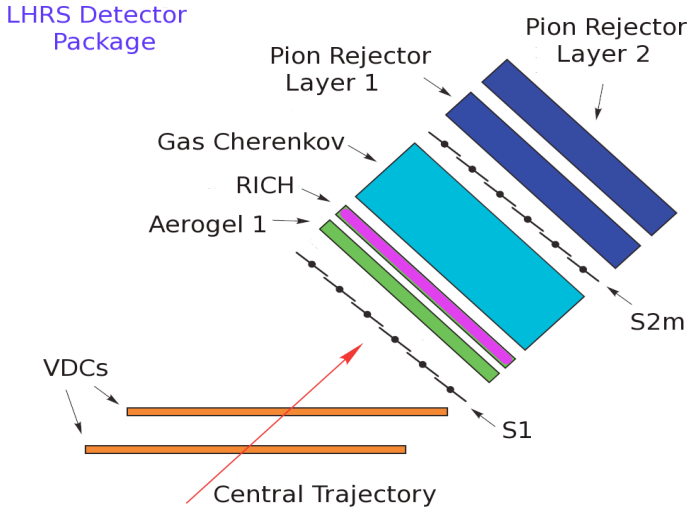

Figure 3.34: Configuration of LHRS detector stack during E06-010 and E06-014, reproduced from Dutta [151].

out by a single PMT and ADC. Pions passing through such a detector will leave a distinctive peak due to minimum ionization, while electrons will produce a full shower and a correspondingly large signal. The pion rejectors and gas Čerenkov together provide a pion rejection factor of 10^4 [180].

3.3.6 Triggers and Trigger Logic

With numerous signals coming from so many detectors, it is impossible to record all information continuously; the volume of data is too great. Instead, we rely on a trigger system to flag short time windows of potential interest, and concentrate our data-recording efforts on these. Electronic logic systems identify these time windows, based on parameters such as whether the signal in a detector has passed a pre-programmed threshold (*i.e.* the detector has *fired*) or whether two detectors have fired at close to the same time. The Hall A data acquisition system is designed to handle up to eight separate triggers, each with its own integer prescale factor; when a trigger has a prescale factor n, an event will be recorded $1/n$ of the times that trigger fires. Several triggers are employed primarily for troubleshooting purposes, and are prescaled away during production running.

Table 3.11 summarizes the triggers in use during E06-014. Most were single-arm triggers, involving only BigBite signals or only LHRS signals. Each arm received a copy of T8, a 1024 Hz clock signal. During low-energy calibration runs early in the experiment, the T5 trigger – a coincidence between the BigBite T1 and the LHRS T3 – was used for a combined, two-arm data acquisition system, but in single-arm mode, T5 was disabled.

Trigger	Spectrometer(s)	Description
T1	BigBite	Low shower threshold
T2	BigBite	Overlap between T6 and T7
T3	LHRS	Overlap between S1 and S2m scintillators
T4	LHRS	Overlap between two of S1, S2m and Čerenkov
T5	BigBite and LHRS	Coincidence between T1 and T3
T6	BigBite	High shower threshold
T7	BigBite	Gas Čerenkov
T8	BigBite and LHRS	1024 Hz clock

Table 3.11: Triggers used during E06-014. The low-threshold trigger selects lower-magnitude pulses in addition to the higher-magnitude pulses selected by the high-threshold trigger.

3.3.6.1 LHRS Triggers

The primary LHRS trigger is the T3 trigger, which requires a hit in both scintillator planes (S1 and S2m). A hit, in turn, requires above-threshold signal in both PMTs (left and right) affixed to a paddle; a T3 event thus means a pulse in four PMTs, two in each scintillator plane. The LeCroy 1875 TDCs used for the scintillator planes had a time resolution of 50 ps; the timing of the T3 trigger is set by the leading edge of the signal in the PMT on the right side of the S2m scintillator paddles [161].

The T4 trigger is used to check the T3 efficiency. The logic for T4 requires a coincidence between the LHRS gas Čerenkov and either of the scintillator planes; T3 events (i.e. coincidences between the two scintillator planes) are vetoed. T4 events therefore represent the population of potentially desirable events that are erroneously rejected by the T3 logic, allowing an analysis of the T3 trigger efficiency. In the E06-014 data, this analysis showed an average T3 efficiency of 99.95% across all kinematic settings [181]. Figure 3.35 shows the logic for T3 and T4.

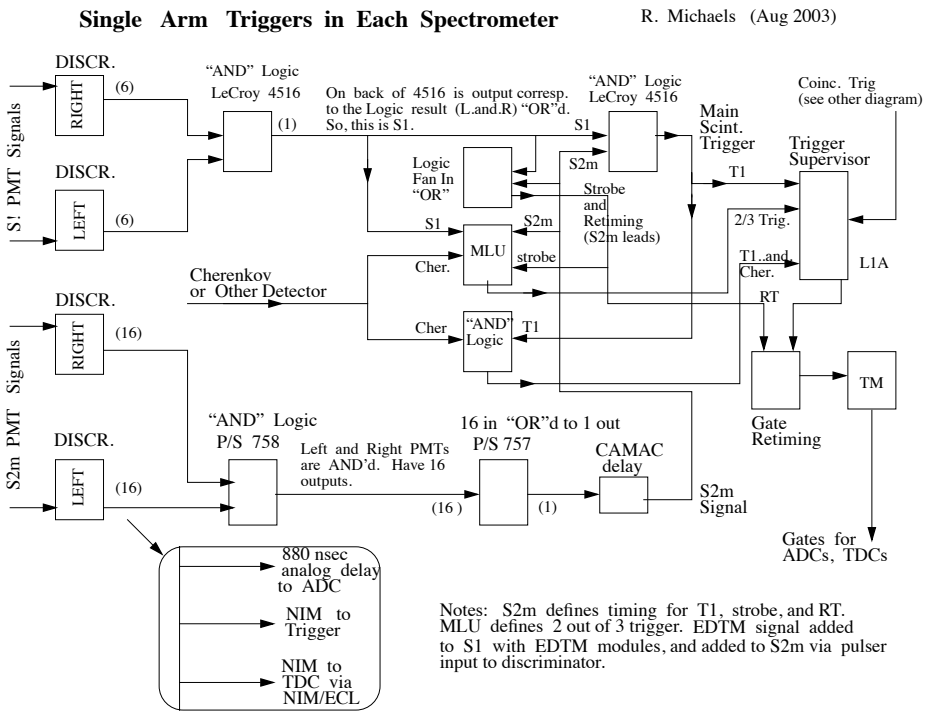

Figure 3.35: Logic diagram for LHRS singles triggers, reproduced from Michaels [182]. This is the standard wiring for both HRSes; the diagram's T1 corresponds to E06-014's T3, while the "2/3 trigger" is E06-014's T4.

3.3.6.2 BigBite Triggers

Four triggers – T1, T2, T6, and T7 – are BigBite singles triggers. Two of them, T1 and T6, are designed to detect whether a predetermined minimum energy has been deposited in the preshower and shower calorimeters. In each case, hardware summing modules are used to add up the signals from two rows of preshower blocks (four blocks, two in each row) and the signals from the two corresponding rows of shower blocks (fourteen blocks, seven in each row). There are 26 of these two-row clusters in all, so every row except the top and bottom rows forms part of two clusters. The high voltages of the shower and preshower are calibrated to provide different active ranges, so the shower signal must be amplified a factor of two more than the preshower signal before the two are combined in a single, total hardware sum.

This hardware sum is directly proportional to the total energy deposited in both parts of the calorimeter. The sum signal proceeds to a discriminator with a programmable threshold; if enough energy has been deposited, the trigger fires. As shown in Figure 3.36, T1 and T6 have the same circuit logic, but their thresholds may be set independently.

The Čerenkov trigger, T7, operates in a similar way, as shown in Figure 3.37. Signals from two adjacent rows of mirrors (four mirrors altogether) are summed; there are nine overlapping mirror clusters altogether. If any of these summed mirror-cluster signals passes a programmable threshold, a T7 trigger is formed.

The primary BigBite trigger for this experiment, however, is T2, which is formed from a geometrical overlap of calorimeter and Čerenkov signals. Figure 3.36 shows the shower part of the T2 logic; the T2 shower threshold is shared with T6. Meanwhile, Figure 3.37 shows the Čerenkov part of the T2 logic (the Čerenkov threshold is shared with T7), as well as the logic that combines signals from

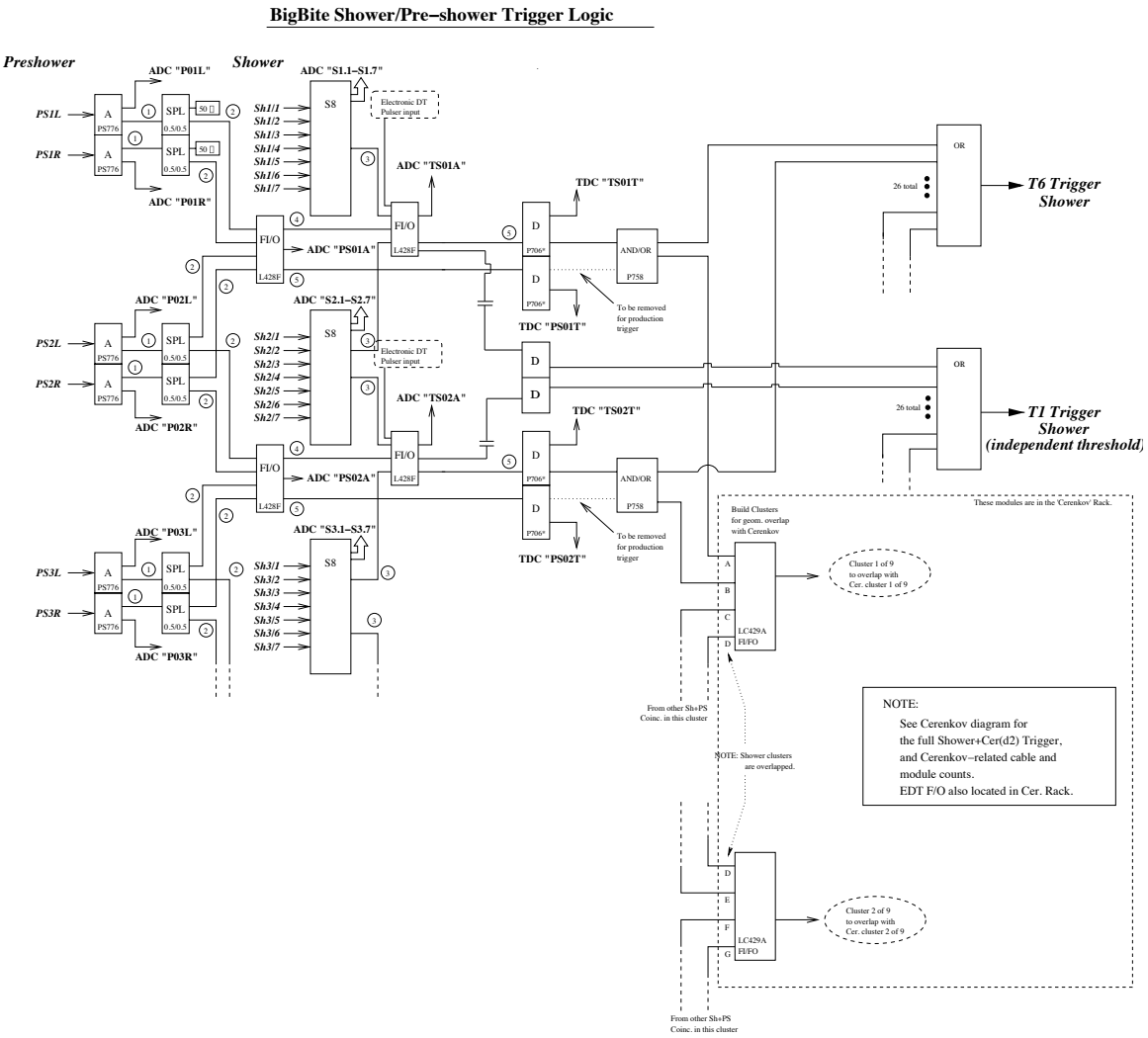

Figure 3.36: Logic diagram for the BigBite shower triggers, T1 and T6, adapted from Sawatzky [183].

the two detectors.

Figure 3.38 demonstrates how the geometrical overlap is defined. The ten rows of Čerenkov mirrors are assigned to nine overlapping two-row clusters, C1 through C9. The twenty-seven rows of the shower and preshower are assigned to twenty-six overlapping two-row clusters, A through Z. The colors of the rows in Figure 3.38 show which Čerenkov clusters overlap with which calorimeter clusters; the shape of the overlaps is determined by the probable paths of charged particles through the detector. The top two rows of Čerenkov mirrors (cluster C1), for example, overlap with the top five rows of the calorimeter (clusters A, B, C, D, and E). Čerenkov rows two and three (C2) overlap with rows four through eight of the calorimeter (D, E, F, and G), and so on. When a signal passes the threshold in both a Čerenkov cluster and any of the four calorimeter clusters with which it overlaps, a T2 trigger is formed.

Since triggers generate gates for ADCs and common stops for TDCs, it is important for the timing of the various triggers to be consistent. During E06-014, the T6 timing was used for both T6 and T2; the retiming circuit is shown in Figure 3.39. The **L1 A**ccept, or L1A, signal is what gates

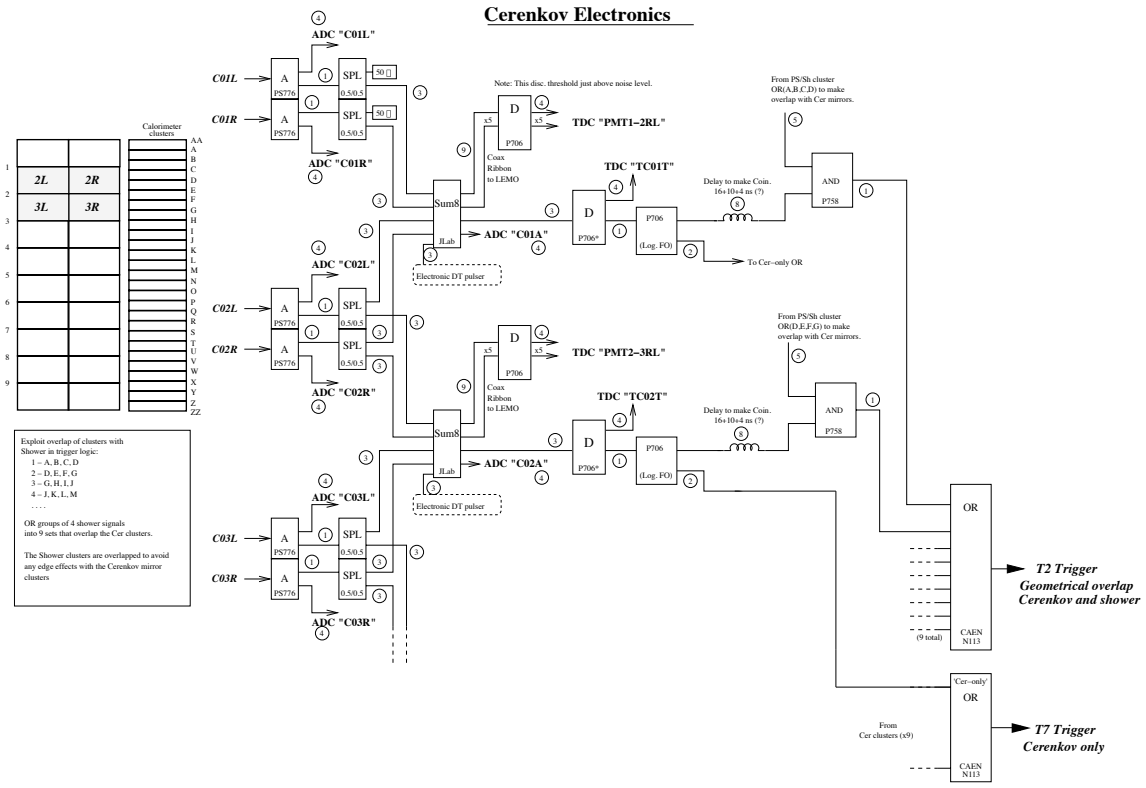

Figure 3.37: Logic diagram for the BigBite Čerenkov triggers, T2 (Čerenkov and shower) and T7 (Čerenkov only), adapted from Sawatzky [183].

the ADCs and TDCs after a trigger is formed, as explained in Section 3.3.7.3.

3.3.6.3 Coincidence Trigger

The coincidence trigger, T5, is designed to detect cases where two particles, one observed in the LHRS and one in BigBite, could have originated in the same interaction. This is determined by the relative timing between triggers T1 and T3. If the two arms were perfectly symmetrical, the T5 trigger condition would be simultaneous hits in each arm. In the E06-014 setup, both particle time-of-flight and trigger-formation time vary between the two spectrometers, so the trigger condition must be set with this in mind. Trigger-formation times are determined by measuring the time it takes a pulser signal to propagate through the trigger logic; time of flight may be determined based on spectrometer geometry and the kinematics of the desired particles. Appropriate cable delays may then be added (or removed) to the circuitry connecting T1 and T3 to the T5 logic, so as to ensure a time overlap between signals with the desired timing.

T5 was in service for only a brief time during E06-014, when hydrogen and helium elastics data were taken with a beam energy of 1.23 GeV. Figure 3.40 shows the relative timing of T1, T3 and T5, as well as the L1A signal that prompts the recording of an event, for this calibration period. The LHRS T3 signal had a width of 140 ns, defining the coincidence window, and the 40-ns T1 signal from BigBite was designed to arrive 60 ns after T3. The T5 timing was set by T1.

For most of this calibration period, the LHRS was in a positive-polarity state so as to detect protons, while BigBite was in a negative-polarity state for electron detection. When production running began, both spectrometers were configured to detect electrons. The LHRS triggers were

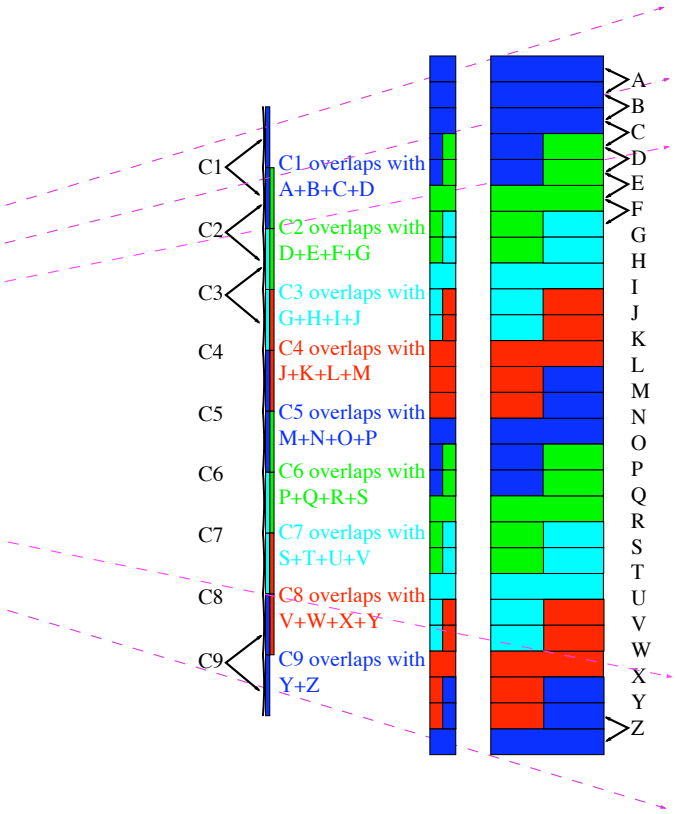

Figure 3.38: Geometric overlap between gas Čerenkov and shower for T2 trigger.

disabled in the BigBite DAQ, and vice versa; the T5 trigger was disabled in both.

3.3.7 Data Acquisition System

The trigger logic for the two spectrometers identifies time periods of potential interest to the experiment, but recording the relevant data from those time periods for later study is a complex undertaking. Timing and analog signals from thousands of PMTs and wires must be stored. Information from beam monitoring devices must be collated with spectrometer signals. Peripheral information about device functionality, from target temperature to the voltage drawn by a particular PMT, must be preserved for troubleshooting and possibly for later corrections. These herculean tasks fall to the **D**ata **A**cquisition **S**ystem, or DAQ.

The **t**rigger **s**upervisor (TS) is the hardware keystone of the DAQ; it decides when to acquire data and write it to disk. The actual data acquisition is handled by two software packages: CODA, a package written at Jefferson Lab to coordinate complicated and configurable detector readouts, and EPICS, which is used at numerous facilities to read peripheral information and remotely control service devices. DAQ modules generally follow the VME (**V**ersa **M**odule **E**uropean) bus standard [185].

3.3.7.1 CODA

The bulk of event acquisition in Jefferson Lab is handled within the framework of the **C**EBAF **O**nline **D**ata-**A**cquisition (CODA) system [186]. CODA provides an interface to the **R**ead-**O**ut **C**ontrollers, or ROCs, that serve as on-board computers for crates of electronics modules. The ROCs, which run

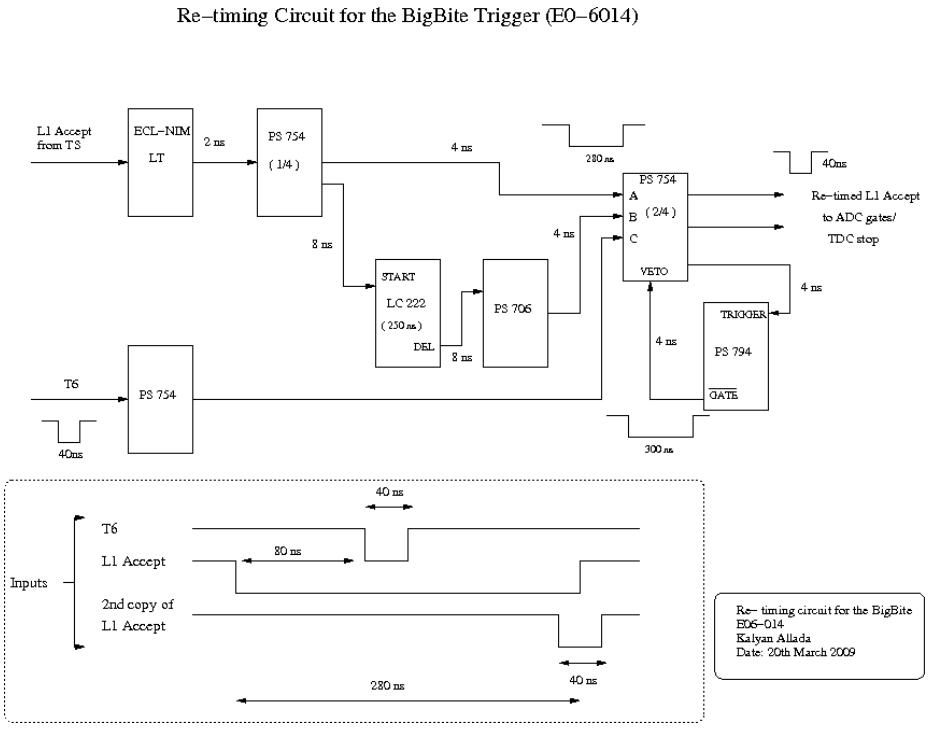

Figure 3.39: Retiming of BigBite trigger, from Allada [184]. In the timing diagram, the "2nd copy of L1 Accept" corresponds to the "Re-timed L1 Accept" from the circuit diagram.

the VxWorks operating system, follow instructions in the C-based CODA readout list (.crl) file to retrieve or store signals from the modules inside the crate, which are most often **A**nalog-to-**D**igital **C**onverters (ADCs) or **T**ime-to-**D**igital **C**onverters (TDCs). On receiving an L1A signal from the trigger supervisor, the ROCs process their data and pass it to the CODA event builder, a software package that combines data from disparate sources into one CODA event with a single timestamp; this CODA event is then written to disk by the event recorder.

This set of processes is coordinated and supervised by the run control system, initially written in Eiffel but now ported to Java [187]. This system, accessible to shift workers through a graphical user interface, includes facilities for choosing between several DAQ configurations, downloading the appropriate CODA readout lists to the ROCs, beginning a run, and ending a run – either manually, or after a pre-set number of CODA events have been recorded. The run control system also monitors the components and processes necessary for good data-taking, from individual ROCs to the status of the event recorder, and produces error messages when a ROC or process stops responding to its commands.

3.3.7.2 EPICS

The **E**xperimental **P**hysics and **I**ndustrial **C**ontrol **S**ystem (EPICS) [188], developed by a collaboration of numerous laboratories, universities and industrial facilities, is used at Jefferson Lab for both device control and the slow readout of selected parameters. EPICS drivers, developed to interface with the native controls for everything from stepper motors to high-voltage power supplies, allow remote changes to the devices' operating instructions, often through a simple graphical interface.

The input to EPICS variables, meanwhile, may be generated from hardware (*e.g.* the vertical position of the target ladder) or from software (*e.g.* the beam current in μA, generated from a

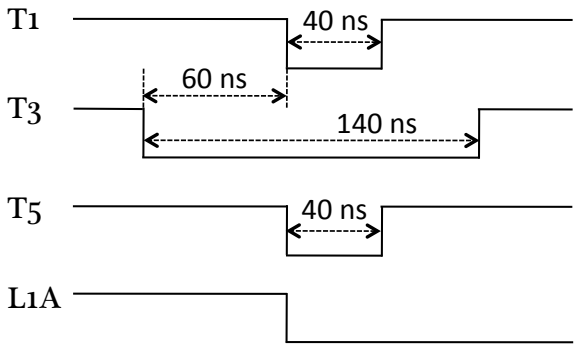

Figure 3.40: Timing of coincidence trigger (T5) relative to BigBite (T1) and LHRS (T3) triggers.

formula involving readouts from two beam current monitors). Each EPICS variable is represented by a record in the EPICS datastream, and is identifiable by its unique name; the channel for this variable defines a path to the appropriate record. When an EPICS client requests a record by name, the system broadcasts to its hardware and software servers to discover the channel and retrieve the value of the variable. This decentralized method is typical of the EPICS philosophy of avoiding single points of failure wherever possible.

In typical Hall A running, an EPICS logger script explicitly identifies records of interest to the experiment. Approximately every thirty seconds, this body of records is retrieved and written to the data file in a special, EPICS-type event. A separate list of EPICS records is logged at the beginning and end of each run and written to the electronic logbook. Alarm handlers, configured separately for each experiment, monitor certain hardware diagnostic variables (such as target temperature or the flow rate of cryogenic fluids) and automatically alert the shift crew when one of these parameters is outside the range they have been programmed to accept.

3.3.7.3 Trigger Supervisor

Each spectrometer has a trigger supervisor, a VME module with eight input channels corresponding to the external triggers generated by the trigger logic (Section 3.3.6). The trigger supervisor prescales the incoming triggers according to pre-set prescale factors for the run; for example, if T2 has a prescale factor of two, then the trigger supervisor will accept only half the incoming T2 triggers.

When the trigger supervisor accepts a trigger, it generates the level-one accept (L1A) logic signal, which gates the ADCs and TDCs and prompts the read-out controllers of each crate to begin processing and recording their data. The trigger supervisor monitors the crates' status via an RS432 cable daisy-chained to all the read-out controllers. No new triggers are accepted while any crates are still busy, ensuring synchronization between all elements of the system [161].

3.4 Hall A Analysis Software

In an experiment like E06-014, the volume and complexity of the recorded data are such that no collaboration could analyze it without computer aid. TDC and ADC information from thousands of wires and PMTs must somehow be converted into information about the behavior of real, physical particles: trajectories, momenta, energies and charges. Information about the beam (its polarization, position, energy, intensity and angle) and target (its temperature, density, and polarization) must inform these reconstructions, as well as the final measurements of asymmetries and cross sections. The software required to perform these tasks is formidable both in breadth and in depth.

Our analysis software is written using ROOT [189], a C++-based package developed by CERN physicists to simplify the processing of large quantities of particle physics data. The free collection of ROOT libraries, licensed under the GNU Lesser General Public License, includes classes for organizing disparate pieces of data, event-by-event; plotting histograms in one, two and three dimensions; and performing fits using the Minuit subpackage. ROOT command-line instructions and macros can be executed through CINT, a C interpreter; ROOT code can also be compiled and run as an executable, which is significantly faster.

The Hall A Analyzer [190, 141], also known as Podd, is an extension of ROOT designed by and for the Hall A Collaboration. Building on the basic ROOT libraries, the Analyzer provides abstract classes for several types of detectors (vertical drift chambers, scintillators, Čerenkov counters, and shower counters) and procedures for decoding the raw data in CODA files and performing some physics analysis. Tracks through wire chambers, for example, are found using one of the many Analyzer libraries. Replay scripts, written for use in an Analyzer environment, provide a framework for combining information from many sources into a *tree*, which allows variables to be compared to each other CODA event by CODA event. This functionality is suitable both for rapid data-quality checks during an experimental run, and for in-depth, offline analysis after the experiment has been completed.

In addition to the replay scripts and libraries defining detector classes, Analyzer code is designed to rely on a collection of database files. These encode certain hardware features of the experiment – for example, the channel, slot and crate numbers belonging to a particular ADC, TDC, or high voltage line – as well as calibration constants. These database files are organized into dated directories so that the software can easily handle configuration changes: each detector class locates the appropriate directory for the timestamp of the run and thereby automatically loads the correct information.

The Analyzer was initially designed for use with the basic beamline equipment and high-resolution spectrometers, but, through the efforts of many experimenters over the years, plug-in libraries extend its operation to the BigBite spectrometer, as well as to several ad hoc detector configurations.

3.5 Run Summary

E06-014 ran immediately after the Transversity experiment (E06-010) [191], which used a very similar setup: a polarized ^{3}He target, the LHRS (positioned at an angle of 16°) and BigBite (positioned at an angle of 30°). This shared apparatus allowed the two experiments to share expertise, some software, and some calibration runs, as well.

Commissioning for E06-014 began with spectrometer moves, installation of new target cells, and a reconfiguration of the spectrometer data acquisition systems to run independently of each other (rather than in coincidence mode). BigBite optics calibration data, including ^{3}He elastic singles and H_2 elastics in coincidence with the LHRS, were taken at a relatively low beam energy (1.23 GeV); the LHRS optics had been calibrated several months earlier, during commissioning for E06-010. Each spectrometer spent calibration time in positive polarity (with the magnetic field optimized for detecting positively charged particles) and in negative polarity (optimized for negatively charged particles.)

Two new detectors were commissioned during E06-014: the BigBite gas Čerenkov (Section 3.3.4.2) and a photon detector for the Compton polarimeter (Section 4.3.2.5). E06-014 saw substantial work on an electron detector for the Compton polarimeter (Section 4.3.2.5), but this detector commissioning was not successful.

At BigBite's position at 45°, it saw very high event rates; at some kinematic settings, rates in the LHRS were also high. In fact, E06-014's data recording rate, which reached 12 MB/s, set a Hall A record; the system was designed for a maximum rate of 10 MB/s. The strain on the network led to transient deadtime spikes and synchronization gaps. At certain kinematic points, we reduced the

production beam current from 15 to 14 μA (and sometimes to 13 μA) in order to alleviate these effects.

Early production running revealed a vertical hole the size of three shower rows in the BigBite acceptance. Three days after the beginning of production running, this was traced to the trigger electronics: a NIM bin was providing insufficient power to a bank of summing modules for the shower signal. After the NIM bin was replaced, the data showed a more uniform acceptance.

The planned kinematic coverage of E06-014 (Figure 3.3) required running at two beam energies: 5.9 and 4.7 GeV, or five and four passes through a fully operational accelerator, respectively. Since a pass change in one experimental hall affects the quality and polarization of the beam delivered to the other two halls, the scheduling of these events requires careful planning and negotiation. E06-014's production data were taken in four distinct run periods: a week and a half of highly polarized beam at 5.9 GeV, three days of minimally polarized beam at 4.7 GeV, a week of highly polarized beam at 5.9 GeV, and a week and a half of moderately polarized beam at 4.7 GeV.

On March 1, 2009, during five-pass production running, power fluctuations during a storm damaged several systems, including the Central Helium Liquefier (used for cryogenic cooling of equipment), the high-voltage systems for the LHRS, and the beam fast-shutdown controls. This event caused steadily worsening problems in several accelerator magnets. A week later, an air leak into the 1L04 cryomodule, located in the North Linac, was discovered. By then, moisture in that cryomodule had contaminated its neighbors. Once the magnitude of the problem was clear, the Machine Control Center elected to bring a chain of three contaminated cryomodules to room temperature and effectively remove them from the accelerator circuit, tuning the linacs to deliver 4.7-GeV electrons in five passes through the accelerator, rather than four. The removal of 1L04 and its neighbors improved the beam quality considerably, however, and a week-long extension of the planned run allowed E06-014 to collect about 80% of the statistics in its proposal.

Chapter 4

Electron Beam Polarimetry

As we have seen in Section 2.1.2, the neutron spin asymmetry A_1^n derives from the measured asymmetries $A_\parallel$ and $A_\perp$, defined for parallel and perpendicular orientations of the electron beam and target polarizations. Since neither the electron beam nor the target ^{3}He nuclei can be perfectly polarized, $A_\parallel$ and $A_\perp$ must be corrected for the degree to which those polarizations fall short of 100%.

We have discussed the target polarization in Section 3.3.3; its analysis will be covered in Section 5.1.2. In this chapter, we will discuss our analysis of the electron beam polarization in depth. The Jefferson Laboratory accelerator produces and delivers a longitudinally polarized beam through methods that were described in Section 3.2.1. Here, we will briefly touch upon methods for polarization measurements via Mott scattering (Section 4.1) and Møller scattering (Section 4.2) before embarking on a detailed description of Compton photon polarimetry in Hall A (Section 4.3); upgrades to the Compton photon detector, data acquisition system, and analysis methods were commissioned during Experiment E06-014. Finally, in Section 4.4, we report our conclusions about the polarization of the electron beam over the course of the experiment.

4.1 Mott Polarimetry

Before the beam has left the injector, a Mott polarimeter may be used to monitor the transverse polarization of the beam prior to its entry into the racetrack accelerator. The electron beam, with an energy of approximately 5 MeV, collides with a gold, silver or copper foil target; due to the coupling between the scattered electron's spin and its orbital angular momentum with respect to the target nucleus's Coulomb potential, a scattering asymmetry may be measured [192]. This method is destructive; none of the three experimental halls can take beam during the few hours a Mott measurement typically lasts.

At Jefferson Lab, Mott polarization measurements are systematically a few percentage points lower than measurements taken by the Hall A and Hall C polarimeters [139]. This discrepancy is partially explained by the effects of photon background in the Mott polarimeter [193].

Due to scheduling constraints, no Mott polarization measurements were made during E06-014. Instead, the experiment relied on two polarimeters in the Hall A beamline: the Møller (Section 4.2) and the Compton (Section 4.3).

4.2 Møller Polarimetry

Historically, Mott scattering became less and less useful for electron-beam polarimetry as electron beam energies increased. The use of Møller scattering as an alternative polarimetry technique was

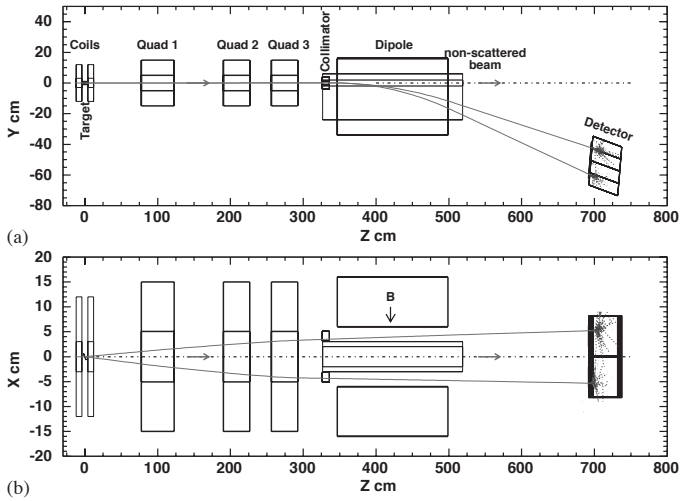

Figure 4.1: Side (a) and top (b) schematic views of the Hall A Møller polarimeter, displayed with trajectories from a simulated Møller scattering event ($E^{beam} = 4$ GeV, $\theta_{CM} = 80°$, and $\phi_{CM} = 0°$). Reproduced from Alcorn *et al.* [140].

first proposed in 1957 by Kresnin and Rozentsveig [194]. They realized that the cross section for Møller scattering ($e^-e^- \to e^-e^-$) is sensitive to the polarizations of the electron beam (P^{beam}) and the atomic electrons of the target (P^{target}), according to

$$\sigma \propto \left[1 + \sum_{i=X,Y,Z} \left(A_{ii} \cdot P_i^{beam} \cdot P_i^{target}\right)\right]. \tag{4.1}$$

Here, $i = X, Y, Z$ are the axes onto which the polarization is projected; A is the analyzing power of Møller scattering as a polarization measurement, which depends on the scattering angle in the center-of-mass frame. The maximum possible analyzing power is 7/9 and corresponds to the measurement of the longitudinal component of the beam polarization [140].

Hall A's Møller polarimeter is located within the experimental hall and has been a standard element of the beamline equipment since 1997. Figure 4.1 shows a schematic representation of the polarimeter, with simulated trajectories of Møller events at $E^{beam} = 4$ GeV and a center-of-mass angle $\theta_{CM} = 80°$. At the upstream end of the detector is the Møller target, a cryogenically cooled 10.9-μm-thick iron foil maintained at a polarization of about 7.1% by a 28-mT magnetic field, courtesy of a set of Helmholtz coils. Møller-scattered electrons pass through three quadrupole magnets and a dipole magnet en route to a two-arm, lead-glass calorimeter capable of measuring coincidences. The longitudinal asymmetry of the beam is computed as the average measurement at two opposing target angles, which approximately cancels transverse contributions [195].

Since it uses a solid target, a Møller measurement is invasive and cannot be undertaken at the same time as primary data-taking downstream, so it cannot be used for continuous monitoring of the beam polarization. Furthermore, since the Møller target foil suffers depolarization due to beam heating, polarization measurements are performed only up to a maximum beam current of about 1.5μA, a factor of ten less than E06-014's production current of 15μA. Despite these shortcomings, the Møller polarimeter's subpercent statistical errors and low ($\sim 2\%$) systematic errors make it a vital component of electron beam polarimetry in Hall A.

During E06-014, seven Møller measurements were taken: approximately one each week in smooth running, as well as one after each major configuration change (e.g. a pass change). The measured

Date	Beam Energy (GeV)	Measured Beam Polarization	IHWP Status
7 February	5.90	$-0.7943 \pm 0.0013_{stat} \pm 0.0159_{syst}$	in
9 February	1.23	$-0.7164 \pm 0.0014_{stat} \pm 0.0143_{syst}$	in
11 February	5.90	$+0.7450 \pm 0.0015_{stat} \pm 0.0149_{syst}$	out
19 February	5.90	$-0.7448 \pm 0.0011_{stat} \pm 0.0149_{syst}$	in
3 March	5.90	$-0.7970 \pm 0.0012_{stat} \pm 0.0159_{syst}$	in
6 March	4.74	$+0.6394 \pm 0.0010_{stat} \pm 0.0128_{syst}$	out
12 March	4.74	$-0.6079 \pm 0.0013_{stat} \pm 0.0122_{syst}$	out

Table 4.1: Results of Møller measurements of electron beam polarization during E06-014 running, corrected for beam energy fluctuation. The status of the insertable half-wave plate at the polarized electron source (Section 3.2.1) is also shown. The sign of the polarization measurement relates the helicity logic signal to the helicity of electrons in the hall, as will be discussed in Section 6.3.1.3.

beam polarizations are reported in Table 4.1.

4.3 Compton Polarimetry

Both Mott and Møller polarimetry are destructive techniques: data-taking with beam on target must be halted, often for several hours, in order to perform these beam polarization measurements. Depending on experimental constraints, beam polarization measurements are thus often separated by several days (for the Møller) or even several weeks (for the Mott). In addition, at Jefferson Lab, these methods cannot be used on electron beams identical to the beam received on target. Mott measurements are taken at the injector, before the electrons are accelerated to their final energies and before they precess in the accelerator; Møller measurements are taken at beam currents that are much lower than typical production currents.

There is thus a clear need for a non-destructive polarimeter that can take continuous measurements of the beam polarization, at the production current and energy, even as data is taken on a nuclear target downstream. In Hall A, the Compton polarimeter meets this need. In this section, we will review the mechanics of Compton scattering, and how this process can be exploited to provide a measurement of electron beam polarization (Section 4.3.1). Upgrades of large portions of the Compton polarimeter – namely the scattered-photon detector and the photon data acquisition system – were commissioned during E06-014, and we will discuss the details of both the upgraded and legacy portions of the apparatus in Sections 4.3.2 and 4.3.3. We will then describe the process of calibrating the polarimeter (Section 4.3.4), the Monte Carlo simulations which have enabled us to determine the analyzing power of our apparatus (Section 4.3.5), and the final analysis of the Compton data (Section 4.3.6).

4.3.1 Principles of Compton Polarimetry

In 1923, when Arthur Holly Compton first observed and described photon-electron scattering, $e^-\gamma \rightarrow e^-\gamma$ (Figure 4.2), with its attendant alteration of the wavelength of the scattered photon [196], the effect was hailed as a vindication of the idea that light has a particle nature as well as a wave nature. In subsequent years, the effect proved to have value beyond its role in that epic debate. In 1929, Oskar Klein and Yoshio Nishina published a first-order cross section for Compton scattering, in one of the very first successes of the nascent field of quantum electrodynamics [197]. As improved experimental techniques allowed greater interest in spin-dependent processes, it was realized that Compton scattering was just such a process: in 1954, Frederick Lipps and Hendrik Tolhoek [198, 199] proved that the Klein-Nishina cross-section is sensitive to the relative spins of the incoming photon

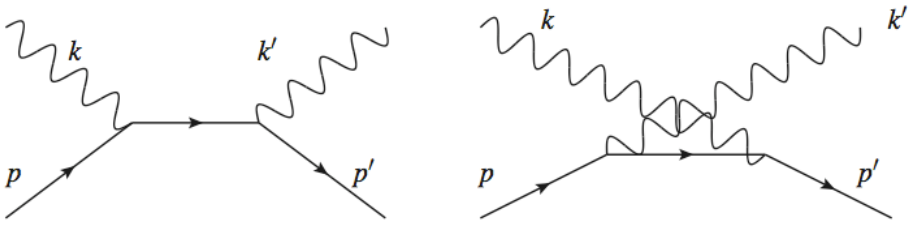

Figure 4.2: Feynman diagrams for Compton scattering.

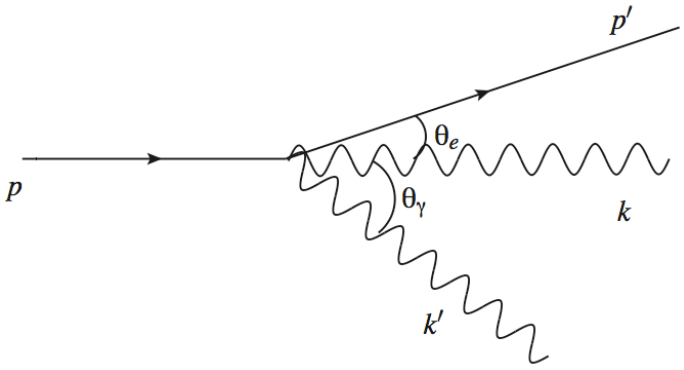

Figure 4.3: Kinematics of head-on Compton scattering with a crossing angle $\alpha_C = 0$.

and electron. (Alternate derivations may be found in a variety of textbooks, e.g. that of Stephen Gasiorowicz [200].)

The earliest applications of spin-dependent Compton scattering involved the production of polarized photon and electron beams; in 1973, as upgrades to the Stanford Linear Accelerator were being planned, Charles Prescott proposed inverting the standard kinematics in order to make routine polarization measurements of accelerated electron beams [201]. Since that time, Compton polarimeters have become standard pieces of equipment at a wide range of accelerators, including SLAC [202], HERA [203, 204], and NIKHEF [205].

In this section, we will cover the kinematics and spin dependence of Compton scattering in some depth before exploring precisely how the detection of Compton scattering can lead to a measurement of the electron beam polarization.

4.3.1.1 Kinematics of Compton Scattering

The kinematics of Compton scattering in the laboratory frame are shown in Figure 4.3. We define the z axis as the momentum direction of the incident electron, which has energy E; the photon, incident at an angle α_c relative to the z axis, has energy k. The scattered electron is displaced by an angle θ_e and has energy E'. The scattered photon, displaced by θ_γ from the z axis, has energy k'. In our kinematics, the incident electron has very high energy compared to the incident photon.

The crossing angle α_c is 23 mrad in our system, a small enough angle that setting it to zero introduces negligible error (on the order of 0.01%) [206]. In the discussion that follows, we will therefore treat the photons and electrons as colliding head-on, neglecting α_c.

It is convenient to define a kinematic parameter y, which is the ratio of the minimum energy of the scattered electron E'_{min} to the energy of the incident electron E [207]

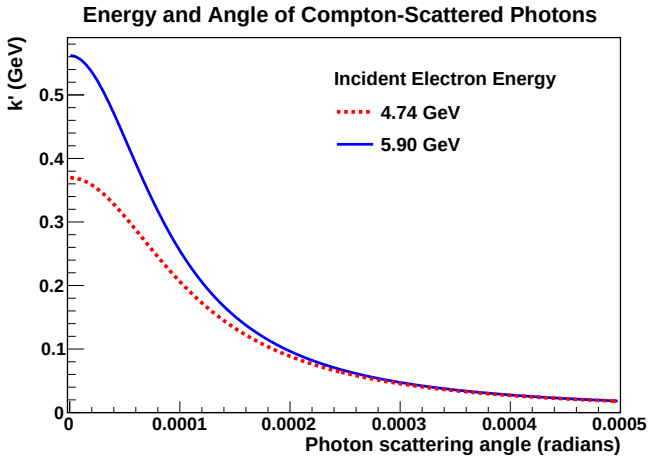

Figure 4.4: Scattered photon energy k' as a function of scattering angle θ_γ for the production beam energies of E06-014, $E_e = 4.7$ GeV and 5.9 GeV. The initial photon energy is $k = 1.1653$ eV for 1064-nm photons, and the crossing angle α_c is taken to be zero.

$$y = \left(1 + \frac{4kE}{m^2}\right)^{-1} \tag{4.2}$$

We may then express the scattered photon energy k' as a function of its scattering angle θ_γ

$$k' = k\frac{4yE^2}{m^2\left(1 + \frac{y\theta_\gamma^2 E^2}{m^2}\right)} \tag{4.3}$$

where we have used the small-angle approximation.

From Equation 4.3, we see that the energy k' of a Compton-scattered photon is uniquely determined by the angle its momentum makes with the z axis. In other words, as we follow the population of photons with energy k' out from the interaction point, we find that their trajectories make a cone centered on the z axis, with θ_γ defining its opening angle.

As Figure 4.4 shows, k' falls off quickly with increasing θ_γ for the kinematics of interest: high-energy back-scattered photons are tightly clustered around the z axis. The minimum possible scattered photon energy $k'_{min} = k$ corresponds to a scattering angle $\theta_\gamma = \pi$: there is no scattering, and the photon continues undisturbed on its original path[1]. Meanwhile, an entirely backscattered photon ($\theta_\gamma = 0$) receives the maximum possible energy in the scattering process

$$k'_{max} = \frac{4ykE^2}{m^2} \tag{4.4}$$

k'_{max} is typically called the *Compton edge*, since, when the Compton cross section is plotted as a function of k', k'_{max} is the location of a sharp and sudden drop of the cross section to zero.

The existence of a well defined k'_{max} allows us to define a dimensionless parameter ρ for the scattered photon momentum

$$\rho \equiv \frac{k'}{k'_{max}}. \tag{4.5}$$

[1]Incidentally, Equation 4.3 is not valid in this case, since the scattering angle is not small.

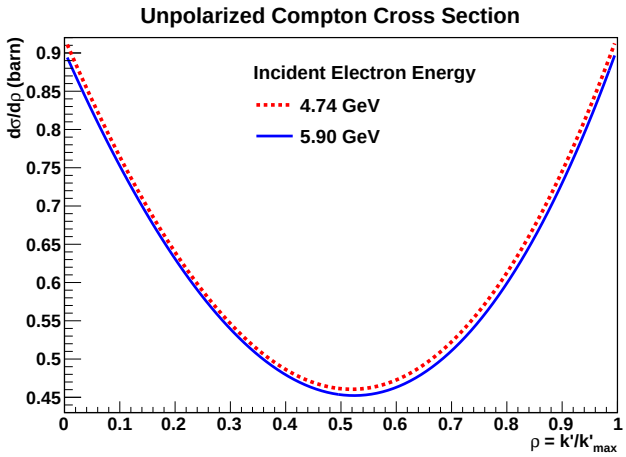

Figure 4.5: Unpolarized Compton cross section as a function of scattered photon energy $\rho = k'/k'_{max}$, calculated for the E06-014 production beam energies, $E_e = 4.7$ GeV and 5.9 GeV. The initial photon energy is $k = 1.1653$ eV for 1064-nm photons, and the crossing angle α_c is taken to be zero. Note the suppressed zero on the vertical axis.

The differential unpolarized cross section for Compton scattering may be expressed as a function of the scattered photon energy ρ. With the classical electron radius $r_0 = \alpha\hbar c/mc^2 = 2.817 \times 10^{-13}$ cm, we have [207]

$$\frac{d\sigma}{d\rho} = 2\pi r_0^2 y \left[\frac{\rho^2 (1-y)^2}{1-\rho(1-y)} + 1 + \left(\frac{1-\rho(1+y)}{1-\rho(1-y)} \right)^2 \right]. \tag{4.6}$$

Figure 4.5 shows the evolution of the cross section in ρ for the E06-014 electron energies.

4.3.1.2 Spin Dependence of Compton Scattering

Compton scattering also has a small spin-dependence, which allows the process to be used in polarization measurements. In the Hall A Compton polarimeter, light with nearly 100% circular polarization interacts with highly longitudinally polarized electrons. In this section, we explore how the spin polarization of the incident particles affects the Compton scattering process.

Electron and Photon Polarizations The incident particles in a Compton scattering process both have spin; the electron has spin 1/2, while the photon has spin 1. As we have seen in Section 3.2, CEBAF routinely delivers a beam with a high degree of longitudinal polarization; that is, most of the electrons in the accelerated beam are spin-aligned, either parallel or anti-parallel to the direction of their momentum. Where $N_e^{+(-)}$ is the number of electrons with spin parallel (antiparallel) to the beam direction, the extent of this longitudinal polarization is defined as

$$P_e = \frac{N_e^+ - N_e^-}{N_e^+ + N_e^-}. \tag{4.7}$$

The definition of photon polarization is worth a more extended discussion. Taking a page from Jackson [208], let us consider a homogeneous plane electromagnetic wave, with wave vector $\vec{k}$ and frequency ω. Two orthogonal linear polarization directions, $\hat{\epsilon}_1$ and $\hat{\epsilon}_2$, both normal to the propagation direction $\hat{k}$, are available to it. The complex amplitudes E_1 and E_2 of each polarization component allow a general formulation for the plane wave

$$\vec{E}\,(\vec{x},t) = (\hat{\epsilon}_1 E_1 + \hat{\epsilon}_2 E_2)\, e^{i\vec{k}\cdot\vec{x}-i\omega t} \tag{4.8}$$

The phase difference between E_1 and E_2 determines the type of polarization carried by the wave. If their phases are the same, the wave is linearly polarized, and its polarization vector forms an angle $\theta = \tan^{-1}(E_2/E_1)$ with $\hat{\epsilon}_1$. If their phases differ, the wave is elliptically polarized. We will be concerned here with the simplest case of elliptical polarization, *circular polarization*, in which $|E_1| = |E_2|$ and their phases are different by 90°. A circularly polarized wave may thus be expressed using a single real amplitude $E_0 = |E_1| = |E_2|$

$$\vec{E}\,(\vec{x},t) = E_0\,(\hat{\epsilon}_1 \pm i\hat{\epsilon}_2)\, e^{i\vec{k}\cdot\vec{x}-i\omega t} \tag{4.9}$$

If we consider this wave at a fixed point in space, we will see that the magnitude of the electric field vector remains constant in time, but its direction rotates about the propagation vector with frequency ω. Suppose that we are looking back on the oncoming wave. If the sign in Equation 4.9 is positive, the electric field vector rotates in a counter-clockwise direction as seen by an observer facing the oncoming wave, and the wave can be said to have positive helicity; such a wave is *left circularly polarized*. A negative sign in Equation 4.9 corresponds to clockwise rotation of the electric field vector (again, as seen looking into an oncoming wave) and a negative-helicity – or *right circularly polarized* – wave. This suggests an alternative generic formalism for a homogeneous plane wave, this time decomposed into positive-and negative-helicity elements

$$\vec{E}\,(\vec{x},t) = (\hat{\epsilon}_+ E_+ + \hat{\epsilon}_- E_-)\, e^{i\vec{k}\cdot\vec{x}-i\omega t} \tag{4.10}$$

where E_+ and E_-, direct equivalents to E_1 and E_2, are complex amplitudes, and the polarization directions are defined by the unit vectors

$$\hat{\epsilon}_\pm = \frac{1}{\sqrt{2}}\,(\hat{\epsilon}_1 \pm i\hat{\epsilon}_2)\,. \tag{4.11}$$

It is convenient to describe the polarization of an electromagnetic wave by means of the four *Stokes parameters*, which allow us to completely describe the polarization solely by making intensity measurements with various combinations of a linear polarizer and a quarter-wave plate. To define the Stokes parameters in the circular-polarization basis of Equation 4.10, we express the coefficients $E_\pm$ as:

$$E_\pm = a_\pm e^{i\delta_\pm} \tag{4.12}$$

We can then define the Stokes parameters themselves as

$$\begin{aligned}
s_0 &= |\vec{\epsilon}_+^{\,*}\cdot\vec{E}|^2 + |\vec{\epsilon}_-^{\,*}\cdot\vec{E}|^2 = a_+^2 + a_-^2 \\
s_1 &= 2\mathrm{Re}\left[\left(\vec{\epsilon}_+^{\,*}\cdot\vec{E}\right)^*\left(\vec{\epsilon}_-^{\,*}\cdot\vec{E}\right)\right] = 2a_+a_-\cos(\delta_- - \delta_+) \\
s_2 &= 2\mathrm{Im}\left[\left(\vec{\epsilon}_+^{\,*}\cdot\vec{E}\right)^*\left(\vec{\epsilon}_-^{\,*}\cdot\vec{E}\right)\right] = 2a_+a_-\sin(\delta_- - \delta_+) \\
s_3 &= |\vec{\epsilon}_+^{\,*}\cdot\vec{E}|^2 - |\vec{\epsilon}_-^{\,*}\cdot\vec{E}|^2 = a_+^2 - a_-^2\,.
\end{aligned} \tag{4.13}$$

These parameters are not independent; they obey the relation $s_0^2 = s_1^2 + s_2^2 + s_3^2$. However, the quartet forms a useful and intuitive way of thinking about the polarization of a plane wave. We see that s_0 is a measure of the wave's intensity, s_1 and s_2 relate the phases of the polarization components, and s_3 gives the intensity difference between the left- and right-circularly polarized components. The degree of circular polarization P_γ of an electromagnetic wave is thus given by

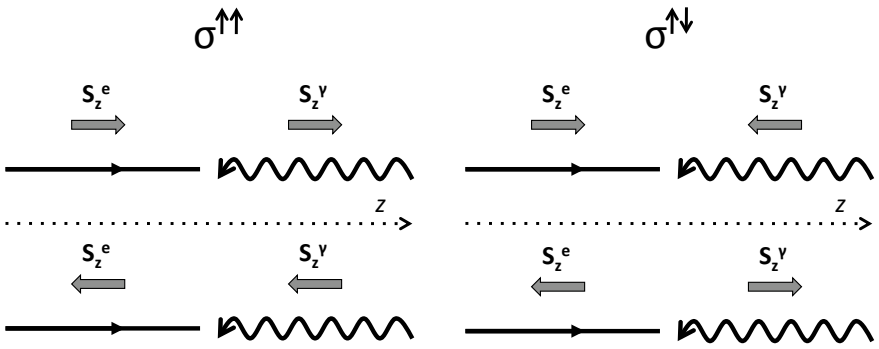

Figure 4.6: The four relative spin orientations for Compton scattering. The two configurations in each column have identical cross sections.

$$P_\gamma = \frac{s_3}{s_0}. \tag{4.14}$$

Doubly-Polarized Compton Scattering Let us apply these frameworks for electron and photon polarization to the problem of Compton scattering. When the incident electron is longitudinally polarized and the incident photon is circularly polarized, there are four possible incident spin configurations for Compton scattering at a small crossing angle α_c (Figure 4.6). Since Compton scattering is an electromagnetic process and thus conserves parity, these four states reduce to two relative spin configurations: parallel and antiparallel, which we will denote by $\uparrow\uparrow$ and $\uparrow\downarrow$ respectively.

In the laboratory, the Compton cross section for photons with circular polarization P_γ and electrons with longitudinal polarization P_e^l and transverse polarization P_e^t is given by [207]

$$\left(\frac{d^2\sigma}{d\rho d\phi}\right)_{Compton} = \frac{1}{2\pi}\left(\frac{d\sigma}{d\rho}\right)_{unpol} \cdot \left[1 + P_\gamma\left(P_e^l A_l(\rho) + P_e^t \cos\phi A_t(\rho)\right)\right] \tag{4.15}$$

where ϕ is the azimuthal angle of the photon with respect to the transverse electron polarization P_e^t and A_l and A_t are the longitudinal and transverse analyzing powers – the asymmetries that would be measured if the photons were perfectly circularly polarized and if the electrons were perfectly polarized along the relevant axis. In terms of ρ, y, and the unpolarized cross section $d\sigma/d\rho$ from Equation 4.6, these differential asymmetries are given by:

$$A_l \equiv \frac{\sigma^{\uparrow\uparrow} - \sigma^{\uparrow\downarrow}}{\sigma^{\uparrow\uparrow} + \sigma^{\uparrow\downarrow}} = \frac{2\pi r_0^2 y}{d\sigma/d\rho}\left(1 - \rho\left(1+y\right)\right)\left[1 - \frac{1}{\left(1-\rho\left(1-y\right)\right)^2}\right] \tag{4.16}$$

$$A_t \equiv \frac{\sigma^{\uparrow\rightarrow} - \sigma^{\uparrow\leftarrow}}{\sigma^{\uparrow\rightarrow} + \sigma^{\uparrow\leftarrow}} = \frac{2\pi r_0^2 y\rho}{d\sigma/d\rho}\left(1-y\right)\frac{\sqrt{4\rho y(1-\rho)}}{1-\rho(1-y)}. \tag{4.17}$$

Because of the large electron momentum in the laboratory frame, the Compton scattering angles are small enough that our detectors (electron and photon), properly centered, catch the entire azimuthal distribution of the scattered particles, integrating over ϕ and removing the transverse asymmetry term $P_\gamma P_e^t \cos\phi A_t(\rho)$ from Equation 4.15 [209]. We are thus left with sensitivity only to the longitudinal term, $P_\gamma P_e^l A_l(\rho)$, and we will henceforth write P_e^l as P_e

$$\left(\frac{d\sigma}{dx}\right)_{Compton} = \left(\frac{d\sigma}{dx}\right)_{unpol} \cdot \left(1 + P_\gamma P_e A_l(\rho)\right). \tag{4.18}$$

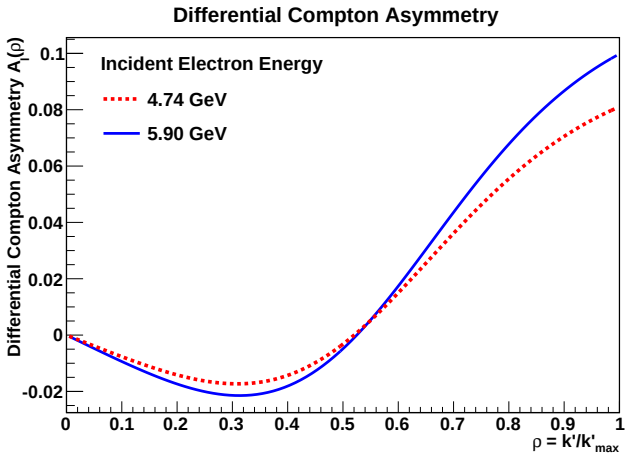

Figure 4.7: Differential Compton asymmetry $A_l(\rho)$ for longitudinally polarized electrons, computed for the two E06-014 production electron beam energies scattering from 1064-nm photons.

Figure 4.7 shows A_l as a function of ρ for the E06-014 electron and photon energies. For low values of ρ, this quantity is negative; it reaches its maximum, $A_l^{max} = (1-y^2)/(1+y^2)$, at the maximum scattered-photon energy $\rho = 1$. The zero crossing is located at $\rho = (1+y)^{-1}$.

4.3.1.3 Counting Asymmetry

Conceptually, the most straightforward way of measuring an experimental Compton asymmetry is by counting the number of times that Compton scattering occurs for each spin configuration and then forming an asymmetry between the counts. There are two methods of performing such a measurement; we will follow the Conceptual Design Report for the Hall A Compton polarimeter [210] in discussing them.

The first method is to sort scattering events according to the energy of the scattered photon and then form an asymmetry for each energy bin. Let the parallel configuration $\uparrow\uparrow$ correspond to the label $+$ and the antiparallel configuration $\uparrow\downarrow$ correspond to the label $-$. For an integrated luminosity $\mathcal{L}$ of incident photons and electrons at the Compton interaction point, the count rate n_i in the i^{th} bin will follow

$$n_i^{\pm} = \mathcal{L} \int_{\rho_i}^{\rho_{i+1}} d\rho \epsilon(\rho) \frac{d\sigma}{d\rho}(\rho)(1 \pm P_e P_\gamma A_l(\rho)) \tag{4.19}$$

where the energy range of the bin goes from a lower bound of ρ_i to an upper bound of ρ_{i+1}, and $\epsilon(\rho)$ is the detector efficiency.

For the i^{th} bin, we then obtain

$$A_{exp}^i = \frac{n_i^{\uparrow\uparrow} - n_i^{\uparrow\downarrow}}{n_i^{\uparrow\uparrow} + n_i^{\uparrow\downarrow}} \simeq P_e P_\gamma A_l^i. \tag{4.20}$$

Using the mean value of the theoretical asymmetry A_l^i for that energy range, the electron polarization P_e^i is extracted for each bin, and a final result is achieved by taking the weighted mean over all bins. In this method, energy bins are chosen so that A_l and ϵ are relatively flat across each bin.

The second method is to integrate the number of counts over the entire energy range of the acceptance. Instead of considering counts per bin n_i, we consider total counts N, defined by an expression identical to Equation 4.19 except for the range of the integral, which runs from a threshold

energy ρ_{min} to the maximum energy 1. We can then form an asymmetry between total counts over all energies

$$A_{exp} = \frac{N^{\uparrow\uparrow} - N^{\uparrow\downarrow}}{N^{\uparrow\uparrow} + N^{\uparrow\downarrow}} = P_e P_\gamma \langle A_l \rangle \tag{4.21}$$

where $\langle A_l \rangle$ is the mean value of A_l over the observed energy range

$$\langle A_l \rangle = \frac{\int_{\rho_{min}}^{1} d\rho \epsilon(\rho) \frac{d\sigma}{d\rho}(\rho) A_l(\rho)}{\int_{\rho_{min}}^{1} d\rho \epsilon(\rho) \frac{d\sigma}{d\rho}(\rho)}. \tag{4.22}$$

In both of these methods, where N_{tot} is the number of scattering events measured, we can estimate the fractional error as

$$\left(\frac{\Delta P_e}{P_e}\right)^2 \simeq \frac{1}{N_{tot} P_e^2 P_\gamma^2 b} \tag{4.23}$$

where $b = \langle A_l^2 \rangle$ for the bin-wise method and $b = \langle A_l \rangle^2$ for the integrated counts method.

Assuming perfect energy resolution, the primary advantage of the bin-wise counting method is that the polarization measurement can be mostly decoupled from the detector efficiency, since the efficiency does not vary much inside a bin and the polarization is computed independently in each bin. The method of integrated counts requires knowledge of the detector efficiency, but, if the hardware threshold ρ_{min} is set appropriately, the measurement may focus on the region where the theoretical asymmetry A_l is positive and large.

4.3.1.4 Integrating Asymmetry

The **f**igure **of m**erit (FOM) of a Compton polarimeter, equal to $\sigma \langle A_l \rangle^2$, is a useful tool for comparing polarimetry performance for different photon and electron energies. With all other parameters held equal, it obeys the scaling law [211]

$$FOM = \sigma \langle A_l \rangle^2 \propto k^2 E^2. \tag{4.24}$$

This relationship generated keen interest during preparations for the lead-radius experiment PREx [212], which ran in Spring 2010 at a beam energy of 1.06 GeV. The experiment's strict requirement of 1% electron beam polarimetry, at a beam energy lower than any previous successful Compton polarization measurement at Jefferson Lab, necessitated extensive upgrades of all aspects of the Compton polarimeter.

We saw in Figure 4.7 that the theoretical asymmetry A_l has its greatest magnitude for high-energy scattered photons ($\rho > 0.5$). This energy range is also less sensitive to low-energy uncertainties in the detector response function. If we measure the Compton asymmetry in the energy-weighted, integrated signal, the maximum contribution will therefore come from the part of the photon spectrum with the highest sensitivity and the best characterization. This measurement requires that scattered photons be detected in a photon calorimeter, which allows their energy to be recorded.

Let $E(\rho)$ be the mean energy deposited in the photon calorimeter by a photon with incident energy ρ. The corresponding signal measured in our system is then $W(\rho)$, which – in an ideal system with perfect detector and PMT response – would be directly proportional to $E(\rho)$. We can define the energy-weighted, integrated signal S as [210]

$$S^{\pm} = \mathcal{L} \int_{\rho_{min}}^{1} d\rho W(\rho) \epsilon(\rho) \frac{d\sigma}{d\rho}(\rho) \left(1 \pm P_e P_\gamma A_l(\rho)\right). \tag{4.25}$$

We note that the detection threshold ρ_{min} in Equation 4.25 may be brought very close to zero, depending on the light yield of the photon detector and the implementation of the integration. This dramatically decreases sensitivity to the detector response.

If we measure S for both polarization configurations, we can form an asymmetry that gives us access to the electron beam polarization

$$A_{exp} = \frac{S^+ - S^-}{S^+ + S^-} = P_e P_\gamma \frac{\langle W A_l \rangle}{\langle W \rangle} \tag{4.26}$$

where the signal-weighted analyzing power is

$$\frac{\langle W A_l \rangle}{\langle W \rangle} = \frac{\int_{\rho_{min}}^1 d\rho W A_l(\rho) \epsilon(\rho) \frac{d\sigma}{d\rho}(\rho)}{\int_{\rho_{min}}^1 d\rho W \epsilon(\rho) \frac{d\sigma}{d\rho}(\rho)}. \tag{4.27}$$

We will treat the problem of imperfect energy resolution in Section 4.3.4.4.

For N_{tot} detected events – a quantity that is not necessarily measured in this method – the fractional error on the measured polarization may be estimated as

$$\left(\frac{\Delta P_e}{P_e}\right)^2 \simeq \frac{1}{N_{tot} P_e^2 P_\gamma^2 \frac{\langle E A_l \rangle^2}{E^2}}. \tag{4.28}$$

Historically, the Hall A Compton polarimeter has used the integrated counts method to measure P_e, but PREx's low production energy necessitated a change to energy-weighted signal integration [211]. E06-014, with its relatively high production energies of 4.74 and 5.90 GeV and its tolerance for polarimetry errors of several percent, made an excellent test case for this new measurement method.

4.3.2 Compton Apparatus in Hall A

The Compton polarimeter is located in the Hall A beamline, in the tunnel just upstream of the hall itself. First installed in 1999, its ability to provide continuous monitoring of the electron beam polarization has made it a vital asset to an extensive experimental program in the hall, but much of the original system proved inadequate for experiments requiring greater and greater precision in beam polarimetry. Driven by the needs of PREx, a wide-ranging Compton upgrade project was launched in 2005. E06-014 ran partway through this upgrade, and was the commissioning experiment for the upgraded photon detector, data acquisition system, and integrating analysis method.

Figure 4.8 shows a schematic of the Compton polarimeter layout, with the angles exaggerated for clarity. In this section, we will describe each of the polarimeter's hardware elements in turn, as they existed during E06-014.

4.3.2.1 Magnetic Chicane

In the approach tunnel to Hall A, operators may choose to direct the beam either through a straight vacuum pipe or through the 15.35-m Compton chicane (Figure 4.9), which consists of four identical magnetic dipoles with maximum fields of 1.5 T each. A distance of 4.4 m separates the first dipole from the second, and the third dipole from the fourth. At the center of the chicane, the diverted beam is parallel to its original path, with a downward displacement of 30 cm. It is in this central region, 2.3 m in length, that the photon cavity (Section 4.3.2.2) is placed and Compton scattering occurs.

An initial tune of the beam through the Compton chicane is an involved process that can take several hours, but periodic refinements of the tune – slight adjustments of the dipole magnet strength in order to optimize the vertical beam position at the Compton interaction point – are straightforward. Since the dipoles are wired in series, slight modifications to their fields affect the beam's

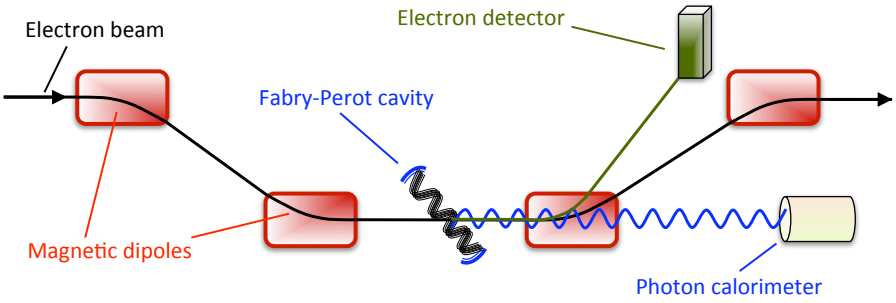

Figure 4.8: Side-view schematic of the Hall A Compton polarimeter apparatus; angles are exaggerated, and distances altered, for clarity. The primary electron beam, shown by a black line, enters the magnetic chicane from the left. Compton scattering occurs in the center of the chicane; scattered electrons and photons may be detected in appropriately placed detectors, while the unscattered beam continues toward the main experimental hall downstream.

position between the second and third dipoles without changing the beam position in the Hall itself; a 1 mm vertical displacement at the Compton interaction point corresponds to a displacement of less than 50 μm at the target [213].

The third dipole magnet, located just downstream of the Compton interaction point, plays an important additional role in the polarimeter. The kinematics of Compton scattering at Jefferson Lab lead to all three beams – unscattered electrons, scattered electrons, and scattered photons – being approximately collinear as they emerge from the interaction point (Figure 4.4). The third magnet separates these beams: scattered and unscattered electrons are bent through different angles, while the scattered photon trajectories are unchanged by its magnetic field.

4.3.2.2 Photon Source

In the Hall A Compton polarimeter, Compton scattering takes place in a Fabry-Perot cavity that is used to amplify the power of polarized laser light. When the wavelength of the source laser is locked to a resonance of the cavity, high gains can be achieved: the intensity of light circulating within the cavity could, in principle, be thousands of times higher than the intensity of the light at the cavity input. Our Fabry-Perot cavity (Figure 4.11) and its supporting optics system are located atop a vibration-damped optics table in the center of the Compton chicane. The laser beam couples to the cavity via the cavity's high-finesse mirrors; the electron beam enters and exits the cavity, which is held at a high vacuum, through a pair of vacuum windows. The crossing angle of the two beams is 23 mrad – just large enough to place the high-finesse mirrors five mm away from the electron beam, thus providing some protection from the beam halo – and the nominal Compton interaction point is at the exact center of the cavity [214]. Below, we discuss the particulars of this cavity and the optical elements that transport, monitor, and optimize the laser light.

During E06-014, the incident photons for Compton scattering were provided by an Innolight Nd:YAG laser with an infrared wavelength of $\lambda = 1064$ nm. The resonant Fabry-Perot cavity to which this 700-mW laser was locked achieved photon powers in the 400-500 W range during the experiment. This cavity, 0.85 m in length, consisted of two confocal mirrors separated by an integral number of half-wavelengths; when a laser of the right wavelength was coupled to this cavity, constructive interference allowed a resonance to build. The resonance was maintained despite vibrations and fluctuations via the Pound-Drever-Hall technique for frequency locking [215, 216]. In this method, two sidebands are introduced to the laser's frequency spectrum; differentiating the signal from these sidebands, reflected from the cavity, yields an error signal that reveals which

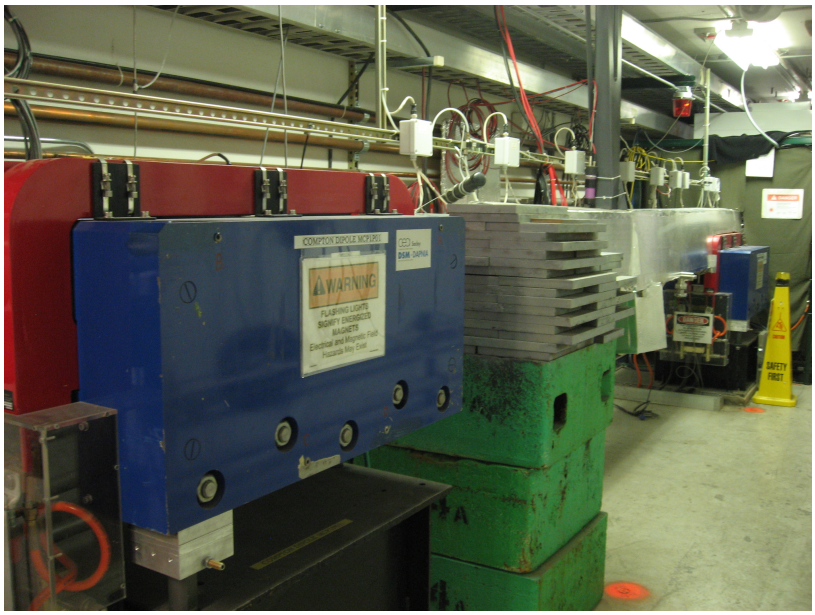

Figure 4.9: The upstream half of the Compton chicane in the Hall A tunnel, looking downstream. The blue return yoke and red coil of the first dipole are visible at left; at right is the second dipole and the laser table (behind an olive-green curtain).

way the central frequency should be adjusted for optimal efficiency. Typically, these fine frequency adjustments can be made by one of two methods: a slow feedback method whereby the temperature of the lasing medium is modified, and a fast feedback method involving a change of voltage to a piezoelectric medium attached to the crystal [217]. The fast feedback method was the primary locking tool for the Hall A Compton laser.

A Fabry-Perot cavity may be characterized by several parameters which depend primarily on the reflectivity R of the mirrors, their transmittivity T, and the distance L that separates them [218]. When the interior of the cavity is held in vacuum, the index of refraction is $n = 1$, and the transmission of the cavity peaks at certain frequencies $\nu_m = mc/2L$ (here, m is a positive integer and c is the speed of light). The *free spectral range* (FSR), which is the frequency separation between two consecutive peaks, is then

$$\Delta\nu_{FSR} = c/2L. \tag{4.29}$$

The frequency bandwidth admitted by the cavity is determined by the width of the transmission peaks relative to the free spectral range. These factors are in turn determined by the reflectivity of the mirrors, which are usually described in terms of their *finesse* $\mathcal{F}$

$$\mathcal{F} = \frac{\pi\sqrt{R}}{(1-R)}. \tag{4.30}$$

The finesse and the free spectral range determine the full-width-at-half-maximum, or passband, of the transmission peaks

$$\Delta\nu_{FWHM} = \frac{\Delta\nu_{FSR}}{\mathcal{F}}. \tag{4.31}$$

Higher-finesse mirrors allow tighter control over the photon frequency within the cavity, as well as higher cavity gain due to their high reflectivity – but they also make it more difficult to achieve a

Cavity parameter	Measured Value
Length L	0.85 ± 10^{-4} m
Free Spectral Range	176.47 ± 0.02 MHz
Decay time	23.5 ± 0.5 μs
Finesse	26040 ± 550
Passband	6.8 ± 0.14 kHz
Average intra-cavity power	1550 ± 35 W

Table 4.2: Nominal parameters of Compton Fabry-Perot cavity, as characterized in February 1999 [219].

stable lock.

The gain $\mathcal{G} = I_{circ}/I_{inc}$ is a function of the finesse, the laser frequency, and the free spectral range [217]

$$\mathcal{G}(\nu) = \frac{\mathcal{G}_0}{1 + (2\mathcal{F}/\pi)^2 \sin^2(\pi\nu/\Delta\nu_{FSR})} \tag{4.32}$$

where the maximum gain $\mathcal{G}_0$ is achieved at resonance, when ν is a multiple of $\Delta\nu_{FSR}$:

$$\mathcal{G}_0 = \frac{1}{(1-R)^2} \tag{4.33}$$

The Compton laser system is designed to periodically take the cavity into and out of resonance, making the decay time – the time needed for the cavity resonance to die down once the laser feeding it has been removed – an important parameter as well. In the limit of an instantaneous shut-off of the laser, the decay of the intra-cavity power as a function of time is described by an exponential curve whose characteristic time is given by

$$T_d \simeq \frac{\mathcal{F}\tau}{\pi} \tag{4.34}$$

where $\tau = L/c$ is the time necessary for an electromagnetic wave to traverse the cavity [219].

Detailed measurements of the cavity's parameters were performed in February 1999, when the cavity and its suite of optics were first installed in the Hall A beamline. Table 4.2 shows the results of these measurements. By the time that E06-014 ran, ten years later, the cavity's performance had naturally degraded, primarily as a result of time and accumulated radiation exposure; for example, the maximum intra-cavity power achieved during this experiment was only 450 W.

Figure 4.10 is a schematic of the optics supporting the Fabry-Perot cavity. The initial, 1064-nm laser beam is linearly polarized. The first element is a Faraday optical isolator, which protects the laser from light reflected back from later optical elements. Next is a half-wave plate (HWP), which rotates the laser output's intrinsic linear polarization to make it parallel to the optical table. Three lenses, marked L in the figure, shape the beam for optimal coupling to the cavity: the beam profile at the cavity entrance and exit must be smaller than the cavity mirrors, and placing the waist (the position of the laser beam's narrowest cross section) at the **C**ompton **i**nteraction **p**oint (CIP) ensures maximum luminosity. Fixed mirrors, marked M, steer the beam. After the first steering mirror is a polarizing beamsplitter cube; this allows light coming directly from the laser to pass, but diverts reflected light from the cavity into an integrating sphere and photodiode. This reflected signal is fed into the locking electronics for the Pound-Drever-Hall method.

After the polarizing beamsplitter is a quarter-wave plate (QWP), which converts the linearly polarized beam into a right- or left-circularly polarized beam. A SURUGA motorized stage allows us to switch between these two modes by remotely rotating the quarter-wave plate. The beam then

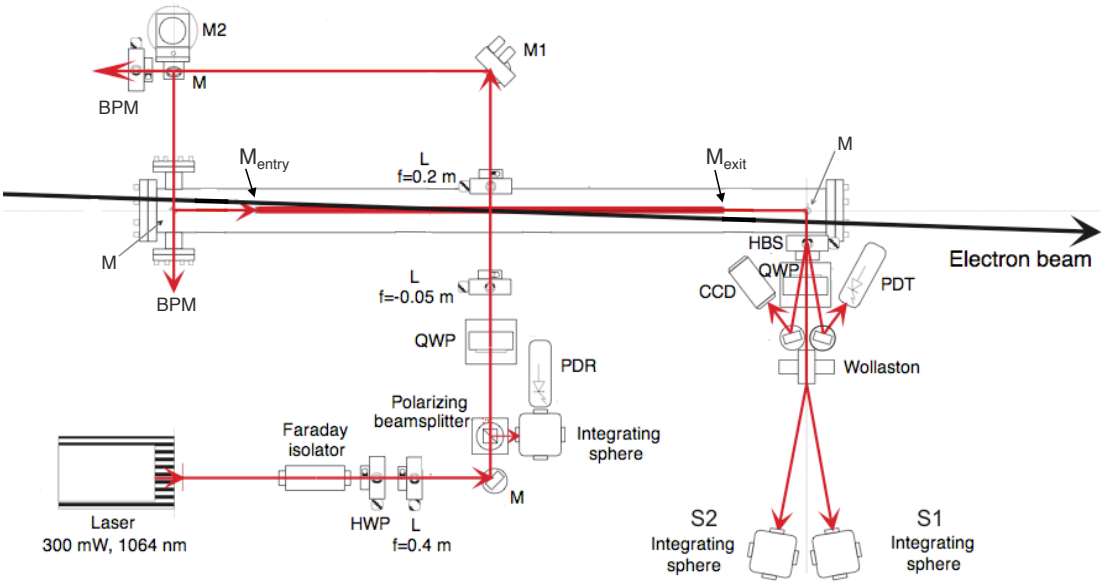

Figure 4.10: Layout of the Compton cavity laser table, adapted from Baylac [214]

passes underneath the cavity before striking the first of two steering mirrors on motorized mounts; periodically, as necessitated by the natural degradation of the optical circuit due to vibrations, one may remotely change their tilt angles in order to optimize the laser's coupling to the cavity. (In Figure 4.10, the motorized steering mirrors are denoted M1 and M2, as opposed to the fixed mirrors, which are not numbered.) The M/M2 mirror set in the upper-left corner of Figure 4.10 brings the beam up to the height of the cavity.

The remaining elements are diagnostic. At the cavity exit, a harmonic beamsplitter (HBS) is used to split off two very low-intensity ($\sim 1\%$ of the incident) beams from the primary transmitted beam; these low-intensity beams can then be monitored by a CCD camera and a photodiode. This transmission photodiode is the source of an intra-cavity power signal, which is both written to the EPICS datastream and fed into a discriminator to produce a binary logic signal reporting whether the cavity is in or out of resonance. We will discuss the use and drawbacks of these signals at some length in Section 4.3.4.1.

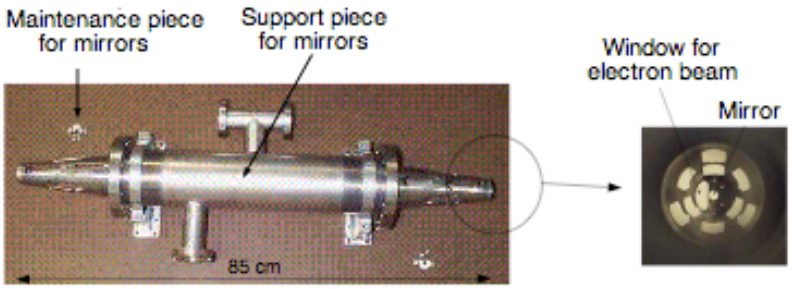

Figure 4.11: Side view of the Fabry-Perot cavity for the Compton polarimeter (left). At right is the cavity endcap, showing the openings for the photon and electron beams. Reproduced from Escoffier [213].

Meanwhile, the bulk of the beam continues through another quarter-wave plate, after which it is linearly polarized again; a Wollaston prism separates the two polarization components. Two integrating spheres each measure the power contained in one component; by combining these measurements with the known cavity optics, we can extrapolate the polarization P_γ of the photons at the Compton interaction point. We describe this process in detail in Section 4.3.2.3.

In order to control systematic errors, the cavity is not continuously left in a resonance state for long periods of time. Instead, it is periodically taken out of resonance and left in a state with essentially zero photon intensity at the Compton interaction point. These periods, during which negligible Compton scattering occurs, allow a direct measurement of background processes, whose effects may then be subtracted from the signal when the cavity is in resonance and Compton scattering is taking place.

During the time when the cavity is out of resonance, the quarter-wave plate is rotated on its motorized stage; when the cavity comes back into resonance, its photons therefore carry a circular polarization opposite to what they had had before. The two polarization states provide independent measurements of the beam polarization. Any systematic disagreement between the two provides an important diagnostic of helicity-dependent effects in the electron beam; for example, electrons of one helicity state or the other might be systematically mis-steered from the optimal Compton interaction point.

The entire cavity cycle, controlled by an EPICS script set into motion whenever a "Start Run" command is sent to the data acquisition system, lasts four minutes. It begins with the cavity in resonance for ninety seconds, with its light in the right-circularly polarized state. The cavity is then taken out of resonance and held empty for thirty seconds. Ninety seconds of resonance with left-circularly polarized light follow, and then another thirty seconds out of resonance. The cavity power is constant to the level of a few Watts (out of 400 to 450 Watts) when the cavity is in resonance; when the cavity is out of resonance, the measured intra-cavity power is a few milliWatts.

4.3.2.3 Measuring the Photon Polarization

The right-hand side of the optics diagram in Figure 4.10 shows the apparatus for measuring the degree to which the photons emerging from the cavity are circularly polarized. We may express this polarization P_γ as the ratio of two of the Stokes parameters defined in Equation 4.13

$$P_\gamma = \frac{s_3}{s_0}. \tag{4.35}$$

where s_0 gives the intensity of the electromagnetic wave and s_3 gives the intensity difference between those components of the wave that are left-circularly polarized and those that are right-circularly polarized.

The first element of the apparatus is a quarter-wave plate, which gives the circularly polarized photons a linear polarization, allowing the Wollaston prism to send each of the two components of this linearly polarized beam to a different integrating sphere. If the slow axis of the quarter-wave plate is at an angle β relative to the horizontal axis of the prism, then the intensity arriving at each sphere is given by

$$I_{S1} = \frac{1}{2}\left[s_0 + s_1\cos^2(2\beta) + s_2\cos(2\beta)\sin(2\beta) - s_3\sin(2\beta)\right] \tag{4.36}$$

$$I_{S2} = \frac{1}{2}\left[s_0 - s_1\cos^2(2\beta) - s_2\cos(2\beta)\sin(2\beta) + s_3\sin(2\beta)\right] \tag{4.37}$$

in terms of the Stokes parameters of the laser light incident on the quarter-wave plate [214]. By changing β, we can make a complete characterization of the polarization, but we are only interested in the degree of circular polarization and we therefore set $\beta = \pi/4$. The asymmetry between the measured intensities at each integrating sphere then gives us the polarization at the cavity exit

$$\frac{I_{S1} - I_{S2}}{I_{S1} + I_{S2}} = \frac{s_3}{s_0} = P_\gamma^{exit}. \tag{4.38}$$

The integrating spheres are not identical; α_{Sn}, the ratio of output signal I_n to input intensity I_{Sn}, is different for each one. At Saclay, where the system was initially tested and built, these calibration constants were measured at $\alpha_{S1} = 4.195 \pm 0.034$ μW/mW and $\alpha_{S2} = 3.735 \pm 0.034$ μW/mW [214]. Equation 4.38 thus becomes

$$P_\gamma^{exit} = \frac{\frac{I_1}{\alpha_{S1}} - \frac{I_2}{\alpha_{S2}}}{\frac{I_1}{\alpha_{S1}} + \frac{I_2}{\alpha_{S2}}} \tag{4.39}$$

where I_1 and I_2 are the power signals reported by the integrating spheres.

Equation 4.39 gives the photon polarization at the cavity exit, but we must know the photon polarization at the Compton interaction point, in the center of the cavity, in order to extract the electron beam polarization through Compton scattering. This value may be deduced from the measured value if the transfer function, which describes the evolution of the beam's circular polarization as it travels from the center of the cavity to the quarter-wave plate at the cavity exit, is known. The transfer function may be measured to subpercent precision by rotating the elliptical polarization of the beam at the cavity entrance and performing a polarization measurement at the cavity exit for each angle [214]. The EPICS programming for the Compton system incorporates the intensity readings from the integrating spheres, the spheres' calibration constants, and a previously measured (but undocumented) transfer function, continuously producing a photon polarization value for the Compton interaction point. This polarization value is read out approximately every 1.7 seconds, along with other data for the Compton system. We will discuss the drawbacks of this EPICS readout, as well as the ultimate determination of cavity polarization during the experiment, in Section 4.3.4.3.

4.3.2.4 Electron Detector

In principle, a Compton asymmetry may be measured using only Compton-scattered photons, only Compton-scattered electrons, or detections of both scattered particles in coincidence. Compton-scattered electrons are separated from the primary beam in passing through the third dipole of the chicane; due to their energy loss in the scattering process, they are bent through a larger angle than the unscattered electrons are. A moveable silicon microstrip detector, kept safely out of the main unscattered electron beam, can then detect electron tracks and reconstruct their energies.

The original Compton electron detector was destroyed after a close encounter with the main electron beam in 2006. An upgraded set of silicon microstrip planes was initially installed in the fall of 2008, but commissioning revealed major problems with the detector; unfortunately, it was not yet usable during E06-014 running. This experiment therefore relied solely on scattered photons for its Compton polarization measurements.

4.3.2.5 Photon Detector

To detect Compton-scattered photons, the original Compton polarimeter used a 5x5 array of $PbWO_4$ crystals as a calorimeter. Each crystal had a 2 cm x 2 cm entry face and extended 23 cm in length, with its own PMT for electronic readout. The crystal gains could be calibrated against each other using photons tagged by the electron detector [220]. Unfortunately, this procedure proved too labor-intensive to be performed routinely, and the typical experiment used only the central crystal to take Compton photon data. For a 100-MeV photon, this simplified configuration degraded the detector response function by a factor of about 2.8. (For Compton scattering with a 5.9-GeV electron beam, the maximum scattered-photon energy was 562 MeV; this dropped to 370 MeV for running with 4.74-GeV electrons.)

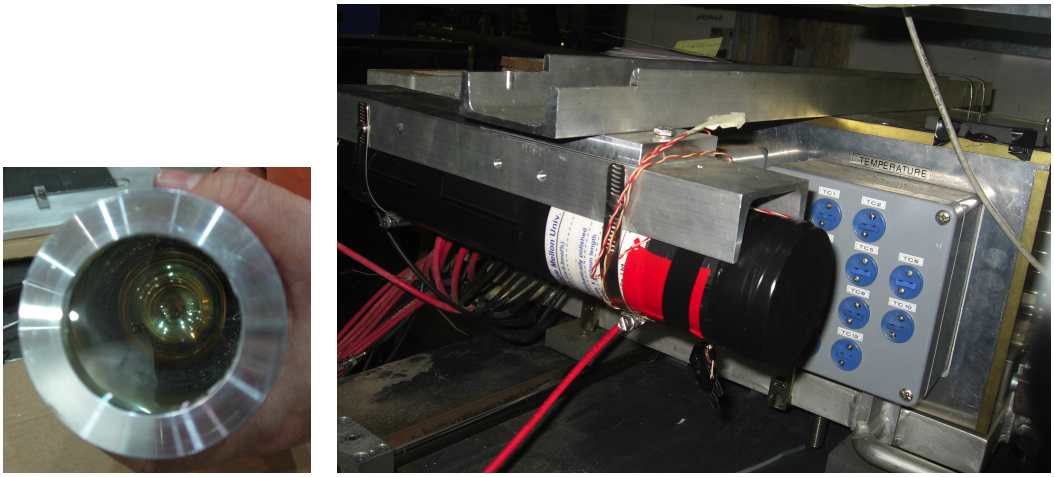

(a) (b)

Figure 4.12: The Compton GSO photon detector, (a) mounted to a PMT and (b) inside a steel-tube housing mounted in the scattered-photon beamline. The tube is suspended alongside the box containing the original photon detector array; the temperature-controller ports are visible on the side of the box. The upstream direction is to the right and the downstream direction to the left.

Before E06-014, as a replacement for this $PbWO_4$ system, we installed a single Gd_2SiO_5 (GSO) crystal (Figure 4.12(a)), grown by Hitachi Chemical and doped with cerium for improved radiation hardness. So as to catch most of the shower, the cylindrical crystal has a diameter of 6 cm and a length of 15 cm. Signal readout is performed with a 12-stage Amperex xp2230 PMT with a custom-built base to maximize linearity. In order to preserve our ability to switch to the original photon calorimeter if the need arose, we mounted our GSO detector alongside the box containing the array of lead tungstate crystals (Figure 4.12(b)). The detector box could slide on rails, installed atop a table with motorized horizontal and vertical motion; in a brief access to the hall, we could slide the box so as to center either photon detector on the beam of Compton-scattered photons, and then clamp it into place. In the event, however, no such changes were necessary: the new GSO detector was used throughout E06-014.

We will discuss the determination of the photon detector system's response function and its non-linearity in Section 4.3.4.4.

4.3.3 Data Acquisition

In its original installation, the Compton polarimeter used a counting data acquisition system. Raw data from a small, prescaled percentage of waveforms were retained from each helicity window. The remainder of the data were subjected to an online analysis by one of two CPU cards in the data acquisition VME crate; only this analyzed summary was written to disk. This strategy to reduce the amount of disk space required to store the Compton data was made possible by equipping the VME crate with a dual CPU: as one CPU handled the acquisition of data from a helicity window, the other worked on the online analysis of data from the previous helicity window. Each CPU card handed off control of the crate at the end of its helicity window. [221]

During E06-014, we commissioned a second data acquisition system, based on a modified 12-bit FADC from Struck DE, running with a sampling rate of 200 MHz. The timing of the readout commands is based on a HAPPEX Timing Board [222] that provides start-acquisition, stop-acquisition, and readout commands based on the master pulse signal (MPS), which marks a brief period of

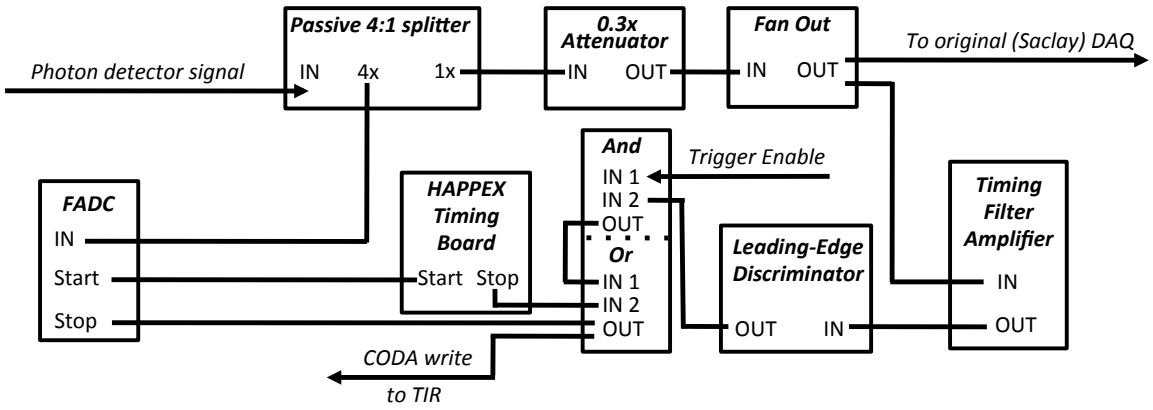

Figure 4.13: A wiring diagram for the newly commissioned integrating data acquisition system for Compton photon data. In integrating mode, the *Trigger Enable* bit is low and data are read out at a *STOP* signal from the HAPPEX timing board. In triggered mode, the *Trigger Enable* bit is high and data are also read out just after a photon pulse has been detected. The original data acquisition system runs in parallel to this one.

indeterminate beam helicity between helicity windows. Integrating data acquisition was set to begin 500 μs after the onset of the low logic level on the MPS line, $\overline{\text{MPS}}$, and continue until the end of the $\overline{\text{MPS}}$, at which time it would be written to disk.

This system was designed to run in parallel with the original counting DAQ, so that the original measurement method could be preserved. Two primary running modes were available during E06-014: triggered mode and integrating mode. Switching between these configurations could be accomplished between runs by downloading the appropriate library to the VME crate containing the FADC. An output bit on the **T**rigger **I**nterface **R**egister (TIR), set by an instruction in this library, gives a high logic level if the system is in triggered mode, and a low-logic level if it is in integrating mode; this logic level enables or disables the trigger logic. Figure 4.13 shows a wiring diagram for the system, which spans one VME crate and one NIM crate.

4.3.3.1 Triggered Mode

In order to troubleshoot our wiring and measure Compton spectra for comparison with Monte Carlo simulations, we implemented a DAQ configuration in which the detection of a photon pulse triggers a readout of the waveform for that pulse. The FADC stores 512 signal samples (taken at 5-ns intervals) in a circular buffer. In triggered mode, when the *Trigger Enable* output bit on the TIR bit is high, a photon detector signal beyond a threshold of -50 mV generates a CODA trigger via the logic shown in Figure 4.13. (Since the PMT has a negative high voltage, a larger signal is more negative than a smaller one.) A readout command is also generated at the transition from one MPS to another via the HAPPEX Timing Board. Two hundred one sample values, defining the waveform of the pulse, are then written to disk. Figure 4.14 shows a typical waveform for a photon pulse with an energy in the Compton region. Such data allow us to measure the pedestal (baseline level) of the FADC, confirm that the trigger timing is correct and that there are no distortions in the pulse shape (which could, for example, arise from reflections in the cable), and measure the distribution of detected photon energies – the Compton spectrum.

This system was designed to generate a trigger on detecting a photon pulse in the signal from the GSO, but the same signal may also be sent to a scaler, which can thereby count the number of photon pulses detected whether the system is in triggered mode or not. One might use this scaler readout to compute a raw counting asymmetry in Compton scattering, which can lead to the

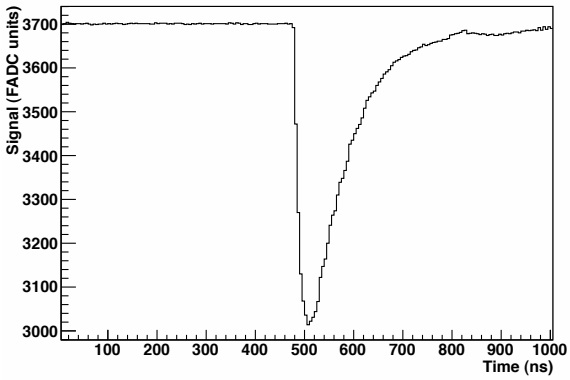

Figure 4.14: A typical Compton pulse from the GSO detector, measured in triggered mode of the new DAQ. The energy carried by this pulse is near the maximum energy that a Compton-scattered photon can carry.

beam polarization; rates were low during E06-014, however, and we did not implement this method. However, as we will see in Section 4.3.4.1, the photon rates proved critically important in limiting our systematic errors.

The chief drawback of this configuration is its deadtime. Between 201 samples per waveform, at 12 bits per sample, and auxiliary data (e.g. accumulator readouts corresponding to the last interval, scaler readouts for beam current and photon rate, or input bits recording the polarization directions of the electron beam and Compton laser), the system was able to take data at only about 1 kHz – less than a third of the actual photon rate when the cavity was in resonance and the beam current was at its production set point of 15 μA. After the completion of E06-014, a refinement of the DAQ configuration alleviated this problem for subsequent experiments.

4.3.3.2 Integrating Mode

Our data acquisition system is designed with the primary goal of accommodating the energy-weighted integrating method of Compton polarimetry, as described in Section 4.3.1.4. This integral is performed automatically by the FADC, so that a minimal amount of information must be written to disk; the manufacturer added this functionality to the FADC's firmware, according to our specifications [223].

A photon detected in the GSO crystal produces an analog pulse much like the one shown in Figure 4.14; the signal registers in the FADC as a number below the baseline level, or pedestal. The area between this waveform and the pedestal is, ideally, proportional to the energy the photon has deposited in the crystal. If we know the pedestal value of our data, we can compute our energy-weighted integral simply by summing the sampled signal in a hardware accumulator; six different accumulators, each performing a slightly different integral, are available to us.

It is helpful to define our terms so as to convert a negative voltage level into a positive integrand. Over an integration period – a single 33-ms helicity window – let $\bar{S}$ represent the (positive) magnitude of the average signal per 5-ns time bin from detected photons, while $\bar{P}$ denotes the average pedestal value; the energy deposited in the crystal during this integration period is proportional to $\left(\bar{P} - \bar{S}\right) t$. At the end of the helicity window, the value Acc_n in the nth accumulator is given by

$$\mathrm{Acc}_n = N_n \left(\bar{P} - \bar{S}\right) \tag{4.40}$$

where N_n, which is written to disk along with the accumulator value Acc_n, is the number of 5-ns samples that have contributed to the final accumulator value. A simple manipulation of Equa-

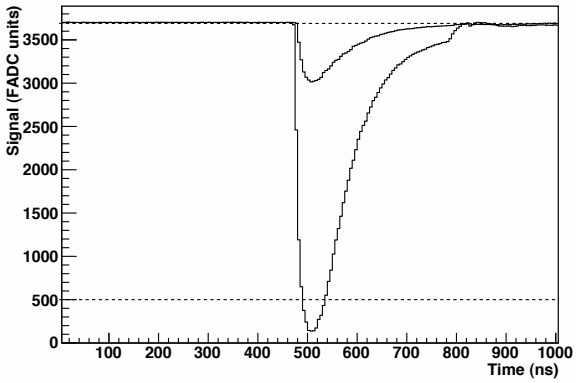

Figure 4.15: Thresholds T_{near} and T_{far} (dashed lines) for the Compton integrating DAQ. The window region lies between the two thresholds. The smaller pulse shown has approximately the maximum energy expected from a Compton photon; the larger pulse belongs to a rare high-energy background event.

tion 4.40 then gives us an expression for the total integrated, energy-weighted signal S_n over the helicity window

$$S_n = N_n \bar{S} = N_n \bar{P} - \mathrm{Acc}_n. \tag{4.41}$$

The six available accumulators are distinguished by their use of several programmable parameters. We introduce two programmable thresholds, one near the pedestal (T_{near}) and one far from the pedestal (T_{far}), shown with a plot of two sample photon pulses in Figure 4.15. The first threshold allows us to integrate over a region including only pedestal noise – or to exclude that region from an integral. The second threshold allows the exclusion of large background pulses from the integral. We may also make use of our ability to store samples in the FADC memory in order to include an entire pulse in the accumulator sum. In this system, when the signal crosses a threshold to enter the range of an accumulator, the N^{before} preceding samples can also be added into the accumulator; the same can be done with the N^{after} samples following a threshold crossing out of the accumulator's range. Six accumulators rely on varying combinations of these programmable parameters:

0. *All:*: Accumulates all signal over the entire input range of the FADC.

1. *Near:* Accumulates signal smaller than T_{near}, which corresponds to signal between the near threshold and the high (pedestal) end of the input range (4095 raw a.d.c. units). This is used to examine pedestal noise.

2. *Window:* Accumulates signal between T_{near} and T_{far}. Ideally, this should be set to include nearly the entire range of Compton-scattered photons (with the possible exception of photons with very low energies).

3. *Far:* Accumulates signal between T_{far} and the low (saturation) end of the input range (0 raw a.d.c. units). This is used to examine high-energy background pulses.

4. *Stretched Window:* Accumulates signal between T_{near} and T_{far}, plus the N_4^{before} samples before the signal crosses T_{near} as it enters the window, plus the N_4^{after} samples after the signal crosses T_{near} as it leaves the window. This accumulator excludes any samples that contribute to the Stretched Far accumulator.

5. *Stretched Far:* Accumulates signal between T_{far} and the low (saturation) end of the input range (0 raw a.d.c. units), plus the N_5^{before} samples before the signal crosses T_{far} as it enters the accumulator range, plus the N_5^{after} samples after the signal crosses T_{far} as it leaves the accumulator range.

In typical running, three accumulators – All, Window, and Stretched Window – access the energy range of Compton-scattered photons and can be used to extract a Compton asymmetry; we will discuss the analysis of these accumulator signals in Section 4.3.6. Table 4.3 shows the programmed values of the accumulation parameters during E06-014.

Accumulator	**Small-signal threshold**	**Large-signal threshold**	N^{before}	N^{after}
All	4095	0	0	0
Near	4095	3690	0	0
Window	3690	500	0	0
Far	500	0	0	0
Stretched Window (exclusive of Stretched Far)	3690	500	10	100
Stretched Far	500	0	10	110

Table 4.3: Values of programmable FADC settings in the Compton DAQ during E06-014 for each of the six accumulators. Thresholds are given in raw ADC units (r.a.u.); as a 12-channel FADC, the input range runs from 4095 to 0 r.a.u. N^{before} and N^{after} are given as numbers of samples, which are taken every 5 ns.

4.3.4 Calibrations

Once the upgraded components of the Compton polarimeter were installed in the Hall, a Compton spectrum and a rough spin asymmetry were quickly measured. However, the full commissioning of the device required the testing and calibration of a variety of factors, from the behavior of the Compton laser cavity to the response and alignment of the photon detector. In this section, we report on the calibrations that were performed before extracting a final asymmetry and an electron beam polarization.

4.3.4.1 Cavity State Identification

In order to measure an accurate asymmetry, there must be a clear distinction in the datastream between intervals when the cavity is in resonance (in which case the photon detector sees both Compton-scattered photons and photons from background processes) and intervals when the cavity is out of resonance (in which case we measure only the products of background reactions). Since the out-of-resonance measurements are used for background subtraction, any confusion between these states will result in a diluted Compton asymmetry. (If a cavity-on interval is misidentified as cavity-off, an asymmetric signal will be subtracted as background; if a cavity-off interval is misidentified as cavity-on, the asymmetry measurement will include an interval without any Compton scattering events.) When the cavity is in resonance, intervals with left-circular and right-circular photon polarization must also be distinguished: since the asymmetries computed for the two polarization states have opposite signs, contamination from the wrong polarization state will partially cancel the Compton asymmetry.

During E06-014, two types of signals in the DAQ directly reported the cavity state. Two binary logic signals in the Trigger Interface Register, read out synchronously with the data from each interval, indicated the cavity's resonance and polarization states. Each of these signals had a counterpart

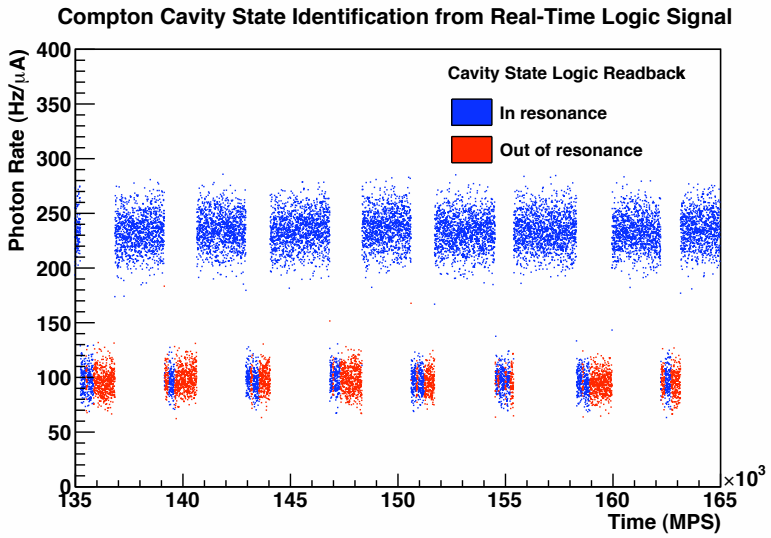

Figure 4.16: Current-normalized rates in the Compton photon detector as a function of time, over 10 minutes of running. The square-wave pattern in the photon rates reflects the characteristic pattern of the cavity power. However, the logic signal encoding the resonance state of the cavity (shown in the color coding) evidently does not report the true state of the cavity.

in the EPICS datastream (Section 3.3.7.2), entered asynchronously in the Compton data files as special events roughly every 1.7 seconds. Ideally, the real-time logic signals could be used to make the cavity state determination, with the EPICS signals providing confirmation.

This strategy worked quite well for distinguishing between the two polarization states, but proved unworkable for telling one resonance state from the other. After ten years and an unknown number of recablings, the real-time logic signal for the cavity power (derived from the output of the transmission photodiode in Figure 4.10) had become unreliable. Figure 4.16 shows the photon rates as a function of time for ten minutes of running. When the cavity is in resonance, we expect the photon rates to be higher, since Compton events contribute in addition to the background; indeed, the photon rates clearly display the square-wave pattern of the cavity power cycle. However, the cavity-state identification from the real-time logic signal tells a different story. Each dot in Figure 4.16 is colored according to the real-time report of the cavity resonance state during that MPS. These reports clearly are not good matches to the actual cavity state, as reflected in the photon rates: when the cavity is out of resonance, the real-time logic signal frequently and erroneously reports that it is in resonance. Figure 4.17 shows the distribution of photon rates for each cavity state, as assigned by this logic signal; the double-peaking of the in-resonance distribution shows that nearly 15% of the signal contributing to the Compton asymmetry is actually contamination from the background.

Unfortunately, the EPICS cavity power signal is a poor substitute for a trustworthy real-time signal, due to its asynchronous nature and relatively infrequent updates. A real-time analog cavity-power signal was available through the original Compton DAQ from Saclay, fed through a voltage-to-frequency converter and into a scaler; unfortunately, since the problems with the digital logic signal were not discovered until after E06-014 had completed its run, this more trustworthy real-time signal was not present in the integrating Compton DAQ during the experiment. (It was, however, incorporated into the DAQ in time for the 2009-2010 Hall A parity program, beginning with the HAPPEX-III experiment [224] in the fall of 2009.) In order to optimize the Compton data for E06-014, a new way of retroactively making cavity state determinations was necessary.

The photon rates, which yield such a clean separation between the resonance states of the cavity,

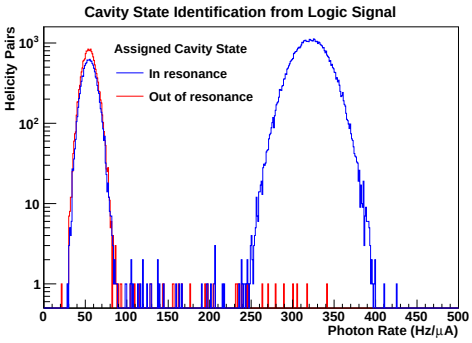

Figure 4.17: Assignment of Compton cavity resonance states from logic readback. The large background contamination in pairs labeled as in-resonance is due to a faulty logic signal.

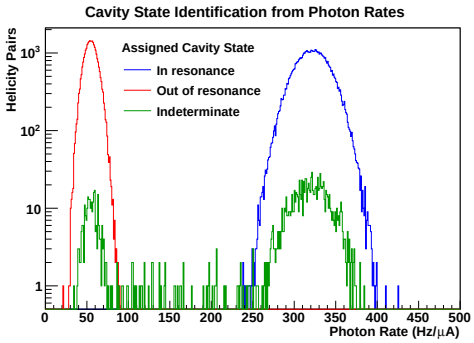

Figure 4.18: Assignment of Compton cavity resonance states from the photon rates of neighboring helicity pairs. Pairs with an indeterminate assignment – arising from a discrepancy between neighboring pairs or from a neighboring pair outside the allowed range for either distribution – are discarded from the final analysis.

provided just such a method. Using the asynchronous EPICS signal and faulty real-time signal to pre-sort the photon-rate data into approximate cavity-state classifications, we could fit a Gaussian distribution to each peak in the photon rates. In the next stage of sorting, we assigned a preliminary resonance state to each helicity pair based on where its average photon rate fell in relation to these peaks: it was assigned to a cavity state if its rate was within 2.5σ of the mean rate for that state. The final cavity-state assignment for each pair was made by considering the classifications of its neighbors: a helicity pair was assigned to a particular resonance state if *both* the preceding *and* the following pairs had rates within the allowed range for that state. If its neighbors did not meet this condition, the helicity pair would be flagged as having an "indeterminate" resonance state and would be excluded from the final analysis. Figure 4.18 shows the photon rate distribution for each cavity state, as assigned by this method; the photon rates of a helicity pair's neighbors are clearly a good proxy for its own photon rate, while allowing us to avoid cutting on the signal we seek to measure.

This method of cavity state identification prevents our asymmetry from being diluted by the inclusion of background signal; the price of this purification is a reduction in statistics by up to 10%, which is reflected in the statistical errors on the final measurements. If an abnormally low photon rate is measured while the cavity is in resonance, or if an abnormally high rate is measured while the cavity is out of resonance, our sorting algorithm may introduce contamination of its own, erroneously classifying an out-of-resonance pair as in resonance or vice versa. We tested the prevalence of this problem by applying our algorithm to Compton data taken during HAPPEX-III, some six months later; in this data set, we were able to compare the cavity states assigned by our algorithm to the actual cavity state reported by a reliable analog cavity power signal. We found that, while our algorithm did discard a significant percentage of events, it made the more serious mis-assignment error in only 0.006% of cases, making this a negligible source of systematic error.

4.3.4.2 False Asymmetries

Helicity-dependent changes in intensity can give rise to so-called *false asymmetries* – that is, to asymmetries not due to the electron polarization. The beam-charge asymmetry is a direct measurement of this effect. During E06-014, a charge asymmetry feedback system [225], which was developed and

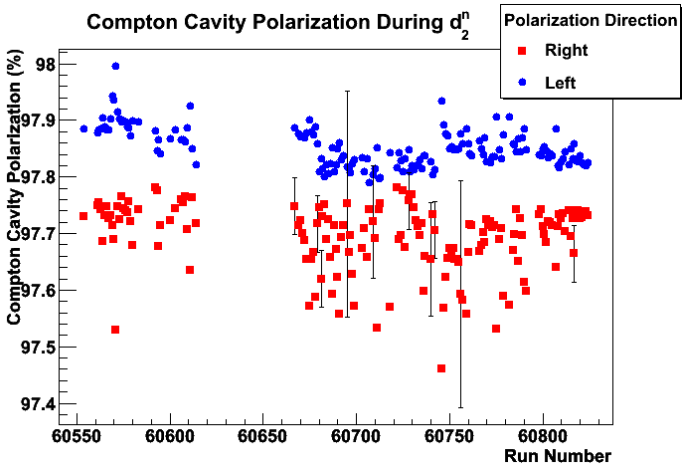

Figure 4.19: Time evolution of Compton photon polarization from EPICS readout. Though the EPICS readout is not reliable in an absolute sense, it suffices to show the stability of P_γ over the course of the experiment.

implemented by the HAPPEX collaboration [222], limited this beam charge asymmetry to within 100 ppm.

4.3.4.3 Photon Polarization

The photon polarization P_γ, computed from power meter measurements and knowledge of the optics system's transfer function (Section 4.3.2.3), is read out from the EPICS data stream every 1.7 seconds. This measurement is unreliable at low transmission powers (*i.e.* when the cavity is out of resonance), but P_γ is not needed in background calculations, so out-of-resonance measurements may be discarded. Transport through any of the optical elements on the Compton table may be affected by the beam's polarization direction, so the left- and right-circularly polarized states must be treated separately.

Figure 4.19 shows the average P_γ EPICS readings for each run over the course of E06-014. While these readings demonstrate the stability of the photon polarization on the level of 0.2%, they rely on an undocumented transfer function that may be up to a decade old. Changes to the transfer function and calibration – caused, for example, by degradation of the cavity mirrors, gain shifts in the power meters, and changes in alignment – are inevitable over such a long period of active running, rendering the EPICS polarization readouts untrustworthy as absolute measurements.

To solve this problem, we turned to the HAPPEX-III experiment [224], which ran in Hall A six months after the conclusion of E06-014. One of the largest sources of systematic error for this experiment was electron beam polarimetry, so the Compton polarimeter received special attention during its run. In order to increase the photon power in the cavity and thus the Compton statistics, the infrared laser was replaced before HAPPEX-III began, but both the cavity and the optics at its entrance and exit were unchanged. Because of the polarizing beamsplitter between the laser and the cavity entrance (Figure 4.10), the laser affects only the power of the light inside the cavity, not its polarization; in the limit of the same alignment, then, P_γ should be the same for both experiments. This, in turn, would allow E06-014 to take advantage of Kent Paschke's careful optics-table measurements of P_γ after HAPPEX-III.

We used data files produced by the original, Saclay-designed counting DAQ to compare polarization values for the two experiments. First, we studied the relative gains of the two integrating spheres by measuring the ratio of their maximum power readouts; this was constant to within 2%

Polarization Direction	P_γ
Right Circular	$0.9884^{+0.0116}_{-0.0212}$
Left Circular	$0.9879^{+0.0121}_{-0.0212}$

Table 4.4: Compton photon polarization P_γ during E06-014.

between E06-014 and HAPPEX-III. Next, using Equation 4.39, we computed the exit polarization for both experiments. We found that the exit polarization during E06-014 was consistently about 0.2% lower than during HAPPEX-III; the relative values of the EPICS polarization readouts, using an outdated transfer function, showed the same polarization shift. A discrepancy at this level may be explained by a small change in the alignment of the laser spot: the transfer function is sensitive to the spot's position on the confocal cavity mirrors.

To determine the value of P_γ during E06-014, we therefore reduced the measured HAPPEX-III polarization values [226] by 0.2%. Table 4.4 shows the results. The error of 2.15% represents the 2% uncertainty in the integrating-sphere gain ratios between the two experiments, combined with an 0.8% uncertainty on the original HAPPEX-III measurement of P_γ.

4.3.4.4 Photon Detector Response Function

The signal-weighted analyzing power $\langle WA_l\rangle/\langle W\rangle$ gives the Compton scattering asymmetry that we would measure with our particular apparatus if both the electron and photon beams were perfectly polarized. A determination of the analyzing power is necessary to use the experimentally measured asymmetry to extract the longitudinal polarization P_e of the electron beam.

Our determination of A_l relies on a simulation of a beam of Compton-backscattered photons and the response of our apparatus to them. (The simulation algorithm will be described in detail in Section 4.3.5). To perform the simulation, we used code written in Geant4 [227, 228], a C++-based platform for Monte Carlo simulations of particles passing through, and interacting with, matter. A program incorporating the characteristics of the incident photons, the geometry of the detector and the chemical composition of GSO modeled the energy deposited in the detector, which is, at least to first order, proportional to the measured integral of the electrical signal. (We used Poisson statistics to model the actual number of photoelectrons produced in the PMT photocathode based on the energy deposited in the crystal, and thus to convert from energy deposited to signal output.) Figure 4.20(a) shows the result of a simple simulation of a small number of incident photons.

To confirm that our simulated photon detector responded to incident photons in the same way as the actual GSO crystal, we brought the crystal to a high-energy gamma source for two days of tests. The **H**igh-**I**ntensity γ **S**ource (HIγS) [229] is a facility jointly operated by the **D**uke **F**ree **E**lectron **L**aser **L**aboratory (DFELL) and the **T**riangle **U**niversities **N**uclear **L**aboratory (TUNL) on the Duke University campus. At HIγS, electrons are first accelerated to 0.18-0.28 GeV in a linear accelerator; a booster synchrotron brings them up to a maximum energy of 1.2 GeV before injecting them into a storage ring, where they pass through wigglers to generate free-electron laser light, which is confined between two mirrors. The HIγS mechanism uses a symmetric two-bunch operating mode, wherein each bunch is separated from the other by half the storage ring's circumference, to generate high-energy, high-intensity light by Compton backscattering: FEL photons generated by the first bunch collide with electrons from the second bunch. The resulting photons are delivered to the experimental hall, some 60 meters downstream, as a nearly monochromatic photon beam whose energy and flux are tunable.

Along with a team from the Hall C Compton polarimetry group, we visited HIγS in October of 2008 to characterize the response of our GSO photon detector, two months before it was installed in Hall A. We measured energy spectra in the crystal for incident photon energies of 20, 22, 25, 30 and

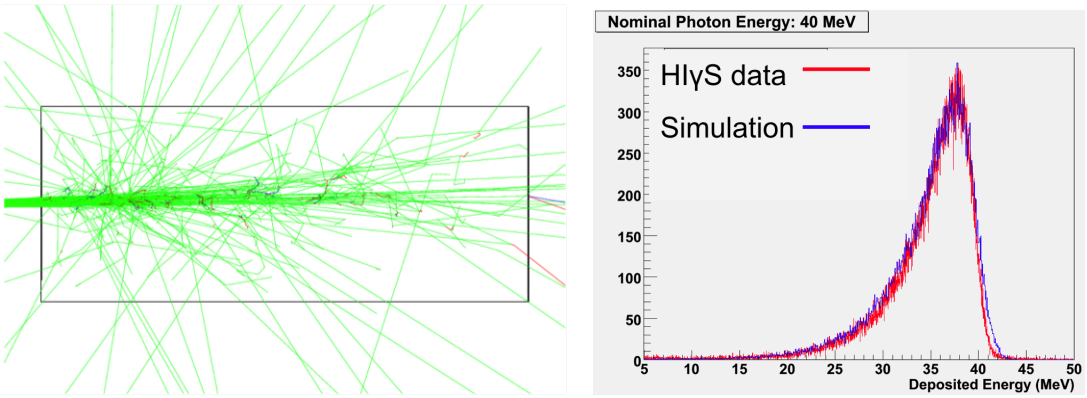

(a) (b)

Figure 4.20: Geant4 simulations of GSO detector response. (a) Simulated particle trajectories in GSO crystal, resulting from incident photons in the 1-20 MeV range. Green trajectories signify electrically neutral particles, while blue trajectories belong to positively charged particles and red trajectories to negatively charged particles. (b) Simulation of GSO detector response to 40-MeV incident photons, compared to real data taken at HIγS.

40 MeV and compared these spectra to the results of our Geant4 simulations. Figure 4.20(b) shows the measured spectrum at 40 MeV, compared to a simulation with an incident photon beam whose energy distribution is Gaussian, with a mean of 40 MeV and a standard deviation of 3% (based on the full width at half maximum of the beam profile calculated by HIγS staff). The simulated spectrum is slightly wider than the measured one, which can be attributed to the fact that the actual incident energy spectrum is more complicated than a simple Gaussian [230]. For the test's intended purpose – a proof-of-principle that our Geant4 model was a good approximation of the photon detector – the agreement shown in Figure 4.20(b) was sufficient. As we will see, further simulation tests in Hall A produced still better agreement.

Once the GSO crystal, its photomultiplier tube and base, and the supporting data acquisition system were installed in the Hall, we made a careful measurement of the response function of the entire apparatus. It is an idealization to state that the integrated signal is directly proportional to the energy deposited in the crystal; a real apparatus will not have a perfectly linear response, and these deviations from linearity are typically greatest at high energies. It is this region that contributes the most to the integral of our signal and thus to our measured asymmetry, so understanding the nonlinearity of our system was of crucial importance.

To measure the response function, Megan Friend designed and built a system of two pulsing **L**ight-**E**mitting **D**iodes (LEDs). One LED flashes with a fixed, small brightness; the other LED produces flashes of variable brightness. A control box, popularly known as a "mini-Megan", flashes the LEDs in a set pattern: first the fixed, or *delta*, LED with brightness δ, then the *variable* LED with brightness x, then the two LEDs together with brightness $x + \delta$. The sequence then repeats at a new variable-LED brightness value. With the two LEDs affixed to the front of the GSO crystal, we can thus measure the response of the photon detector and PMT to two pulses with closely separated energy, x and $x + \delta$, as a function of x.

Figure 4.21(a) shows the result of this measurement. The horizontal axis shows the brightness x of the variable LED as measured by our system in FADC units, scaled by a factor of $b = 36688.3$ in order to improve software performance. The vertical axis shows the measured finite difference $y_{S(x)}$, scaled by the same factor. Where $S(x)$ is the signal resulting from an incident brightness x, the finite difference is given by

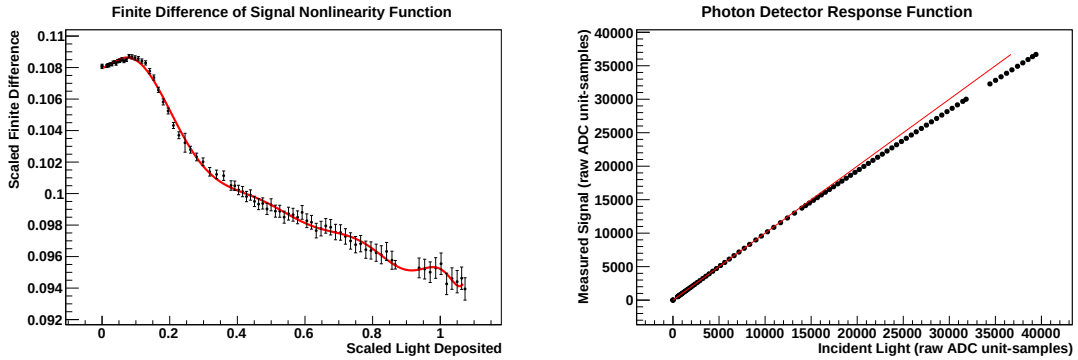

(a) (b)

Figure 4.21: Nonlinearity of photon detection system, measured in April 2009. (a) Measured finite difference (Equation 4.42) as a function of incident brightness. The finite difference function of a sixteenth-degree polynomial has been fit to the data. (b) Photon detector response as a function of incident light energy from the mini-Megan LEDs. A line is drawn to show the deviation from linearity at high incident brightness. Plots are from M. Friend [231].

$$y_{S(x)} = \frac{S(x+\delta) - S(x)}{b}. \tag{4.42}$$

The data in Figure 4.21(a) were then fit to the finite difference function $y_{f(x)}$ of a sixteenth-degree polynomial $f(x)$

$$y_{f(x)} = f(x+\delta) - f(x) \tag{4.43}$$

where

$$f(x) = a_0 + a_1 x + a_2 x^2 + a_3 x^3 \cdots + a_{15} x^{15} + a_{16} x^{16}. \tag{4.44}$$

The fit, shown as the red line in Figure 4.21(a), set the coefficients a_n of the nonlinearity function $f(x)$; these coefficients, as calculated by Megan Friend, are reported in Table 4.5. Figure 4.21(b) plots the measured signal as a function of the incident light as determined from $f(x)$.

The inclusion of the system's nonlinearity improved our Geant4 simulations of Compton spectra measured during the experiment. Figure 4.22 shows the Compton spectrum for each of the two production energies, plotted as a function of the integrated signal in units of **r**aw **A**DC **u**nits-**s**amples, which are ideally proportional to MeV. Two simulations were fit to the data with a single parameter: a simulation incorporating the nonlinearity (red) and a simulation assuming a perfectly linear system (blue). Including the nonlinearity clearly produces a more accurate simulation.

4.3.4.5 Alignment

On their way to the photon detector, backscattered photons pass through a 6-m beam pipe and a lead collimator whose aperture is only 1 cm in diameter. The beam pipe is suspended from the ceiling; the lead collimator is welded to supports that are bolted to the floor; a persistent groundwater leak has changed the topography of the tunnel in the years since the system's installation. Given these facts, the relative alignment of the scattered photon beam, the collimator aperture, and the photon detector cannot be assumed.

We saw in Equation 4.3 that, when initial conditions are held constant, the scattered photon energy k' has a one-to-one relationship with the photon's scattering angle θ_γ: the larger the scattering

Coefficient	Value
a_0	0
a_1	1
a_2	-0.240032
a_3	3.7366
a_4	-18.9917
a_5	34.1222
a_6	4.10522
a_7	-88.0712
a_8	82.3791
a_9	26.4962
a_{10}	-46.936
a_{11}	-29.1891
a_{12}	31.8129
a_{13}	11.2298
a_{14}	-4.71173
a_{15}	-10.4581
a_{16}	4.6505

Table 4.5: Coefficients of the nonlinearity function $f(x)$, a sixteenth-degree polynomial of the form $a_0 + a_1x + a_2x^2 + \cdots + a_{16}x^{16}$, as determined by M. Friend [231].

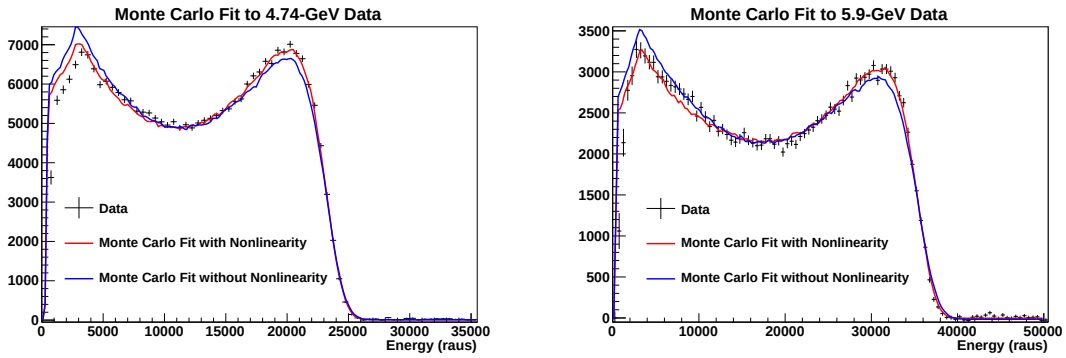

(a) (b)

Figure 4.22: Monte Carlo fits to Compton spectrum with and without nonlinearity function, for 4.74-GeV (a) and 5.90-GeV (b) electrons. Plots are from M. Friend [231].

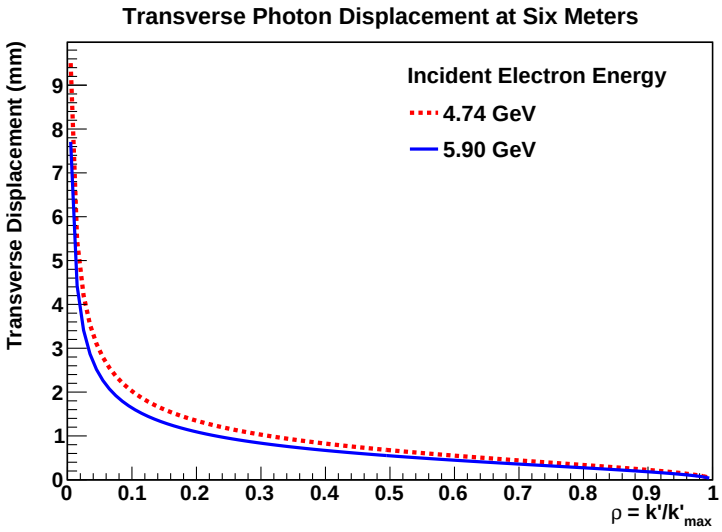

Figure 4.23: Transverse displacement of Compton-scattered photons for both production E06-014 electron energies, at the approximate location of the collimator (six meters from the Compton interaction point).

angle, the lower the photon energy. At the collimator location six meters from the interaction point, even photons with small scattering angles are significantly displaced from their central axis, as shown in Figure 4.23. A slightly misaligned collimator aperture, then, may be expected to exclude disproportionately more photons from the low-energy end of the Compton spectrum: the cone of Compton-scattered light projects a circle onto the collimator plane, and less of the circumference falls within its acceptance the lower k' becomes.

Our integrating method of measurement limits our sensitivity to alignment problems, since the affected parts of the spectrum are low energy and thus carry low weight in the integral, but, if uncorrected, this is still a potential source of systematic error. To study this effect, we took a few hours of triggered-mode data at each beam energy and compared the resulting Compton spectra to the results of Geant4 simulations with varying degrees of misalignment. Figure 4.24 shows the measured Compton spectrum, plotted in crosses, as well as fits of the Monte Carlo simulations with aperture offsets ranging from two to four mm. (Due to the radial symmetry of the backscattered photon beam, we could model offsets in a single, arbitrary direction.)

At the high-energy end of the Compton spectrum, we see that the five simulated spectra are equivalent to each other, and fit the data equally well, as we would expect given the small scattering angle of these photons. At the low-energy end of the spectrum, the models diverge, and we can distinguish among them with the measured spectra. The 5.9-GeV data (Figure 4.24(b)) show almost perfect agreement with the model assuming a 3.3-mm offset of the collimator aperture; in the 4.7-GeV data (Figure 4.24(a)), the offset appears to fall between 3.3 mm and 3.7 mm. The slight disagreement between the two data sets is not cause for concern; we will see in Section 4.3.5 that displacements on the order of 0.1 mm have a negligible effect on the analyzing power.

During the experiment, the photon detector was aligned to the center of the collimator. Given the GSO crystal's six-centimeter diameter, the effects of millimeter-level misalignment of the photon detector itself are negligible compared to the effects of collimator misalignment.

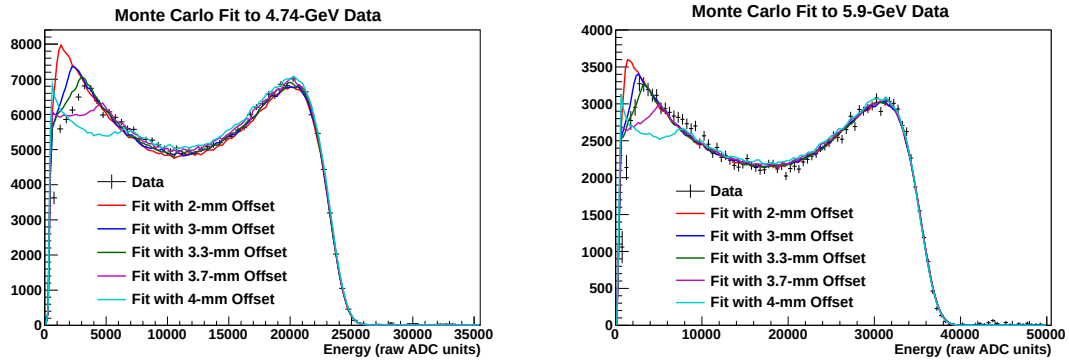

(a) (b)

Figure 4.24: Monte Carlo fits to Compton spectrum for varying collimator misalignment, for electron beam energies of 4.74 GeV (a) and 5.90 GeV (b). Plots are from M. Friend [231].

4.3.5 Analyzing Power

The signal-weighted analyzing power, $\langle WA_l \rangle / \langle W \rangle$, allows us to calculate the electron beam polarization from our measured asymmetry in the integrated signal: it is the asymmetry that we would measure with our particular apparatus if both the electron and photon beams were perfectly polarized. Our Monte Carlo simulations of the photon detector system, done in Geant4, are crucial to this calculation.

Our simulation includes both the GSO crystal and the latter part of the photon beamline: the lead collimator, the millimeter-thick lead disk (placed immediately downstream of the collimator aperture) that serves as a synchrotron radiation absorber, and the air between the collimator and the crystal. (Nearly all of the six-meter distance traversed by the backscattered photons is in vacuum.) We simulate a beam of incident photons with energy and spatial distributions that match a Compton-backscattered beam with our kinematics, and allow each photon to travel through our apparatus in turn. The effects of variations in shower formation, affecting photon collection statistics, were encoded in the Monte Carlo by Vahe Mamyan and give a smearing effect of about 3%. The simulation also includes the nonlinear detector response function $f(x)$ (Section 4.3.4.4). The number of photoelectrons released by the PMT cathode per MeV deposited in the crystal was assigned for each event based on a Poisson distribution with a mean of 300.

The resulting statistics for the integrated signal of each pulse were weighted by the theoretical Compton asymmetry A_l (Equation 4.16), giving us the mean asymmetry as a function of integrated signal that we would measure in our detector if the incident particles in the Compton interaction were perfectly polarized. Our Monte Carlo, which takes into account the quirks of the photon beamline, detector, PMT and DAQ, may thus be thought of as a means of converting an ideal theoretical asymmetry calculated in the framework of quantum electrodynamics to a measurable asymmetry unique to our apparatus.

The final stage of this computation was the computation of $\langle WA_l \rangle / \langle W \rangle$, the signal-weighted integral of A_l, according to Equation 4.27. High-statistics simulations allowed us to achieve a statistical error on $\langle WA_l \rangle / \langle W \rangle$ of 0.074%.

During E06-014, we did not take enough pulse-by-pulse (triggered mode) data to test this Geant4 model empirically. For the HAPPEX-III experiment six months later, however, the Compton integrating DAQ was redesigned to include the integrated signal for a few dozen pulses each helicity window, while still providing deadtime-less integrating-mode accumulator measurements. The resulting high statistics in each photon energy bin allowed an experimental measurement of the differ-

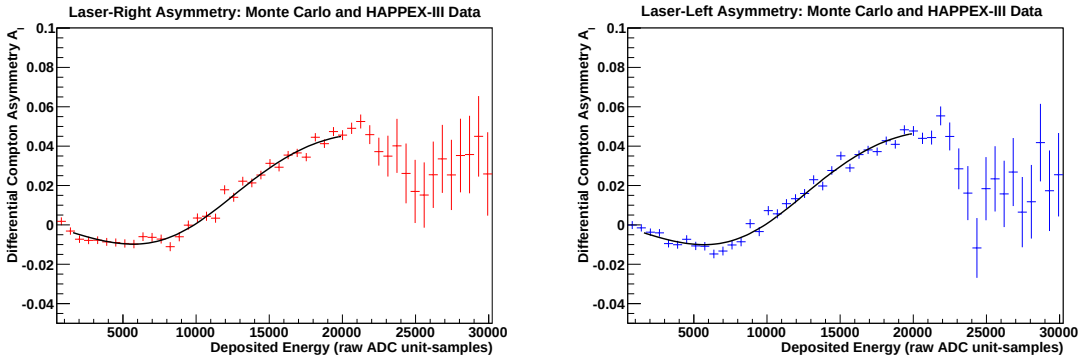

(a) Right-circularly polarized photons

(b) Left-circularly polarized photons

Figure 4.25: Measured and simulated Compton counting asymmetries during HAPPEX-III, plotted as functions of deposited energy for right (a) and left (b) circular laser polarization. The data points report the measured values for each energy bin; the smooth lines give the simulated A_l curve, fit to the data with a single ADC-scale parameter, up to the Compton edge. Plots are from G. Franklin [148].

Source of Error	**Error (%)**
Statistical	0.074
Collimator Misalignment	0.2
Beam Energy	0.2
Detector Response	1.0
Total Systematic	1.039
Total	1.042

Table 4.6: Errors on analyzing power $\langle WA_l \rangle / \langle W \rangle$.

ential Compton asymmetry A_l as a function of photon energy. Figure 4.25 compares this measured asymmetry for both laser polarization states to the asymmetry function produced by the Monte Carlo simulation. Although the collimator was replaced between E06-014 and HAPPEX-III, altering the photon beamline and necessitating changes to the Monte Carlo, the close agreement between experiment and simulation for HAPPEX-III is strong support for the use of a similar model in the E06-014 Compton analysis.

The imperfection of our calibrations corresponds to systematic error in the signal-weighted analyzing power from the Monte Carlo. Uncertainty in the nonlinearity of the photon detector response function (Section 4.3.4.4), for example, corresponds to an error of less than 1% on the analyzing power, while the 2.5-MeV uncertainty in the electron energy contributes about 0.2% [231].

As we saw in Section 4.3.4.5, the collimator misalignment was more difficult to measure precisely. To determine the effect of this uncertainty, we ran five Monte Carlo calculations of the analyzing power, one for each choice of misalignment from 2 mm to 4 mm. Figure 4.26 shows the analyzing power as a function of collimator misalignment. Suppose that we assume that the offset falls between 3.3 and 3.7 mm, as Figure 4.24 indicates, and take the average of the analyzing powers at each end of the range. The difference in analyzing powers over this range of offsets corresponds to a relative uncertainty of only 0.2%.

Table 4.6 gives a breakdown of sources of error in the analyzing power. Table 4.7 shows the final analyzing powers of integrating-mode Compton photon polarimetry for the E06-014 kinematics.

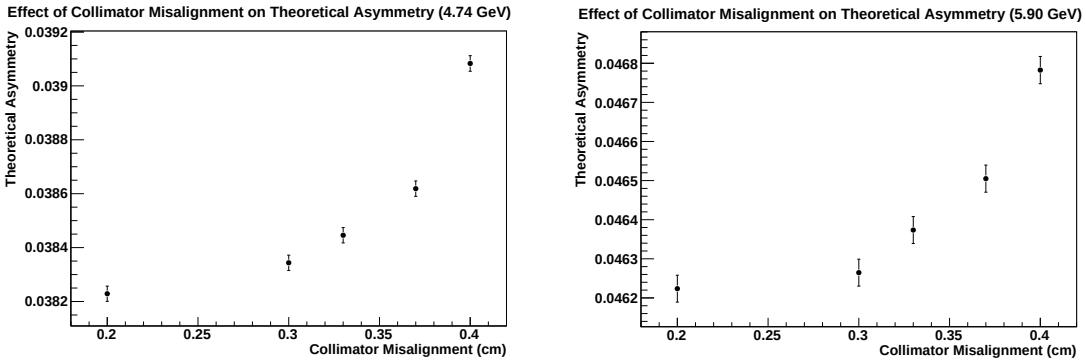

(a) $E_e = 4.74$ GeV (b) $E_e = 5.90$ GeV

Figure 4.26: Analyzing power as a function of collimator misalignment for 4.74-GeV (a) and 5.90-GeV (b) electrons. Note that the vertical axis does not go to zero. Plots are from M. Friend [231].

Incident Electron Energy	Analyzing Power
4.74 GeV	0.03853 ± 0.00040
5.90 GeV	0.04644 ± 0.00048

Table 4.7: Compton analyzing powers $\langle W A_l \rangle / \langle W \rangle$ for E06-014.

4.3.6 Data Analysis

Our primary Compton data analysis process consisted of compiling and analyzing Compton data separately for each individual run, as described in Section 4.3.6.1. Each run lasted, on average, about two hours, resulting in a statistical error of about 3.5%.

The results of this analysis showed that the beam polarization was remarkably stable during each of four distinct periods of production running. The statistical error on the beam polarization during each run period could then be almost eliminated by combining runs to form a single polarization measurement with a systematic error of 2.49%. We discuss this process in Section 4.3.6.2.

4.3.6.1 Run-by-Run Analysis

We developed a ROOT-based analysis suite to decode data from the CODA file for each run, manipulate the raw signal data (*e.g.* by performing pedestal subtraction), and group variables into ROOT trees (saved to ROOT files) that would enable further analysis. A primary function of this analysis package is background subtraction. The basic expression for the experimental asymmetry in the energy-weighted integrated signal, given in Equation 4.26, is somewhat simplified. In actuality, the signal S from Compton scattering is added to an underlying background signal B, which arises largely from synchrotron and bremsstrahlung radiation. Figure 4.27 shows the measured photon spectra for the two cavity states. The experimental asymmetry is thus properly represented as

$$A_{exp} = \frac{(S^+ + B^+) - (S^- + B^-)}{(S^+ + B^+) + (S^- + B^-)}. \tag{4.45}$$

If $B^+ = B^-$, the background signal cancels in the numerator, but not in the denominator; the background thus *dilutes* the measured asymmetry, reducing it from the asymmetry purely due to Compton scattering. As we discuss in detail below, we may correct this dilution in our analysis by taking measurements when the cavity is not in resonance. The underlying background B of the

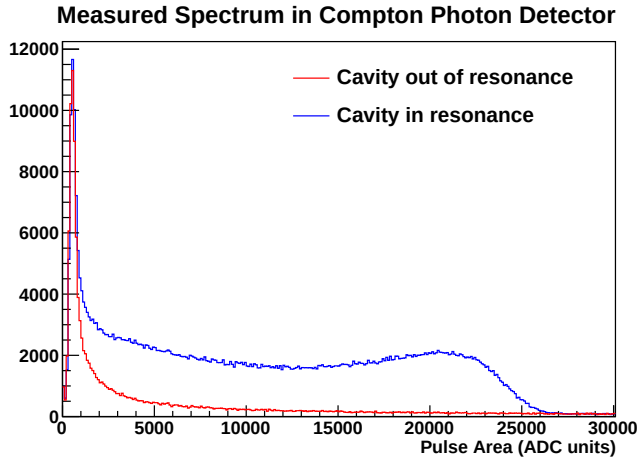

Figure 4.27: Compton-polarimeter spectra measured in triggered mode with the cavity in (blue) and out (red) of resonance. The out-of-resonance spectrum has been scaled to correct for the duration difference in the measurements. We see the distinctive Compton edge in the in-resonance spectrum, which has not had background subtracted; in the out-of-resonance spectrum, we see the prevalence of low-energy background.

in-resonance data is thus corrected using the measured background $\mathcal{B}$ from the out-of-resonance data.

The analysis suite has two main tracks. The triggered-mode analysis track treats data photon-pulse by photon-pulse, subtracting the pedestal from the signal and computing the pulse amplitude and integral. The distribution of these integrated pulse signals gives us the energy spectrum for the run, producing Compton spectrum plots like the ones in Figures 4.22 and 4.24. The analysis also saves to the ROOT file a number of pulse *snapshots*, which preserve the entire waveform as shown in Figure 4.14. This information is vital for determining ideal gain and threshold settings, as well as for troubleshooting problems with electronics and wiring.

The integrating-mode analysis track operates helicity-pair by helicity-pair. The analysis begins with the first full helicity-quartet; starting from that point, each pair of consecutive helicity windows includes one window with negative helicity and one window with positive helicity. We first confirm that the cavity state has not changed during the helicity pair, and that the windows that make up the pair actually have opposite helicities. We then compute the average beam current and photon rate over the pair, and compute the pedestal- and background-subtracted numerator $(S^+ - S^-)$ and denominator $(S^+ + S^-)$ of the Compton asymmetry, using the Stretched Window Accumulator (Accumulator 4). Figure 4.28 shows the distribution of the latter two variables over the course of a typical two-hour run.

Once the first pass through the data has been completed and the corresponding ROOT trees generated, a second pass is necessary in order to set a cut on beam current and identify the cavity state for each helicity pair. Each of these functions requires an examination of the existing data – in order to determine the distribution of beam current and photon rates over the course of the run – and this cannot be done until the entire data file has been decoded. This second-pass analysis generates a second set of ROOT trees, which are friends to the original ROOT trees and can thus access all the data from the first-pass analysis. Trees from each analysis stage are then written to a ROOT file for the run.

The cavity-state identification algorithm is described in detail in Section 4.3.4.1. The algorithm for finding a beam-current cut – necessary because the energy-weighted integrated signal depends on photon rates, which are unstable during recovery from a beam trip – is straightforward. The

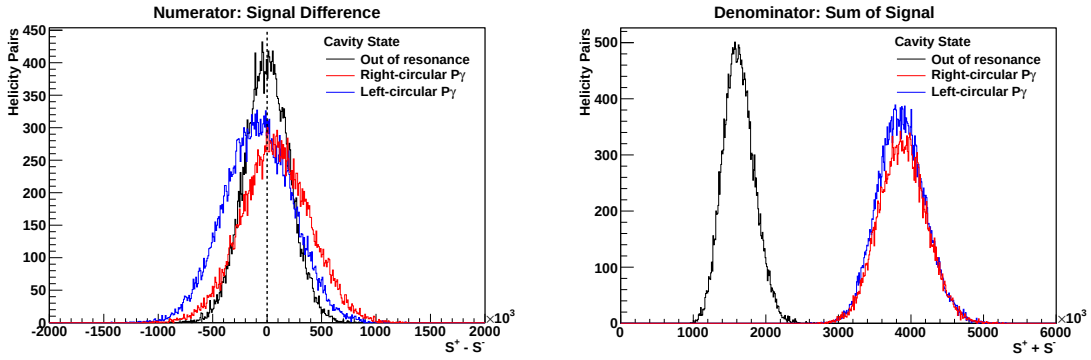

(a) Signal difference

(b) Signal sum

Figure 4.28: Distribution of the numerator (a) (measured signal difference) and denominator (b) (measured signal sum) of the Compton asymmetry for helicity pairs in a representative two-hour run, without background subtraction. The numerator distribution shows both the fact that the background signal difference is consistent with zero (marked by the vertical dotted line) and the sign change between the signal difference for left- and for right-circularly polarized photons. The denominator distribution reflects the fact that cavity-in-resonance rates, which combine Compton events with background events, are significantly higher than background rates alone.

algorithm searches for the beam-current setpoint by starting with a 1-μA window around the nominal production current of 15 μA. If 4.3 minutes of Compton data – enough for a little more than one complete laser cycle – are recorded within that current window, the algorithm takes 15 μA to be the setpoint; if not, it steps down to 10 μA, one μA at a time, and looks for 4.3 minutes of data at each step. Once the setpoint has been located, the cut requires the beam current to be within 5% of the setpoint.

The final stage of the analysis, in which a Compton asymmetry is extracted for the run, is performed on the ROOT file produced by the first two stages. We produce signal-difference and signal-sum histograms, like the ones in Figure 4.28, for each of five cavity states: two in-resonance states (one for each laser polarization direction) and three out-of-resonance states (one for each laser polarization direction, and a third combining data for both directions). The separation of the two polarization directions, even for background events, allows partial correction for beam drifts on a time scale shorter than a laser cycle, as well as possible pedestal shifts in the DAQ electronics due to the polarization-direction bit being high or low.

We treat events with left- and right-circularly polarized photons separately, giving us two independent asymmetry measurements for each run. The asymmetry for each polarization direction is computed according to Equation 4.45, with signals assigned to S^+ and S^- solely based on the electron helicity direction; consequently, the asymmetries measured for the two photon polarization directions have opposite sign.

Since the Compton laser cycle allows us to take measurements of the background signal every minute and a half, we may mitigate the dilution of the asymmetry by performing background subtraction. In the numerator of Equation 4.45, we wish to subtract $B^+ - B^-$; if $B^+ = B^-$, this is unnecessary (and has no effect), but B^+ and B^- may differ due to helicity-dependent changes in beam tune or intensity, in which case the false asymmetry is partially canceled by the subtraction. In the denominator, we wish to subtract $B^+ + B^-$, which is never zero. Of course, what we measure is $\mathcal{B}^\pm$, which may differ from $B^\pm$ if the beam conditions are different; the two are related by the ratio of the average beam currents during each cavity state.

To compute the asymmetry for a given polarization direction, we produce two histograms each

of the signal sum (Figure 4.28(a)) and signal difference (Figure 4.28(b)): one set for helicity pairs with the cavity in resonance ($(S^+ + B^+) \pm (S^- - B^-)$), and one set for pairs with the cavity out of resonance ($\mathcal{B}^+ \pm \mathcal{B}^-$). Both sets of histograms include only pairs from the chosen polarization direction. We then find the mean of each histogram and use these values to compute the asymmetry over the entire run.

Let us represent the mean signal sum as μ^{sum} and the mean signal difference as μ^{diff}. We will use the subscripts *in* and *out* to represent cavity-in-resonance data and cavity-out-of-resonance data, respectively. Recall that B represents the underlying background during in-resonance measurements and $\mathcal{B}$ represents the measured background with the cavity out of resonance. We then have

$$\begin{aligned}
\mu_{in}^{diff} &= \langle (S^+ + B^+) - (S^- + B^-) \rangle \\
\mu_{out}^{diff} &= \frac{\langle I_{in} \rangle}{\langle I_{out} \rangle} \langle \mathcal{B}^+ - \mathcal{B}^- \rangle \\
\mu_{in}^{sum} &= \langle (S^+ + B^+) + (S^- + B^-) \rangle \\
\mu_{out}^{sum} &= \frac{\langle I_{in} \rangle}{\langle I_{out} \rangle} \langle \mathcal{B}^+ + \mathcal{B}^- \rangle
\end{aligned} \tag{4.46}$$

where $\langle I_{in} \rangle / \langle I_{out} \rangle$ is the ratio of the average electron beam current while the cavity is in resonance to the average electron beam current while the cavity is out of resonance. Although the loose beam current cut removes beam trips, random beam variations in the beam current can mean that the background rate is mismatched between the two cavity states, especially during short runs. The normalization factor corrects for this problem, allowing us to translate our measurements of $\mathcal{B}$ into measurements of B.

The variable definitions in Equation 4.46 give us a simple expression for the background-subtracted asymmetry

$$A_{exp} = \frac{\mu_{in}^{diff} - \mu_{out}^{diff}}{\mu_{in}^{sum} - \mu_{out}^{sum}}. \tag{4.47}$$

The statistical error on A_{exp} is computed from the errors on the means.

Finally, the absolute magnitude of the asymmetry computed from Equation 4.47 is divided by the photon polarization P_γ (Section 4.3.4.3) and the predicted analyzing power $\langle W A_l \rangle / \langle W \rangle$ (Section 4.3.5) to obtain the electron polarization P_e. A single value of P_e for the run is extracted by taking the weighted average of the measurements for the two photon polarization directions.

During E06-014, the insertable half-wave plate (Section 3.2.1) was periodically moved into and out of position in the photon beamline at the polarized electron source. This inverts the meaning of the electron helicity labels and is useful for controlling false asymmetries. In the Compton data, a half-wave plate change flips the sign of A_{exp}, which serves as a check on our algorithm. When a change occurs partway through a run, however, we must take special precautions to ensure that the asymmetries from the two parts of the run do not cancel each other; in this special case, we give the same sign to data from both half-wave plate states. The status of the half-wave plate is present in the data stream as an EPICS variable, and is recorded as part of the Compton data. When our code detects a change in status during a run, we fill one set of signal-difference histograms for each half-wave plate state, and flip the sign of the half-wave-plate-in data before combining it with the half-wave-plate-out data. The signal difference used in the asymmetry calculation then carries the sign of data with the half-wave plate removed from the beamline.

Three of the accumulators described in Section 4.3.3.2 will yield a Compton asymmetry A_{exp} if we apply the above algorithm to their signal. These are the All Accumulator, which integrates all signal without thresholds; the Window Accumulator, which integrates signal while it falls between two

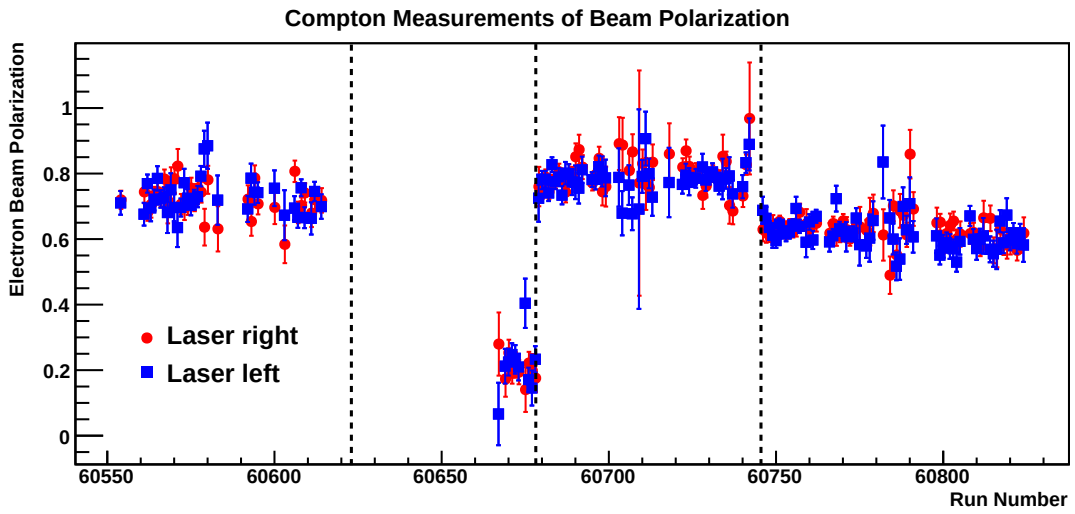

Figure 4.29: Compton polarization measurements during E06-014. Measurements with the laser right-circularly polarized are shown in red, while measurements with the laser left-circularly polarized are shown in blue. Transitions between beam configurations (*i.e.* pass changes) are marked with dashed lines. The errors shown are statistical only.

thresholds; and the Stretched Window Accumulator, which is much like the Window Accumulator, but adds signal from short time windows before and after the pulse enters the integration window, in order to include both tails of each pulse. The Stretched Window Accumulator also excludes the tails of very large pulses whose peaks exceed a large-signal threshold.

In principle, the All Accumulator is the most straightforward choice, since its signal includes the entire energy range of the Compton-scattered photons and since the resulting asymmetries are not sensitive to errors in our knowledge of the pedestal. In practice, low-energy noise during E06-014 made it impossible to rely on this accumulator; the ten-channel, near-pedestal threshold on the Window Accumulators stabilized the measured asymmetries dramatically. (Recall that, in an asymmetry in the energy-weighted signal, low-energy signals should make a small contribution.)

We used the Stretched Window Accumulators, which integrates the signal within a large window as well as the pulse tails on either side of the near-pedestal threshold, to compute asymmetries for E06-014. Data taken during HAPPEX-III, when shifts in the FADC pedestal could be measured throughout the experiment and low-energy noise was better controlled, suggest that, over the course of three months of running, the average pedestal value during a run varies over a range of about 0.3 channels. A 0.5-channel pedestal shift in the E06-014 data gives rise to a 0.7% systematic error on A_{exp} [231].

4.3.6.2 Combining Data from Multiple Runs

Figure 4.29 shows the Compton measurements of P_e, with results from the two laser polarization states shown separately. We see that each of E06-014's four production run periods, separated from its neighbors by pass changes, has a stable beam polarization. This allows us to combine data from all runs in a run period in order to compute four values of P_e that describe the beam polarization over the whole experiment.

For each run, we compute a single P_e^{run} by taking the error-weighted average of its two P_e measurements, one for each photon polarization direction. This average is formed according to

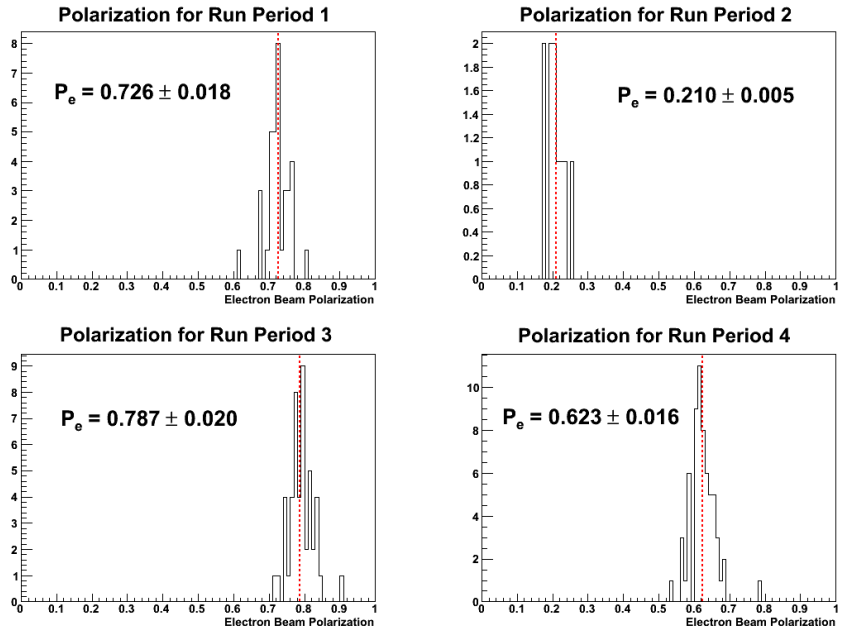

Figure 4.30: Compton polarization measurements for each run period. The dashed red line and text give their weighted average, the P_e measurement from Compton polarimetry for the run period.

$$\bar{x} = \frac{\sum_{i=1}^{N} x_i/\sigma_i^2}{\sum_{j=1}^{N} 1/\sigma_j^2} \tag{4.48}$$

where x_i is i^{th} measurement of the quantity of interest (in this case, P_e) and σ_i is the statistical error on that measurement. The variance of $\bar{x}$ is then given by

$$\sigma_{\bar{x}}^2 = \frac{1}{\sum_{i=1}^{N} 1/\sigma_i^2}. \tag{4.49}$$

We then repeat this procedure for each run period, taking the weighted average of the P_e^{run} values computed for each run. Again, we weight only according to the statistical error; for example, a three-hour run receives more weight than a one-hour run. Figure 4.30 shows the one-dimensional distribution of P_e^{run} for each run period, along with the results of the weighted averages.

Finally, we apply a systematic error of 2.49% to each of the four P_e values. This error reflects systematic uncertainties in the photon polarization P_γ (Section 4.3.4.3); in the analyzing power $\langle WA_l \rangle / \langle W \rangle$ (Section 4.3.5); and in the experimental asymmetry A_{exp} arising from the use of thresholds (Section 4.3.6.1). These errors are tabulated in Table 4.8.

Table 4.9 shows the final P_e results from Compton polarimetry.

4.4 Electron Beam Polarization Measurements

Our final Compton results for the electron beam polarization P_e have comparable uncertainty to the Møller measurements of P_e (Table 4.1). Since the two polarimeters have entirely independent

Source of Error	Error (%)
Photon polarization P_γ	2.15
Analyzing power $\langle WA_l \rangle / \langle W \rangle$	1.04
Experimental asymmetry A_{exp}	0.7
Total Systematic	2.49

Table 4.8: Systematic errors on Compton measurements of P_e.

systematics, we may reduce our overall uncertainty by combining the two sets of measurements.

For each run period, we computed the weighted average of the Compton polarization measurements (Section 4.3.6.2) and the weighted average of the Møller polarization measurements, where they existed. (No Møller measurements were taken during the second run period, when the beam was nominally unpolarized.) We then combined the measurements from the two polarimeters in a final weighted average. Table 4.9 shows P_e values from the Compton and from the Møller, as well as the final combined values from the two polarimeters.

For run periods with both Compton and Møller polarimetry, we achieved a relative error of 1.56% on the beam polarimetry. (In the second run period, our error was 5.24%.) Later experiments, notably HAPPEX-III, were able to achieve beam polarimetry with subpercent accuracy [231] due to an upgrade of the Møller DAQ and continued upgrades to the Compton polarimetry. Guided by experiences during E06-014, the Compton team installed shielding to reduce the level of synchrotron radiation in the photon detector, allowing signal integration without thresholds. The Compton DAQ's integrating mode was modified to allow a small number of pulse waveforms to be stored for each MPS, as well as pulse area for a larger number of waveforms, advances which allowed a better understanding of the analyzing power. A new collimator and photon-detector alignment system mitigated the problem of scattered-photon misalignment. Better determination of the cavity state improved statistics, as did a new infrared laser with greater output power, and careful study of the photon polarization (both during and after the experiment) dramatically reduced the largest source of systematic error. After HAPPEX-III and its sister experiment PVDIS [168], the entire Compton laser system was replaced with a green (532-nm) laser and optics appropriate to the new wavelength; at a stroke, this doubled the analyzing power at any given electron energy. E06-014 was the first commissioning experiment for this suite of Compton upgrades; despite the fact that these upgrades were unfinished, we were able to halve the proposal's error budget for beam polarimetry while preparing the ground for even more profound changes to the Compton system.

Run Period	Beam Energy (GeV)	P_e from Compton	P_e from Møller	Combined P_e Value
1	5.90	0.726 ± 0.018	0.745 ± 0.015	0.737 ± 0.012
2	4.74	0.210 ± 0.011	–	0.210 ± 0.011
3	5.90	0.787 ± 0.020	0.797 ± 0.016	0.793 ± 0.012
4	4.74	0.623 ± 0.016	0.628 ± 0.012	0.626 ± 0.010

Table 4.9: Final P_e measurements. No Møller measurement was taken during the second run period.

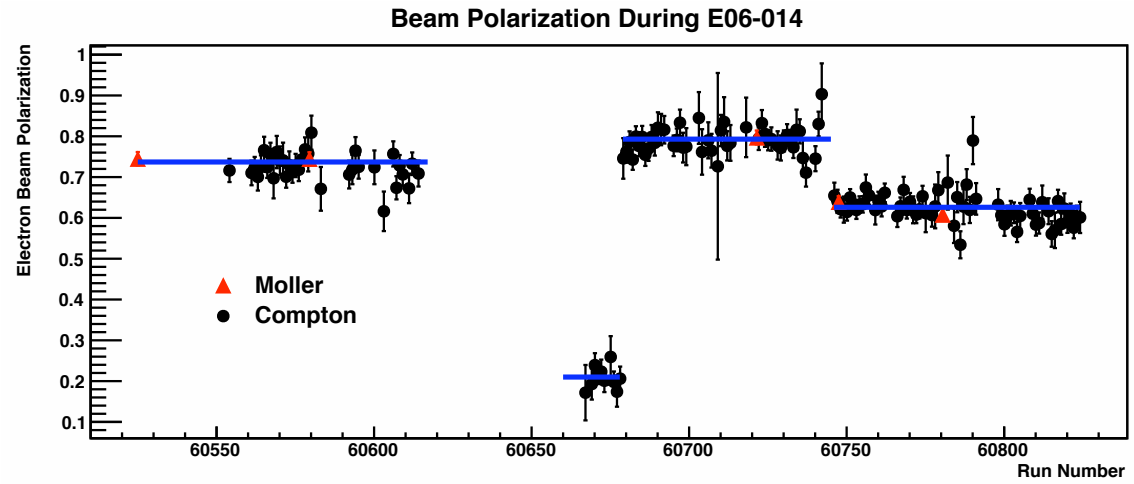

Figure 4.31: Møller (red) and Compton (black) polarization measurements during E06-014. The error bars reflect a combination of systematic and statistical errors. The blue, horizontal lines show the final P_e values for each run period, found by combining Møller and Compton measurements.

Chapter 5

Target and Detector Calibrations

In Chapter 3, we described the apparatus – the polarized electron source, the beamline diagnostics, the highly polarized ^{3}He target, and the complicated spectrometers – that make the measurement of A_1^n possible. It is not enough to have this equipment and confirm that it is in good working order, however; conditions may change dramatically between and even during experiments, and the transformation of thousands of detector signals into valid kinematics variables requires thorough calibration. That is the subject of this chapter.

In Chapter 4, we delved into the calibration of the Compton polarimeter, which allows us to extract the polarization P_e of the electron beam. A measurement of A_1^n also requires us to know the polarization of the ^{3}He target, which we discuss in Section 5.1. In Section 5.2, we discuss the calibration of the BigBite spectrometer; the angles, momenta, and energies derived from BigBite data form the basis of our A_1 measurement. Finally, in Section 5.3, we give a brief discussion of the problem of electron energy loss, which is otherwise neglected in this dissertation.

5.1 Target Calibrations

The polarized ^{3}He target (Section 3.3.3) is a complex system. The gas density inside the target cell is affected by beam heating (in the target chamber) and oven heating (in the pumping chamber). Heating effects depolarize the target ^{3}He, while continuous hybrid spin-exchange optical pumping re-polarizes it. Changing density affects the interpretation of polarization measurements performed during the experiment. In this section, we discuss the calibration of these essential aspects of the target, beginning with the target density in Section 5.1.1 and continuing to the target polarization (Section 5.1.2).

5.1.1 Target Density

While the number of ^{3}He atoms in the target is constant, the ^{3}He density in the two compartments may vary due to heating by the beam (in the target chamber) and by the circularly polarized lasers (in the pumping chamber). Since the ^{3}He density is required in calculations of the target polarization from both NMR and EPR measurements (Section 3.3.3.3), a full understanding of the density is important. Seven **r**esistive **t**hermal **d**evices (RTDs) are placed on the outside of the target and pumping chambers in order to measure temperatures during the experiment; their output is part of the EPICS datastream.

The target number density is measured in units of amagat (amg), the number of molecules of an ideal gas present per unit volume at a pressure of 1 atm and a temperature of 0°C. One amg is equal to 2.687×10^{25} m^{-3}. Two types of ^{3}He density measurement are available. One, the fill density, is the density measured during cell construction, while the target cell was initially filled

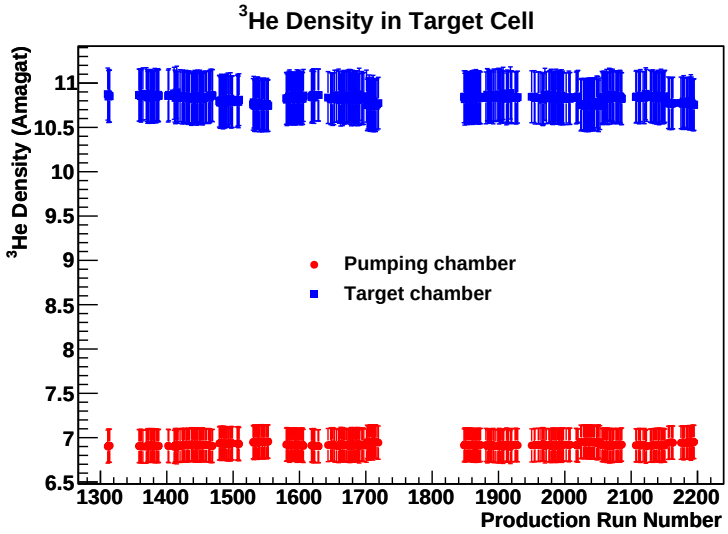

Figure 5.1: ^{3}He density as a function of BigBite production run number during E06-014 [235].

with ^{3}He and other gases. For our production target cell, Samantha, this fill density was measured to be 7.847 ± 0.070 amg [232].

The second type of density measurement exploits the fact that collisions with ^{3}He atoms broaden the D1 and D2 absorption lines of rubidium [152]. By measuring the width of the D1 and D2 line shapes at varying temperatures and subtracting the 1% contribution of N_2 to that linewidth, we can measure the ^{3}He density in the pumping chamber. Two such scans have been performed for Samantha: a scan at the University of Virginia, done before the experiment, gave a density of 7.99 ± 0.01 amg. After the experiment, a measurement at Jefferson Lab by Lamiaa El Fassi yielded a density of 8.099 ± 0.032 amg [233].

Where n_0 is the room-temperature number density measured from broadening of the Rb absorption lines, V and T are the volume and temperature of a chamber, and the subscripts pc and tc represent the pumping chamber and target chamber, respectively, we may write the following expressions for the number density in each chamber:

$$n_{tc} = n_0 \left[1 + \frac{V_{pc}}{V_{tot}} \left(\frac{T_{tc}}{T_{pc}} - 1 \right) \right]^{-1} \tag{5.1}$$

$$n_{pc} = n_0 \left[1 + \frac{V_{tc}}{V_{tot}} \left(\frac{T_{pc}}{T_{tc}} - 1 \right) \right]^{-1}. \tag{5.2}$$

Here, V_{tot} is the total internal volume of the target cell. These expressions arise from the ideal gas law [234].

The target temperature, as measured by the RTDs, was stable to within 2°C during production running. Combining the calibrated temperature measurements, our knowledge of the cell geometry, and the measurements of n_0, Lamiaa El Fassi and Yawei Zhang used Equations 5.1 and 5.2 to extract average density numbers for both chambers over the course of the experiment; Table 5.1 gives the results. Figure 5.1 demonstrates that these values were extremely stable over the course of the experiment.

Chamber	^{3}He Density (amg)
Pumping	6.93 ± 0.19
Target	10.81 ± 0.29

Table 5.1: Average ^{3}He densities in target cell during E06-014 [233].

5.1.2 Target Polarization

As we saw in Section 3.3.3.3, the target polarization was measured in two complementary ways during E06-014: electron-paramagnetic-resonance (EPR) measurements of the potassium in the pumping chamber, and nuclear magnetic resonance (NMR) measurements of the ^{3}He in the target chamber. EPR measurements were performed infrequently, with several days separating each set of measurements, while NMR measurements were performed every four hours, twice each shift.

In the EPR method, we measure the frequency shift of potassium level transitions in the presence of polarized ^{3}He; Equation 3.23 relates the frequency shift $\Delta\nu_{EPR}$ to the target polarization $P_{^3\mathrm{He}}$

$$\Delta\nu_{EPR} = \frac{4\mu_0}{3}\frac{d\nu_{EPR}}{dB}\kappa_0\mu_{3He}n_{pc}P_{^3\mathrm{He}}. \tag{5.3}$$

The vacuum permeability μ_0 and ^{3}He magnetic moment $\mu_{^3\mathrm{He}}$ are well known [236]. The derivative of the EPR frequency with respect to the magnetic field, $d\nu_{EPR}/dB$, may be parameterized based on the $g-$factors of electrons and of the alkali atoms, the nuclear magneton, and the nuclear spin [237]. The enhancement factor κ_0 has been measured over a range of alkali atoms and temperatures in atomic-physics experiments [238]. The pumping-chamber number density n_{pc} averages out to 6.928 ± 0.002, as we saw in Section 5.1.1, but this value may also be computed on a run-by-run basis using measured temperature data [239]. The frequency shift $\Delta\nu_{EPR}$, meanwhile, is what is measured over the course of the experiment. Table 5.2 shows the error on each of these parameters, combining for a total error of 4.08% on $P_{^3\mathrm{He}}$ as measured via EPR.

During each EPR measurement, NMR polarization measurements were performed simultaneously. Comparison of these results yields a conversion constant c' between the NMR amplitude h and the polarization as measured by EPR

$$c' = \frac{P_{^3\mathrm{He}}}{h}. \tag{5.4}$$

This relationship allows an NMR measurement to be converted into an absolute number for the ^{3}He polarization. Independently, c' may be calculated from a calibration with a water target; the final NMR polarization number is then the weighted average of the polarization computed from the water calibration and the polarization computed from the EPR calibration.

For E06-014, the water calibration has not yet been completed, but Yawei Zhang has computed c' for each of the ten EPR measurements (Table 5.3). By combining results from measurements with the same polarization direction, he obtained average values of c' for both longitudinal and transverse target polarization (Table 5.4), with a combined systematic and statistical error of 4.9%. As shown in Table 5.2, this error is dominated by uncertainties in the value of the enhancement factor κ_0 and in the value of the target density during E06-014 running. He applied these conversion constants to the NMR measurements taken at four-hour intervals, and then performed a linear interpolation to find the target polarization on a run-by-run basis. The result is shown in Figure 5.2. These results are preliminary; once the water calibration analysis is finished, those data will be combined with these in order to obtain final run-by-run values for $P_{^3\mathrm{He}}$.

Parameter	Relative Uncertainty (%)
$\Delta\nu_{EPR}$	~ 0.6
μ_0	negligible
$\frac{d\nu_{EPR}}{dB}$	negligible
κ_0	3.0%
$\mu_{^3\mathrm{He}}$	negligible
n_{pc}	2.7%
h	~ 0.6

Table 5.2: Error breakdown for calculation of $P_{^3\mathrm{He}}$ and c' from EPR measurements [239].

Date	Polarization Direction	$P_{^3\mathrm{He}}$ (%)	c' (%/mV)
7 February	Longitudinal	42.92 ± 1.75	2.89 ± 0.12
7 February	Longitudinal	41.39 ± 1.69	2.89 ± 0.12
9 February	Transverse	47.64 ± 1.94	1.73 ± 0.07
17 February	Transverse	60.29 ± 2.46	1.73 ± 0.07
17 February	Transverse	54.73 ± 2.23	1.72 ± 0.07
23 February	Longitudinal	52.32 ± 2.13	2.75 ± 0.11
11 March	Transverse	53.45 ± 2.18	1.84 ± 0.08
11 March	Transverse	50.90 ± 2.08	1.81 ± 0.07
16 March	Transverse	56.84 ± 2.32	1.78 ± 0.07
16 March	Transverse	52.11 ± 2.13	1.80 ± 0.07

Table 5.3: Results of EPR measurements of target polarization during E06-014 running [239]. All measurements were designed to exploit the level splitting of potassium in the pumping chamber.

Polarization Direction	c' (%/mV)
Transverse	1.77 ± 0.09
Longitudinal	2.84 ± 0.14

Table 5.4: NMR-EPR conversion factors c' [239].

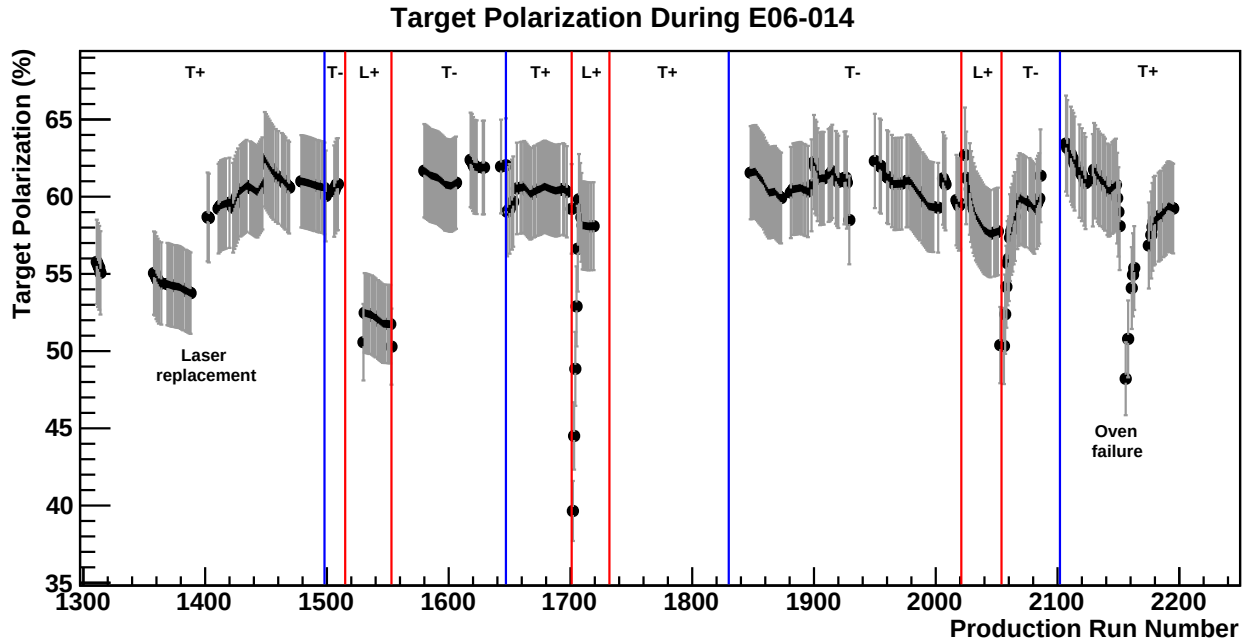

Figure 5.2: Preliminary target polarization during E06-014 [235], based on a linear interpolation of NMR polarization measurements calibrated using EPR results. Red lines show the timing of spin rotations between planes, *i.e.* a transition between transverse and longitudinal target polarization; blue lines indicate 180° spin rotations within a polarization plane. The labels at the top of the graph give the polarization direction for that time period: L+ is 0°, T− is 90°, and T+ is 270°. Two hardware changes also affected the target polarization: a laser with a broad linewidth was replaced by a narrow-linewidth COMET laser around Run 1400, and a failure in the target oven led to a marked depolarization near Run 2150. The target slowly repolarized after the replacement of a heating element.

5.2 BigBite Calibrations

The BigBite spectrometer (Section 3.3.4) has four main components, which work together, online and offline, to give us comprehensive information about a vast sample of scattered particles. The BigBite magnet itself allows us to differentiate between particles with different momenta; the wire chamber gives us the information necessary to tell how the particles behaved inside the magnet. The shower and preshower calorimeters measure the energy deposited by a particle, while the Čerenkov, which is sensitive to particle velocity, gives us a strong tool for particle identification.

Extensive calibration is necessary in order to combine data from these varied sources into a coherent whole. We will begin, in Section 5.2.1, by describing how information from the wire chambers gives us information about particle trajectories. The determination of scattering vertices and particle momenta, by combining tracking information with our knowledge of the magnet, will be the subject of Section 5.2.2. In Section 5.2.3, we discuss the interpretation of data from the gas Čerenkov, while Section 5.2.4 gives a mechanism for extracting particle energies from the calorimeter signals.

5.2.1 Multi-Wire Drift Chambers

The three multi-wire drift chambers (MWDCs, Section 3.3.4.1) record a pattern of hits with high position resolution as a charged particle makes its way through them. Manipulating this information is computationally intensive, so MWDC signals are not used in forming the online trigger; in offline analysis, however, they are crucial. By assembling information about the hits recorded during an event, we can reconstruct the trajectory a particle followed on its way through the wire chambers – its *track*. From the track, we may infer both the particle's behavior before it reached the first wire chamber – *i.e.* its point of origin and the way it curved in BigBite's magnetic field (and thus its momentum) – and its behavior afterward, *i.e.* which parts of the gas Čerenkov, preshower and shower detectors the particle should have interacted with. Before we can determine this information with any confidence, however, we must have both a solid understanding of the actual layout and behavior of the wires, and an algorithm for transforming a hit pattern into a physically valid track.

5.2.1.1 Wire Positions

The low-level calibration of the wire chambers begins with a calibration of their timing and proceeds to the determination of the absolute position of each wire. For E06-014, this calibration was performed by Matthew Posik, building on the E06-010 calibration by Xin Qian [170].

Each of the MWDC wires has a TDC channel for which the BigBite trigger controls the common stop. The readout time $t_{TDC,i}$ for the i^{th} wire thus depends on two propagation times: the time $t_{sig,i}$ that it takes for a particle passing near the i^{th} wire to generate a signal in the TDC, and the time t_{trig} it takes for the trigger signal to reach the TDC and generate the common stop. Following Riordan [144], let us consider each of these times in turn.

Two physical processes contribute to $t_{sig,i}$. In the wake of an ionizing particle in a drift chamber, electrons resulting from the ionization of the gas take some time t_{drift} to reach the nearest wire and produce a signal. Once they have reached the wire, the signal takes some time $t_{delay,i}$ to propagate from the wire to its TDC. We thus have

$$t_{sig,i} = t_{drift} + t_{delay,i}. \tag{5.5}$$

Meanwhile, the charged particle will take some finite time t_{flight} to reach the trigger detector (*i.e.* the shower) after causing a hit on the wire. (Variations in t_{flight} for particles in the BigBite acceptance are less than 1 ns [170, 240] and are neglected in this analysis; the TDC resolution is 0.5 ns.) Once the trigger condition has been satisfied, the trigger logic takes time to operate, and the trigger signal must propagate from its source to the TDCs; we denote the combined time for these processes as t_{logic}. This gives us

$$t_{trig} = t_{flight} + t_{logic}. \tag{5.6}$$

The recorded time $t_{TDC,i}$ is the difference between $t_{sig,i}$ and t_{trig}

$$t_{TDC,i} = t_{drift} + t_{delay,i} - t_{flight} - t_{logic} \approx t_{drift} + t_{0,i} \tag{5.7}$$

where we have combined all times except the drift time into one offset, $t_{0,i}$. Determining $t_{0,i}$ for each wire thus allows us to find the drift time corresponding to any TDC reading.

The correct $t_{0,i}$ time offsets place the rising edge of each wire's drift-time spectrum at 0, removing the sensitivity of the timing to differences between wires. Figure 5.3(a) shows the combined drift-time spectrum for the wires of one wire plane after the t_0 calibration. These results allow us to convert computed drift times to drift distances, which are inputs to the tracking algorithm. We approximate the drift distance as the distance between the known position of the hit wire (from survey reports and from prior calibrations [170]) and the position at which the reconstructed track intersects the hit plane. By plotting this drift distance against the drift time for a given plane, as in Figure 5.3,

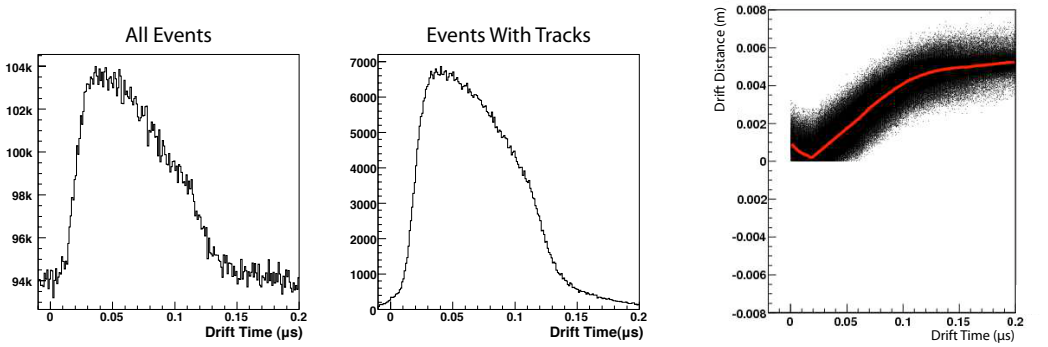

(a) t_0 calibration (b) Time-to-distance calibration

Figure 5.3: MWDC time and distance calibrations. (a) Calibrated t_0 spectrum for second V plane of first MWDC in BigBite, shown for all hits (left) and for hits that are determined by software to be part of tracks. (b) Data (black dots) and parameterization (red line) for time-to-distance conversion in the second U plane of the first MWDC in BigBite. Figures from M. Posik [240].

we may parameterize the time-to-distance conversion function as a continuous function in many sections, each section fitted with a polynomial. In the next iteration of the analysis, this conversion function generates a drift distance for each hit that may be used to improve the performance of the tracking algorithm.

To ensure that the wire positions are accurate in our analysis, we compute track residuals – the distances between the calculated hit wire positions and the reconstructed track positions – for each wire. This residual peak should be centered at zero; if it is not, the wire position is shifted to place the peak at zero, and the whole process ($t_{0,i}$ and position calibration for the wire) is repeated. Figure 5.4 shows the final residuals for the six U planes of the MWDCs; track residuals for all planes range from 190 to 265 μm.

This iterative process is quite time- and data-intensive, but the bulk of the labor was performed only once, by Xin Qian, for both the E06-010 and E06-014 experiments. Minor, E06-014-specific corrections were made by Matthew Posik.

5.2.1.2 Tracking

As we saw in Section 3.3.4.1, the three multi-wire drift chambers in the BigBite stack contain eighteen wire planes altogether. These planes have three *orientations* – U, V, and X – each of which makes a different angle with the horizontal. The BigBite tracking algorithm, developed by Ole Hansen, combines hit data from all eighteen planes to reconstruct straight-line particle tracks through the wire chambers.

In the first stage of track reconstruction, each of the three orientation groups is considered separately. A track through the six planes of the orientation is found using a tree-search pattern-matching algorithm first proposed by Mauro Dell'Orso and Luciano Ristori in 1990 [241]. In this system, we begin by comparing the measured hit pattern in the planes with a set of very low-resolution templates of possible hit patterns, as shown in the top left panel of Figure 5.5; these low-resolution templates may be obtained by ORing together series of wires. Once a match has been found, the successful template is used to generate a set of templates with higher resolution, typically two bins for every single bin in the parent template; these daughter templates are then searched until the one that matches the hit pattern is found (top right panel). This successful daughter template then generates its own daughters with still finer granularity, and the process continues

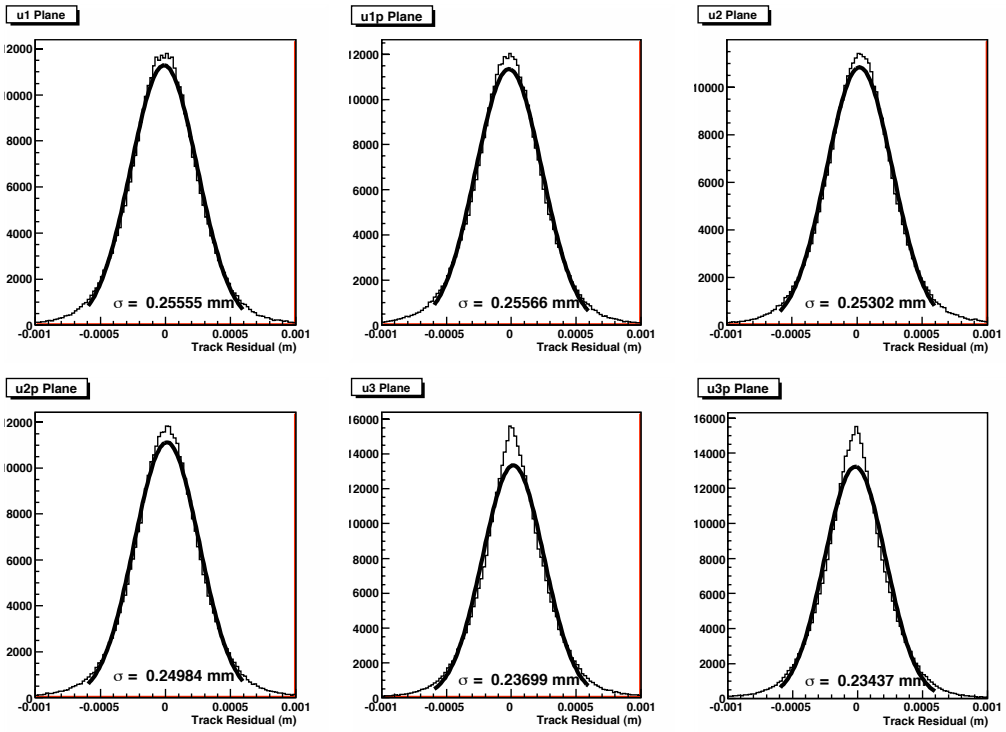

Figure 5.4: Residuals for the six MWDC U planes; residuals for the X and V planes follow similar distributions. Figure from M. Posik [240].

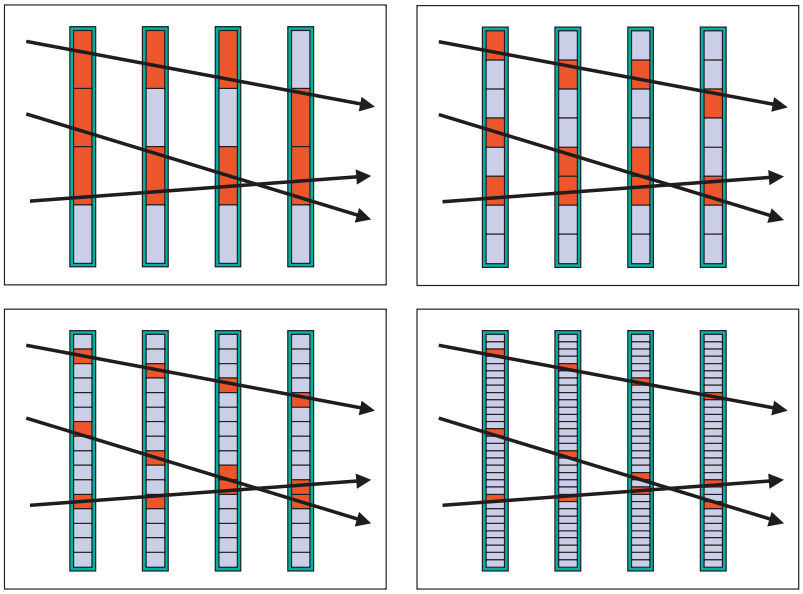

Figure 5.5: A schematic representation of the tree-search tracking algorithm used for BigBite, reproduced from Mankel [242]. At each stage, increasingly higher-resolution templates are matched to each track.

until it reaches templates with the same resolution as the detector (*i.e.* one bin per wire). If a match is found at this final stage, we have a successful track reconstruction; if, at any stage, a template cannot be found that matches the hit pattern, then the track finding has failed and the hit pattern must be attributed to a random collection of hits. At all points in the process, at least five of six planes must match for the algorithm to advance to the next stage.

This tree-search method offers a substantial improvement over a sequential search through all possible templates at the highest granularity. In a sequential search, all patterns must be generated and stored initially, and the average number of patterns that must be considered in finding a match is $\mathcal{O}(n^2)$, where n is the number of bins in each pattern. For a tree search, however, the number of patterns (which is proportional to the time needed for the algorithm to complete) is $\mathcal{O}(\log_2(n))$ [241].

Once the tree-search method has been used to find two-dimensional tracks, or *roads*, in each wire plane orientation, the roads are combined and fit to reconstruct three-dimensional tracks. *Clone* or ghost tracks are removed by allowing each road to contribute only to one track. A successful track must include hits from at least fifteen wire planes (and hence has hits from all three orientations); where two possible tracks are found, the one with the lower χ^2 value is chosen.

In a Geant3 Monte Carlo study of the E06-010 BigBite data, Xin Qian found a software tracking efficiency of 95%. Combined with an average hardware tracking efficiency (*i.e.* the rate at which particles in the desired kinematic range produce enough hits for the software to generate a track) of 98%, this gives a total tracking efficiency of 93% [170]. As both experiments used the same tracking software and the same MWDC configuration, this tracking efficiency figure is also applicable to E06-014.

Despite the high rates observed in BigBite, high track multiplicity was not a problem during E06-014. Of events for which any tracks were reconstructed at all, an average of 93% had exactly one reconstructed track. The remainder were mostly events with two tracks; three- and four-track events made up fewer than 0.3% of events with tracks.

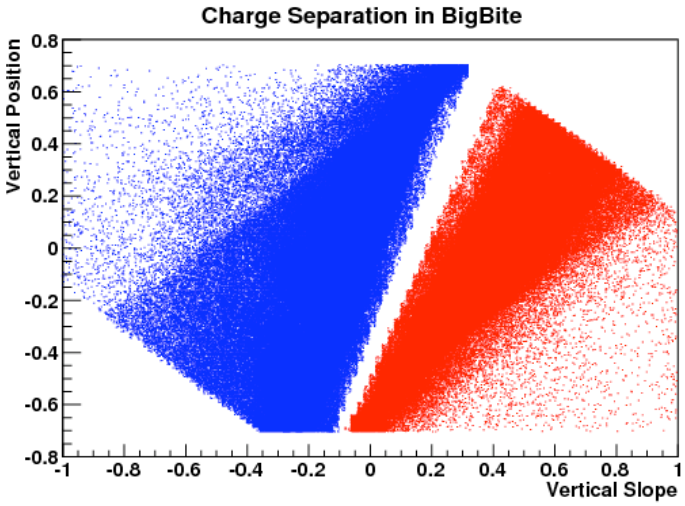

Figure 5.6: Charge separation in BigBite optics, shown with data from a run with 4.74-GeV electrons incident on a polarized ^{3}He target. The vertical position of the track is plotted against the track's vertical slope x', both measured at the first wire chamber. Red points mark tracks assigned a positive charge, while blue points mark tracks assigned a negative charge, based on vertical position and slope. Tracks passing through the gap in the center cannot be assigned a charge.

5.2.2 Optics

The goal of an optics package is to take a track through the chambers and relate it to the trajectory of the detected particle immediately after it scattered from the nuclear target. This is made challenging by the fact that our charged particle has passed through an imperfectly understood magnetic field between the target and our detectors. A careful modeling of the optics allows us to derive both a position for the initial vertex (*i.e.* scattering interaction) and also the momentum of the particle just after scattering, based on the position and direction of its observed track in the spectrometer.

We begin in Section 5.2.2.1 by describing how positively and negatively charged particles may be distinguished from each other. In Section 5.2.2.2, we introduce a first-order model for the BigBite optics, and we refine and calibrate that model in Section 5.2.2.3.

5.2.2.1 Charge Separation

When BigBite is configured with negative polarity, negatively charged particles bend upward in the magnet, while positively charged particles bend downward; when BigBite is run with positive polarity, the directions are reversed. The bend direction of a track can therefore be used to determine the charge of the particle responsible for it.

As shown in Figure 5.6, we determine a track's bend direction by comparing its vertical position (x) at the first wire chamber with its vertical slope (x') at the same location. This calibration was done by Xin Qian for E06-010, and did not require modification for E06-014. Empirically, particles that bend upward in the BigBite magnetic field – *i.e.* negatively charged particles (marked blue in the figure) – have tracks that satisfy the inequality

$$x > 3.17x' - 0.31 \tag{5.8}$$

while downward-bending, or positively charged, particles (shown in red) have tracks that satisfy

$$x < 2.73x' - 0.17. \tag{5.9}$$

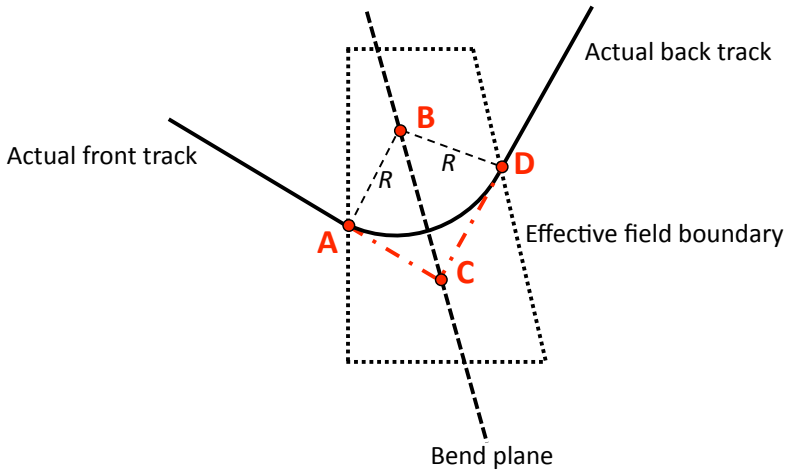

Figure 5.7: A schematic of the effective bending plane model for BigBite. Angles are exaggerated for clarity.

Tracks that satisfy neither inequality are so-called *stiff tracks*, high-momentum tracks that pass through the magnet with little or no apparent bending. They must have a nonzero electrical charge, or we would not be able to measure tracks for them at all, but they do not bend enough to distinguish the sign of the charge.

The E06-014 optics package begins its analysis of each track by assigning it a charge according to Equations 5.8 and 5.9. The vertex and momentum reconstruction processes for positively and negatively charged particles are then handled separately. In the following sections, we will discuss only the optics package for negatively charged particles.

5.2.2.2 First-Order Optics Model

The BigBite optics package takes the observed path of a particle traversing the wire chambers, projects this path backward to the BigBite magnet, and then uses our knowledge of the magnetic field to deduce where this trajectory originated (*i.e.* the scattering vertex) and how it curved in response to the magnetic field (*i.e.* its momentum). To achieve this, we rely on a simple model with a carefully defined geometry.

We begin with the assumption that the BigBite magnet is a perfect dipole – *i.e.* that its magnetic field is uniform throughout its volume. The particle trajectory in the magnetic field therefore describes an arc of a circle with radius R. Outside the volume of the magnet (defined by some effective field boundary), we assume that the magnetic field is zero. Deviations from this model can be corrected in later iterations of the optics calibration process.

We make a first-order approximation of the total particle trajectory by defining an effective bend plane passing through the center of the magnet; we then project a straight-line track (the *back track*) back from the wire chambers to the bend plane, and another straight-line track (the *front track*) from the bend plane to the target [144].

Figure 5.7 defines the geometry of the first-order optics model as implemented for E06-010. The solid line shows the actual trajectory of the charged particle; the dotted line shows the effective field boundary of the magnet. The particle enters the magnetic field at point A and leaves it at point D. We model its interactions as occurring at a single point C on the bend plane (thick dashed line); its path through the magnetic field is then given by two straight-line segments $\overline{AC}$ and $\overline{CD}$ (red dash-dotted lines). The center of the bending arc, part of a circle with radius R, is at point B. We

also define $\ell = \overline{AC} + \overline{CD}$, noting that $\overline{AC} = \overline{CD} = \ell/2$ since the bend plane bisects the bending arc.

Because $\overline{AC}$ is tangent to the arc of curvature, it is perpendicular to the radius $\overline{AB}$, making angle $\angle BAC$ a right angle. If we define $\theta_{bend} = \angle ABD$ as the angle through which the particle trajectory bends in the plane perpendicular to the magnetic field, then $\theta_{bend}/2 = \angle ABC$ and we can express the radius of curvature R as

$$R = \frac{\ell}{2\tan\left(\frac{\theta_{bend}}{2}\right)}. \tag{5.10}$$

We note that the *deflection angle* used in some similar models (*e.g.* Riordan [144]) is the supplementary angle to $\angle ACD$ as defined in Figure 5.7.

From the radius of curvature, we can derive the momentum component $p_\perp$ perpendicular to the magnetic field direction. For a magnetic field of magnitude B, this is

$$p_\perp = |q|BR = \frac{|q|\ell B}{2\tan\left(\frac{\theta_{bend}}{2}\right)}. \tag{5.11}$$

In order to compute the total momentum of the particle, rather than just that component perpendicular to $\vec{B}$, we require one more angle, not shown in Figure 5.7, to complete our picture. We define Φ as the angle between the particle momentum and the magnetic field; in the approximation of BigBite as a perfect dipole, Φ for any given track is fixed throughout the volume of the magnet.

$$\cos\Phi = \frac{\vec{B}\cdot\vec{p}}{|B||p|}. \tag{5.12}$$

The perpendicular momentum component $p_\perp$ is related to the magnitude p of the total momentum by $p_\perp = p\sin\Phi$. Equation 5.11 thus leads us to a first-order expression for the magnitude of the complete electron momentum

$$p = \frac{|q|\ell B}{2\sin\Phi\tan\left(\frac{\theta_{bend}}{2}\right)}. \tag{5.13}$$

Determining the momentum according to this method requires a good first-order determination of $\overline{AC}$ and thus of the front track and the vertex of the scattering interaction. This problem, too, is simplified by the effective bending plane model. First, the back track reconstructed in the multi-wire drift chambers is extrapolated back to find the point C where it intersects with the bend plane; the front track must also intersect the bend plane at the same point. Furthermore, any valid front track must make the same angle Φ with the magnetic field that the back track does. At this stage, the complete set of possible solutions to the front-track problem forms a cone with an apex at C and an opening angle of Φ.

This cone of solutions will intersect with the beamline; since Φ is fairly large, there will be only one intersection point within a reasonable distance of the nominal target. This intersection point defines the first-order interaction vertex, and the front track becomes the line connecting this vertex to the bend plane at C [170]. From a back track measured in the wire chambers, we thus obtain a front track that intersects with the beamline and the target – and the geometry of these two tracks gives us the particle momentum.

5.2.2.3 Refinements to First-Order Optics Model

The first-order optics model is only a beginning: corrections to both the interaction vertex and the momentum are necessary to account for deviations from our approximation. In E06-010, these corrections were determined using data from both first-pass (1.2306 GeV) and second-pass (2.396 GeV), in a six-step process [170]. In E06-014, where BigBite was positioned at a different angle,

there is enough optics data to redo the lower-order calibrations, but any higher-order calibration constants must be taken directly from the E060-010 results or neglected entirely.

Correlation Variables In a non-uniform magnet, the trajectory of a charged particle will depend on the particular regions of the magnetic field that it traverses. This manifests itself in the data as correlations between reconstructed momentum or vertex and variables describing the location and direction of the particle trajectory. We use a set of six variables to describe how and where the particle passes through the magnetic field.

The first pair, x and y, define the hit position (in detector coordinates) of the reconstructed track in the first wire chamber. The second pair, x' and y' (also known as, respectively, $\tan\theta$ and $\tan\phi$ [144]), define the track's direction in the detector coordinate system

$$x' = \frac{dx_{det}}{dz_{det}} \tag{5.14}$$

$$y' = \frac{dy_{det}}{dz_{det}}. \tag{5.15}$$

The final pair of relevant variables are x_{bend} and y_{bend}, which specify the position of point C, the location where the track intersects the effective bending plane. We note that these two variables are in magnet coordinates, which means that the axes are reversed relative to detector coordinates. x, x', and y_{bend} are vertical; y, y', and x_{bend} are horizontal.

Apparatus Locations The first step of our calibration was to determine the locations of the target and of the BigBite magnet (via the sieve-slit position) from Hall A survey reports; without knowing their relative positions, it would be impossible to reconstruct the front track. The survey reports also gave initial values for the wire chamber positions, which allowed a more accurate first-order optics model.

In the second step, the positions of the wire chamber were improved and finalized empirically, using runs during which the BigBite magnet was turned off. Without any bending by the magnetic field, the front track aligns perfectly with the back track, and a good reconstruction of the sieve pattern indicates accurate positions for the wire chamber. This calibration was performed for E06-014 by Xin Qian. The resulting sieve reconstruction is shown in Figure 5.8.

Vertex Calibration The third step was to improve the reconstruction of the interaction vertex, using an iterative algorithm and software package developed by Xin Qian [170]. In runs with a multifoil carbon target and the sieve-slit removed from the BigBite magnet face, the first-order vertex-z position $Z_v^{(0)}$ (in Hall A coordinates) could be compared to the absolute reference of that foil's surveyed position. The discrepancy in Z_v may be correlated to one of the six correlation variables. Studying these correlations allows us to define first- and second-order corrections for the vertex-z position

$$Z_v^{(1)} = Z_v^{(0)} + b_1 + a_1 y \tag{5.16}$$

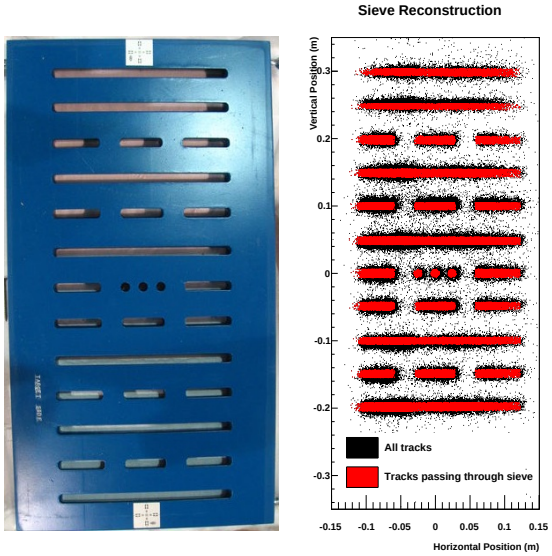

(a) (b)

Figure 5.8: (a) Photograph of BigBite sieve-slit, from Transversity Photo Diary [166]. (b) Reconstruction of sieve pattern from data with the magnet turned off. Black points represent the positions of all tracks in the sieve plane; red points correspond to those tracks which the optics software identifies as passing through a sieve slot.

$$\begin{aligned} Z_v^{(2)} = Z_v^{(1)} &+ \left(a_{20} + a_{21} Z_v^{(1)}\right) + x\left(b_{20} + b_{21} Z_v^{(1)}\right) \\ &+ \left(a_{22} + a_{23} Z_v^{(1)}\right) + y\left(b_{22} + b_{23} Z_v^{(1)}\right) \\ &+ \left(a_{24} + a_{25} Z_v^{(1)}\right) + x'\left(b_{24} + b_{25} Z_v^{(1)}\right) \\ &+ \left(a_{26} + a_{27} Z_v^{(1)}\right) + y'\left(b_{26} + b_{27} Z_v^{(1)}\right) \\ &+ \left(a_{28} + a_{29} Z_v^{(1)}\right) + x_{bend}\left(b_{28} + b_{29} Z_v^{(1)}\right) \\ &+ \left(a_{30} + a_{31} Z_v^{(1)}\right) + y_{bend}\left(b_{30} + b_{31} Z_v^{(1)}\right). \end{aligned} \tag{5.17}$$

There is some redundancy in the expression of Equation 5.17: to show more clearly that the coefficients of each line of the equation are determined independently (in a separate calibration for each variable), the a_{mn} terms have not been recombined, nor have coefficients which go to zero been removed.

Optics corrections are an iterative process, and the procedure defined by Equation 5.17 was immediately repeated to give the third-order vertex position Z_v^3. At this stage, the discrepancies were resolved as well as they could be using only the six variables describing the track position and direction; the next phase of the vertex calibration required the inclusion of momentum-dependent corrections. Using the front track defined by Z_v^3, a first-order momentum $p^{(0)}$ was computed from Equation 5.13. Then first- and second-order corrections – only approximate, due to the wide momentum spectrum of scattering from a carbon-foil target – were defined, based on momentum variations with the six track direction and position variables

$$\begin{aligned} p^{(1)} = p^{(0)} &\cdot \left(c_0 + c_1 y_{bend} + c_2 y_{bend}^2\right) \\ &\cdot \left(d_0 + d_1 x_{bend}\right) \\ &\cdot \left(e_0 + e_1 Z_v^{(3)}\right) \\ &\cdot \left(f_0 + f_1 x + f_2 x^2\right) \\ &\cdot \left(g_0 + g_1 x' + g_2 x'^2\right) \\ &\cdot \left(h_0 + h_1 y + h_2 y^2\right) \\ &\cdot \left(i_0 + i_1 y' + i_2 y'^2\right) \end{aligned} \tag{5.18}$$

$$\begin{aligned} p^{(2)} = p^{(1)} &\cdot \left(j_0 + j_1 x_{bend} + j_2 x_{bend}^2\right) \\ &\cdot \left(k_0 + k_1 y_{bend} + k_2 y_{bend}^2\right) \\ &\cdot \left(l_0 + l_1 p^{(1)}\right). \end{aligned} \tag{5.19}$$

By examining the correlation of the vertex discrepancy with the approximate second-order momentum $p^{(2)}$, we can obtain coefficients for momentum-dependent vertex corrections

$$\begin{aligned} Z_v^{(4)} = Z_v^{(3)} &- x_{bend} Z_v^{(3)} \left(m_0 + m_1 p^{(2)}\right) \\ &+ \left(n_0 + n_1 Z_v^{(3)}\right)\left(o_0 + o_1 p^{(2)}\right) \\ &+ e^{\left(p_0 + p_1 p^{(2)}\right)\left(q_0 + q_1 Z_v^{(3)}\right)}. \end{aligned} \tag{5.20}$$

A second round of momentum-dependent corrections, done according to Equation 5.20, resulted in a fifth-order vertex position $Z_v^{(5)}$.

The final set of vertex corrections relied on a set of lookup tables. The three-dimensional phase space described by $(x_{bend}, y_{bend}, Z_v)$ can be delineated by a fine grid. Any point within the phase space is contained within a cubical volume defined by eight corners with various values of x_{bend}, y_{bend}, and $Z_v^{(m)}$; a linear interpolation between those corners gives the nth-order vertex position $Z_v^{(n)}$. Two additional lookup tables are defined for the phase spaces $\left(x_{bend}, p^{(2)}, Z_v\right)$ and $\left(y_{bend}, p^{(2)}, Z_v\right)$. The final three orders of vertex positions are thus defined by

$$Z_v^{(6)} = f_1\left(x_{bend}, y_{bend}, Z_v^{(5)}\right) \tag{5.21}$$

$$Z_v^{(7)} = f_2\left(x_{bend}, p^{(2)}, Z_v^{(6)}\right) \tag{5.22}$$

$$Z_v^{(8)} = f_3\left(y_{bend}, p^{(2)}, Z_v^{(7)}\right) \tag{5.23}$$

where f_1, f_2 and f_3 are the linear interpolation functions.

In the analysis of each track, the vertex reconstruction begins with the first-order calculation ($Z_v^{(0)}$) and proceeds through each step to a final value given by $Z_v^{(8)}$. The bulk of the calibration, including the look-up tables, was performed by Xin Qian for E06-010, and was extended to E06-014 with minor corrections by Matthew Posik. The calibration was performed with carbon-foil data and 1.23-GeV electrons. Figure 5.9 shows a test of the calibration using carbon-foil data at the full production energy of 5.9 GeV; even at these high energies, we observe 1.0-cm vertex resolution in BigBite.

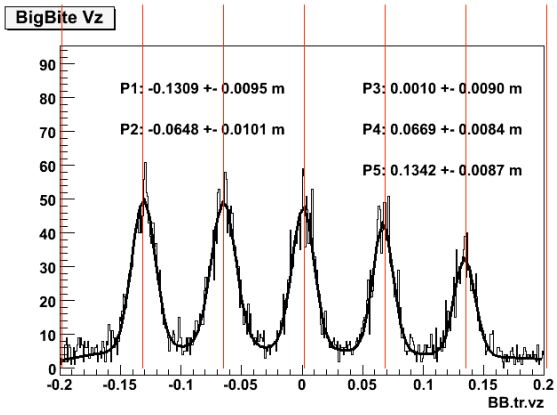

Figure 5.9: Test of vertex reconstruction with 5.90-GeV electrons on the carbon-foil target. Red lines indicate the known positions of the foils. Figure is from M. Posik [240].

Angle Calibration The fourth step of the optics calibration, performed by Xin Qian, relied on runs with both carbon and hydrogen gas targets, taken with the sieve-slit positioned in front of the magnet. The goal was to improve on the first-order estimates of the angles Φ and θ_{bend} (defined in Section 5.2.2.2), which are determined from the front track connecting the final vertex position and the middle point C on the bend plane. At this calibration stage, the alignment of the measured sieve pattern with the predicted sieve pattern is optimized via the inclusion of offsets and higher-order corrections dependent on the vertex position. Once the actual and modeled patterns are in agreement, the angles of the tracks may be taken as accurate to within 10 mrad.

Momentum Calibration With trustworthy values for the vertex position and angles in hand, elastic scattering data from H_2 target runs could be used to perform a calibration of the momentum. The final momentum $p_{elastic}$ of an elastically scattered electron can be calculated exactly from its initial momentum p_i and its scattering angle θ

$$p_{elastic} = \frac{p_i M}{M + p_i\,(1 - \cos\theta)} \tag{5.24}$$

where M is the mass of the target particle. (The electron mass is assumed to be negligible compared to p). The reconstructed momentum of an electron, of known incident momentum, that has undergone elastic scattering from a proton should match the expected momentum $p_{elastic}$ for its observed scattering angle θ; if it does not, and if the angle measurements have already been calibrated, then it is the momentum reconstruction that requires correction.

In the original E06-010 optics model [170], the first correction to the first-order momentum is a linear correction applied to momenta below 0.9 GeV, according to

$$p = \begin{cases} p^{(0)} & \text{for } p^{(0)} > 0.9 \text{ GeV} \\ p^{(0)} + 0.148\,\left(p^{(0)} - 0.9 \text{ GeV}\right) & \text{for } p^{(0)} \leq 0.9 \text{ GeV}. \end{cases} \tag{5.25}$$

The purpose of this correction was to align the secondary W peak in the H_2 BigBite data (see Figure 5.11) to the Δ mass of 1.232 GeV. While the resulting momentum $p^{(0)}$ is continuous at the boundary of $p = 0.9$ GeV, its first derivative is not, introducing a discontinuity in the reconstructed momentum spectrum (Figure 5.10). Further corrections, based on an extensive lookup table, failed to correct this unphysical behavior.

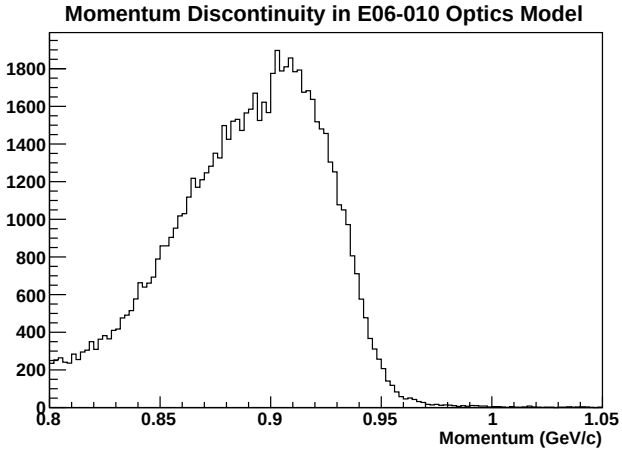

Figure 5.10: Partial momentum spectrum for calibration events with 1.23-GeV electrons incident on a hydrogen target, showing the momentum discontinuity at $p = 0.9$ GeV in the E06-010 optics model.

Subsequently, a simplified Monte Carlo simulation of BigBite showed that the inelastic peak in the W spectrum, which is affected by variations in Q^2 and by the spectrometer acceptance, should not coincide with the Δ mass; instead, it should fall at 1.215 ± 0.005 GeV [148]. We therefore removed the low-momentum correction in Equation 5.25 from the E06-014 optics package, as well as the corrections based on lookup tables; we kept only E06-010's first-order momentum model.

To fine-tune the overall scale factor, we combined data from five runs taken with 1.23-GeV electrons on a hydrogen target. BigBite had negative polarity, so negatively charged particles were bent upward in the magnet; we included only upward-bending particles in our sample. We also excluded tracks that passed through portions of the magnet with large known field gradients, as well as tracks whose scattering vertices were more than 17 cm from the nominal center of the target. Finally, we required a T1 (low shower threshold) trigger for tracks in our sample, since this trigger had the most uniform coverage of the BigBite acceptance.

Figure 5.11 shows the resulting W spectrum, after the overall scale factor from E06-010 has been adjusted by a factor of 1.041. The high, narrow peak contains events for which the electron has undergone elastic scattering from a proton; the low, broad inelastic peak is located at $W = 1.212$ GeV.

To measure the momentum resolution of our optics package, we calculated the discrepancy between the reconstructed momentum p and the predicted momentum $p_{elastic}$ (Equation 5.24) for events in the elastic peak

$$\frac{\delta p}{p} = \frac{p - p_{elastic}}{p}. \tag{5.26}$$

Figure 5.12 shows the result. We achieve a momentum resolution of 1.07%.

5.2.3 Gas Čerenkov

E06-014 was the commissioning experiment for the BigBite gas Čerenkov (Section 3.3.4.2), which was used in the T2 and T7 triggers (Section 3.3.6). Particle identification was the primary purpose of the gas Čerenkov: through the T2 trigger, the Čerenkov was responsible for removing the bulk of incident pions from the online sample. Rates were higher than expected, on the order of 100 kHz on the large-angle side of the Čerenkov and on the order of 1 MHz on the small-angle side. Nonetheless,

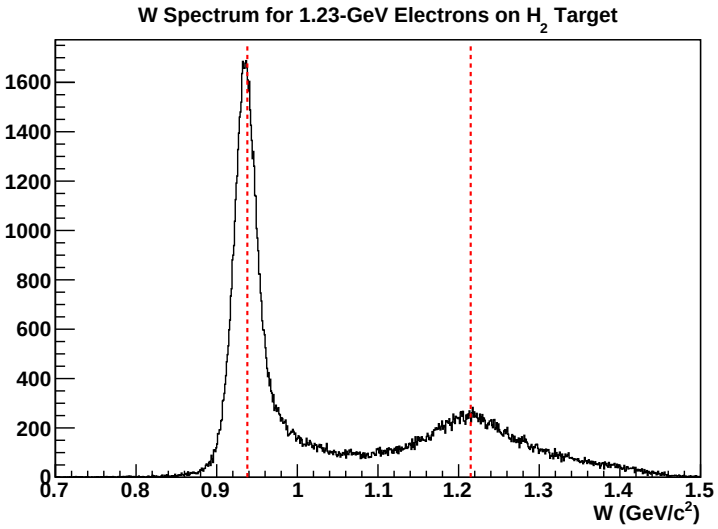

Figure 5.11: W spectrum for 1.23-GeV electrons on a hydrogen target. The dotted red lines mark the proton mass (0.938 GeV) and the predicted location of the inelastic peak.

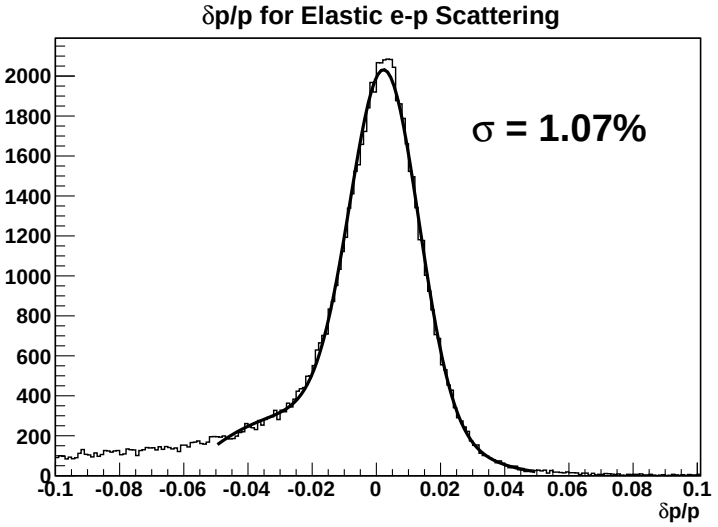

Figure 5.12: Momentum resolution for E06-014 optics package. We have plotted the discrepancy between the reconstructed and predicted momentum (Equation 5.26) for elastic events. The fit function is the sum of a Gaussian and a third-degree polynomial.

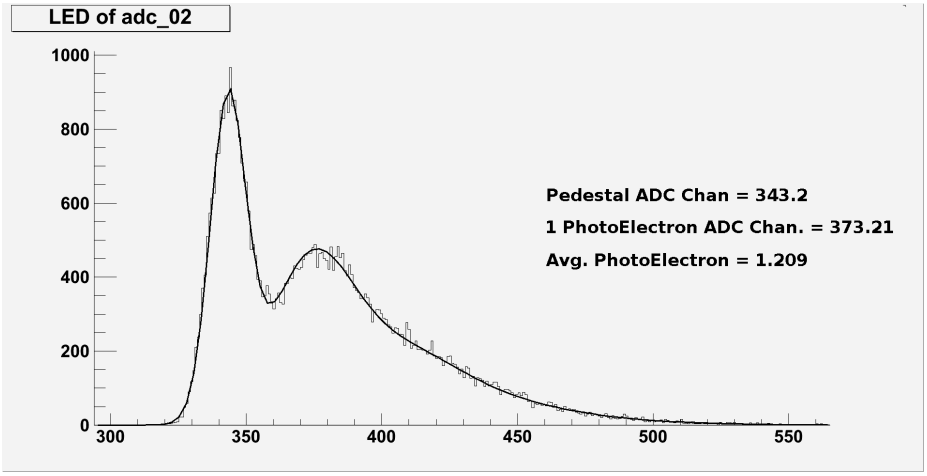

Figure 5.13: ADC spectrum of a BigBite gas Čerenkov PMT for an LED run. Fits to the pedestal and single-photoelectron peak allowed the latter to be aligned at the 30-channel mark. Figure from M. Posik [240].

the inclusion of the Čerenkov in the T2 trigger reduced the trigger rate to the 2-3 kHz range, which allowed data-taking to proceed without prescaling [171].

Including Čerenkov data in the offline analysis further improves our removal of pions from the final sample. This offline analysis requires the calibration of three types of Čerenkov information: ADC amplitudes, TDC timing ranges, and geometrical information about the acceptance of each PMT.

5.2.3.1 ADC Spectra

Signals from the twenty PMTs of the gas Čerenkov, each with coverage of a slightly different region of the detector, are calibrated using special LED runs performed during the experiment. Figure 5.13 shows a representative ADC spectrum from such a run. During the experiment, these data were used to gain-match the PMTs to place the one-photoelectron peak at about 50 mV and the hardware threshold at about the 1.5-photoelectron level; after the experiment, a more detailed analysis allowed the measured spectra to be matched to higher precision in software.

We used a convolution of Gaussian and Poisson functions to fit the pedestal and the single-photoelectron peak, allowing us to adjust our software settings to place the single-photoelectron peak at thirty ADC channels above the pedestal. Any cut on the ADC signal may thus be expressed in terms of number of photoelectrons, rather than in terms of ADC channels. This calibration was performed by Matthew Posik for E06-014.

5.2.3.2 TDC Timing

Timing information for hits in each gas Čerenkov PMT, relative to the shower timing, is recorded in a dedicated TDC channel. Each TDC has a resolution of 0.5 ns [243] and is capable of recording timing information for up to 16 hits, but the hardware settings during E06-014 were such that only the first hit could be used in forming the trigger. A hit recorded by a TDC might be an accidental, or it might be responsible for forming the trigger for that event; to distinguish between these two types of hit, we turn to the spectrum of recorded TDC times.

Figure 5.14 shows the TDC spectrum for PMT17. Atop the spectrum of accidentals, we see two clear structures: a sharp peak, centered at 227 channels for this PMT, and a square-shaped shoulder

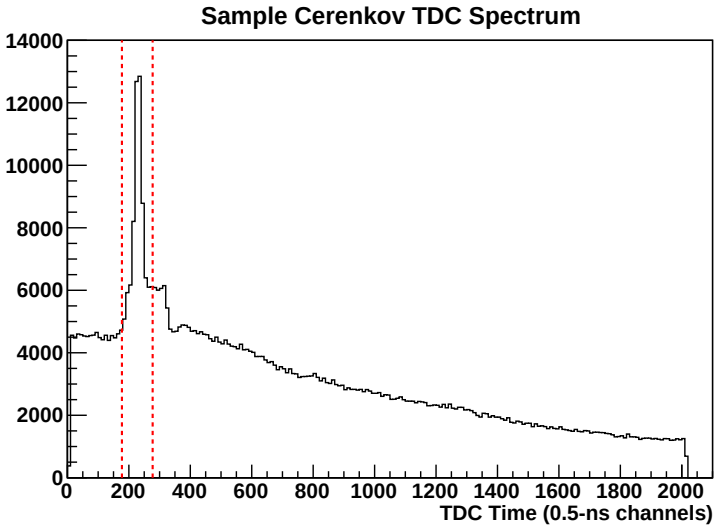

Figure 5.14: Sample Čerenkov TDC spectrum in units of 0.5 ns. The region between the dashed red lines is the trigger timing window used in our analysis.

region whose width is approximately equal to the width of the logic signal generated by T6 (a hit in the shower). The shoulder arises from the fact that the T2 timing is set by the shower hit, rather than by the hit in the Čerenkov: accidentals that fall within the T6 window may cause a T2 trigger.

The region enclosed by the dashed red lines in Figure 5.14 is the trigger timing window; it is about 100 channels, or 50 ns, wide. The precise location of the window varies from PMT to PMT, but is stable over a running period of at least a few weeks. Timing within the trigger window is a necessary condition for associating a Čerenkov hit with the trigger, but it is not sufficient; a significant percentage of hits within the window are accidentals.

5.2.3.3 PMT Acceptance

We wish to associate a particle track in the MWDCs with a hit in the Čerenkov (and, later, with hits in the preshower and shower; see Section 5.2.4.4). If the particle we have tracked was responsible for the T2 trigger, the high hardware thresholds make it more likely to have been an electron rather than a pion. In order to make this determination, we must relate the geometry of the Čerenkov to the trajectories of tracks measured in the MWDCs, so that we can determine which PMT should have observed a particular track.

As we saw in Section 3.3.4.2, the acceptances of the twenty Čerenkov PMTs are defined by the twenty spherical mirrors arranged in two columns in the tank, facing back toward the magnet. For our acceptance study, we take the "Čerenkov plane", or effective mirror plane, as being located 0.8 m downstream from the first MWDC, a somewhat arbitrary choice: we compare the track positions projected forward from the MWDC to this plane, to the effective PMT acceptances on this plane.

Figure 5.15 shows the projected vertical and horizontal track positions on the Čerenkov plane for events taken with the T2 trigger (for which the Čerenkov must fire). The rate difference between the small- and large-angle sides is immediately apparent, as is a dead region in the top half of the magnet. The boundary between the two columns may be seen in the sparse region running up and down the center of the plane; some vertical boundaries between mirrors in each column may also be distinguished.

In order to define the vertical acceptance of each PMT, we must associate the various regions in

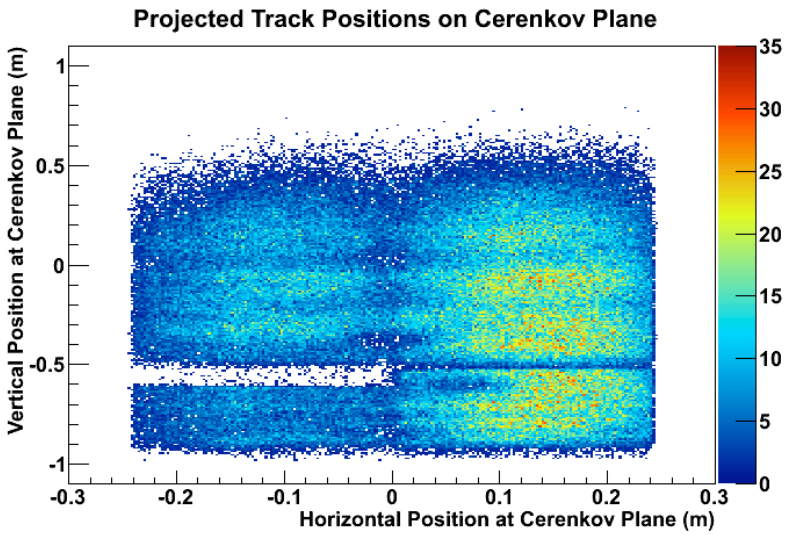

Figure 5.15: Projected track positions on the Čerenkov plane. These tracks are associated with negative particles and T2 triggers. In accordance with Hall A convention, the top of this plot corresponds to the bottom of the BigBite detector stack, and vice versa. The right side of the plot is toward the beamline ("small-angle side"), while the left side is away from the beam ("large-angle side").

Figure 5.15 with their PMTs. We rely on TDC and ADC information to accomplish this identification. If a PMT's TDC has registered a hit in the trigger timing window, and if its ADC shows a signal of at least three photoelectrons, then we assign the projected vertical position for that track to that PMT. This assignment is not exclusive; the PMT may have seen an accidental, or the cone of Čerenkov light associated with the primary track may have straddled the boundary between two mirrors. In such cases, a single track might be associated with several PMTs.

Figure 5.16 shows the result of these assignments for PMTs in the small-angle-side column. Each colored histogram represents the vertical positions, on the Čerenkov plane, for those tracks assigned to a particular PMT. While each PMT clearly sees many accidentals, the division of the vertical acceptance among the PMTs is clear, as well as the several centimeters of overlap between the low-effeiciency edges of the acceptances of each pair of neighboring PMTs. Based on this plot, we set loose boundaries around each vertical-acceptance peak, including the vertical range of tracks that could shed light on each mirror while excluding the bulk of the accidentals; these acceptance boundaries were also valid for the PMTs in the large-angle-side column. Only the topmost quartet of PMTs – PMT08 and PMT09 on the small-angle side, and PMT18 and PMT20 on the large-angle side – were excluded from this analysis, as they were outside the Čerenkov acceptance for negatively charged particles.

The PMTs' horizontal acceptances cannot be assigned with anything like this precision, since the whole horizontal acceptance of the gas Čerenkov is divided between only two columns of mirrors. Figure 5.17 shows the distribution of projected horizontal positions on the Čerenkov plane. The dip near 0 marks the centerline of the mirror arrangement; the rate difference between the two columns is reflected in the relative amplitudes of the positive and negative sides of the histogram.

Since a track passing near the center of the Čerenkov may register as a hit in both a small-angle-side and a large-angle-side PMT, the final horizontal acceptances of the two columns must overlap. We achieve this behavior by placing two boundary lines, bracketing the dip in acceptance at the centerline. A track falls in the small-angle-side horizontal acceptance if its projected horizontal

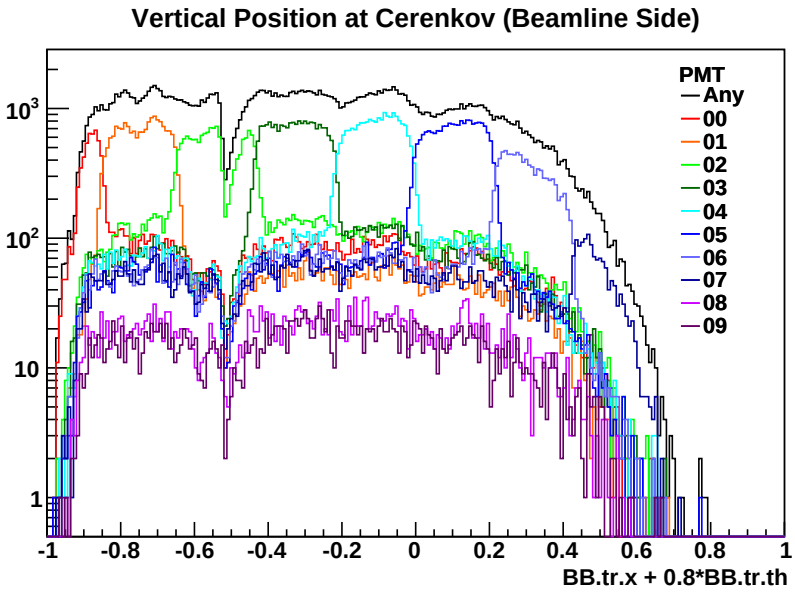

Figure 5.16: Determining the vertical positions of the small-angle-side Čerenkov mirrors. We have projected the tracks to the Čerenkov plane and plotted the distribution of vertical positions in meters, using TDC and ADC cuts to identify each distribution with the acceptance of a specific PMT. The black histogram shows the vertical distribution of tracks for which any small-angle-side PMT has fired; each of the colored histograms represents the vertical distribution of tracks for which a different PMT has fired in particular. In the broad peaks rising an order of magnitude above the accidentals, we can see the vertical distribution and geometrical overlap of the PMT acceptances, from PMT00 at the top of the Čerenkov to PMT07 near the bottom.

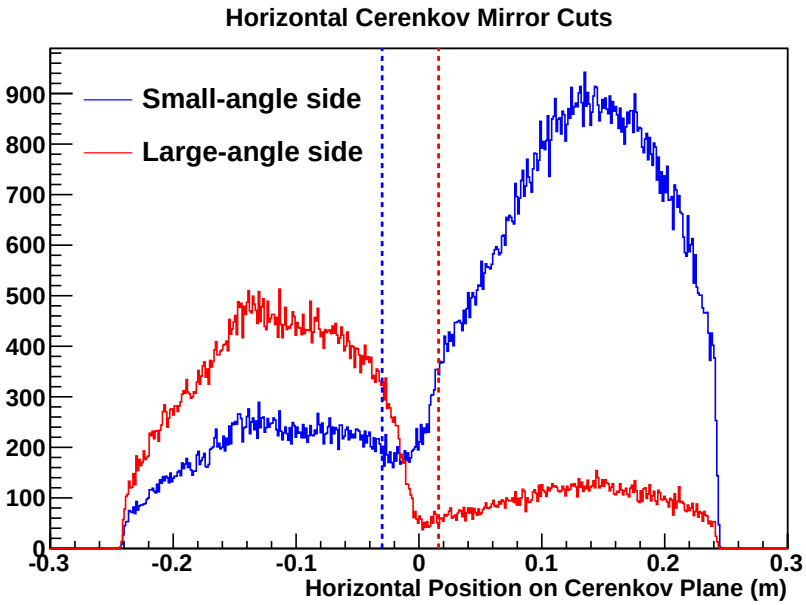

Figure 5.17: Definition of horizontal Čerenkov mirror position cuts. The red histogram shows the distribution of horizontal positions on the Čerenkov plane for events in which one of the large-angle Čerenkov TDCs has fired; for events in the blue histogram, one of the small-angle Čerenkov TDCs has fired. In both cases, we see a sharp dropoff between the true horizontal acceptance of the PMTs and the region populated only by accidentals. To match with a small-angle-side mirror, we require that a track's projected horizontal position fall to the right of the blue dashed line; to match with an large-angle-side mirror, the track position must fall to the left of the red dashed line.

position is more positive than the blue line; it falls in the large-angle-side horizontal acceptance if that position is more negative than the red line.

With this division of the horizontal and vertical PMT acceptances, 99.93% of all tracks fall within the acceptance of at least one PMT, but each track can be identified with a specific subset of PMTs, at least one of which should have fired if the track belonged to a good electron.

5.2.4 Preshower and Shower

The preshower and shower detectors (Section 3.3.4.4) are used in the formation of the T1, T2 and T6 triggers (Section 3.3.6) and in offline energy measurements of the scattered particles; the latter functionality allows us to distinguish electrons from minimum ionizing particles, and to identify possible problems in our data. The amplitude of the signal from each block is proportional to the energy deposited in that block; a typical particle, however, deposits energy in two clusters of blocks, one in each layer. To determine the total energy, we must combine signals from multiple shower and preshower blocks, which requires us to calibrate the signal of each block to a known deposited energy.

5.2.4.1 Rough Hardware Calibration

For a uniform trigger acceptance across the calorimeter, a given energy deposit must produce approximately the same ADC signal, no matter which block of the layer was involved. Each block is mated to a single PMT, which produces a signal whose amplitude is proportional to the energy deposited in the block. Achieving this behavior thus requires adjustment of the high voltage of each PMT so as to equalize the gain across all blocks in a layer.

Cosmic rays are a useful tool in performing this calibration: since high-energy cosmic rays at this altitude are primarily muons, they behave as minimum ionizing particles. For a muon passing vertically through a calorimeter layer, the energy deposited in each block should then be approximately the same. We identify cosmic rays via two plastic scintillators, one at the top of the detector and one at the bottom, and each with two PMTs. A cosmic-ray trigger can then be constructed through a logical AND of all four PMTs, so as to select particles passing vertically down through the calorimeter. In an iterative procedure, the high voltages on the shower blocks are adjusted to align the minimum energy-loss peak to ADC channel 120; the same peak in the preshower blocks is aligned to ADC channel 240 [161]. This rough calibration, good to about 5-10 channels, was performed for E06-014 by Kalyan Allada.

5.2.4.2 Cluster Reconstruction

Before discussing the software calibration of the total energy measured by the calorimeter in Section 5.2.4.3, we must first review the algorithm for reconstructing shower clusters. Since the shower produced by an electron is not confined to a single block, we must combine data from several blocks in order to measure the total energy that the electron has deposited in the calorimeter.

In the analysis of a BigBite event, the cluster reconstruction software begins by finding the shower block that saw the largest energy deposit. This block is taken as the center of a 3×3 cluster whose total energy is the sum of the energies deposited in each of the nine blocks. The procedure is then repeated for the preshower, identifying the 3×2 preshower cluster with the largest energy deposited. In contrast to the E06-010 data analysis, only the clusters with the largest energy are saved.

Where N is the number of blocks in a cluster and E_i is the energy deposited in the i^{th} block, the total energy E of a preshower or shower cluster is calculated according to

$$E = \sum_{i=1}^{N} E_i. \tag{5.27}$$

The x and y positions of each cluster, which are used in data analysis to determine whether a given track and preshower/shower cluster pair could have been produced by the same particle, are computed as the energy-weighted average of the cluster's block positions. Where the coordinates of the i^{th} block are given by (x_i, y_i), we thus have

$$x = \frac{1}{E}\sum_{i=1}^{N} E_i x_i \tag{5.28}$$

$$y = \frac{1}{E}\sum_{i=1}^{N} E_i y_i. \tag{5.29}$$

5.2.4.3 Offline Energy Calibration

The cosmic-ray calibration of Section 5.2.4.1 gives only a rough calibration; to use the calorimeter for particle identification, we must perform a more precise calibration. The result is a set of 243 coefficients C_i, one for each block in the preshower and shower, that transform the measured ADC amplitude to an energy in MeV, according to

$$E_i = C_i(A_i - P_i) \tag{5.30}$$

where A_i is the raw amplitude in the i^{th} ADC and P_i is the ADC pedestal.

We compute all 243 coefficients simultaneously using a linear fit to minimize χ^2, the square of the difference between the reconstructed momentum p and the total energy reported by both the preshower and the shower. Over M good electron tracks, χ^2 is given by

$$\chi^2 = \sum_{i=1}^{M}\left[p_i - \sum_{j=1}^{N^{ps}} C_{ij}^{ps}\left(A_{ij}^{ps} - P_j^{ps}\right) - \sum_{k=1}^{N^{sh}} C_{ik}^{sh}\left(A_{ik}^{sh} - P_k^{sh}\right)\right]^2 \tag{5.31}$$

where $N^{ps} = 6$ and $N^{sh} = 9$ are the number of blocks in a preshower cluster and in a shower cluster, respectively, and the pedestals are measured independently. Errors are assumed to be uniform. The minimization procedure is detailed by Allada [161].

For E06-014, this calibration was performed by Matthew Posik on production data with an incident beam energy of 4.74 GeV, using the reconstructed momentum with its 1.1% resolution as the expected electron energy. Events selected for the calibration had track and shower positions aligned within 3σ. Their tracks passed through understood portions of the BigBite magnet and had an assigned charge of -1. The events passed an electron cut in the gas Čerenkov data as well as a loose E/p cut to select the electron population. Figure 5.18 shows the resulting energy resolution of 8.4%.

5.2.4.4 Calorimeter Position

The calorimeter's energy measurement is a potent tool in particle identification: for an electron, $E \simeq p$, while $E < p$ for a pion. In order to make a meaningful comparison between the energy measured in the calorimeter and the momentum measured in the wire chambers, we must be able to determine whether the same particle could have been responsible for the track through the wire chambers and for the hits in the preshower and shower. As we will discuss in greater detail in Section 6.2.1.4, we test this alignment by comparing the preshower and shower cluster positions to the track position projected to the preshower and shower planes. The effective distance between the first MWDC and each calorimeter plane must be determined in order for this projection to be accurate.

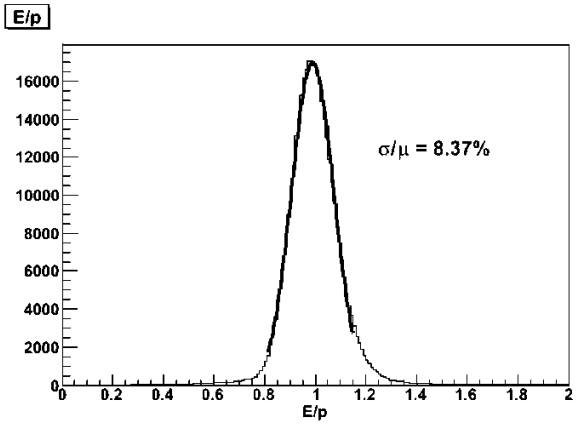

Figure 5.18: BigBite energy resolution for $E_e = 4.74$ GeV. The plot, showing the total energy (measured in preshower and shower) divided by the momentum (reconstructed by the optics package), is from M. Posik [240].

The rough distances from the first MWDC to each calorimeter layer were known (1 m for the preshower, and 1.2 m for the shower). In order to optimize the effective values of these distances, we performed a study of the misalignment between the projected track position and the cluster position. Let x_{cal} be the x position of a shower or preshower cluster, as determined by Equation 5.28. Let x_{tr} and x'_{tr} be the vertical position and slope, respectively, of the track at the first MWDC, the origin of the detector coordinate system. We can then define the vertical misalignment Δx according to

$$\Delta x = x_{cal} - (x_{tr} + d \cdot x'_{tr}) \tag{5.32}$$

where d is the z position, in detector coordinates, of the calorimeter layer in question. A similar equation may be defined for the horizontal misalignment Δy

$$\Delta y = y_{cal} - (y_{tr} + d \cdot y'_{tr})\,. \tag{5.33}$$

Given the low position-resolution dictated by the shower and preshower blocks, the alignment will necessarily be imperfect. If there is an error in d, however, then we will find that the alignment will be systematically worse at larger track angles, since the projected track position will be more and more at odds with the actual position of the particle at the calorimeter. An accurate value of d, then, will eliminate the correlation of Δ_x with x'_{tr} and of Δy with y'_{tr}.

Figure 5.19 shows the results of a sample calibration for the shower. At the nominal distance $d = 1.2$ m, Δx is strongly correlated with x'_{tr}; with a distance value of 1.28 m, however, the correlation has disappeared. Table 5.5 shows the distances determined for the shower and for the preshower.

Layer	d **(m)**
Preshower	0.97
Shower	1.28

Table 5.5: Calibrated distances d between first MWDC and calorimeter layers.

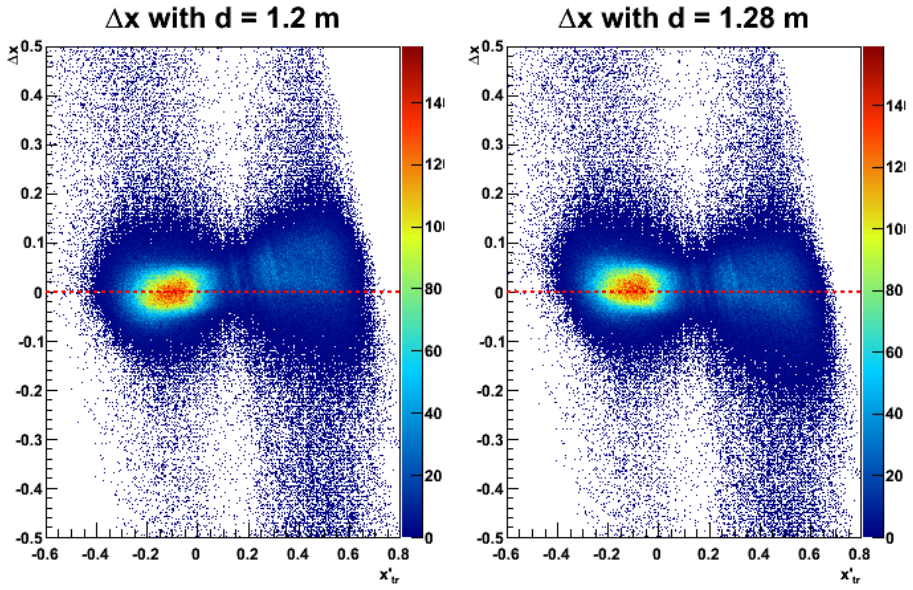

Figure 5.19: Determining the shower position in detector coordinates. We plot the vertical misalignment Δx between shower and projected track position as a function of the track slope x'_{tr}. The correct position d, at right, is the one for which Δx is uncorrelated with x'_{tr}. Positively and negatively charged particles form two distinct populations in this figure. A horizontal line is drawn at $\Delta x = 0$ to guide the eye.

5.3 Energy Loss

In an idealized model, the electron beam would travel through vacuum before striking free ^{3}He gas in a windowless target, and scattered electrons would pass directly through the BigBite magnet and into the detector stack with the same energy they had immediately after scattering. In a real experiment, however, the ^{3}He gas is contained in a glass cell, the experimental hall is not under vacuum, and the electron beam must leave its pipe and enter the target cell before the desired scattering interactions can take place. In traversing these obstacles, high-energy electrons naturally tend to lose energy due to various processes, primarily bremsstrahlung. The radiation length X_0 is the characteristic scale length of these interactions; it is the mean distance in a material over which a high-energy electron's energy is reduced to $1/e$ of its initial value [11, 208].

Table 5.6 summarizes the materials encountered by the electron beam on its way out of the beam pipe and into the center of the target; these comprise a total of 0.0029 radiation lengths. Scattered electrons emerging from the side of the target toward BigBite, meanwhile, encounter about 0.0273 radiation lengths of material, as shown in Table 5.7; most of this is due to the side wall of the target.

The calculated energy-loss values can, in principle, be applied to the optics code as corrections to the reconstructed momentum: the electrons interacting with ^{3}He nuclei have slightly less than their nominal energy, and scattered electrons detected in the wire chambers have slightly less energy than they did immediately after scattering. The mean energy loss in these materials is about 2%, but this dramatically overstates the problem: the mean is dominated by the unlikely occurrence of very, very large energy losses. Geant4 simulations showed that the most likely energy loss for our configuration was only about 0.1% [244], on the level of a few MeV. Applying event-by-event energy loss corrections made no appreciable change to our momentum resolution, so we have ignored them in this work.

Object	**Material**	X_0 **(cm)**	**Thickness (cm)**	**Thickness** (X_0)
Beam pipe exit window	Be	35.28	0.0254	0.00072
Gas in target enclosure	^{4}He	5.281×10^5	22.86	0.00004
Target cell entrance window	GE-180 glass	7.038	0.0121	0.00172
Gas in first half of cell	^{3}He	4.342×10^4	19.8	0.00045

Table 5.6: Materials in the path of incoming electrons. X_0 is the material's radiation length.

Object	**Material**	X_0 **(cm)**	**Thickness (cm)**	**Thickness** (X_0)
Gas between vertex and sidewall	^{3}He	4.342×10^4	1.34	0.00003
Target sidewall	GE-180 glass	7.038	0.156	0.02216
Gas in target enclosure	^{4}He	5.281×10^5	79.05	0.00015
Yellow cover	Plastic	34.5	0.0889	0.00257
Open air	Air	3.042×10^5	150.0	0.00493

Table 5.7: Materials in the path of scattered electrons going to BigBite. X_0 is the material's radiation length. Thicknesses are calculated for a nominal scattering angle of 45°. The type of plastic in the yellow cover is unknown; values were taken for polycarbonate, which has a relatively short radiation length compared to many other plastics.

Chapter 6

Data Analysis

With our detectors calibrated (Section 5.2), we turn to the extraction of meaningful physics information from the data we have collected on disk. In this chapter, we discuss the analysis of the data collected with an incident beam energy of 4.74 GeV, during the final week and a half of the experiment. Although this dataset represents less than half of our production data, it was collected during a period of exceptionally stable running, with no changes to the trigger configuration. The 4.74-GeV data set is thus an ideal testbed for our analysis; we will extend the lessons learned here to our 5.9-GeV dataset, making the necessary adjustments for run periods with different trigger configurations or faulty PMTs.

We begin in Section 6.1 with a discussion of how we analyze our raw data files in order to produce physically interpretable data. In Section 6.2, we give a detailed breakdown of our event selection, which is extremely successful at removing pions and other sources of background from our sample. In Section 6.3, we discuss the calculation of electron-nucleus scattering asymmetries and extract the raw and physics asymmetries for all three target spin configurations in our 4.74-GeV data. Finally, in Section 6.4, we extract the kinematic variables that define the dynamics of each x bin.

In Chapter 7, we will combine these asymmetries and these kinematic variables to form both the electron-nucleus asymmetries $A_{\parallel}^{^3\mathrm{He}}$ and $A_{\perp}^{^3\mathrm{He}}$, and the virtual photon-nucleus asymmetries $A_1^{^3\mathrm{He}}$ and $A_2^{^3\mathrm{He}}$, at which point we will discuss the outlook for finalizing these measurements.

6.1 Analysis Procedure

The conversion of terabytes of raw data[1] into usable, organized physical quantities is a delicate and time-consuming process. For E06-014, the conversion of raw data in CODA files (Section 3.3.7.1) to organized data in ROOT files (Section 3.4) was a two-step process taking advantage of Jefferson Lab's considerable batch computing resources.

The first step was the *replay* step, in which the Hall A Analyzer was used to perform the bulk of the data processing. As described in Section 3.4, the Analyzer includes analysis packages for every type of detector found in Hall A, and matches electronic signals to their hardware sources with the aid of user-written database files. Calibrations performed on a small set of replayed runs gave us a set of further database inputs to translate hardware signals into energies, currents, or positions; the shower and preshower calibration coefficients (Section 5.2.4.3) comprise two such sets of database inputs. With these inputs finalized, we used the Jefferson Lab batch farm to perform a full replay of the entire BigBite data set with polarized 4.74-GeV beam.

A replay using the Hall A analyzer has three stages [144]. In the *decoding* stage, raw data from a CODA event are converted to physical values; for example, a set of TDC values might be read

[1] The 4.7-GeV production data set alone accounts for about 2.2 TB in raw format.

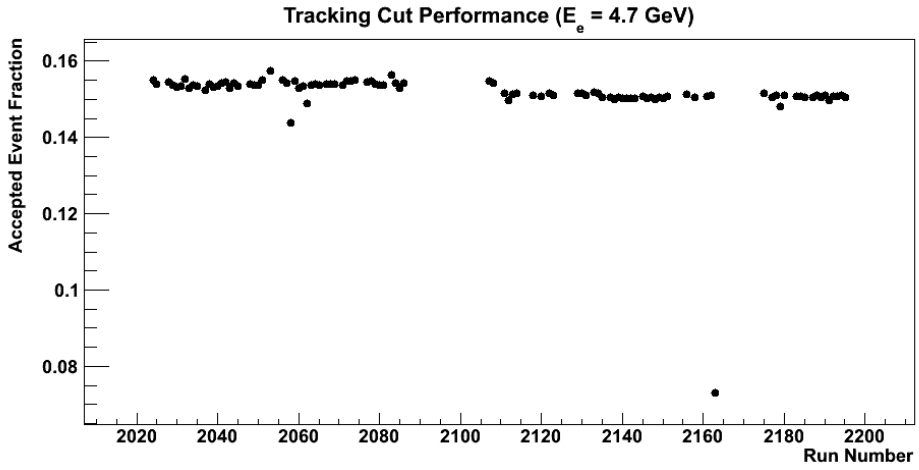

Figure 6.1: Performance of tracking cut over 4.74-GeV dataset. The vertical axis gives the rate at which CODA events met the requirement that they include at least one reconstructed track. The outlier is Run 2163; partway through this run, a poorly seated cable caused multiple pulsing of the T8 (clock) trigger. Consequently, most triggers were not caused by physical particles, and we saw a corresponding drop in the percentage of triggers associated with good tracks.

in from the event buffer, associated with their respective wires in the drift chamber, and converted to drift times. The next stage is *coarse processing*, in which the software produces rough tracks and does quick calculations of certain other detector variables. Some of these variables – such as the measured beam position – are used as inputs for other detectors in the *fine processing* stage, in which the final outputs for each detector – *e.g.* tracks, cluster positions, measured energies and hit timing – are computed.

In order to limit the disk space required for the replayed ROOT files, we imposed a basic tracking cut on our replay software: only events for which a valid track was found were written to disk as part of a ROOT file. This requirement reduced the number of saved events, and consequently the amount of required disk space, by 84% or better, as shown in Figure 6.1.

The second step in our analysis was the *skim* step. After some analysis of each replayed run (*e.g.* to pinpoint beam problems, as described in Section 6.2.1.1), we computed kinematic variables (such as x, W and Q^2) and set boolean flags to enable later cuts on undesirable time periods. We then copied the original replayed ROOT tree to a new file, grafting on these flags and kinematic variables. The final analysis – background studies and the calculation of asymmetries – was performed on these skim files.

6.2 Event Selection

Our goal is an inclusive measurement of an asymmetry in doubly-polarized deep inelastic scattering of electrons from ^{3}He nuclei. In this type of measurement, we must ensure that the scattering events in our sample are valid examples of the events that we seek, in which an electron has scattered somewhere in the volume of the target cell. Final-state hadrons form a significant potential background. So that we may accurately reconstruct the kinematics of the original scattering interaction, the electron must have passed through a region of the BigBite magnet that we understand well, it must have produced a signal in the gas Čerenkov and in the calorimeter, and it must not have re-scattered in pole pieces, coil housings, or other structural components of the magnet and detector stack. In this section, we describe the cuts with which we reduce terabytes of data to a relatively

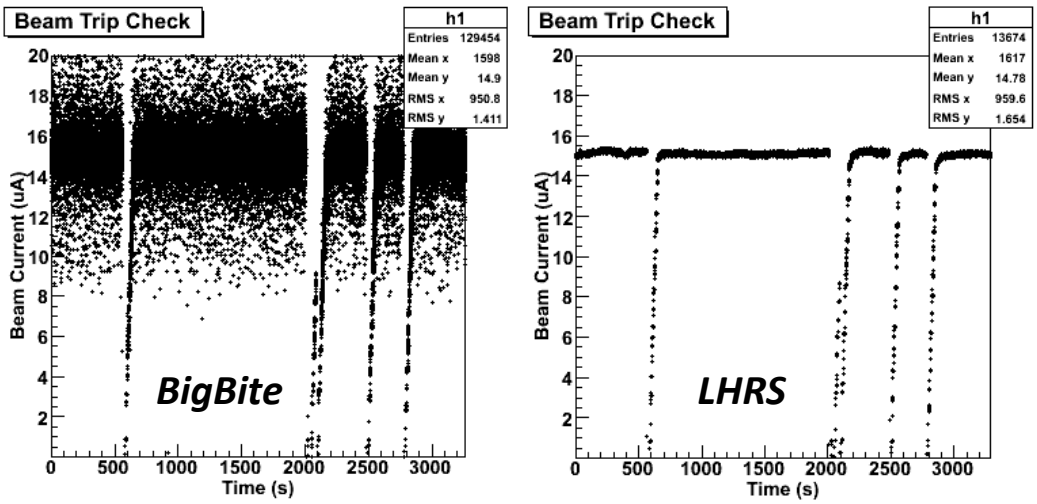

Figure 6.2: Beam-current readouts, converted to μA, in BigBite DAQ (left) and LHRS DAQ (right) for the same period of time. The slower LHRS readout rate effectively averages out the noise.

clean electron sample. As this measurement is preliminary, these cuts are not yet fully finalized.

6.2.1 Data Quality

Our first set of cuts may be broadly described as data-quality cuts. They reject events taken during times when the beam was unstable, electrons with scattering vertices outside the target volume (*e.g.* in the beam-pipe exit window), and particles whose paths took them through poorly understood parts of the magnet. They also impose the requirement that data from the MWDCs and the calorimeter tell a coherent story, *i.e.* that the signals measured in both detectors could plausibly have been generated by the same particle.

6.2.1.1 Beam Stability

Despite the generally high quality of Jefferson Lab's electron beam, beam trips – brief interruptions in beam delivery when the current drops suddenly to zero – were a frequent occurrence during E06-014, especially during periods of extended accelerator problems (Section 3.5). When beam returned after a trip, the current was ramped up to the set point over several seconds in order to avoid damage to the target cell. During this ramp-up period, the beam position and charge asymmetry were unstable compared to normal running [16], and the accumulated beam charge could not be accurately measured since Hall A's beam-current monitors (BCMs, Section 3.3.2.1) are not linear at low currents [170]. For these reasons, beam trips and recoveries must be removed from our final data set.

We identify beam trips using readouts from the $u3$ BCM scaler. Scaler values are read out and stored in the CODA data stream once every 100 triggered reads [170]; 100 consecutive CODA events thus share the same scaler reading before the next update. The scaler rate in Hz, and thus the beam current, is calculated from the count difference between two consecutive scaler readings. In the relatively low-rate scaler readout of the LHRS, the result is a fairly clean description of the beam current as a function of time. The scaler readout rate for BigBite, however, is up to an order of magnitude higher than that of the LHRS; due to the high readout rate, beam-current readings at a setpoint of 15 μA have scatter ranging from 10 to 20 μA, as shown in Figure 6.2. This complicates the

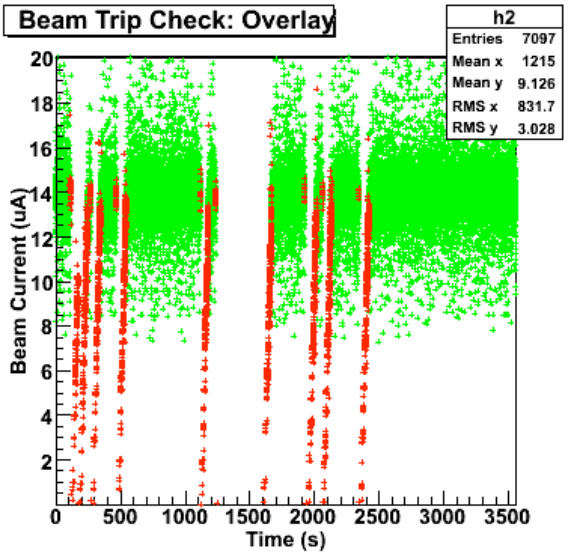

Figure 6.3: Identification of beam trips in BigBite. The plot is of single beam-current readouts, converted to units of μA, as a function of time in second. Red points have been identified as belonging to beam trips (or beam recovery periods) and are excluded from the final data analysis. Green points have been identified as belonging to periods of stable running

problem of selecting and removing true beam trips: we wish to exclude the entire trip-and-recovery period, without excluding normal variation on the reading of the current set-point.

Our solution is to reduce the noise by artificially reducing the readout rate. To produce beam-current samples, BigBite scaler readings are averaged over groups of fifty consecutive readouts. We then fit a Gaussian distribution to the histogram of beam-current samples. Any group of fifty readouts whose average falls within 1.5σ of the overall high-current mean for the run is accepted as belonging to a period of stable running; any group whose average falls outside that window is rejected. We identify the edges of each beam trip with a pair of time stamps marking the transitions between accepted and rejected readout groups. On average, fifty consecutive BigBite scaler readouts account for about 1.25 seconds of runtime, so the identification of beam trips using this method is still fairly fine-grained.

The identification of beam trips proceeds in two stages. First, the beam-current fits and the identification of the acceptable current windows are performed automatically, and a database of the time stamps defining each cut is generated. These functions are performed on a run-by-run basis, since the beam-current setpoint may vary from run to run; for example, a high online deadtime during one run may have led the shift crew to request a lower operating current for the next run. Once this first stage is complete, a plot like Figure 6.3 is generated, overlaying the rejected beam-current readouts onto the accepted ones. The second analysis stage consists of the visual examination of these plots, checking for false positives or false negatives. The cut time stamps are then modified so that every beam trip is fully accounted for and so that false beam trips (typically at the beginning of the run) are removed.

During the skim stage of the global analysis, a flag is set for each event whose time stamp falls within one of the beam-trip windows for that run. A cut on this flag removes these events from the analysis.

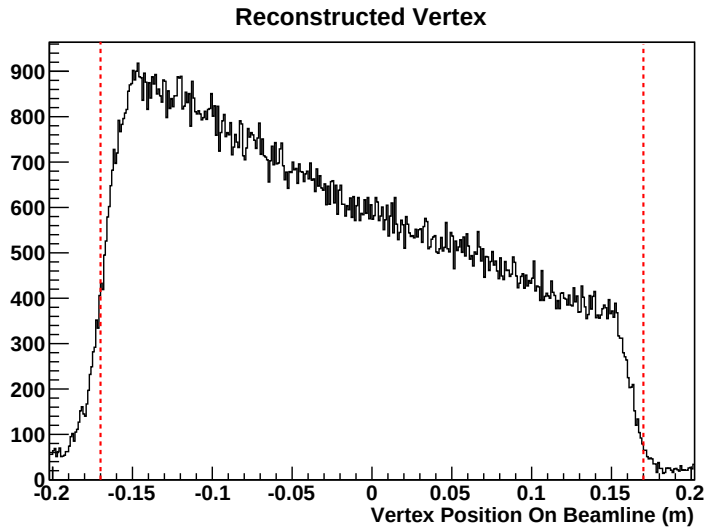

Figure 6.4: Scattering vertex reconstruction for a run with 4.74-GeV electrons incident on a polarized ^{3}He target. All scattering events pictured have passed cuts designed to ensure that they are electrons with valid tracking and optics information. If the reconstructed vertex position along the beamline falls between the dashed red line, it passes the cut on vertex location.

6.2.1.2 Location of Scattering Vertex

We are interested in events in which electrons have scattered from ^{3}He nuclei; the ^{3}He in our target is contained within a glass cell whose 40-cm axis is oriented along the beamline. Any scattering events of interest, then, must originate within the volume contained by the glass cell. To limit background rates from the windows of the target cell, a tungsten-powder collimator with a 10-cm thickness was installed between each target window and the BigBite spectrometer [170]. Further background reduction must be achieved via a software cut on the location of the scattering vertex, as reconstructed by the optics package (Section 5.2.2).

Figure 6.4 shows a typical distribution of reconstructed vertex positions for apparent electrons. As shown by the dashed red lines, we require the scattering vertex to fall within 17 cm of the nominal target center at $z_v = 0$ m.

6.2.1.3 Particle Paths Through Magnet

Our first-order optics model (Section 5.2.2.2) assumes a uniform magnetic field throughout the BigBite magnet, but this is more accurate for some parts of the magnet than for others. In regions where the field strength deviates significantly from our model, we must either make path-dependent corrections to the momenta of the affected particles, or we must remove the regions from consideration by cutting out particles whose tracks have passed through them. Given the high production statistics in BigBite and the relatively small amount of elastic calibration data, as well as the fact that the asymmetries we seek to measure do not depend on normalization, we elected to ignore problematic regions of the magnet.

Optics Validity Cuts Tracking and optics reconstruction algorithms sometimes fail; depending on the implementation of these algorithms, this failure may result in some physical quantity being set either to zero or to some very large number. We remove such failed tracks from our analysis by imposing a very loose cut on the reconstructed momentum

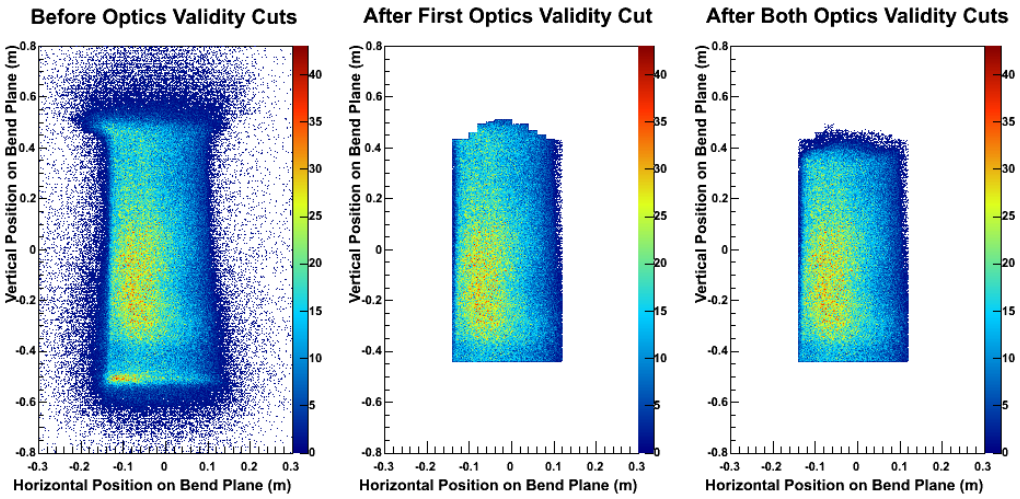

Figure 6.5: Geometrical optics validity cuts. At left is the distribution of all track intersection points with the bend plane during a typical production run; in the center are the track intersection points that survive the first optics validity cut, based on track intersection with bend plane; and at right are the track intersection points that also survive the second optics validity cut, based on front-track slope. Per Hall A convention, the top of the magnet is at the bottom of each plot, and the beam direction is to the right.

$$0 < p < 10 \text{ GeV/c}. \tag{6.1}$$

This removes both tracks with zero momentum (which should not be traveling through our wire chambers at all) and tracks with putative momenta too high to have resulted from the scattering from a fixed target of electrons with initial energy less than 6 GeV.

We also impose two geometric cuts ensure that we reject particles that have passed through portions of the BigBite magnet where a high field gradient renders our optics reconstruction untrustworthy. The first geometric cut in the magnet is based on the position at which the projected front and back tracks intersect with the bend plane, which bisects the magnet. If the particle passes through an undesirable region near the edge of the bend plane, it may be inferred that it passed through an undesirable part of the magnet volume as well. This cut was set by Xin Qian [170], whose optics model for E06-010 is the basis for the E06-014 optics. The optics code sets a flag for tracks that fail this cut. Figure 6.5 shows the distribution of track positions on the bend plane before (left) and after (center) this cut.

For E06-014, we tightened this cut by adding a second geometric cut targeting the bottom of the magnet. Even in the region accepted by the first cut, the field gradient is quite high and complicates any attempts at a systematic correction; the resulting reconstructed momentum is thus overstated. We found that a cut on x'_{tg}, the vertical slope of the front track – the particle's trajectory between the scattering vertex and the magnet – is the cleanest way to remove tracks affected by this problem. A study of elastic-scattering data led us to set this cut so as to require $x'_{tg} < 0.2$, as this boundary marks a sharp change in the reconstructed momentum. The rightmost panel of Figure 6.5 shows the acceptance at the bend plane after applying both optics validity cuts.

Re-Scattering Cut The BigBite magnet is not entirely free of obstructions. If an electron strikes an iron pole piece or coil housing, it will start to shower prematurely, resulting in an artificially

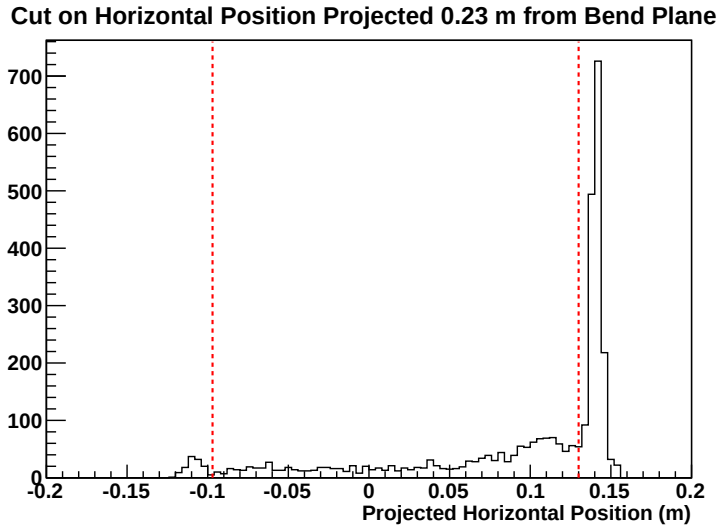

Figure 6.6: Projected horizontal position of low-energy ($E < 1$ GeV), high-momentum ($p > 1.5$ GeV/c) particles on a plane 0.23 m upstream of the BigBite bend plane. The peaks at the extremes presumably correspond to re-scattering locations. The re-scattering cut accepts only those tracks whose projected horizontal positions on this plane fall between the dashed red lines.

low energy deposit measured in the calorimeter. If the electron re-scatters so as to strike the wire chambers, vertex and momentum reconstruction will be affected; such tracks often mimic stiff, or high-momentum, tracks.

To study this problem, we investigated the behavior of particles whose energies, measured in the calorimeter, were less than 1 GeV, and whose reconstructed momenta were greater than 1.5 GeV/c. It emerged that such particles are disproportionately likely to intersect the bend plane at its horizontal edges. By measuring the correlation between these track's horizontal positions on the bend plane and their horizontal slopes at the wire chambers, we determined that re-scattering likely began on a plane 0.23 m upstream of the bend plane. When we plotted the projected horizontal position on this plane, we found well-defined peaks at either extreme, as shown in Figure 6.6: low-energy, high-momentum tracks are strongly associated with paths that cross the horizontal edges of the bend plane. To remove these tracks from our sample, as well as re-scattered tracks that are less severely affected, we placed a cut on the projected horizontal track position on the plane 0.23 m upstream of the bend plane. The boundaries of this cut are shown by the red lines in Figure 6.6: tracks within the red lines are accepted, and tracks outside the red lines are rejected. Where y_{bend} is the horizontal position, in detector coordinates, of the track's intersection point with the bend plane, and y' is the horizontal slope of the track in the wire chambers, this cut is defined by

$$-0.097\text{m} < 0.23\text{m} \cdot y' - y_{bend} < 0.13\text{m}. \tag{6.2}$$

6.2.1.4 Track-Calorimeter Alignment

The energies measured in our calorimeter layers are crucial for particle identification and the subsequent removal of hadrons from our data set. In order to compare measured energies to reconstructed momenta, however, we must ensure that the two quantities belong to the same particle. To do this, we test the distance between the central position of the shower in each layer (as computed by Equations 5.28 and 5.29) and the track position projected to that layer. The projection distance for each

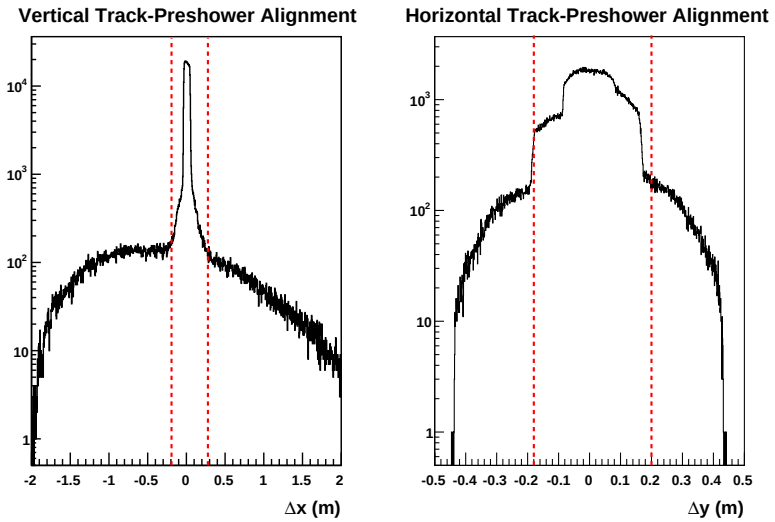

Figure 6.7: Vertical (Δx, left) and horizontal (Δy, right) misalignment between the preshower position and the track position projected to the location of the preshower detector. Tracks whose Δx and Δy fall between the appropriate set of dashed red lines are accepted by the track-preshower misalignment cut defined in Table 6.1.

layer is its location in detector coordinates, from Table 5.5.

Recall from Section 5.2.4.2 that the preshower and shower cluster reconstruction are independent of each other: the replay software simply looks for the cluster with the largest energy deposit in each layer. Since data from both layers are combined to compute the total energy deposited by the particle, we must check the misalignment of both the preshower and shower cluster positions with the projected track position.

Figure 6.7 shows the vertical and horizontal misalignments (Δx and Δy, computed according to Equations 5.32 and 5.33, respectively) between the preshower cluster position and the track position projected to the preshower detector. Tracks for which the preshower and projected track positions are correlated make up the peaks near 0 in each distribution; we reject the broad, flat distribution of accidentals by accepting only tracks for which Δx and Δy fall between the two red lines. Figure 6.8 shows the Δx and Δy distributions and cut definitions resulting from a similar analysis of the shower detector.

Table 6.1 gives the final definition of the cuts on Δx and Δy for both calorimeter layers.

Layer	**Accepted Δx range (m)**	**Accepted Δy range (m)**
Preshower	$-0.192 < \Delta x < 0.278$	$-0.18 < \Delta y < 0.20$
Shower	$-0.1 < \Delta x < 0.1$	$-0.1 < \Delta y < 0.1$

Table 6.1: Definition of track position misalignment cuts for preshower and shower detectors.

6.2.1.5 Track Quality

The quality of a track may be determined from its residuals: how well does the computed track position in each wire plane agree with the reconstructed hit position in that plane? Accordingly, we may define a χ^2 value for each track

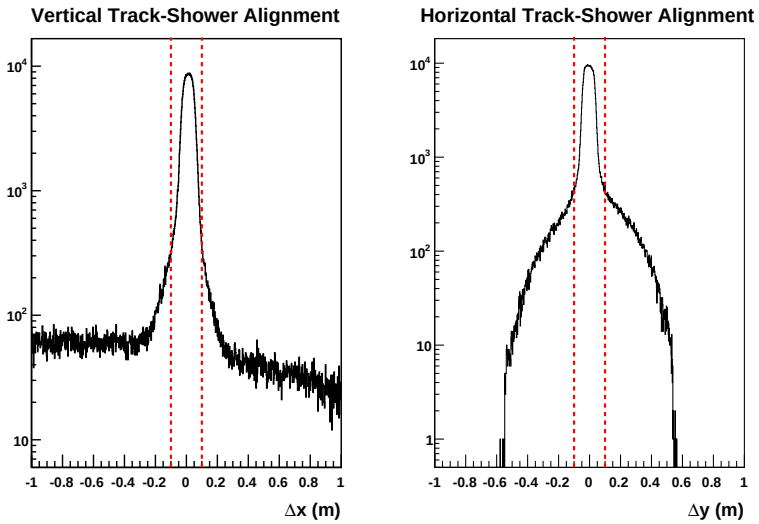

Figure 6.8: Vertical (Δx, left) and horizontal (Δy, right) misalignment between the shower position and the track position projected to the location of the shower detector. Tracks whose Δx and Δy fall between the appropriate set of dashed red lines are accepted by the track-shower misalignment cut defined in Table 6.1.

$$\chi^2 = \sum_i \frac{\left(x_i^{reconstructed} - x_i^{track}\right)^2}{R_i^2} \tag{6.3}$$

where the x values represent the track and hit positions in the i^{th} plane (recall that each plane produces a one-dimensional position measurement) and R_i is the plane resolution used in the tracking software [161].

The fit for each track also has a certain number of degrees of freedom, N_{dof}. This value is equal to the number of data points used in the track fit – *i.e.* the number of planes that fired – minus the number of parameters adjusted by the fit. Each track has four independent parameters – the positions x and y and the slopes x' and y' – so we have

$$N_{dof} = N_{planes} - 4. \tag{6.4}$$

As we saw in Section 5.2.1.2, the tracking algorithm is programmed to incorporate data from at least fifteen planes in its analysis. For the majority of tracks, then, $N_{dof} = 11$.

Dividing χ^2 by N_{dof} gives us χ^2/N_{dof}, the classic measurement of fit quality. For good fits, this value should be close to one. As we see in Figure 6.9, the quantity denoted χ^2/N_{dof} by the BigBite tracking software peaks at a value significantly less than one, as the assumed resolution values are too high. This quantity is still a useful measure of track quality, but to avoid confusion with the classic measurement, we will denote it k^2/N_{dof}. Somewhat arbitrarily, we place our k^2/N_{dof} cut at

$$k^2/N_{dof} < 5 \tag{6.5}$$

as shown by the dashed red line in Figure 6.9. The track k^2/N_{dof} value does not seem to be correlated with unusual or unphysical reconstructed particle behavior.

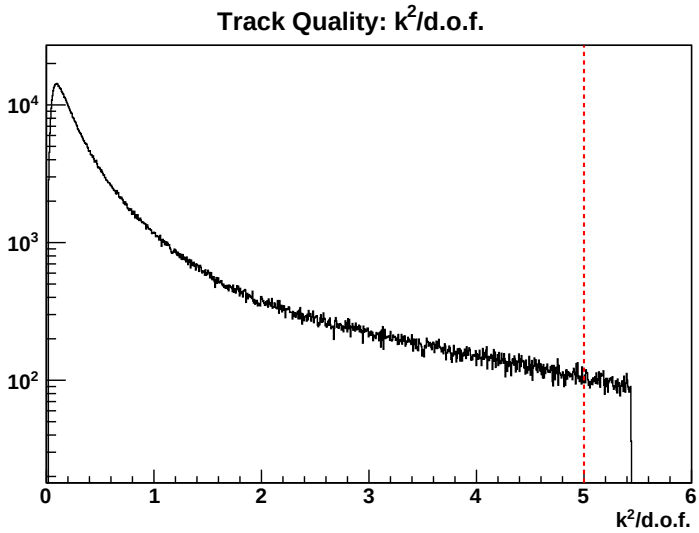

Figure 6.9: k^2/N_{dof} distribution for all tracks in a typical production run. The track-quality cut accepts tracks whose k^2/N_{dof} values are to the left of the dashed red line.

6.2.2 Particle Identification

The second category of cuts targets tracks that appear to be physically valid but may not belong to electrons scattered from the target. These particles are typically pions, positrons, or protons; electrically neutral particles are excluded by the requirement of valid tracking. To exclude particles that are not electrons from our sample, we turn to charge information, trigger information, and energy deposition profiles in the calorimeter.

6.2.2.1 Charge Cut

Since we seek an asymmetry in inclusive scattering, the only final-state particle we wish to measure is the scattered electron. The most fundamental cut we can make is a requirement that any particle included in our measurement have negative charge – that is, it bends upward in the BigBite magnet in its standard, negative-polarity configuration. As discussed in Section 5.2.2.1, the sign of the particle charge is determined as part of the replay software's optics package. We require that the charge be negative, which eliminates approximately 40% of tracks at a single stroke.

6.2.2.2 Trigger Cuts

Our next set of particle-identification cuts is related to the BigBite trigger. The primary trigger during E06-014 production running was the T2 trigger; as we saw in Section 3.3.6.2, this trigger is formed from a geometrical overlap of signals from the shower and from the gas Čerenkov. The latter detector, which is sensitive to a particle's velocity rather than to its total energy, removed most pions from the online trigger by imposing a hardware threshold on the amount of light deposited in a given PMT (Section 5.2.3).

In the offline analysis, our electron sample may be further improved via a requirement that the particle under consideration could have been responsible for a T2 trigger. This removes particles that were accepted due to other, prescaled triggers, as well as accidentals during T2 trigger windows.

T2 Trigger Cut First, we require the T2 trigger to have fired during the CODA event in question. This is enforced by means of the trigger word, a byte of information that encodes the value of each trigger (1 if the trigger has fired, 0 if it has not) as a single bit. The existence of prescaling means that the trigger bit need not be set to 1 every time the trigger condition is satisfied, but T2 data were not typically prescaled during E06-014. By requiring that the T2 bit be set to 1, we ensure that a T2 trigger is associated with every CODA event that contributes to our sample.

Gas Čerenkov Cuts The next question is whether a particular particle can have been responsible for the T2 trigger. We combine gas Čerenkov and tracking data to find the answer. For each of the twenty PMTs in the gas Čerenkov, we test three conditions:

1. Did the PMT record a hit in its TDC?
2. Did the timing of this hit fall within the trigger timing window for that TDC, as described in Section 5.2.3.2?
3. When we project the track to the Čerenkov plane, does its position fall within the geometrical acceptance of this PMT, as determined in Section 5.2.3.3?

If, for any PMT, the answer to all three of these questions is "yes", then the track passes the gas Čerenkov cuts: it can reasonably be supposed to have caused the trigger.

No cut on Čerenkov ADC levels is used; such a cut was found to reduce statistics fairly uniformly across the board, without improving the characteristics of the sample. Low ADC levels tend to be associated with tracks that pass near the edges of the PMT acceptance [240], so that the total signal is shared between two or more PMTs (and their associated ADCs). This makes the use of a hard threshold on a single ADC inappropriate.

6.2.2.3 Calorimeter Cuts

The two layers of the BigBite calorimeter, the preshower and shower, allow us to distinguish between electrons and non-showering particles by means of their energy deposition profiles (Section 3.3.4.4). In the preshower layer, with its depth of only 8.5 cm, particles that do not shower deposit only a small amount of energy; in the calorimeter as a whole, electrons are the only negatively charged particles that may be expected to deposit nearly all of their energy.

Preshower Energy Deposit The low preshower energy deposit characteristic of non-showering particles gives us a powerful tool for studying pion contamination of the sample. Figure 6.10 shows the pion energy spectra of three types of events, all of which have passed our charge cut (Section 6.2.2.1) and our data-quality cuts (Section 6.2.1). If we consider only events that have been rejected by the Čerenkov timing and acceptance cuts defined in Section 6.2.2.2, we see a spectrum that is dominated by pions, with a strong peak at about 100 MeV. Applying the Čerenkov cuts suppresses this peak dramatically; adding a cut on E/p (Equation 6.7 below) eliminates the visible signs of pion presence in the sample.

We set a cut on preshower energy at

$$E_{ps} > 200 \text{ MeV} \tag{6.6}$$

as marked by the dashed black line in Figure 6.10. Even without the assistance of the Čerenkov cuts, this cut would eliminate the bulk of pions. Combining the preshower cut, Čerenkov cuts and E/p cut renders pion contamination negligible.

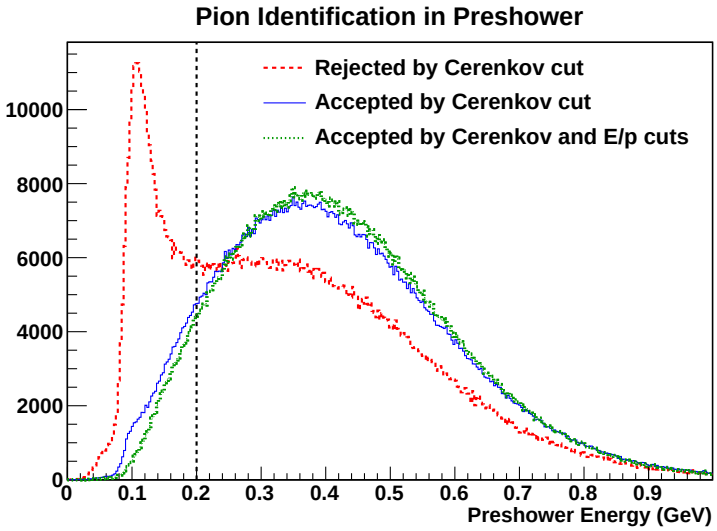

Figure 6.10: Definition of preshower energy cut. The three histograms, scaled to equal area, show the distribution of deposited energy in the shower for three samples of events that have passed the charge and data-quality cuts. Events that have been rejected by the Čerenkov cuts (red dashed curve) show a strong pion peak, but this peak is almost entirely suppressed by the application of the Čerenkov cuts (solid blue line). The addition of a cut on E/p (green dotted curve) removes this final visible vestige of pions. The location of the preshower energy cut is marked by the vertical, dashed black line.

Energy-Momentum Ratio In the kinematics of E06-014, the rest mass of the scattered electron is negligible compared to its momentum. Since an electron should deposit nearly all of its energy in our calorimeter via an electromagnetic cascade, we anticipate that such particles should have $E \approx p$, or $E/p \approx 1$.

Figure 6.11 shows the distribution of E/p values for events that pass all the cuts described up to this point. In order to place a cut on this variable, we fit a Gaussian distribution to the peak; only events that fall within 2σ of the mean, as shown by the dashed red lines, are accepted. The cut is defined as

$$0.833 < \frac{E}{p} < 1.158. \tag{6.7}$$

6.2.3 Cut Performance

Taken together, the cuts defined in Sections 6.2.1 and 6.2.2 provide us with a remarkably clean sample of scattered electrons. Figure 6.12 shows the cumulative effect of applying each cut to the sample from five production runs; in the end, we are left with a clean, approximately Gaussian distribution centered at $E/p = 1$. About 17.8% of tracks survive the complete set of cuts, including the E/p cut.

Our resulting sample is extremely clean. To better understand the source of any remaining background, we studied the black histogram in Figure 6.12: the E/p spectrum when all cuts, except for the 2σ cut on E/p itself, have been applied. We divided the data in the range $0.1 < x < 1.0$ into nine bins of uniform width and plotted the equivalent of the black histogram for each. We then experimented with fitting various functional forms to the E/p spectrum in each x bin; the sum of four Gaussian distributions, one of which is centered on the E/p peak, produced the best results.

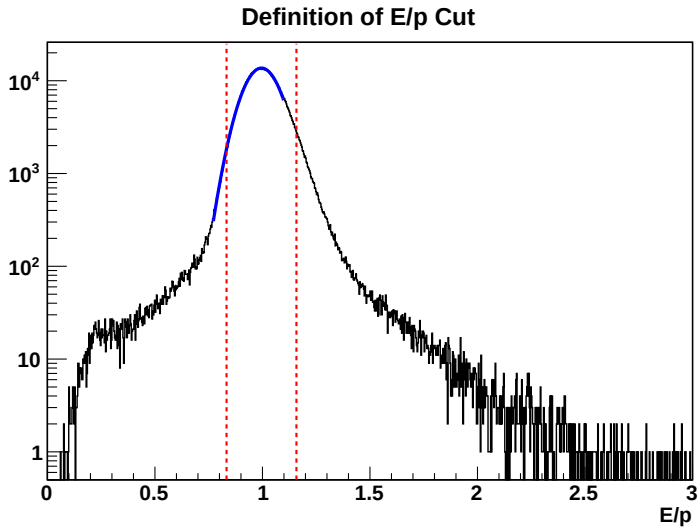

Figure 6.11: Definition of E/p cut. The blue line shows the fit to the electron peak; the dashed red lines give the boundaries of the 2σ cut. Note the logarithmic scale.

Figure 6.13 shows the data and corresponding four-Gaussian fit for each x bin.

With a functional description of the E/p spectrum, we may attempt to separate signal from background in the model, using the fit to the overall E/p peak shown in Figure 6.11. If one of the Gaussian functions making up the binned fit function has a mean that falls within 3σ of the E/p mean in the overall fit, we assume that it is signal; if the mean falls outside that range, we assume that it is background of some kind. This relatively wide signal region prevents us from classifying as background a sizeable population of events with $E/p \sim 1$, based solely on a fit to fewer than 20 events at low E/p, in the $0.2 \leq x < 0.3$ bin. Figure 6.14 shows the resulting models for signal (blue) and background (red) in each x bin.

We may use these results to estimate the degree to which background contaminates the final sample. We integrate both the signal and background functions over the acceptance region defined by the E/p cut (Equation 6.7). The relative amount of background contamination f_{bg} is then the ratio of the number of accepted events from the background function N_{bg} to the total number of accepted events

$$f_{bg} = \frac{N_{bg}}{N_{bg} + N_{sig}}. \tag{6.8}$$

where N_{sig} is the number of accepted events from the signal function. The modeled f_{bg} value for each x bin is given in Table 6.2, along with the percentage of modeled signal events that are rejected by the E/p cut.

This model of the background suggests that a negligible number of pions are present in the final sample. We expect pions to have relatively low measured energy relative to their reconstructed momenta, and to be more numerous at moderate values of x, like electrons. As we see in Figure 6.14, it is only in the higher x bins that the dominant source of background has $E/p < 1$. Furthermore, we expect pions of any momentum to deposit an approximately constant, low amount of energy in the preshower layer, when compared to the energy deposited in the shower. Figure 6.15 shows, however, that the background events that survive our cut on preshower energy do not show this relationship; instead, in any given x bin, they look much more like electrons from a different x bin. We conclude that errors in the reconstructed momentum comprise the dominant source of background in our

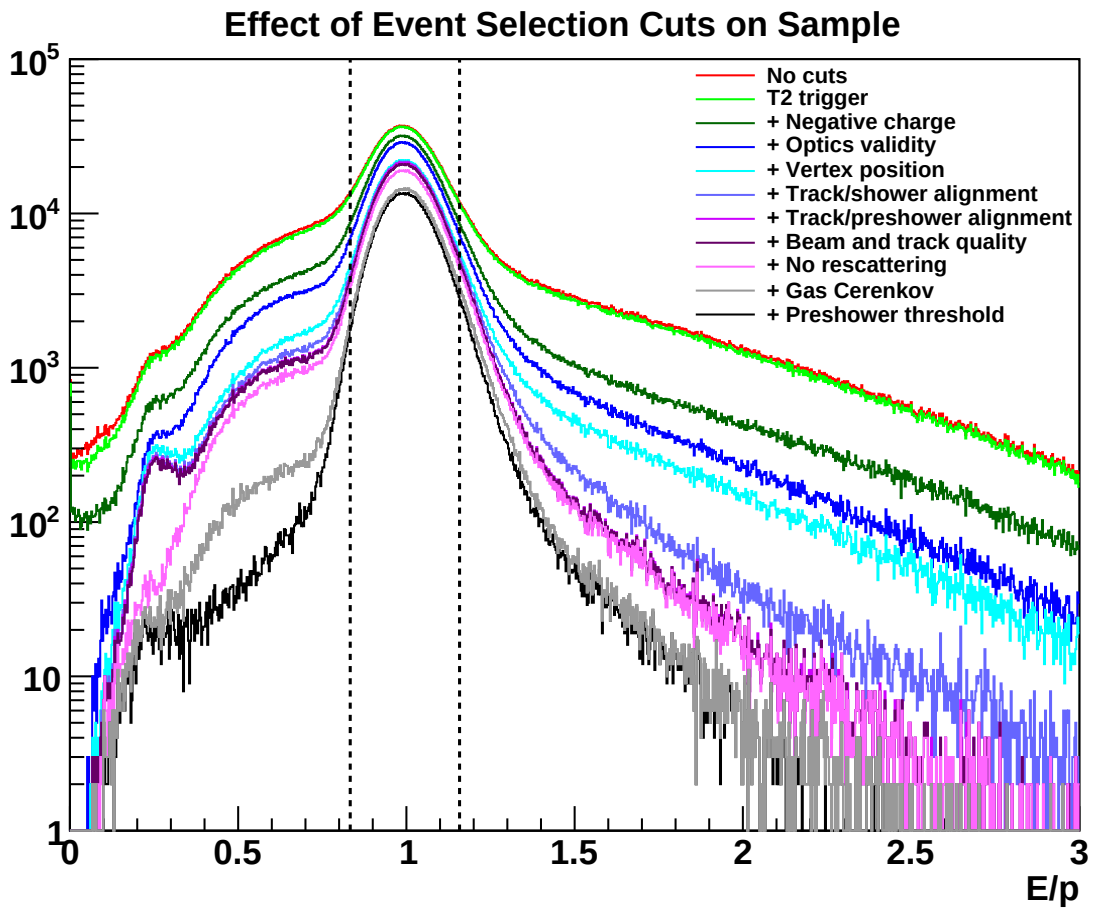

Figure 6.12: Electron sample after cumulative application of each cut. The red histogram represents the raw sample with no cuts applied; the light-green histogram shows the sample once a cut on trigger type has been applied. Each successive cut, applied to those events that survive the previous cuts, reduces the total number of events and reduces or eliminates a source of background. The final cut, on the value of E/p, admits events in the black histogram that fall between the dashed lines.

final sample; in extreme cases, such errors may result in the assignment of an event to a radically incorrect x bin. The resulting error on the asymmetry measured in a given x bin may be estimated by multiplying the contamination factor f_{bg} by the measured asymmetry in the most populated x bin, *i.e.* the most likely source of mis-binned electrons. More detail about this determination will be given in Section 6.3.5.

6.3 Asymmetries

Our goal is to measure an asymmetry in the scattering cross sections for two spin configurations. If all other experimental parameters (*e.g.* cuts, acceptance, beam energy, beam and target polarization, etc.) are held constant, the raw experimental asymmetry will manifest itself as an asymmetry in observed counts

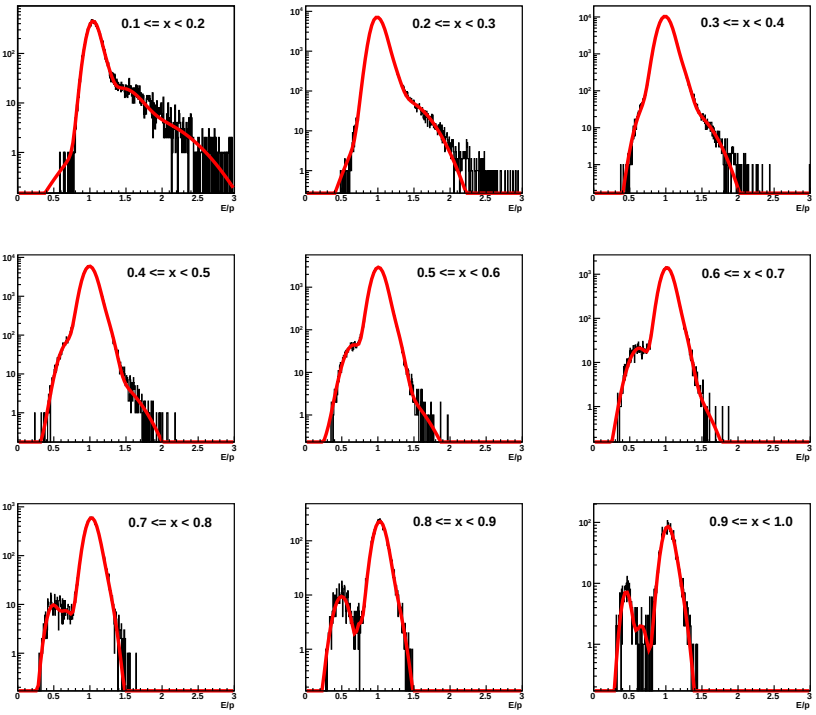

Figure 6.13: Fit of the sum of four Gaussians (red curve) to the measured E/p spectrum (black histogram) in nine x bins. Note the logarithmic scale. In the $0.0 < x < 0.1$ range, there were insufficient data to perform a fit.

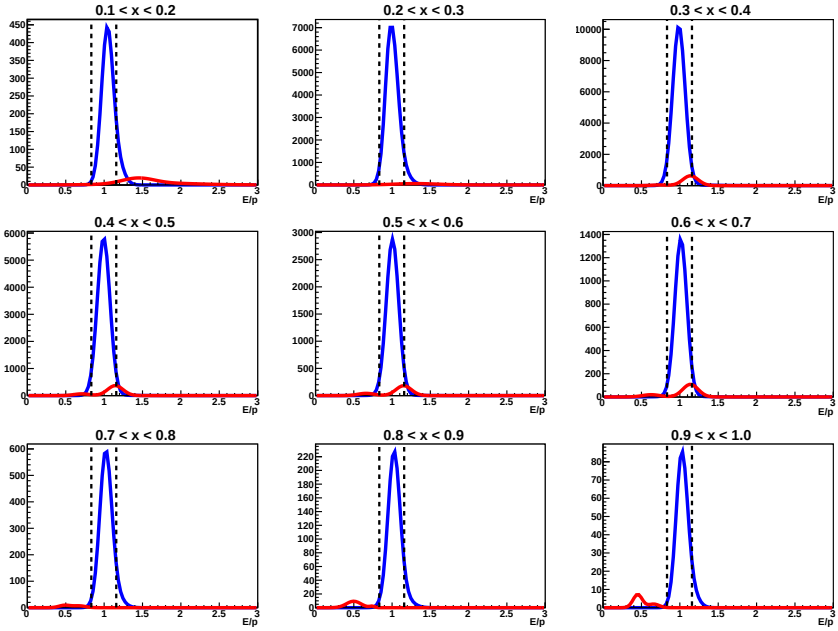

Figure 6.14: Signal (blue curve) and background (red curve) in the E/p fits shown in Figure 6.13. The vertical scale is now linear. The dashed vertical lines show the location of the E/p cut.

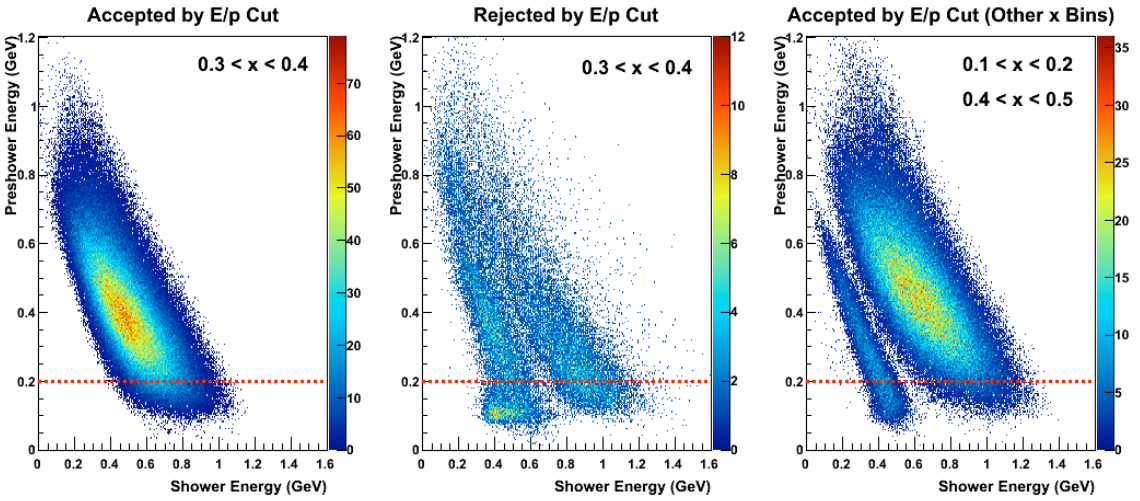

Figure 6.15: Evidence that events with mis-reconstructed momenta comprise the primary background in our sample. In each panel, we plot the energy deposited in the preshower layer versus the energy deposited in the shower layer for a given population of events; the location of the preshower-energy cut is marked by the dashed red line. In the left panel, we show events with $0.3 < x < 0.4$ that have passed all cuts except the one on preshower energy (which has not been applied). The central panel shows events from the same x range that have failed the cut on E/p, but have otherwise passed the same cuts as in the left panel. A population of pions is visible as a horizontal band outside the acceptance of the preshower-energy cut. The other background populations echo the behavior of good electrons from other x bins. The right panel shows a sample of such events, which have passed the E/p and other cuts. The population at left contains electrons with an assigned range of $0.1 < x < 0.2$; the population at right contains electrons from a range of $0.4 < x < 0.5$.

x **Range**	**Background Contamination** f_{bg} **(%)**	**% Signal Rejected**
$0.1 \leq x < 0.2$	1.54	12.6
$0.2 \leq x < 0.3$	0.72	7.20
$0.3 \leq x < 0.4$	4.45	5.19
$0.4 \leq x < 0.5$	4.37	5.26
$0.5 \leq x < 0.6$	4.22	5.08
$0.6 \leq x < 0.7$	5.84	4.99
$0.7 \leq x < 0.8$	0.04	8.31
$0.8 \leq x < 0.9$	0.002	8.76
$0.9 \leq x < 1.0$	0.01	8.69

Table 6.2: Background contamination and signal rejection of final sample, computed in the four-Gaussian model shown in Figures 6.13 and 6.14. Sharp changes between bins reflect the movement of secondary Gaussian peaks into (or out of) the signal region.

$$A_{raw} = \frac{N^{\downarrow,S} - N^{\uparrow,S}}{N^{\downarrow,S} + N^{\uparrow,S}} \tag{6.9}$$

where $\downarrow$ represents negative electron helicity, $\uparrow$ represents positive electron helicity, and S is the target spin direction. We give a detailed discussion of our sign convention and spin-configuration definitions in Section 6.3.1.

However, these raw counting asymmetries, measured for longitudinal and transverse spin configurations, are not the same as the physics asymmetries $A_\parallel$ and $A_\perp$ that we defined in Equations 1.34 and 1.35. The definitions of the physics asymmetries assume that the ^{3}He target and electron beam were perfectly polarized. They assume that electron scattering occurs from identical particles, but the ^{3}He in our target is diluted by the presence of N_2 nuclei, which also undergo electron scattering[2]. We may recover the physics asymmetry for electrons scattering from ^{3}He by accounting for these effects:

$$A_{phys}^{^3\mathrm{He}} = \frac{A_{raw}}{P_e P_{^3\mathrm{He}} D_{\mathrm{N}_2}}. \tag{6.10}$$

Here, P_e is the polarization of the electron beam, given in Table 4.9. $P_{^3\mathrm{He}}$, the polarization of the ^{3}He nuclei inside the target, is given for the 4.74-GeV dataset by Table 6.5. The dilution factor D_{N_2}, which corrects for the dilution caused by the presence of N_2 in the target, is calculated according to the procedure described in Section 6.3.3; the resulting D_{N_2} values for the 4.74-GeV dataset are given for each x bin in Table 6.4. If we were computing A_{phys}^n, the physics asymmetry for deep inelastic scattering from the neutron, we would need additional correction factors for the polarization of the neutron within the ^{3}He nucleus, and for the dilution and false asymmetry caused by electrons scattering from protons rather than from neutrons.

We have assumed that particle detection efficiencies are independent of spin configuration. This is not strictly true: the detector deadtime is correlated to rates. An asymmetry in the scattering cross sections therefore means that there will be less deadtime during measurements of one spin configuration than during measurements of the other. At the E06-014 kinematics, however, the raw asymmetries are typically less than one percent, and the BigBite deadtime is on the order of ten percent. The resulting subpercent correction due to an asymmetry in deadtime can, to first order, be ignored.

In this section, we discuss the mechanics of computing raw and physics asymmetries. One fundamental problem is that of sign convention: which beam-target spin configuration is positive, and how do we know for certain which one holds during a given helicity window? We discuss this issue in Section 6.3.1. In Section 6.3.2, we address the problem of so-called *false asymmetries*, which arise from changes in beam tune or intensity rather than from changes in the scattering cross section. We calculate the nitrogen dilution factor D_{N_2} in Section 6.3.3, and discuss our methods for combining data from multiple runs, which may have different target polarizations and accumulated beam charges, in Section 6.3.4. In Section 6.3.5, we present the measured raw and physics asymmetries for each of our three target spin configurations.

6.3.1 Asymmetry Sign

In order to avoid a sign error in our measured asymmetry, we must take care to define a consistent sign convention: which spin configuration takes the negative sign, and which takes the positive sign, in forming the asymmetry? We must also identify which data belong to which spin configuration, which requires certain knowledge of the physical direction of the beam helicity and target spin.

As shown in Figure 6.16, E06-014 ran with three target spin configurations, one longitudinal and two transverse, all in the horizontal plane. In Sections 6.3.1.1 and 6.3.1.2, we will define the

[2]Counts from N_2 scattering cancel out in the numerator of A_{raw}, but not in the denominator, artificially shrinking (or *diluting*) the asymmetry.

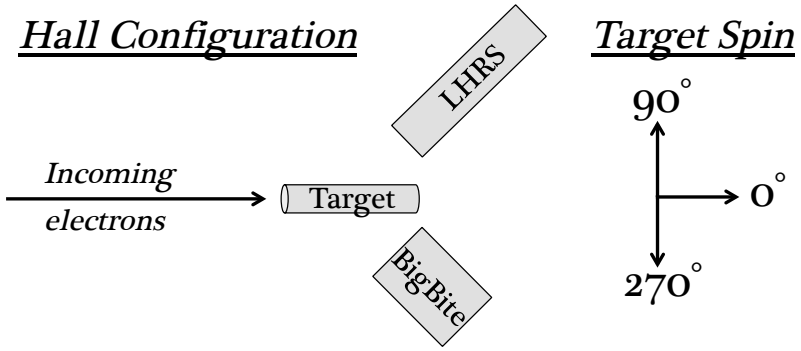

Figure 6.16: Definition of the three target spin directions used during E06-014. Looking down at the hall, a target spin at 0° is longitudinal, while target spins of 90° and 270° are transverse.

signs of the spin configurations for the longitudinal and transverse asymmetries, respectively; it then remains to classify our data according to those spin configurations. E06-014 ran with anti-parallel optical pumping, so that the target spin direction during any given target configuration was oriented opposite to that of the holding field. Information about the magnetic field, recorded at each configuration change, can thus be used to determine the target spin orientation for a given set of runs, according to the definition in Figure 6.16. As we will see in Section 6.3.1.3, the problem of defining the beam helicity is more complex.

6.3.1.1 Longitudinal Asymmetry

Our electron beam is longitudinally polarized; when the target is longitudinally polarized as well, the electron spin may be either parallel or antiparallel to target spin. Following the convention of previous experiments (*e.g.* E99-117 [41]), the numerator of the longitudinal asymmetry is the number of counts in the parallel spin configuration, subtracted from the number of counts in the antiparallel spin configuration, as in Equation 1.34.

When the E06-014 ^{3}He target was longitudinally polarized, it was always configured so that its spin was at 0° relative to the electron beam, *i.e.* its spin pointed downstream, toward the beam dump. Counts with negative electron helicity – that is, with the electron spin pointing upstream – are therefore given a positive sign in the numerator of the longitudinal asymmetry. Counts with positive electron helicity are given a negative sign.

6.3.1.2 Transverse Asymmetry

When forming the transverse asymmetry (Equation 1.35), we again assign a positive sign to events with negative-helicity electrons and a negative sign to events with positive-helicity electrons. We have two choices of transverse spin configuration, however: one in which the target spin is oriented at 90° (pointing to beam left), and one in which the target spin is oriented at 270° (pointing to beam right) in the horizontal plane. Which sense of the target spin is positive?

As we saw in Section 1.3.2, $\vec{k} \cdot \hat{S} = 0$ in either transverse spin configuration, so the target spin enters into the cross section only through $\vec{k}' \cdot \hat{S} = E \sin\theta \cos\phi$. (Recall that θ is the electron scattering angle and ϕ is the angle between the scattering and polarization planes, as defined in Figure 1.5.) Figure 6.17 shows the situation for $\phi = 0$. We can see that the positive sense of the target spin is the direction that points to the side of the beamline where the scattered electron is detected. In these asymmetry measurements, we detect scattered electrons in BigBite, on beam right. When combining asymmetries from the two transverse spin configurations, it is therefore the asymmetry

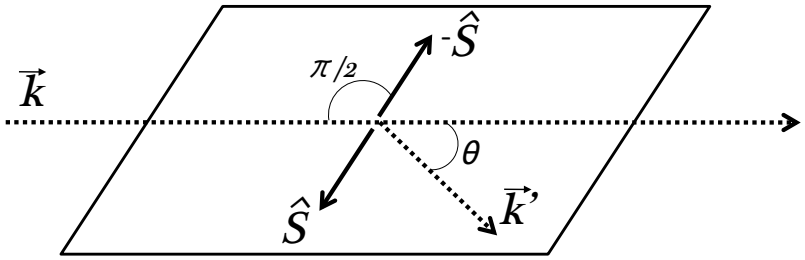

Figure 6.17: Sign convention for transverse target spin $\hat{S}$. The spin of the incident electron is parallel or anti-parallel to its momentum $\vec{k}$. The scattered electron has momentum $\vec{k}'$.

measured with the target spin at 270° that takes the positive sign; if we were also measuring the asymmetry using the LHRS, we would have to use the opposite sign convention for those data.

6.3.1.3 Beam Helicity Determination

As we saw in Section 3.2.1, polarized electrons emerge from the source with their polarization direction set by the Wien filter. The helicity logic signal, used in the DAQ to assign a spin direction to a given bunch of electrons, also originates at the source, as the polarization direction of the laser light that released those electrons from the photocathode.

As the electrons are accelerated in the injector, in their passes through the linac sections, and especially in the recirculation arcs and switchyard magnets, their spin precesses in the magnetic fields. A careful choice of Wien angle, coupled with thorough studies of spin precession in the accelerator, nonetheless allows delivery of beams with high longitudinal polarization to the halls. However, beam configuration changes – especially changes in the number of passes through the linac pair – can easily alter the precession angle enough to produce a reversal in the observed beam helicity relative to the helicity logic signal [139].

Møller polarimetry measurements after a configuration change check not only the beam polarization, but also the absolute helicity of electrons in Hall A: the sign of the Møller polarization measurement gives the relationship of the actual helicity to the Møller standard. Suppose that the insertable half-wave plate at the polarized electron source, which inverts the relationship of the helicity logic signal to the helicity of the emitted electrons, were not a consideration. This measurement would still be necessary to determine the relationship between the helicity logic signal and the helicity of electrons delivered to the Hall.

In order to find the relationship between the helicity logic signal, as recorded in the BigBite DAQ, and the Møller helicity standard, Matthew Posik performed a rough measurement of the asymmetry in quasielastic scattering of longitudinally polarized electrons from longitudinally polarized ^{3}He, using calibration data taken with an incident beam energy of 1.23 GeV. With $N^{\downarrow\Uparrow}$ representing counts where the helicity logic signal indicates that the electron and target spins are anti-aligned, and $N^{\uparrow\Uparrow}$ the inverse, we calculated that we should measure a raw asymmetry at $\theta = 45°$ of [148]:

$$A_{raw}^{QE} = \frac{N^{\downarrow\Uparrow} - N^{\uparrow\Uparrow}}{N^{\downarrow\Uparrow} + N^{\uparrow\Uparrow}} \approx +0.02 \tag{6.11}$$

Although the measured asymmetry has not yet been finalized, due in part to trigger problems during 1.23-GeV running, it is consistent with the predicted asymmetry to within a factor of 2, and the sign is clearly positive [240]. During the measurement, then, with the insertable half-wave plate out, the helicity logic signal measured in the BigBite DAQ (and, incidentally, the LHRS DAQ) accurately reflected the helicity of the electrons arriving at the Hall A target. Meanwhile, the Møller measurement for that beam configuration, conducted with the insertable half-wave plate in, gave

Target Spin Direction	Run Numbers	Helicity Mapping (IHWP out)
0°	2024 – 2053	+
90°	2056 – 2086	+
270°	2107 – 2195	−

Table 6.3: Mapping between actual helicity and helicity logic signal for 4.74-GeV target configurations, reported as the sign of the Møller polarization. When the + mapping is used, the helicity assigned to an electron bunch matches the helicity logic signal; when the − mapping is used, the helicity logic signal must be inverted to find the electron helicity. When the insertable half-wave plate (IHWP) is in, the helicity mapping shown here is inverted.

a negative beam polarization (Table 4.1). This result may be corrected for the status of the half-wave plate through multiplication by -1 to give a positive beam polarization with the half-wave plate out. We combine these observations to conclude that, when the half-wave plate is *out* of the photon beamline at the polarized source, a positive Møller polarization measurement means that BigBite events labeled as positive-helicity really do have positive helicity, and those labeled as negative-helicity really do have negative helicity. This determination is consistent with similar conclusions reached by Jin Huang for the experiments immediately before and after E06-014, which used virtually the same DAQ wiring [245].

Our 4.74-GeV dataset was interrupted by a major configuration change, as recounted in Section 3.5. We began our data-taking with electrons that had made four passes through the accelerator. After several days, however, it became clear that water contamination in a trio of cryomodules was critically degrading their performance. In a herculean effort, the accelerator team warmed these cryomodules to room temperature and tuned the accelerator to deliver 4.74 GeV electrons in *five* passes through the linacs. This pass change induced a reversal in the meaning of the helicity logic signal, confirmed by both the Møller and Compton polarimeters. As it happens, this configuration change coincided with a rotation of the target spin from 90° to 270°, so that the same mapping between helicity and helicity logic signal (defined for the *out* state of the insertable half-wave plate) may be used within each target configuration.

6.3.2 False Asymmetries

As we saw in Section 4.3.4.2, a *false asymmetry* arises from helicity-correlated changes in the character of the electron beam, rather than from the spin dependence of the scattering interaction being measured. The most problematic type of false asymmetry would be a beam-charge asymmetry, in which the intensity of the electron beam differs between one helicity state and the other. During E06-014, a feedback loop controlled by a specialized DAQ [225], as described in Section 3.2.1, controlled the charge asymmetry to within about 100 ppm.

Helicity-dependent changes in DAQ deadtime, as described at the beginning of Section 6.3, are another potential source of false asymmetry. This asymmetry may be estimated at $\sim$ 1000 ppm or less. Like the charge asymmetry, it is negligible compared to the statistical errors.

A false asymmetry could also be inadvertently introduced in software; for example, if the rates are high enough, it may be more difficult to reconstruct good tracks for the higher-rate helicity state than for the lower-rate one [144]. However, since track multiplicity was low during E06-014 - fewer than 4% of CODA events with any tracks had more than one – we may conclude that our rates were not high enough for this to be a concern.

Other potential sources of false asymmetry – *e.g.* slow drifts in beam tune or detector efficiency – are mitigated by the fast, 30 Hz helicity flip of the electron beam: drifts on a longer time scale affect both helicity states equally. For each target configuration, we took roughly equal amounts of data with the IHWP (insertable half-wave plate) in and out of the photon beamline at the polarized

electron source; since a change in IHWP status inverts the definition of the helicity logic signal and thus the apparent sign of the physics asymmetry, combining data from the two IHWP states cancels any false asymmetries that do not change sign with an IHWP change, such as those due to electronics cross-talk [222].

6.3.3 Dilution Factor

Practical considerations dictate that our target cell cannot be filled with pure ^{3}He: rubidium and potassium atoms are necessary to polarize the ^{3}He, and N_2 is necessary as a buffer gas to keep this process reasonably efficient. While rubidium and potassium may be confined to the pumping chamber by means of a temperature gradient, N_2 diffuses freely through both chambers just as ^{3}He does. The presence of N_2 in the target chamber dilutes our measured asymmetry, since some of the electrons we measure have scattered from a nitrogen nucleus rather than from a polarized ^{3}He nucleus.

We may find the correction for this dilution effect by taking data with a pure nitrogen target. Knowing the relationship between the N_2 density in the nitrogen target and that in the production ^{3}He target, we may scale to find the number of counts due to $e-N_2$ scattering in our production running. During E06-014, we frequently took data using the reference cell filled with nitrogen (Section 3.3.3.4), so that a nitrogen reference run would be available for each LHRS kinematic point. For the BigBite analysis, we selected three representative nitrogen runs with a beam energy of 4.74 GeV for our analysis.

Let Σ_{N_2} be the total number of counts (in both beam helicity states) due to $e-N_2$ scattering; $\Sigma_{N_2}(^3\mathrm{He})$ and $\Sigma_{N_2}(N_2)$ are then the counts from nitrogen in the production and reference cells, respectively. Let $\rho_{N_2}(^3\mathrm{He})$ and $\rho_{N_2}(N_2)$ be the nitrogen number densities in the two targets, and $Q(^3\mathrm{He})$ and $Q(N_2)$ be the total charge incident on the two targets during data-taking. The number of counts due to N_2 in production data is then given by [144]

$$\Sigma_{N_2}(^3\mathrm{He}) = \Sigma_{N_2}(N_2)\frac{Q(^3\mathrm{He})\rho_{N_2}(^3\mathrm{He})}{Q(N_2)\rho_{N_2}(N_2)}. \tag{6.12}$$

From the number of counts due to N_2 scattering in our production cell, we may form a dilution factor $D_{N_2} < 1$, which appears in the denominator of the physics asymmetry in Equation 6.10. This dilution factor should be the proportion of detected electrons that scattered from ^{3}He nuclei. It is thus equal to the difference between unity and the proportion of detected electrons that scattered from N_2 nuclei

$$D_{N_2} = 1 - \frac{\Sigma_{N_2}(^3\mathrm{He})}{\Sigma_{total}(^3\mathrm{He})} = 1 - \frac{\Sigma_{N_2}(N_2)}{\Sigma_{total}(^3\mathrm{He})} \cdot \frac{Q(^3\mathrm{He})\rho_{N_2}(^3\mathrm{He})}{Q(N_2)\rho_{N_2}(N_2)} \tag{6.13}$$

where $\Sigma_{total}(^3\mathrm{He})$ is the total number of counts, from ^{3}He scattering and N_2 scattering combined, with the production target in position. We note that, in tallying the counts for each target, we consider only those tracks that have passed all of the cuts described in Section 6.2.

While the reference cell is in the beam, typical values for its pressure and density are 116 psig and 42°C; the ideal gas law may then be used to extract a number density of $\rho_{N_2}(N_2) = 7.71$ amg, with an uncertainty of 2.2%, estimated by calculating the density for pressure and temperature excursions of up to 2 psig and 2°C. For $\rho_{N_2}(^3\mathrm{He})$, we use an N_2 density of 0.113 amg, as recorded while the target was initially being filled; pressure-curve analyses conducted for E06-010 suggest that this value is accurate to within about 3% [246], for an overall relative systematic error of 3.7%.

Figure 6.18 shows the evolution of D_{N_2} in x, as computed according to Equation 6.13. The x bins have a uniform size of 0.05; there are not enough data at $x < 0.15$ to make a meaningful determination. The value of D_{N_2} in each x bin is reported in Table 6.4. The only significant source of statistical error is the number of counts in the N_2 runs, $\delta\Sigma_{N_2}(N_2) = \sqrt{\Sigma_{N_2}(N_2)}$. The overall error on D_{N_2} in any x bin is then

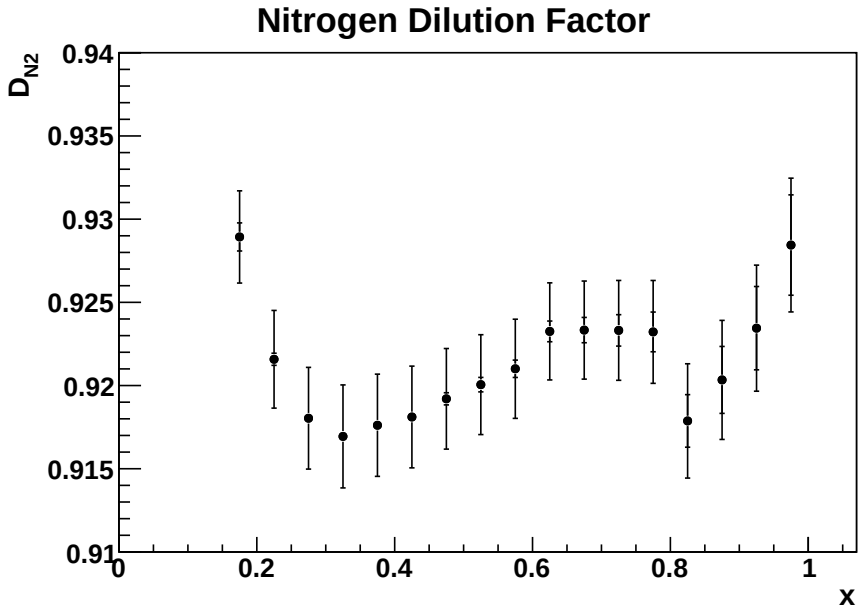

Figure 6.18: Nitrogen dilution factor D_{N_2} as a function of x. Outer error bars show combined statistical and systematic errors; inner error bars show statistical errors. In some bins, the statistical error is too small to be seen in the graph.

$$\delta D_{\mathrm{N}_2} = \sqrt{\left(\frac{\sqrt{\Sigma_{\mathrm{N}_2}(\mathrm{N}_2)}}{\Sigma_{total}(^3\mathrm{He})} \cdot \frac{Q(^3\mathrm{He})\rho_{\mathrm{N}_2}(^3\mathrm{He})}{Q(\mathrm{N}_2)\rho_{\mathrm{N}_2}(\mathrm{N}_2)}\right)^2 + (0.037(1 - D_{\mathrm{N}_2}))^2}. \tag{6.14}$$

6.3.4 Combining Data from Multiple Runs

We saw in Section 4.4 that the electron beam polarization was remarkably stable during each of the experiment's beam configurations; we therefore use the same beam-polarization value P_e (Table 4.9) for each run period. The target polarization, derived from EPR-calibrated NMR measurements, was also fairly stable within its error bars, as we saw in Section 5.1.2. For this analysis, we have therefore extracted a single target-polarization value $P_{^3He}$ for each of the three target configurations during the last run period. For a given target configuration, $P_{^3He}$ represents the average of the run-by-run polarizations for that run period, weighted by the amount of charge incident on the target during data-taking for that run[3]. Table 6.5 shows the resulting values of $P_{^3He}$ for each target polarization direction.

Given the overall stability of conditions in the Hall during the 4.74-GeV data-taking, we computed our asymmetries over all runs associated with each target spin configuration, rather than finding asymmetries on a run-by-run (or even helicity-pair-by-helicity-pair) basis and then combining them. We divided the range $0 \leq x \leq 1$ into twenty uniform bins. For each run, we looped through the x bins and counted the number of tracks in each that survived the event-selection cuts described in Section 6.2, using the helicity logic signal to separate counts from the two electron-helicity states. (Some tracks were detected during an MPS transition and thus had an indeterminate helicity state;

[3]This number excludes charge incident during beam trips and recoveries, since we have discarded those times from our data set.

Central x Value	Dilution Factor D_{N_2}	Overall Error δD_{N_2}
0.175	$0.9289 \pm 0.0008_{stat} \pm 0.0026_{syst}$	0.0028
0.225	$0.9216 \pm 0.0004_{stat} \pm 0.0029_{syst}$	0.0029
0.275	$0.9180 \pm 0.0003_{stat} \pm 0.0030_{syst}$	0.0031
0.325	$0.9169 \pm 0.0002_{stat} \pm 0.0031_{syst}$	0.0031
0.375	$0.9176 \pm 0.0003_{stat} \pm 0.0031_{syst}$	0.0031
0.425	$0.9181 \pm 0.0003_{stat} \pm 0.0030_{syst}$	0.0031
0.475	$0.9192 \pm 0.0004_{stat} \pm 0.0030_{syst}$	0.0030
0.525	$0.9201 \pm 0.0004_{stat} \pm 0.0030_{syst}$	0.0030
0.575	$0.9210 \pm 0.0005_{stat} \pm 0.0029_{syst}$	0.0030
0.625	$0.9233 \pm 0.0006_{stat} \pm 0.0029_{syst}$	0.0029
0.675	$0.9233 \pm 0.0008_{stat} \pm 0.0028_{syst}$	0.0029
0.725	$0.9233 \pm 0.0009_{stat} \pm 0.0028_{syst}$	0.0030
0.775	$0.9232 \pm 0.0012_{stat} \pm 0.0029_{syst}$	0.0031
0.825	$0.9179 \pm 0.0016_{stat} \pm 0.0031_{syst}$	0.0034
0.875	$0.9203 \pm 0.0020_{stat} \pm 0.0030_{syst}$	0.0036
0.925	$0.9234 \pm 0.0025_{stat} \pm 0.0028_{syst}$	0.0038
0.975	$0.9284 \pm 0.0030_{stat} \pm 0.0027_{syst}$	0.0040

Table 6.4: Nitrogen dilution factor D_{N_2} for each x value, including statistical and systematic errors.

these were flagged in the analysis software and discarded from our analysis.) This operation took about four hours for the data set as a whole, and its results were stored in a text database for quick access. For each x bin, we then summed up the number of surviving tracks for positive-helicity windows over all runs, as well as the number of surviving tracks for negative-helicity windows. It is from these global counts that we computed the asymmetry for that bin.

Changes in IHWP state were recorded during the experiment, both in an electronic logbook and in the EPICS datastream. Since these transitions only occurred between runs, each run may be assigned a definitive IHWP status, which – along with the helicity mapping defined in Table 6.3 – defines which value of the helicity logic variable corresponds to positive electron helicity, and which value corresponds to negative electron helicity. For each target configuration, the numerator of the asymmetry is computed as the number of counts with negative helicity minus the number of counts with positive helicity. Table 6.5 shows the IHWP state for runs during the 4.74-GeV dataset.

Target Spin Direction	$P_{^3He}$ (%)	IHWP-Out Runs	IHWP-In Runs
0°	58.4 ± 2.9	2024-2039	2040-2053
90°	59.3 ± 2.9	2081-2086	2056-2080
270°	58.2 ± 2.8	2107-2151	2156-2195

Table 6.5: Charge-weighted average target polarization, BigBite run numbers, and IHWP status for each 4.74-GeV target spin configuration. Not all BigBite runs in each range were production runs.

6.3.5 Raw and Physics Asymmetries for $E_e = 4.74$ GeV

The raw asymmetries measured at $E_e = 4.74$ GeV for each of E06-014's target spin configurations (as defined in Figure 6.16) are shown in Figure 6.19, along with their statistical errors. We have divided the range $0 \leq x \leq 1$ into twenty x bins of uniform size; we have measured asymmetries in

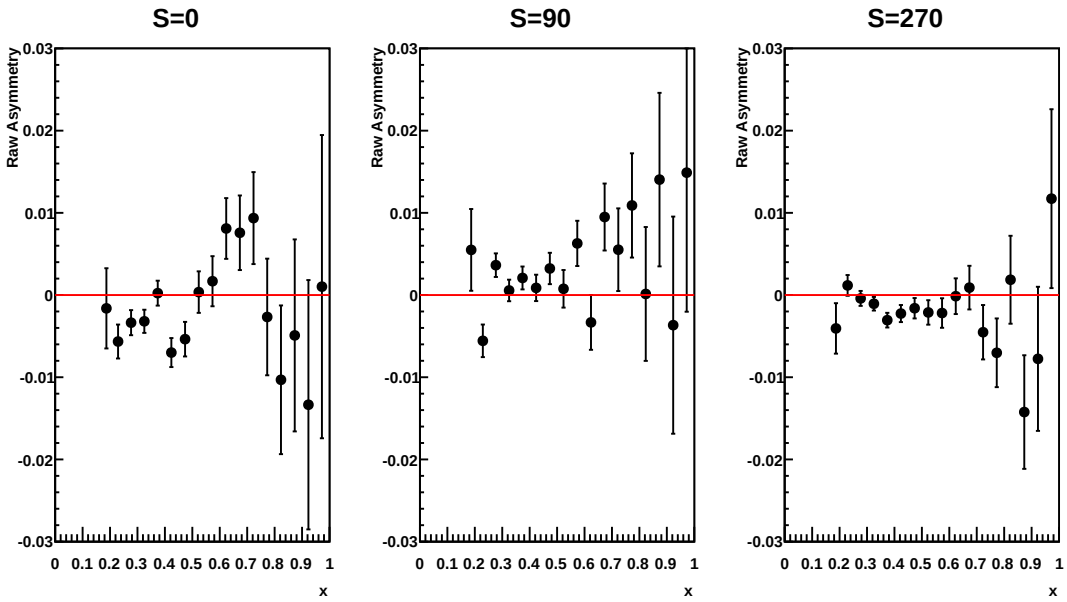

Figure 6.19: Raw asymmetries measured at $E_e = 4.74$ GeV for each of the three target spin configurations. Only statistical errors are shown.

seventeen of those x bins, covering $0.15 \leq x \leq 1$. Bins with lower x values have insufficient statistics for a measurement. We note that only data points with $x \leq 0.55$ truly represent data from deep inelastic scattering; at higher x, the scattering kinematics are in the resonance region.

We have computed these asymmetries according to the helicity sign convention discussed in Section 6.3.1, subtracting positive-helicity counts from negative-helicity counts. We see in the central and right panels of Figure 6.19 that the asymmetries measured for the two transverse spin configurations have opposite sign; when these asymmetries are combined into a single transverse asymmetry $A_\perp$, it will take the sign of the asymmetries measured with a target spin at 270°, as explained in Section 6.3.1.2.

The statistical error on a raw asymmetry may be calculated based on the number of counts in each configuration. We recall that the statistical error on $N_\downarrow$ counts is given by $\sqrt{N_\downarrow}$; likewise, $\delta N_\uparrow = \sqrt{N_\uparrow}$. The statistical errors on the two spin configurations are uncorrelated; we then use the definition of the raw asymmetry in Equation 6.9 to derive

$$\delta A_{raw}^2 = \frac{4N_\downarrow^2(\delta N_\uparrow)^2 + 4N_\uparrow^2(\delta N_\downarrow)^2}{(N_\downarrow + N_\uparrow)^4} = \frac{4N_\downarrow N_\uparrow}{(N_\downarrow + N_\uparrow)^3}. \tag{6.15}$$

For small asymmetries – that is, $N_\downarrow \sim N_\uparrow$ – the error on the asymmetry may be approximated as $1/\sqrt{N}$, where N is the total number of counts in both helicity states. Figure 6.20 shows N in each x bin for each of the three target configurations.

After computing the raw asymmetries for each target configuration, we then applied Equation 6.10 to compute the physics asymmetries, drawing the beam polarization P_e from Table 4.9, the target polarization $P_{^3\mathrm{He}}$ from Table 6.5, and the nitrogen dilution factor $D_{\mathrm{N}_2}(x)$ from Table 6.4. Figure 6.21 shows the results, with statistical and systematic errors included.

We can bound the error due to mis-binning electrons in our computation (Section 6.2.3) by calculating its effect on the measured physics asymmetry. This contribution from counts that belong in different bins, δA_{phys}^{misbin}, is an additive effect. We have

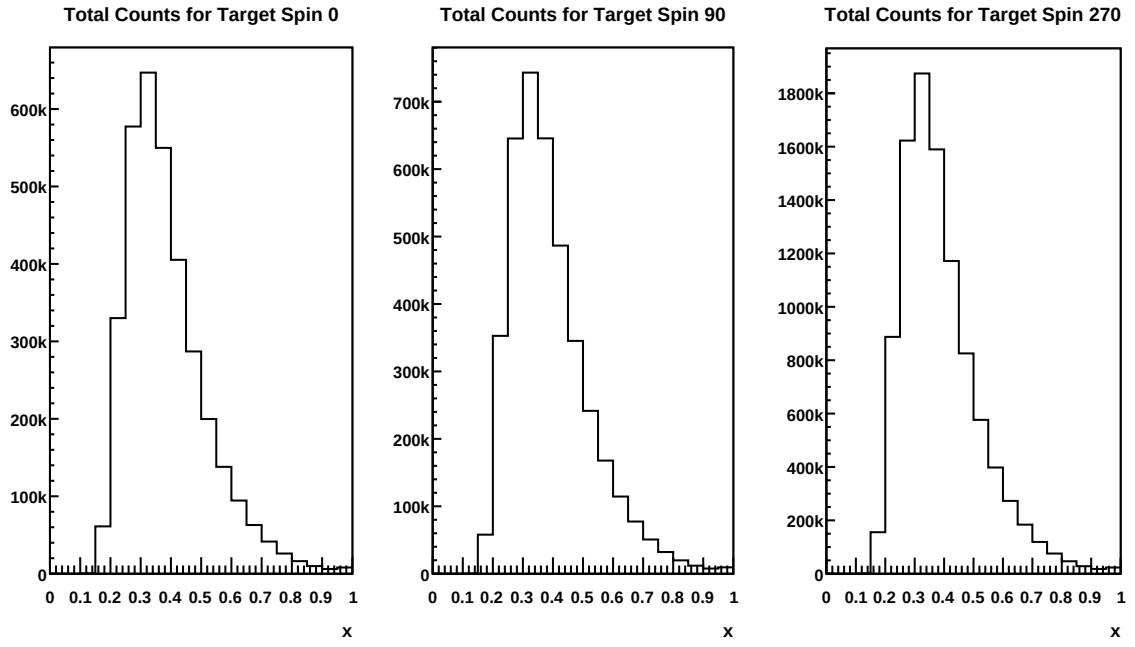

Figure 6.20: Total counts detected in each x bin at $E_e = 4.74$ GeV for each of the three target spin configurations. This represents a total of 3.374 C incident on the target: 0.690 C in the 0° configuration, 0.804 C in the 90° configuration, and 1.879 C in the 270° configuration.

$$A_{phys} = A_{phys}^{true} + \delta A_{phys}^{misbin} \tag{6.16}$$

where A_{phys}^{true} is the physics asymmetry we would measure if our binning were perfect. Let us suppose that all of these mis-assigned counts properly belong to the same x bin. As they are good electrons from that original bin, the asymmetry contribution δA_{phys}^{misbin} of these misassigned counts must then be proportional to the physics asymmetry in the bin to which they belong – and the constant of proportionality is the background contamination factor f_{bg} from Table 6.2. In actuality, misassigned counts need not all originate from the same x range, but we may nevertheless use this insight to bound their contribution to the asymmetry

$$\delta A_{phys}^{misbin} \leq f_{bg} \Delta A_{phys}^{max} \tag{6.17}$$

where ΔA_{phys}^{max} is the maximum difference in physics asymmetries measured between two bins with $x < 0.75$. (At lower x values, bins have higher statistics and thus are more likely to be the source of any misaligned electrons. At $x > 0.75$, the statistics are so low compared to other x bins that these events cannot be said to be significant contributors to the background in other bins.) The values of A_{phys}^{max} for each target spin orientation are given in Table 6.6.

The systematic errors on A_{phys} come in two varieties: multiplicative and additive. We combine them to form the overall systematic error δA_{phys}^{syst} as follows:

$$\left.\frac{\delta A_{phys}^{syst}}{A_{phys}}\right|_{mult} = \sqrt{\left(\frac{\delta P_e}{P_e}\right)^2 + \left(\frac{\delta P_{^3\mathrm{He}}}{P_{^3\mathrm{He}}}\right)^2 + \left(\frac{\delta D_{\mathrm{N}_2}}{D_{\mathrm{N}_2}}\right)^2} \tag{6.18}$$

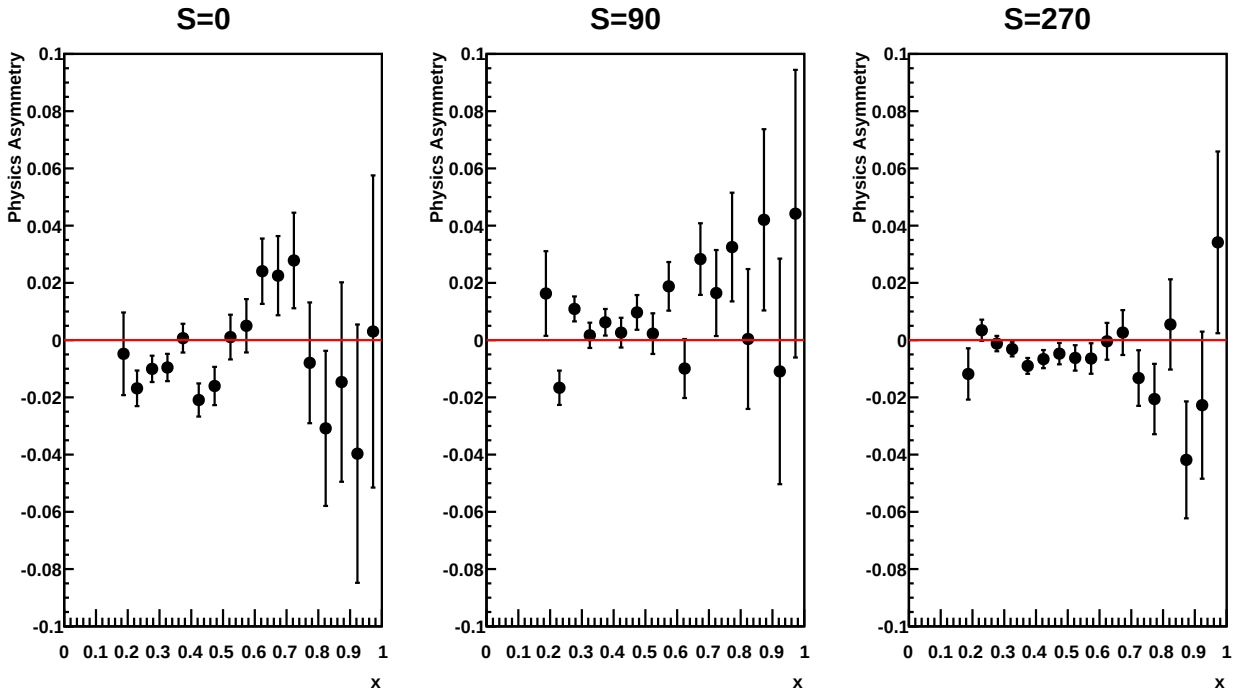

Figure 6.21: Physics asymmetries measured at $E_e = 4.74$ GeV for each of the three target spin configurations. The error bars show combined statistical and systematic errors.

$$\delta A_{phys}^{syst} = \sqrt{\left(A_{phys} \left. \frac{\delta A_{phys}^{syst}}{A_{phys}} \right|_{mult} \right)^2 + \left(f_{bg} A_{phys}^{max} \right)^2}. \tag{6.19}$$

Table 6.6 summarizes the sources of systematic error. The measured raw and physics asymmetries, with their statistical and systematic errors, are given for each x bin and each target spin orientation in Tables 6.7, 6.8, and 6.9.

6.4 Variables for Construction of $A_\parallel$, $A_\perp$, A_1 and A_2

The physics asymmetries we computed in Section 6.3.5 translate fairly readily to $A_\parallel$ and $A_\perp$; in fact, $A_\parallel = A_0^{phys}$, and $A_\perp$ is formed by combining A_{90}^{phys} and A_{270}^{phys} and correcting for the azimuthal angle ϕ. Forming A_1 and A_2, however, requires some additional algebra. Recall the expressions for the nucleon-virtual photon asymmetries given in Equations 2.30 and 2.31

$$A_1 = \frac{1}{D\,(1+\eta\xi)} A_\parallel - \frac{\eta}{d\,(1+\eta\xi)} A_\perp \tag{6.20}$$

$$A_2 = \frac{\xi}{D\,(1+\eta\xi)} A_\parallel + \frac{1}{d\,(1+\eta\xi)} A_\perp. \tag{6.21}$$

To find A_1 and A_2 in a given x bin, we must determine the values of D, d, η, and ξ in each x bin.

We begin in Section 6.4.1 by examining the basic kinematic parameters – k', x, Q^2, θ, ϕ, and ν – in each x bin. These parameters have been calculated for each event in the skim stage of our

Source of Error	Error	Error Range	Cross-Reference
Beam polarization	0.010	0.010	Table 4.9
N_2 dilution	$\delta D_{N_2}(x)$	$0.0024 - 0.0033$	Table 6.4
Target polarization	$0°$: 0.029 $90°$: 0.029 $270°$: 0.028	0.029 0.029 0.028	Table 6.5
Mis-binning	$0°$: $\leq 0.0487 f_{bg}(x)$ $90°$: $\leq 0.0449 f_{bg}(x)$ $270°$: $\leq 0.0167 f_{bg}(x)$	≤ 0.0028 ≤ 0.0026 ≤ 0.001	Table 6.2

Table 6.6: Sources of systematic error in physics asymmetry at $E_e = 4.74$ GeV, along with references to the tables originally presenting them. Where the error varies depending on the target spin, we report the value for each spin configuration. Where the error varies in x, the x-dependent quantity may be found in the referenced table.

Target Spin at $0°$		
$\langle x \rangle$	A_{raw}	A_{phys}
0.187	$-0.0016 \pm 0.0049_{stat}$	$-0.0048 \pm 0.0144_{stat} \pm 0.0008_{syst}$
0.229	$-0.0057 \pm 0.0021_{stat}$	$-0.0168 \pm 0.0061_{stat} \pm 0.0009_{syst}$
0.277	$-0.0034 \pm 0.0015_{stat}$	$-0.0100 \pm 0.0046_{stat} \pm 0.0006_{syst}$
0.325	$-0.0032 \pm 0.0014_{stat}$	$-0.0096 \pm 0.0042_{stat} \pm 0.0022_{syst}$
0.374	$0.0002 \pm 0.0015_{stat}$	$0.0007 \pm 0.0045_{stat} \pm 0.0022_{syst}$
0.424	$-0.0070 \pm 0.0018_{stat}$	$-0.0209 \pm 0.0053_{stat} \pm 0.0024_{syst}$
0.474	$-0.0054 \pm 0.0021_{stat}$	$-0.0160 \pm 0.0063_{stat} \pm 0.0023_{syst}$
0.523	$0.0004 \pm 0.0025_{stat}$	$0.0011 \pm 0.0075_{stat} \pm 0.0021_{syst}$
0.574	$0.0017 \pm 0.0030_{stat}$	$0.0050 \pm 0.0091_{stat} \pm 0.0021_{syst}$
0.624	$0.0081 \pm 0.0037_{stat}$	$0.0241 \pm 0.0110_{stat} \pm 0.0031_{syst}$
0.673	$0.0076 \pm 0.0045_{stat}$	$0.0225 \pm 0.0135_{stat} \pm 0.0031_{syst}$
0.723	$0.0094 \pm 0.0056_{stat}$	$0.0278 \pm 0.0166_{stat} \pm 0.0014_{syst}$
0.773	$-0.0027 \pm 0.0071_{stat}$	$-0.0079 \pm 0.0211_{stat} \pm 0.0004_{syst}$
0.823	$-0.0103 \pm 0.0090_{stat}$	$-0.0308 \pm 0.0271_{stat} \pm 0.0016_{syst}$
0.873	$-0.0049 \pm 0.0117_{stat}$	$-0.0146 \pm 0.0348_{stat} \pm 0.0008_{syst}$
0.923	$-0.0133 \pm 0.0152_{stat}$	$-0.0397 \pm 0.0451_{stat} \pm 0.0021_{syst}$
0.972	$0.0010 \pm 0.0184_{stat}$	$0.0030 \pm 0.0545_{stat} \pm 0.0002_{syst}$

Table 6.7: Raw asymmetries A_{raw} and physics asymmetries A_{phys} in E06-014 production data with a target spin orientation of $0°$.

Target Spin at 90°		
$\langle x \rangle$	A_{raw}	A_{phys}
0.187	$0.0055 \pm 0.0050_{stat}$	$0.0163 \pm 0.0147_{stat} \pm 0.0011_{syst}$
0.229	$-0.0056 \pm 0.0020_{stat}$	$-0.0166 \pm 0.0059_{stat} \pm 0.0009_{syst}$
0.277	$0.0036 \pm 0.0014_{stat}$	$0.0109 \pm 0.0043_{stat} \pm 0.0006_{syst}$
0.325	$0.0006 \pm 0.0013_{stat}$	$0.0017 \pm 0.0039_{stat} \pm 0.0020_{syst}$
0.374	$0.0021 \pm 0.0014_{stat}$	$0.0062 \pm 0.0042_{stat} \pm 0.0020_{syst}$
0.424	$0.0009 \pm 0.0016_{stat}$	$0.0026 \pm 0.0048_{stat} \pm 0.0020_{syst}$
0.474	$0.0032 \pm 0.0019_{stat}$	$0.0097 \pm 0.0057_{stat} \pm 0.0020_{syst}$
0.523	$0.0008 \pm 0.0023_{stat}$	$0.0023 \pm 0.0068_{stat} \pm 0.0019_{syst}$
0.574	$0.0063 \pm 0.0028_{stat}$	$0.0188 \pm 0.0082_{stat} \pm 0.0021_{syst}$
0.624	$-0.0033 \pm 0.0033_{stat}$	$-0.0099 \pm 0.0100_{stat} \pm 0.0027_{syst}$
0.673	$0.0095 \pm 0.0041_{stat}$	$0.0283 \pm 0.0122_{stat} \pm 0.0030_{syst}$
0.723	$0.0055 \pm 0.0050_{stat}$	$0.0165 \pm 0.0150_{stat} \pm 0.0009_{syst}$
0.773	$0.0109 \pm 0.0063_{stat}$	$0.0325 \pm 0.0189_{stat} \pm 0.0017_{syst}$
0.823	$0.0001 \pm 0.0081_{stat}$	$0.0004 \pm 0.0244_{stat} \pm 0.0000_{syst}$
0.873	$0.0140 \pm 0.0106_{stat}$	$0.0420 \pm 0.0316_{stat} \pm 0.0022_{syst}$
0.923	$-0.0037 \pm 0.0132_{stat}$	$-0.0109 \pm 0.0394_{stat} \pm 0.0006_{syst}$
0.972	$0.0149 \pm 0.0169_{stat}$	$0.0442 \pm 0.0502_{stat} \pm 0.0023_{syst}$

Table 6.8: Raw asymmetries A_{raw} and physics asymmetries A_{phys} in E06-014 production data with a target spin orientation of 90°.

Target Spin at 270°		
$\langle x \rangle$	A_{raw}	A_{phys}
0.187	$-0.0041 \pm 0.0031_{stat}$	$-0.0118 \pm 0.0089_{stat} \pm 0.0007_{syst}$
0.229	$0.0012 \pm 0.0013_{stat}$	$0.0034 \pm 0.0037_{stat} \pm 0.0002_{syst}$
0.277	$-0.0004 \pm 0.0009_{stat}$	$-0.0012 \pm 0.0027_{stat} \pm 0.0001_{syst}$
0.325	$-0.0011 \pm 0.0008_{stat}$	$-0.0031 \pm 0.0024_{stat} \pm 0.0008_{syst}$
0.374	$-0.0031 \pm 0.0009_{stat}$	$-0.0090 \pm 0.0026_{stat} \pm 0.0009_{syst}$
0.424	$-0.0023 \pm 0.0010_{stat}$	$-0.0066 \pm 0.0031_{stat} \pm 0.0008_{syst}$
0.474	$-0.0016 \pm 0.0012_{stat}$	$-0.0047 \pm 0.0037_{stat} \pm 0.0008_{syst}$
0.523	$-0.0021 \pm 0.0015_{stat}$	$-0.0062 \pm 0.0044_{stat} \pm 0.0008_{syst}$
0.574	$-0.0022 \pm 0.0018_{stat}$	$-0.0064 \pm 0.0053_{stat} \pm 0.0008_{syst}$
0.624	$-0.0001 \pm 0.0022_{stat}$	$-0.0004 \pm 0.0064_{stat} \pm 0.0010_{syst}$
0.673	$0.0009 \pm 0.0027_{stat}$	$0.0026 \pm 0.0078_{stat} \pm 0.0010_{syst}$
0.723	$-0.0045 \pm 0.0033_{stat}$	$-0.0133 \pm 0.0097_{stat} \pm 0.0007_{syst}$
0.773	$-0.0070 \pm 0.0042_{stat}$	$-0.0206 \pm 0.0122_{stat} \pm 0.0011_{syst}$
0.823	$0.0019 \pm 0.0053_{stat}$	$0.0055 \pm 0.0158_{stat} \pm 0.0003_{syst}$
0.873	$-0.0142 \pm 0.0069_{stat}$	$-0.0418 \pm 0.0203_{stat} \pm 0.0022_{syst}$
0.923	$-0.0078 \pm 0.0088_{stat}$	$-0.0227 \pm 0.0257_{stat} \pm 0.0012_{syst}$
0.972	$0.0117 \pm 0.0109_{stat}$	$0.0342 \pm 0.0317_{stat} \pm 0.0018_{syst}$

Table 6.9: Raw asymmetries A_{raw} and physics asymmetries A_{phys} in E06-014 production data with a target spin orientation of 270°.

analysis. In Section 6.4.2, we review a parameterization that allows us to calculate the value of $R = \sigma_L/\sigma_T$ for each x bin. Finally, in Section 6.4.3, we calculate ϵ, D, d, η, and ξ in each x bin, based on the values we have computed in Sections 6.4.1 and 6.4.2.

6.4.1 Kinematic Parameters by x Bin

Our computation of kinematic parameters over our x range is heavily dependent on the BigBite optics reconstruction package (Section 5.2.2). From knowledge of the BigBite magnetic field, the reconstructed track in the BigBite wire chambers, and the locations of the target and beam relative to the spectrometer and detectors, this package computes the momentum $\vec{k}'$ of the scattered electron, the scattering angle θ, and the azimuthal angle ϕ between the scattering plane and polarization plane (defined in Figure 1.5). The distributions of these variables in each of our x bins are plotted in Figure 6.22 ($|\vec{k}'| = E'$), Figure 6.23 (θ), and Figure 6.24 (ϕ). Figure 6.24 highlights an apparent hole in our ϕ acceptance, but the variation of these parameters otherwise appears smooth.

The incident energy E of the electron beam is taken from Tiefenback monitoring (Section 3.3.2.4), which has an uncertainty of about 0.05%. Readouts from the beam position monitors (Section 3.3.2.2) give the momentum direction of the electron beam. Combining this information about the incident electron vector $\vec{k}$ with our reconstruction of the scattered electron vector $\vec{k}'$, we may compute ν according to Equation 1.3, Q^2 according to Equation 1.5, and x according to Equation 1.7. Figure 6.25 shows the distributions of ν^2 (this, rather than ν, is an input to the calculation of ϵ) in each x bin. The Q^2 and x distributions are plotted in Figures 6.26 and 6.27, respectively.

We take the mean value of each parameter in an x bin as the single, representative value for that bin. Let us review the uncertainties on our determination of these parameters. Angular measurements ultimately rely on survey reports of the BigBite detector stack [247], which give the positions of the wire chambers relative to the nominal target center to mm-level accuracy. Since the first (and closest) wire chamber is located 2.75 m from the origin, this corresponds to a systematic uncertainty of about 0.4 mrad on θ and ϕ, which is negligible compared to the systematic 10-mrad uncertainty in angle reconstruction [170]. We know the momentum of the scattered particle to about 1%; uncertainty in the momentum of the scattered particle dominates uncertainty about the incident beam.

We may bound the uncertainty on each parameter by re-calculating it with a $|\vec{k}'|$ increased by 1% and with θ and ϕ increased by 10 mrad. The result is bin-dependent; the maximum relative deviation in each parameter is given in Table 6.10. The final mean values of each parameter in each x bin, along with the corresponding resolution errors, are summarized in Table 6.11 and Figure 6.28.

Parameter	**Dependence**	**Maximum Relative Error (%)**
$\lvert\vec{k}'\rvert = E'$	$\lvert\vec{k}'\rvert$	1.0
θ	θ	1.4
$\tan^2(\theta/2)$	θ	3.0
$\cos\phi$	ϕ	0.02
x	θ, $\lvert\vec{k}'\rvert$	4.6
ν^2	$\lvert\vec{k}'\rvert$	1.5
Q^2	θ, $\lvert\vec{k}'\rvert$	4.2

Table 6.10: Resolution errors on kinematic parameters used as input for $A_\perp$, A_1 and A_2.

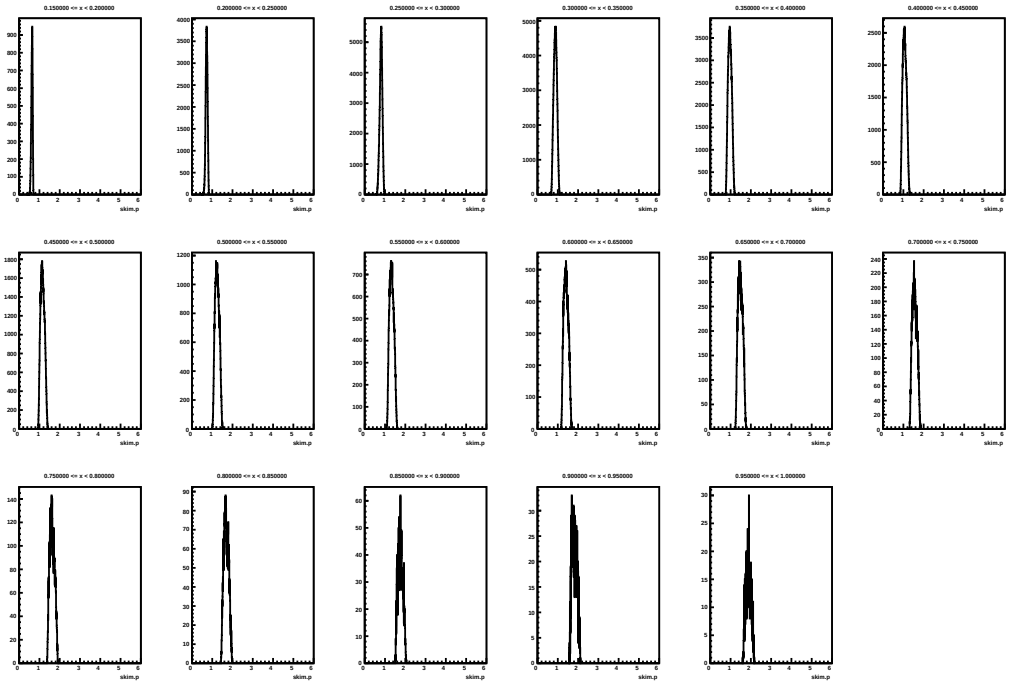

Figure 6.22: Measured distribution of scattered momentum k' in each x bin. Distributions are shown in order of increasing x, left to right and top to bottom.

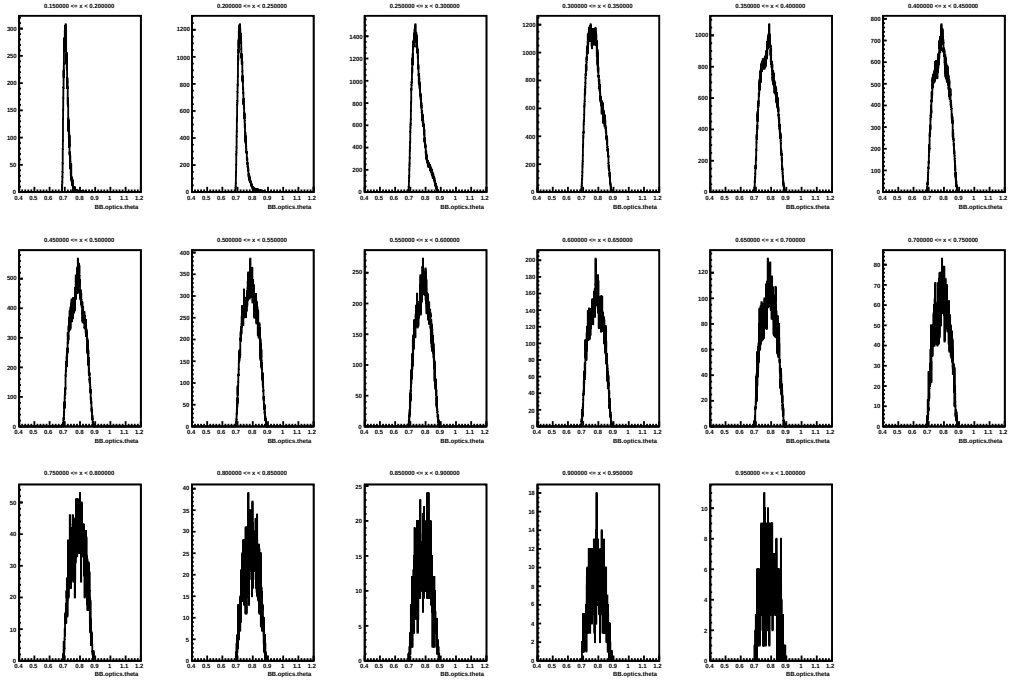

Figure 6.23: Measured distribution of scattering angle θ in each x bin.

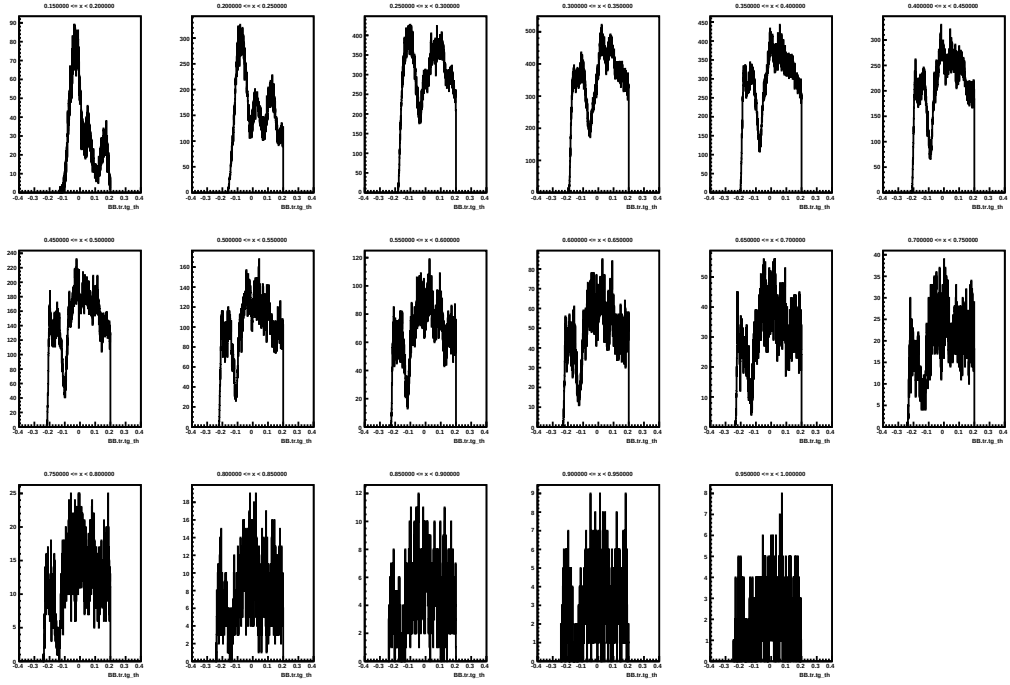

Figure 6.24: Measured distribution of ϕ, the azimuthal angle between the scattering plane and the polarization plane, in each x bin. The acceptance hole is under investigation but does not appear to be a problem.

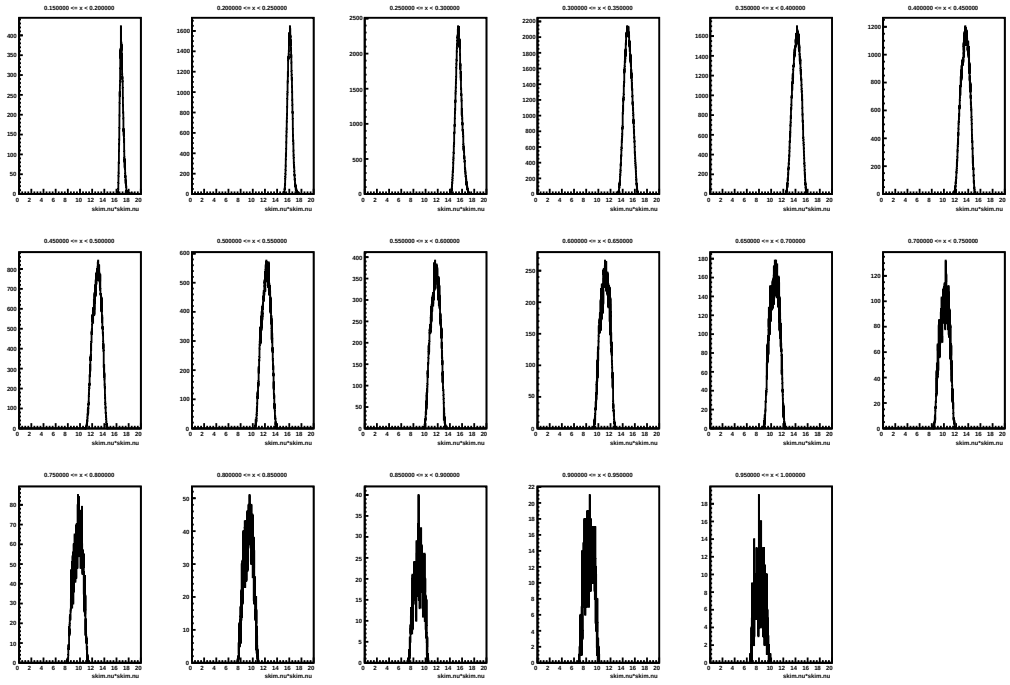

Figure 6.25: Measured distribution of ν^2 in each x bin.

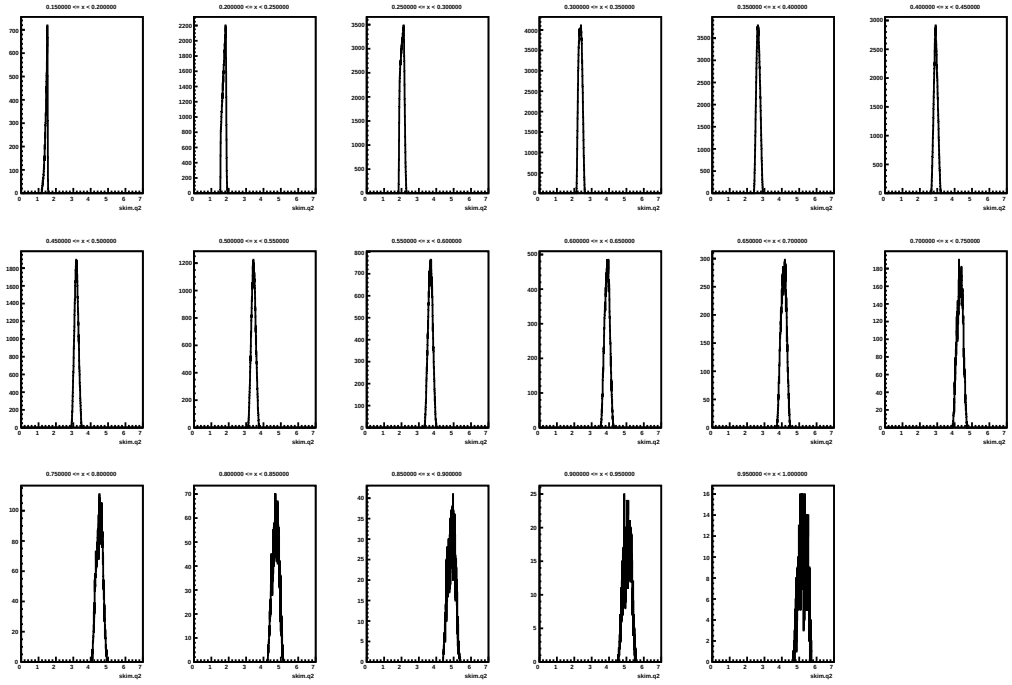

Figure 6.26: Measured distribution of four-momentum transfer Q^2 in each x bin.

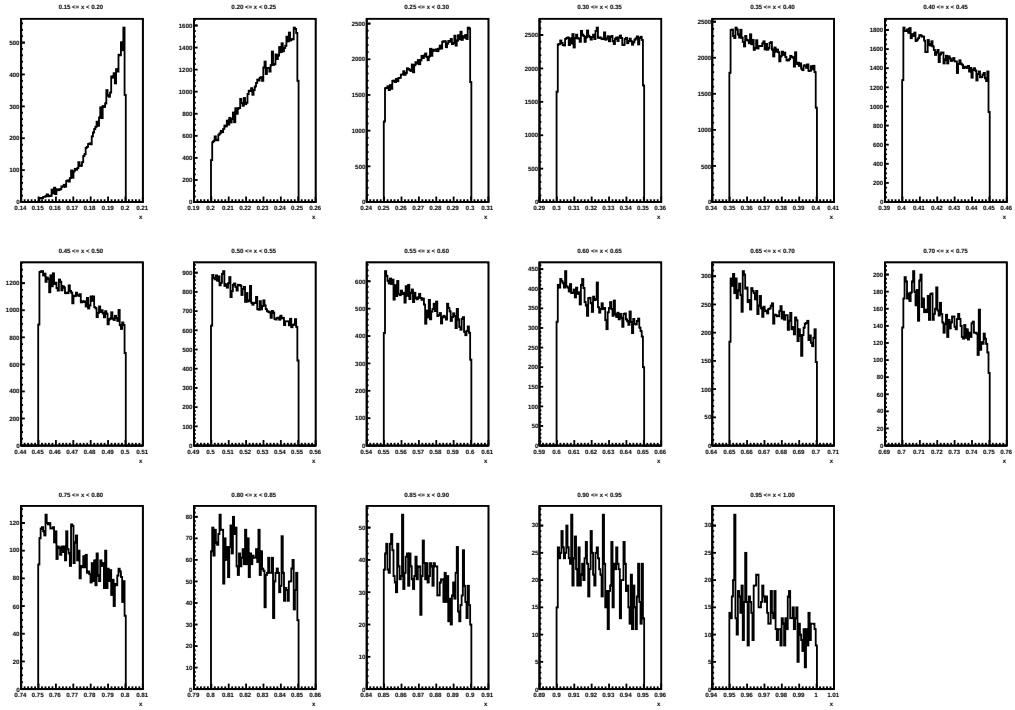

Figure 6.27: Measured distribution of Bjorken x in each x bin. The horizontal range of each histogram is chosen to be slightly wider than the x bin.

$\langle x \rangle$	$\langle \theta \rangle$	$\langle \tan^2(\theta/2) \rangle$	$\langle \cos\phi \rangle$	$\langle \lvert\vec{k}'\rvert = E' \rangle$ (GeV)	$\langle \nu^2 \rangle$ (GeV^2)	$\langle Q^2 \rangle$ ((GeV/c)^2)
0.187 ± 0.007	0.710 ± 0.010	0.137 ± 0.004	0.997 ± 0.0002	0.629 ± 0.006	16.854 ± 0.048	1.438 ± 0.055
0.229 ± 0.009	0.727 ± 0.010	0.145 ± 0.004	0.995 ± 0.0002	0.722 ± 0.007	16.105 ± 0.055	1.726 ± 0.066
0.277 ± 0.012	0.753 ± 0.010	0.157 ± 0.005	0.994 ± 0.0002	0.801 ± 0.008	15.472 ± 0.063	2.042 ± 0.083
0.325 ± 0.014	0.774 ± 0.010	0.167 ± 0.005	0.994 ± 0.0002	0.877 ± 0.009	14.883 ± 0.069	2.352 ± 0.098
0.374 ± 0.016	0.782 ± 0.010	0.171 ± 0.005	0.994 ± 0.0002	0.967 ± 0.010	14.201 ± 0.076	2.642 ± 0.110
0.424 ± 0.019	0.784 ± 0.010	0.172 ± 0.005	0.994 ± 0.0001	1.062 ± 0.011	13.493 ± 0.082	2.918 ± 0.121
0.474 ± 0.021	0.785 ± 0.010	0.172 ± 0.005	0.994 ± 0.0001	1.155 ± 0.012	12.820 ± 0.088	3.180 ± 0.130
0.523 ± 0.023	0.785 ± 0.010	0.172 ± 0.005	0.994 ± 0.0001	1.245 ± 0.012	12.189 ± 0.093	3.427 ± 0.140
0.574 ± 0.025	0.785 ± 0.010	0.172 ± 0.005	0.993 ± 0.0000	1.329 ± 0.013	11.604 ± 0.097	3.664 ± 0.149
0.624 ± 0.028	0.786 ± 0.010	0.173 ± 0.005	0.993 ± 0.0000	1.409 ± 0.014	11.071 ± 0.102	3.891 ± 0.157
0.673 ± 0.030	0.786 ± 0.010	0.173 ± 0.005	0.993 ± 0.0000	1.486 ± 0.015	10.567 ± 0.105	4.104 ± 0.165
0.723 ± 0.032	0.787 ± 0.010	0.173 ± 0.005	0.993 ± 0.0000	1.557 ± 0.016	10.110 ± 0.108	4.311 ± 0.173
0.773 ± 0.035	0.787 ± 0.010	0.173 ± 0.005	0.993 ± 0.0000	1.627 ± 0.016	9.671 ± 0.111	4.507 ± 0.180
0.823 ± 0.037	0.788 ± 0.010	0.174 ± 0.005	0.993 ± 0.0000	1.691 ± 0.017	9.277 ± 0.113	4.701 ± 0.186
0.873 ± 0.040	0.787 ± 0.010	0.173 ± 0.005	0.993 ± 0.0000	1.758 ± 0.018	8.872 ± 0.116	4.877 ± 0.193
0.923 ± 0.042	0.788 ± 0.010	0.174 ± 0.005	0.993 ± 0.0000	1.819 ± 0.018	8.517 ± 0.117	5.051 ± 0.199
0.972 ± 0.045	0.787 ± 0.010	0.173 ± 0.005	0.993 ± 0.0000	1.879 ± 0.019	8.171 ± 0.119	5.211 ± 0.205

Table 6.11: Kinematic parameters in each x bin, with resolution errors. At $x > 0.55$, the error on $\cos\phi$ is less than 100 ppm.

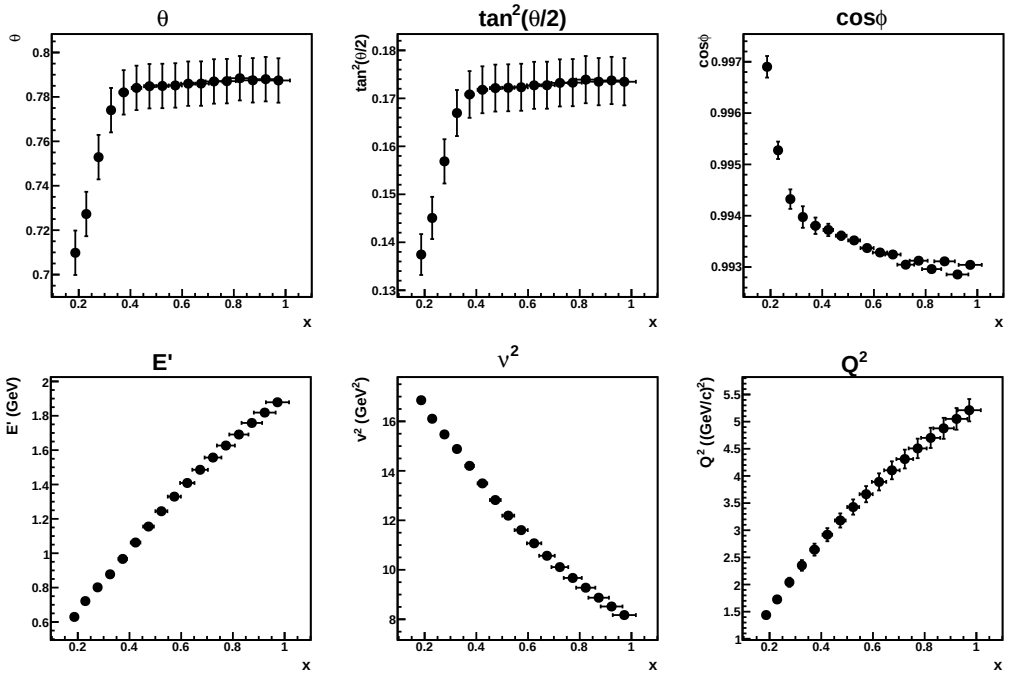

Figure 6.28: Mean values of kinematic parameters as functions of x. Error bars correspond to resolution errors.

6.4.2 Determination of $R = \sigma_L/\sigma_T$

In Equation 2.20, we defined $R = \sigma_L/\sigma_T$, the ratio of the absorption cross sections for virtual photons with longitudinal and transverse polarization. This ratio allows us to remove the dependence on F_2 of our final result; it features in the calculation of D and d, two of the variables used in calculating A_1 and A_2. R has been measured experimentally over a wide range of x and Q^2, and parameterizations of the world data allow us to calculate its value at an arbitrary kinematic point.

The first such parameterization, performed by Whitlow *et al.* in 1990 [31, 248], was an average of three three-parameter fits, each with a different functional form, and each of which was a good fit to the available data; this final parameterization is typically denoted $R1990$. Their analysis also led to the useful result that $R^p = R^n = R^d$; later, R was also found to be approximately constant over a variety of nuclei [249, 250]. This equivalence allows a wide range of data, taken with different targets, to be combined for the purposes of a world fit.

In 1999, the E143 collaboration, using their own new measurements of R as well as other world data that had accumulated over the preceding years, updated the $R1990$ parameterization. The resulting $R1998$ parameterization [80] is again the average of three functional forms, though these have each been extended to six-parameter functions in order to better fit the data at low x. With the final parameter values from the fit, these three functions – R_a, R_b, and R_c – are given by

$$R_a = \frac{0.0485}{\ln(Q^2/0.04)}\Theta(x,Q^2) + \frac{0.5470}{\sqrt[4]{Q^8 + 2.0621^4}}\left[1 - 0.3804x + 0.5090x^2\right]x^{-0.0285} \tag{6.22}$$

$$R_b = \frac{0.0481}{\ln(Q^2/0.04)}\Theta(x,Q^2) + \left[\frac{0.6114}{Q^2} - \frac{0.3509}{Q^4 + 0.3^2}\right]\left[1 - 0.4611x + 0.7172x^2\right]x^{-0.0317} \tag{6.23}$$

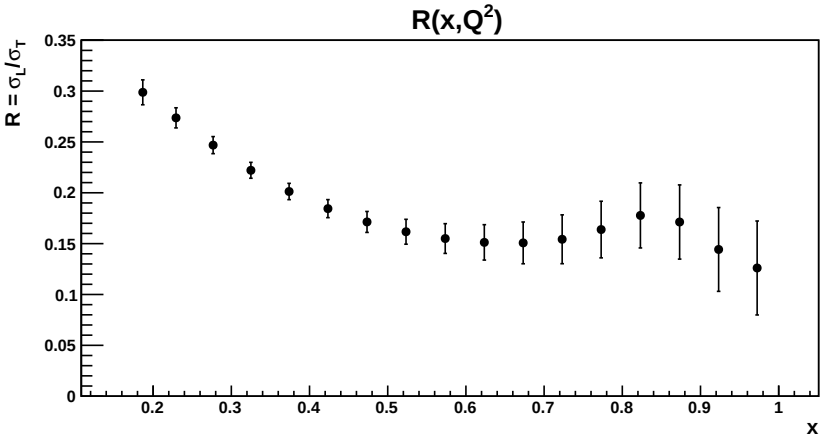

Figure 6.29: $R = \sigma_L/\sigma_T$ values for 4.74-GeV kinematics, based on a parameterization of world data by the E143 collaboration at SLAC [80].

$$R_c = \frac{0.0577}{\ln(Q^2/0.04)}\Theta(x,Q^2) + 0.4644\left[1.8288^2 + (Q^2 - 12.3708x + 43.1043x^2 - 41.7415x^3)^2\right]^{-1/2} \tag{6.24}$$

where $\Theta(x,Q^2)$ is given by

$$\Theta(x,Q^2) = 1 + 12\left(\frac{Q^2}{Q^2+1}\right)\left(\frac{0.125^2}{0.125^2+x^2}\right) \tag{6.25}$$

and the overall parameterization $R1998$ is the average of R_a, R_b, and R_c

$$R1998 = \frac{R_a + R_b + R_c}{3}. \tag{6.26}$$

The approximate fitting error is

$$\delta R1998 = 0.0078 - 0.013x + \frac{0.070 - 0.39x + 0.70x^2}{1.7 + Q^2}. \tag{6.27}$$

We used the $R1998$ parameterization to calculate the value of R in each of our bins, using the mean x and Q^2 values from Table 6.11. Figure 6.29 and Table 6.12 give the results, with errors calculated according to Equation 6.27. The resolution errors on $\langle x \rangle$ and $\langle Q^2 \rangle$ are negligible.

6.4.3 Construction of ϵ, D, η, d, and ξ

Armed with values of R (Table 6.12) as well as of E', x, Q^2, ν^2, and $\tan^2(\theta/2)$ (Table 6.11), we may compute the intermediate variables that enter directly into the calculation of A_1 and A_2. We compute the ratio of the virtual photon's longitudinal polarization to its transverse polarization, ϵ, according to Equation 2.3. Expressions for the quartet of variables D, η, d, and ξ are given in Equations 2.26, 2.27, 2.28, and 2.29, respectively.

Table 6.13 gives the resulting values of ϵ, D, η, d, and ξ in each x bin; these values are shown graphically in Figure 6.30. Errors are derived from those in Tables 6.11 and 6.12.

$\langle x \rangle$	R
0.187	0.299 ± 0.012
0.229	0.274 ± 0.010
0.277	0.247 ± 0.008
0.325	0.222 ± 0.008
0.374	0.201 ± 0.008
0.424	0.184 ± 0.009
0.474	0.171 ± 0.010
0.523	0.162 ± 0.012
0.574	0.155 ± 0.015
0.624	0.151 ± 0.017
0.673	0.151 ± 0.020
0.723	0.154 ± 0.024
0.773	0.164 ± 0.028
0.823	0.178 ± 0.032
0.873	0.171 ± 0.036
0.923	0.144 ± 0.041
0.972	0.126 ± 0.046

Table 6.12: $R(x, Q^2) = \sigma_L/\sigma_T$ for each x bin, based on the parameterization by the E143 collaboration at SLAC [80].

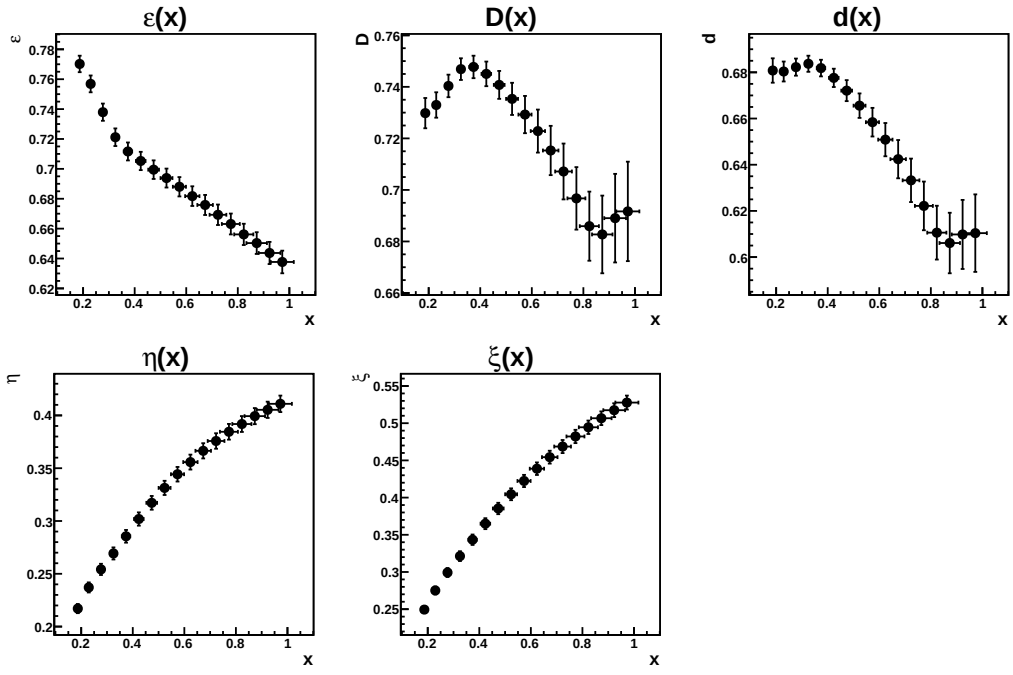

Figure 6.30: Kinematic variables ϵ, D, η, d, and ξ as functions of x.

$\langle x \rangle$	ϵ	D	d	η	ξ
0.187	0.7702 ± 0.0055	0.7298 ± 0.0059	0.6808 ± 0.0053	0.2171 ± 0.0043	0.2494 ± 0.0048
0.229	0.7569 ± 0.0056	0.7330 ± 0.0049	0.6804 ± 0.0043	0.2371 ± 0.0048	0.2752 ± 0.0053
0.277	0.7379 ± 0.0058	0.7404 ± 0.0044	0.6823 ± 0.0037	0.2542 ± 0.0053	0.2993 ± 0.0060
0.325	0.7212 ± 0.0059	0.7469 ± 0.0042	0.6837 ± 0.0035	0.2693 ± 0.0057	0.3213 ± 0.0066
0.374	0.7116 ± 0.0060	0.7477 ± 0.0044	0.6818 ± 0.0036	0.2855 ± 0.0060	0.3434 ± 0.0070
0.424	0.7053 ± 0.0061	0.7450 ± 0.0048	0.6776 ± 0.0040	0.3019 ± 0.0063	0.3650 ± 0.0074
0.474	0.6995 ± 0.0062	0.7408 ± 0.0054	0.6721 ± 0.0045	0.3172 ± 0.0065	0.3854 ± 0.0077
0.523	0.6938 ± 0.0063	0.7353 ± 0.0062	0.6656 ± 0.0053	0.3314 ± 0.0067	0.4045 ± 0.0079
0.574	0.6880 ± 0.0065	0.7292 ± 0.0072	0.6584 ± 0.0062	0.3443 ± 0.0069	0.4223 ± 0.0082
0.624	0.6817 ± 0.0066	0.7228 ± 0.0083	0.6509 ± 0.0072	0.3558 ± 0.0071	0.4388 ± 0.0084
0.673	0.6758 ± 0.0067	0.7153 ± 0.0096	0.6424 ± 0.0083	0.3665 ± 0.0072	0.4544 ± 0.0086
0.723	0.6693 ± 0.0068	0.7072 ± 0.0108	0.6332 ± 0.0094	0.3758 ± 0.0073	0.4686 ± 0.0088
0.773	0.6631 ± 0.0070	0.6967 ± 0.0121	0.6222 ± 0.0105	0.3845 ± 0.0074	0.4822 ± 0.0089
0.823	0.6561 ± 0.0071	0.6859 ± 0.0134	0.6106 ± 0.0116	0.3918 ± 0.0075	0.4945 ± 0.0090
0.873	0.6503 ± 0.0073	0.6827 ± 0.0151	0.6061 ± 0.0131	0.3993 ± 0.0076	0.5067 ± 0.0092
0.923	0.6437 ± 0.0074	0.6890 ± 0.0172	0.6098 ± 0.0150	0.4053 ± 0.0077	0.5175 ± 0.0093
0.972	0.6377 ± 0.0076	0.6917 ± 0.0193	0.6104 ± 0.0168	0.4110 ± 0.0078	0.5277 ± 0.0094

Table 6.13: Kinematic variables for calculation of A_1 and A_2.

Chapter 7

Results

Building on the analysis presented in Chapter 6, we present results for two pairs of asymmetries – $A_\parallel$ and $A_\perp$ (Section 7.1) and A_1 and A_2 (Section 7.2) – measured on the ^{3}He nucleus with an incident beam energy of 4.74 GeV. In Section 7.3, we describe the strategy for finalizing these results and outline a method of extracting the neutron asymmetries.

7.1 $A_\parallel$ and $A_\perp$ on ^{3}He

In Section 6.3.5, we measured the physics asymmetry for each of the three target spin orientations: 0°, 90°, and 270°, as defined in Figure 6.16. In order to compute A_1 and A_2, we must relate these asymmetries to the parallel and perpendicular electron asymmetries, $A_\parallel$ and $A_\perp$, which we defined in Equations 1.34 and 1.35, respectively. In the case of $A_\parallel$, our work is already done: we have only one longitudinal target spin orientation to consider, so $A_\parallel = A_0^{phys}$.

The computation of $A_\perp$ is slightly more involved. We must combine the data from the two transverse spin orientations; as explained in Section 6.3.1.2, we take the sign from the physics asymmetry measured with the target spin at 270°. We find the magnitude of the total transverse physics asymmetry by computing the weighted average of $|A_{90}^{phys}|$ and $|A_{270}^{phys}|$, with weights given solely by statistical errors.

In our BigBite data, the azimuthal angle ϕ varied over a range of about 0.4 radians. To correct for this angle's deviation from 0, we divide the transverse asymmetry by the mean $\cos\phi$ value in each x bin, drawn from Table 6.11. This value is quite close to 1 and its systematic error is negligible. We thus have

$$A_\perp = \frac{1}{|\langle\cos\phi\rangle|} \frac{\frac{A_{270}}{(\delta A_{270})^2} - \frac{A_{90}}{(\delta A_{90})^2}}{\frac{1}{(\delta A_{270})^2} + \frac{1}{(\delta A_{90})^2}} \tag{7.1}$$

where we have dropped the *phys* superscript for simplicity.

Figure 7.1 and Table 7.1 show our measurements of $A_\parallel$ and $A_\perp$ in e-^{3}He scattering for the 4.74-GeV dataset. Table 7.2 gives a breakdown of statistical and systematic errors in each bin.

7.2 A_1 and A_2 on ^{3}He

The virtual photon-nucleus asymmetries $A_1^{^3\mathrm{He}}$ and $A_2^{^3\mathrm{He}}$ are formed from linear combinations of $A_\parallel^{^3\mathrm{He}}$ and $A_\perp^{^3\mathrm{He}}$. The exact expressions were given in Equations 2.30 and 2.31

$$A_1 = \frac{1}{D\,(1+\eta\xi)} A_\parallel - \frac{\eta}{d\,(1+\eta\xi)} A_\perp \tag{7.2}$$

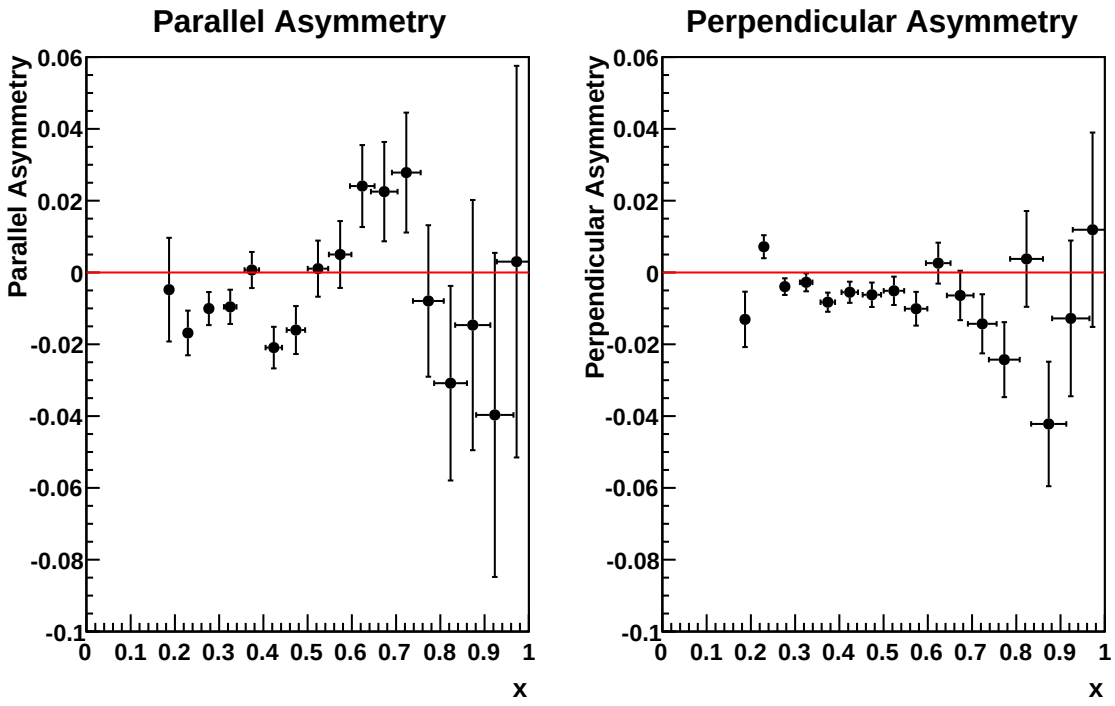

Figure 7.1: $A_{\parallel}^{^3\mathrm{He}}$ and $A_{\perp}^{^3\mathrm{He}}$ measured with $E_e = 4.74$ GeV.

$\langle x \rangle$	$A_{\parallel}^{^3\mathrm{He}}$	$A_{\perp}^{^3\mathrm{He}}$
0.187	$-0.0048 \pm 0.0144_{stat} \pm 0.0008_{syst}$	$-0.0131 \pm 0.0077_{stat} \pm 0.0009_{syst}$
0.229	$-0.0168 \pm 0.0061_{stat} \pm 0.0009_{syst}$	$0.0072 \pm 0.0032_{stat} \pm 0.0006_{syst}$
0.277	$-0.0100 \pm 0.0046_{stat} \pm 0.0006_{syst}$	$-0.0039 \pm 0.0023_{stat} \pm 0.0004_{syst}$
0.325	$-0.0096 \pm 0.0042_{stat} \pm 0.0022_{syst}$	$-0.0027 \pm 0.0021_{stat} \pm 0.0014_{syst}$
0.374	$0.0007 \pm 0.0045_{stat} \pm 0.0022_{syst}$	$-0.0083 \pm 0.0022_{stat} \pm 0.0015_{syst}$
0.424	$-0.0209 \pm 0.0053_{stat} \pm 0.0024_{syst}$	$-0.0055 \pm 0.0026_{stat} \pm 0.0014_{syst}$
0.474	$-0.0160 \pm 0.0063_{stat} \pm 0.0023_{syst}$	$-0.0062 \pm 0.0031_{stat} \pm 0.0014_{syst}$
0.523	$0.0011 \pm 0.0075_{stat} \pm 0.0021_{syst}$	$-0.0051 \pm 0.0037_{stat} \pm 0.0013_{syst}$
0.574	$0.0050 \pm 0.0091_{stat} \pm 0.0021_{syst}$	$-0.0101 \pm 0.0045_{stat} \pm 0.0015_{syst}$
0.624	$0.0241 \pm 0.0110_{stat} \pm 0.0031_{syst}$	$0.0026 \pm 0.0054_{stat} \pm 0.0018_{syst}$
0.673	$0.0225 \pm 0.0135_{stat} \pm 0.0031_{syst}$	$-0.0064 \pm 0.0066_{stat} \pm 0.0020_{syst}$
0.723	$0.0278 \pm 0.0166_{stat} \pm 0.0014_{syst}$	$-0.0143 \pm 0.0082_{stat} \pm 0.0008_{syst}$
0.773	$-0.0079 \pm 0.0211_{stat} \pm 0.0004_{syst}$	$-0.0243 \pm 0.0104_{stat} \pm 0.0014_{syst}$
0.823	$-0.0308 \pm 0.0271_{stat} \pm 0.0016_{syst}$	$0.0038 \pm 0.0133_{stat} \pm 0.0002_{syst}$
0.873	$-0.0146 \pm 0.0348_{stat} \pm 0.0008_{syst}$	$-0.0422 \pm 0.0172_{stat} \pm 0.0022_{syst}$
0.923	$-0.0397 \pm 0.0451_{stat} \pm 0.0021_{syst}$	$-0.0128 \pm 0.0217_{stat} \pm 0.0009_{syst}$
0.972	$0.0030 \pm 0.0545_{stat} \pm 0.0002_{syst}$	$0.0119 \pm 0.0270_{stat} \pm 0.0020_{syst}$

Table 7.1: $A_{\parallel}^{^3\mathrm{He}}$ and $A_{\perp}^{^3\mathrm{He}}$ for each x bin, with $E_e = 4.74$ GeV. A detailed error breakdown may be found in Table 7.2.

	Errors on $A_{\parallel}^{^3\mathrm{He}}$					Errors on $A_{\perp}^{^3\mathrm{He}}$				
$\langle x \rangle$	Statistical	P_e	$P_{^3\mathrm{He}}$	D_{N_2}	$f_{bg}\Delta A$	Statistical	P_e	$P_{^3\mathrm{He}}$	D_{N_2}	$f_{bg}\Delta A$
0.187	0.0144	0.0100	0.0286	0.0028	0.0007	0.0077	0.0100	0.0289	0.0028	0.0004
0.229	0.0061	0.0100	0.0286	0.0029	0.0004	0.0032	0.0100	0.0289	0.0029	0.0002
0.277	0.0046	0.0100	0.0286	0.0031	0.0004	0.0023	0.0100	0.0289	0.0031	0.0002
0.325	0.0042	0.0100	0.0286	0.0031	0.0022	0.0021	0.0100	0.0289	0.0031	0.0011
0.374	0.0045	0.0100	0.0286	0.0031	0.0022	0.0022	0.0100	0.0289	0.0031	0.0011
0.424	0.0053	0.0100	0.0286	0.0031	0.0021	0.0026	0.0100	0.0289	0.0031	0.0011
0.474	0.0063	0.0100	0.0286	0.0030	0.0021	0.0031	0.0100	0.0289	0.0030	0.0011
0.523	0.0075	0.0100	0.0286	0.0030	0.0021	0.0037	0.0100	0.0289	0.0030	0.0010
0.574	0.0091	0.0100	0.0286	0.0030	0.0021	0.0045	0.0100	0.0289	0.0030	0.0011
0.624	0.0110	0.0100	0.0286	0.0029	0.0028	0.0054	0.0100	0.0289	0.0029	0.0015
0.673	0.0135	0.0100	0.0286	0.0029	0.0028	0.0066	0.0100	0.0289	0.0029	0.0015
0.723	0.0166	0.0100	0.0286	0.0030	0.0000	0.0082	0.0100	0.0289	0.0030	0.0000
0.773	0.0211	0.0100	0.0286	0.0031	0.0000	0.0104	0.0100	0.0289	0.0031	0.0000
0.823	0.0271	0.0100	0.0286	0.0034	0.0000	0.0133	0.0100	0.0289	0.0034	0.0000
0.873	0.0348	0.0100	0.0286	0.0036	0.0000	0.0172	0.0100	0.0289	0.0036	0.0000
0.923	0.0451	0.0100	0.0286	0.0038	0.0000	0.0217	0.0100	0.0289	0.0038	0.0000
0.972	0.0545	0.0100	0.0286	0.0034	0.0000	0.0270	0.0100	0.0289	0.0034	0.0000

Table 7.2: Error breakdown for $A_{\parallel}^{^3\mathrm{He}}$ and $A_{\perp}^{^3\mathrm{He}}$ for each x bin, with $E_e = 4.74$ GeV.

$$A_2 = \frac{\xi}{D\,(1+\eta\xi)} A_{\parallel} + \frac{1}{d\,(1+\eta\xi)} A_{\perp}. \tag{7.3}$$

The variables used in these expressions are taken from Table 6.13. The coefficients of $A_{\parallel}$ and $A_{\perp}$ in the calculation of A_1 and A_2 are plotted for our kinematics in Figure 7.2, and recorded numerically in Table 7.3. We see that $A_{\parallel}$ has a larger contribution to A_1 than $A_{\perp}$ does, and that this relationship is reversed in the calculation of A_2.

Figure 7.3 and Table 7.4 give our final results: $A_1^{^3\mathrm{He}}$ and $A_2^{^3\mathrm{He}}$. Following Equation 2.15, we can use these results to form the structure-function ratio $g_1^{^3\mathrm{He}}/F_1^{^3\mathrm{He}}$, plotted in Figure 7.4. In Figures 7.5 and 7.6, we plot our A_1 and A_2 measurements along with existing ^{3}He data from the E142 experiment at SLAC [51] and from the E99-117 experiment in Hall A of Jefferson Lab [41]. We note that, in these kinematics, our measurements are in the deep-inelastic scattering region only up to about $x \sim 0.55$; at higher x, we are in the resonance region. Our results are largely consistent with previous measurements in this area; in the case of $A_2^{^3\mathrm{He}}$, we have substantially improved the accuracy of the available data.

7.3 Summary and Outlook

We have successfully commissioned a new detector, data acquisition system, and analysis method for beam polarimetry in Hall A (Section 4.3), establishing an upgraded Compton polarimeter that will improve beam polarimetry throughout the remainder of Hall A's 6-GeV physics program. We have measured the virtual photon asymmetries A_1 and A_2 on a ^{3}He target for $0.15 \leq x \leq 1.0$, in both the deep-inelastic scattering region and the resonance region, for an incident beam energy of 4.74 GeV. Additional analysis activities, conducted primarily by the two other students in the collaboration and

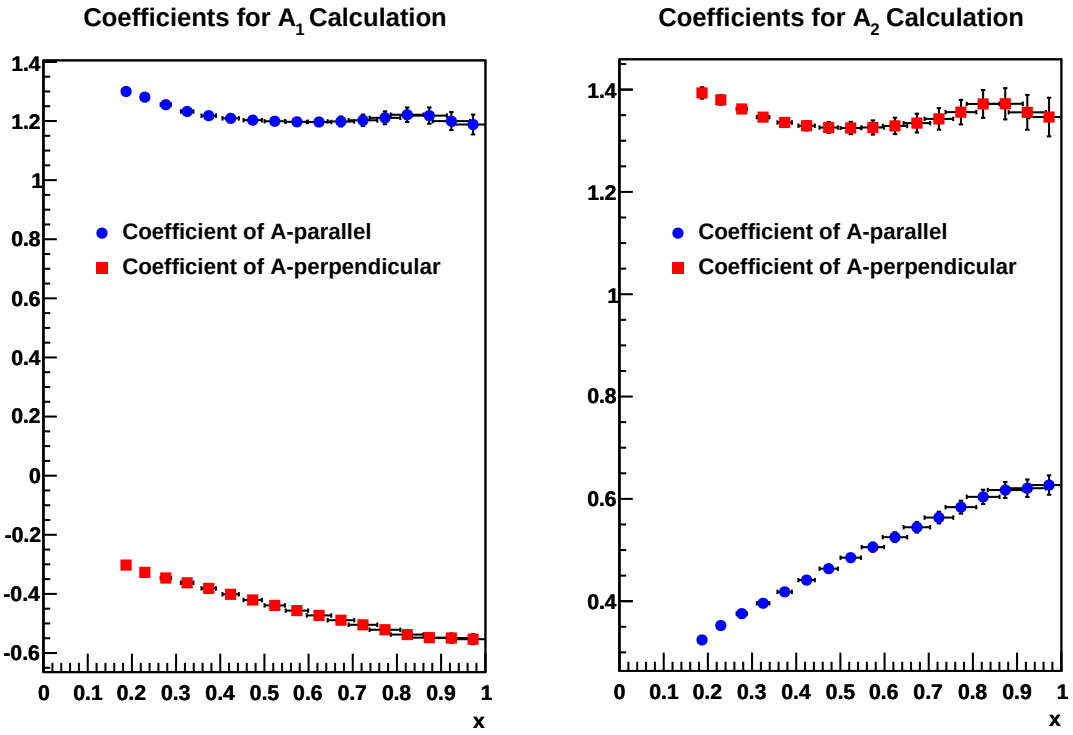

Figure 7.2: Coefficients used in calculation of A_1 and A_2 at 4.74-GeV kinematics.

$\langle x \rangle$	$\frac{1}{D(1+\eta\xi)}$	$\frac{-\eta}{d(1+\eta\xi)}$	$\frac{\xi}{D(1+\eta\xi)}$	$\frac{1}{d(1+\eta\xi)}$
0.187	1.2998 ± 0.0106	-0.3025 ± 0.0060	0.3242 ± 0.0062	1.3934 ± 0.0111
0.229	1.2808 ± 0.0089	-0.3271 ± 0.0062	0.3524 ± 0.0065	1.3798 ± 0.0093
0.277	1.2552 ± 0.0080	-0.3462 ± 0.0066	0.3757 ± 0.0069	1.3621 ± 0.0083
0.325	1.2323 ± 0.0078	-0.3625 ± 0.0068	0.3960 ± 0.0072	1.3461 ± 0.0081
0.374	1.2180 ± 0.0081	-0.3813 ± 0.0070	0.4182 ± 0.0075	1.3357 ± 0.0085
0.424	1.2090 ± 0.0088	-0.4013 ± 0.0072	0.4412 ± 0.0077	1.3293 ± 0.0093
0.474	1.2029 ± 0.0099	-0.4206 ± 0.0075	0.4636 ± 0.0080	1.3258 ± 0.0105
0.523	1.1992 ± 0.0113	-0.4390 ± 0.0078	0.4850 ± 0.0084	1.3249 ± 0.0120
0.574	1.1972 ± 0.0129	-0.4565 ± 0.0083	0.5056 ± 0.0089	1.3260 ± 0.0139
0.624	1.1966 ± 0.0148	-0.4728 ± 0.0089	0.5251 ± 0.0096	1.3289 ± 0.0160
0.673	1.1985 ± 0.0169	-0.4890 ± 0.0096	0.5445 ± 0.0104	1.3345 ± 0.0184
0.723	1.2024 ± 0.0193	-0.5046 ± 0.0105	0.5635 ± 0.0114	1.3427 ± 0.0211
0.773	1.2108 ± 0.0218	-0.5213 ± 0.0116	0.5838 ± 0.0126	1.3559 ± 0.0240
0.823	1.2212 ± 0.0246	-0.5376 ± 0.0128	0.6039 ± 0.0140	1.3719 ± 0.0271
0.873	1.2182 ± 0.0275	-0.5480 ± 0.0141	0.6173 ± 0.0155	1.3723 ± 0.0306
0.923	1.1997 ± 0.0305	-0.5494 ± 0.0155	0.6208 ± 0.0171	1.3556 ± 0.0340
0.972	1.1881 ± 0.0336	-0.5533 ± 0.0170	0.6270 ± 0.0189	1.3463 ± 0.0378

Table 7.3: Coefficients used in calculation of A_1 and A_2 for each x bin, with $E_e = 4.74$ GeV.

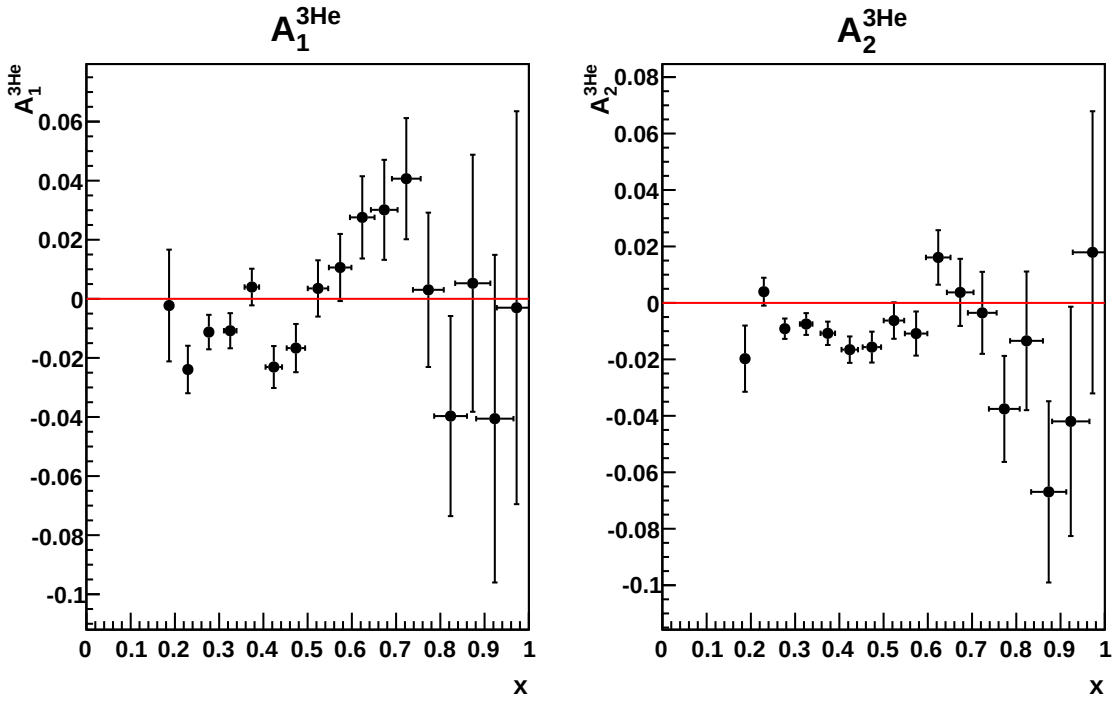

Figure 7.3: $A_1^{^3\mathrm{He}}$ and $A_2^{^3\mathrm{He}}$ from 4.74-GeV dataset.

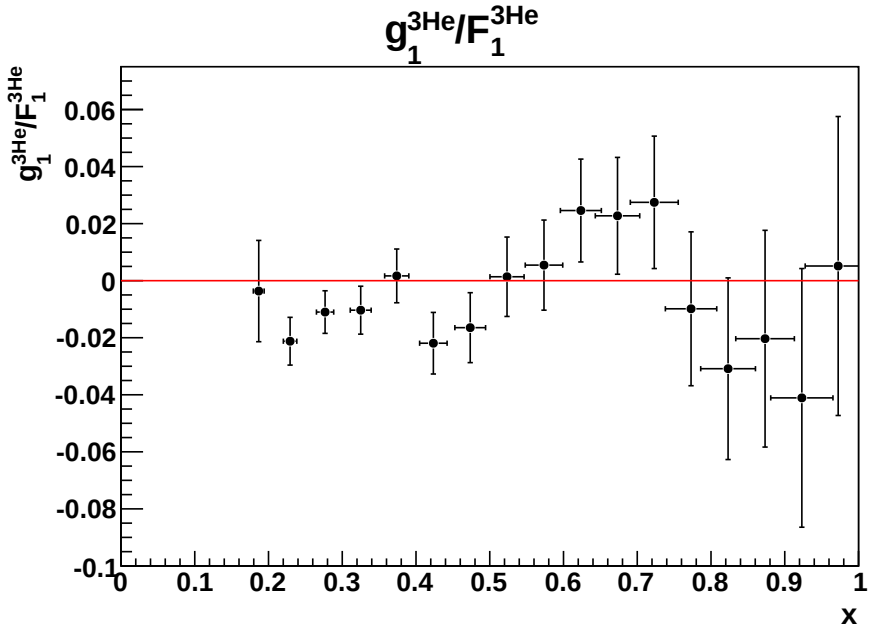

Figure 7.4: Structure-function ratio $g_1^{^3\mathrm{He}}/F_1^{^3\mathrm{He}}$ from 4.74-GeV dataset, computed from $A_1^{^3\mathrm{He}}$ and $A_2^{^3\mathrm{He}}$.

$\langle x \rangle$	$A_1^{^3\mathrm{He}}$	$A_2^{^3\mathrm{He}}$	$g_1^{^3\mathrm{He}}/F_1^{^3\mathrm{He}}$
0.187	$-0.002 \pm 0.019_{stat} \pm 0.001_{syst}$	$-0.020 \pm 0.012_{stat} \pm 0.001_{syst}$	-0.004 ± 0.018
0.229	$-0.024 \pm 0.008_{stat} \pm 0.001_{syst}$	$0.004 \pm 0.005_{stat} \pm 0.001_{syst}$	-0.021 ± 0.008
0.277	$-0.011 \pm 0.006_{stat} \pm 0.001_{syst}$	$-0.009 \pm 0.004_{stat} \pm 0.001_{syst}$	-0.011 ± 0.007
0.325	$-0.011 \pm 0.005_{stat} \pm 0.003_{syst}$	$-0.007 \pm 0.003_{stat} \pm 0.002_{syst}$	-0.010 ± 0.008
0.374	$0.004 \pm 0.006_{stat} \pm 0.003_{syst}$	$-0.011 \pm 0.004_{stat} \pm 0.002_{syst}$	0.002 ± 0.009
0.424	$-0.023 \pm 0.006_{stat} \pm 0.003_{syst}$	$-0.017 \pm 0.004_{stat} \pm 0.002_{syst}$	-0.022 ± 0.011
0.474	$-0.017 \pm 0.008_{stat} \pm 0.003_{syst}$	$-0.016 \pm 0.005_{stat} \pm 0.002_{syst}$	-0.016 ± 0.012
0.523	$0.004 \pm 0.009_{stat} \pm 0.003_{syst}$	$-0.006 \pm 0.006_{stat} \pm 0.002_{syst}$	0.001 ± 0.014
0.574	$0.011 \pm 0.011_{stat} \pm 0.003_{syst}$	$-0.011 \pm 0.007_{stat} \pm 0.002_{syst}$	0.005 ± 0.016
0.624	$0.028 \pm 0.013_{stat} \pm 0.004_{syst}$	$0.016 \pm 0.009_{stat} \pm 0.003_{syst}$	0.025 ± 0.018
0.673	$0.030 \pm 0.016_{stat} \pm 0.004_{syst}$	$0.004 \pm 0.011_{stat} \pm 0.003_{syst}$	0.023 ± 0.020
0.723	$0.041 \pm 0.020_{stat} \pm 0.002_{syst}$	$-0.004 \pm 0.014_{stat} \pm 0.001_{syst}$	0.027 ± 0.023
0.773	$0.003 \pm 0.026_{stat} \pm 0.001_{syst}$	$-0.038 \pm 0.019_{stat} \pm 0.002_{syst}$	-0.010 ± 0.027
0.823	$-0.040 \pm 0.034_{stat} \pm 0.002_{syst}$	$-0.013 \pm 0.025_{stat} \pm 0.001_{syst}$	-0.031 ± 0.032
0.873	$0.005 \pm 0.043_{stat} \pm 0.002_{syst}$	$-0.067 \pm 0.032_{stat} \pm 0.003_{syst}$	-0.020 ± 0.038
0.923	$-0.041 \pm 0.055_{stat} \pm 0.003_{syst}$	$-0.042 \pm 0.041_{stat} \pm 0.002_{syst}$	-0.041 ± 0.045
0.972	$-0.003 \pm 0.066_{stat} \pm 0.001_{syst}$	$0.018 \pm 0.050_{stat} \pm 0.003_{syst}$	0.005 ± 0.052

Table 7.4: Measured $A_1^{^3\mathrm{He}}$, $A_2^{^3\mathrm{He}}$ and $g_1^{^3\mathrm{He}}/F_1^{^3\mathrm{He}}$ values for $E_e = 4.74$ GeV. The error breakdown for $A_\parallel^{^3\mathrm{He}}$ and $A_\perp^{^3\mathrm{He}}$ may be found in Table 7.2; Table 7.3 shows the errors from the coefficients of these asymmetries.

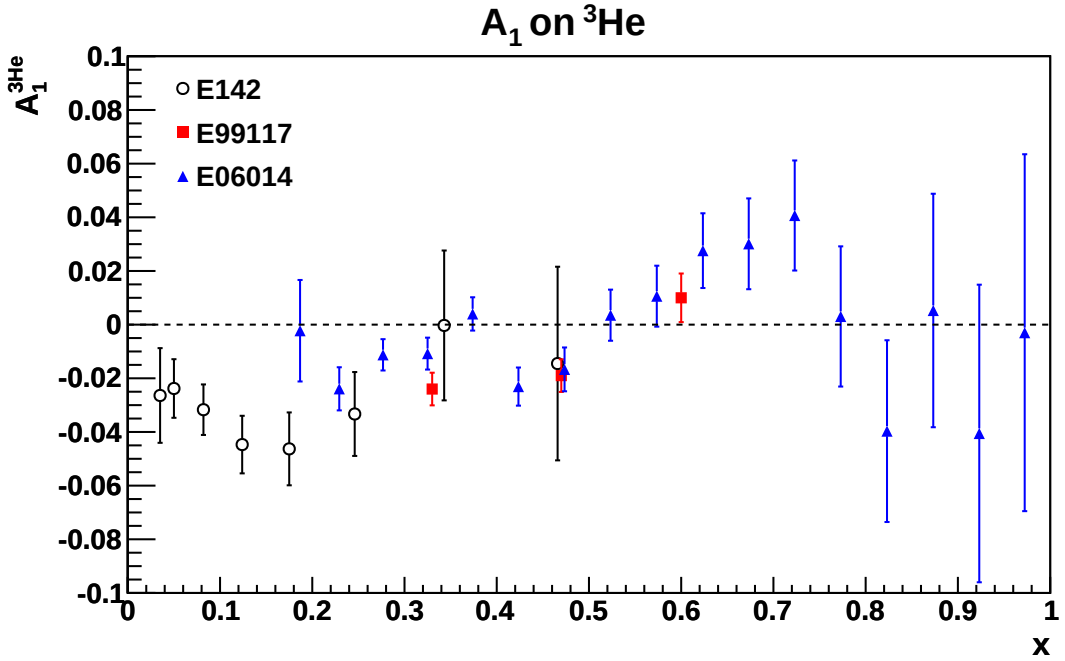

Figure 7.5: E06-014 measurement of $A_1^{^3\mathrm{He}}$ at 4.74 GeV, compared to world ^{3}He data.

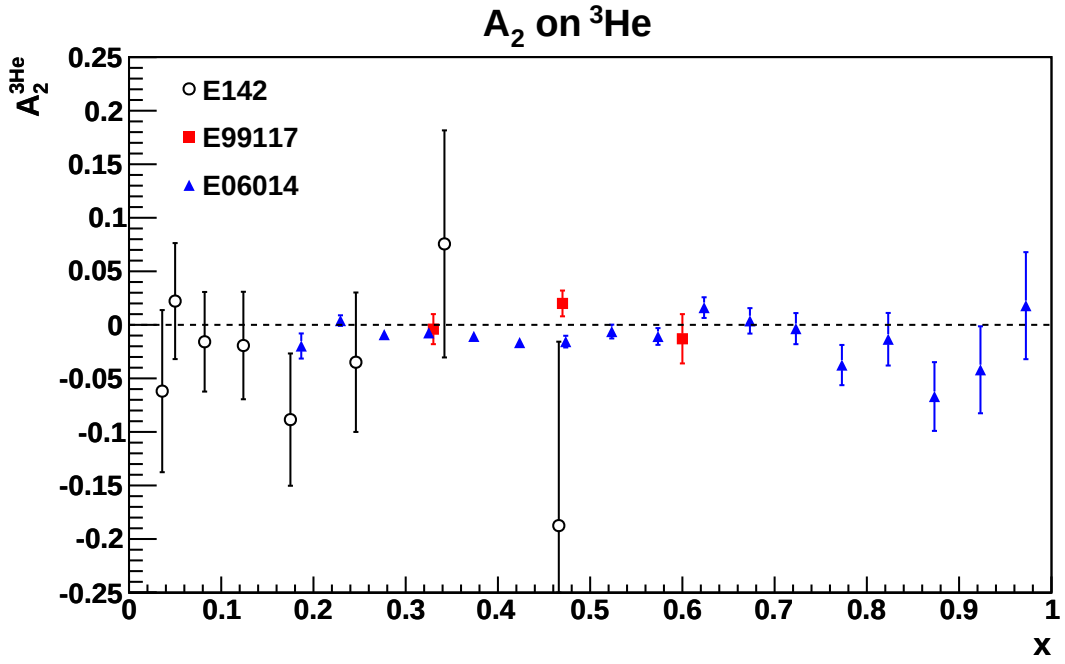

Figure 7.6: E06-014 measurement of $A_2^{^3\mathrm{He}}$ at 4.74 GeV, compared to world ^{3}He data.

currently underway, will extend our kinematic range and improve our understanding of systematics within the next year or so.

Analysis of the beam polarization is complete (Section 4.4), but further work on the target polarization analysis (Section 5.1.2) will add a second set of absolute polarization measurements (water-calibrated NMR measurements) to our existing data; the final target polarization values will be the weighted average of these new measurements and the EPR-calibrated NMR measurements that we have used in this work. This change is not expected to shift the physics asymmetries significantly, but will reduce the systematic error due to target polarization. A second, more careful round of event selection analysis will give us a better understanding of systematic errors due to background contamination and acceptance effects in our kinematic parameters. This, in turn, will allow us to estimate the error due to these sources rather than setting upper bounds.

At low x, we must also account for an additional dilution factor due to pair production. The initial scattering interaction may produce a π^0, which decays to photons that may in turn produce electron-positron pairs. Unlike electrons scattered directly from the target, pair-produced electrons will not display the same helicity-dependent asymmetry, and so their inclusion in our sample changes the measured asymmetry. The experience of prior experiments [41] suggests that this effect should be small, but we can quantify (and correct for) the contribution of pair-produced electrons by measuring the positron yield. We have data from both the LHRS and BigBite, operating with positive polarity (reversed from the standard electron-detection mode), which will allow us to perform this study.

While the ^{3}He results from the 4.74-GeV dataset from E06-014 constitute a complete and interesting measurement by themselves, the full analysis of the 5.9-GeV dataset will be a useful complement to them in the final, published data. By interpolating the measurements from the two datasets, we may obtain asymmetry measurements varying in x but with Q^2 held constant, with reduced statistical errors.

Of course, the primary theoretical interest in a measurement of $A_1^{^3\mathrm{He}}$ is that it makes possible a measurement of A_1^n. As we saw in Section 2.3, measurements of A_1^n, A_2^n, and consequently (from

Equation 2.15) g_1^n/F_1^n have the potential to distinguish among a wide field of theories, models and assumptions about nucleon spin structure, especially when combined with recent data on the proton (Section 2.1.3). Our ^{3}He results support the earlier Hall A observation that $A_1^{^3\mathrm{He}}$ becomes positive at high x [41]; confirmation of a sign change in A_1^n would be an exciting result.

The extraction of neutron results from a measurement on ^{3}He requires a careful theoretical study of nuclear dynamics. The neutron polarized structure function g_1^n need not be equal to $g_1^{^3\mathrm{He}}$: a range of nuclear effects, including spin depolarization, proton polarization, non-nucleonic degrees of freedom, nuclear binding effects, and nucleon Fermi motion [251] induce differences between the two. At finite values of Q^2, structure-function smearing complicates the picture further, particularly in the resonance region [252].

The previous A_1^n measurement in Hall A used the nuclear model of Bissey *et al.* [251], in which A_1^n is expressed as a function of $A_1^{^3\mathrm{He}}$ and several quantities extracted from world data

$$A_1^n = \frac{F_2^{^3\mathrm{He}}}{P_n F_2^n \left(1 + \frac{0.056}{P_n}\right)} \left(A_1^{^3\mathrm{He}} - 2\frac{F_2^p}{F_2^{^3\mathrm{He}}} P_p A_1^p \left(1 - \frac{0.014}{2P_p}\right)\right). \tag{7.4}$$

This model is valid only for deep-inelastic scattering in the large-x region and cannot be used for measurements in the resonance region. P_n and P_p represent the effective polarizations of neutrons and protons, respectively, inside the ^{3}He nucleus. These values are computed from three-body models of the ^{3}He wave functions. The results of E05-102 [253], a Hall A experiment that ran in 2009 with the goal of settling discrepancies between Fadeev models of the ^{3}He nucleus, are expected to improve the accuracy of these values.

We have measured $A_1^{^3\mathrm{He}}$ in deep inelastic scattering and in the resonance region for an incident beam energy of 4.74 GeV. Our treatment of the target polarization and other sources of systematic error is being finalized, and the analysis of an additional data set with an incident beam energy of 5.9 GeV is underway. Our results appear to support the recent high-x data from E99-117 [41]. The extraction of neutron asymmetries for our data, which awaits theoretical input and new data on ^{3}He wave functions, will help test theoretical assumptions about nucleon spin structure and quark orbital angular momentum. The proton spin puzzle has not been solved, but these measurements will put another piece in place.

Bibliography

[1] D. Binosi and L. Theußl, *JaxoDraw: A graphical user interface for drawing Feynman diagrams.* Comp. Phys. Comm. **161**: 76 (2004) (Referenced on page 17.)

[2] M. J. Alguard, W. W. Ash, G. Baum, *et al.*, (E-080 Collaboration), *Deep inelastic scattering of polarized electrons by polarized protons.* Phys. Rev. Lett. **37**: 1261 (1976) (Referenced on pages 17 and 41.)

[3] M. J. Alguard, W. W. Ash, G. Baum, *et al.*, (E-080 Collaboration), *Deep-inelastic $e-p$ asymmetry measurements and comparison with the Bjorken sum rule and models of proton spin structure.* Phys. Rev. Lett. **41** (2): 70 (1978) (Referenced on pages 17 and 41.)

[4] G. Baum, M. R. Bergström, J. E. Clendenin, *et al.*, (E-130 Collaboration), *Measurement of asymmetry in spin-dependent $e-p$ resonance-region scattering.* Phys. Rev. Lett. **45** (25): 2000 (1980) (Referenced on page 17.)

[5] G. Baum, M. R. Bergström, P. R. Bolton, *et al.*, (E-130 Collaboration), *New measurement of deep-inelastic $e-p$ asymmetries.* Phys. Rev. Lett. **51** (13): 1135 (1983) (Referenced on page 17.)

[6] J. Ashman, B. Badelek, G. Baum, *et al.*, (European Muon Collaboration), *A measurement of the spin asymmetry and determination of the structure function g_1 in deep inelastic muon-proton scattering.* Phys. Lett. B **206**: 364 (1988) (Referenced on page 17.)

[7] J. Ashman, B. Badelek, G. Baum, *et al.*, (European Muon Collaboration), *An investigation of the spin structure of the proton in deep inelastic scattering of polarised muons on polarised protons.* Nucl. Phys. B **328**: 1 (1989) (Referenced on pages 17, 18, and 41.)

[8] J. Ellis and R. Jaffe, *Sum rule for deep-inelastic electroproduction from polarized protons.* Phys. Rev. D **9**: 1444 (1974) (Referenced on page 18.)

[9] E. Leader and M. Anselmino, *A crisis in the parton model: where, oh where is the proton's spin?* Z. Physik C **41**: 239 (1988) (Referenced on pages 18 and 41.)

[10] S. E. Kuhn, J.-P. Chen, and E. Leader, *Spin structure of the nucleon – status and recent results.* Prog. Nucl. Part. Phys. **63**: 1 (2009) (Referenced on pages 18 and 27.)

[11] K. Nakamura *et al.*, (Particle Data Group), *Review of Particle Physics.* J. Phys. G **37**: 075021 (2010) (Referenced on pages 18, 29, 54, 61, 91, 94, and 172.)

[12] G. Bunce, N. Saito, J. Soffer, *et al.*, *Prospects for spin physics at RHIC.* Annu. Rev. Nucl. Part. Sci. **50**: 525 (2000) (Referenced on page 19.)

[13] C. Aidala, M. Bai, L. Bland, *et al.*, *Research plan for spin physics at RHIC.* Report for DOE (2005), http://spin.riken.bnl.gov/rsc/report/masterspin.pdf (Referenced on page 19.)

[14] S. D. Drell and T.-M. Yan, *Massive lepton-pair production in hadron-hadron collisions at high energies*. Phys. Rev. Lett. **25**: 316 (1970) (Referenced on page 19.)

[15] F. Halzen and A. D. Martin, *Quarks and Leptons*. John Wiley and Sons, Inc. (1984) (Referenced on pages 20, 23, 32, and 33.)

[16] X. Zheng, *Precision measurement of neutron spin asymmetry A_1^n at large x_{B_j} using CEBAF at 5.7 GeV*. Ph.D. thesis, Massachusetts Institute of Technology (2002) (Referenced on pages 21, 33, 37, 40, 47, 74, 75, 83, and 176.)

[17] B. Povh, K. Rith, C. Scholz, *et al.*, *Particles and Nuclei*. 4th edition, Springer (2004) (Referenced on page 22.)

[18] M. Anselmino, A. Efremov, and E. Leader, *The theory and phenomenology of polarized deep inelastic scattering*. Phys. Rep. **261**: 1 (1995) , see erratum in Phys. Rep. **281**: 399 (1997) (Referenced on pages 22, 25, and 29.)

[19] R. G. Roberts, *The Structure of the Proton: Deep Inelastic Scattering*. Cambridge Monographs on Mathematical Physics, Cambridge University Press (1990) (Referenced on page 27.)

[20] J. D. Bjorken and E. A. Paschos, *Inelastic electron-proton and γ-proton scattering and the structure of the nucleon*. Phys. Rev. **185**: 1975 (1969) (Referenced on pages 27 and 41.)

[21] C. G. Callan and D. J. Gross, *High-energy electroproduction and the constitution of the electric current*. Phys. Rev. Lett. **22**: 156 (1969) (Referenced on page 27.)

[22] K. G. Wilson, *Non-Lagrangian models of current algebra*. Phys. Rev. **179**: 1499 (1969) (Referenced on page 30.)

[23] A. V. Manohar, *An introduction to spin dependent deep inelastic scattering*. In B. A. Campbell, editor, *Symmetry and spin in the Standard Model: Proceedings of the seventh Lake Louise Winter Institute*, World Scientific (1992), hep-ph/9204208v1 (Referenced on page 30.)

[24] S. Wandzura and F. Wilczek, *Sum rules for spin-dependent electroproduction – Test of relativistic constituent quarks*. Phys. Lett. B **72**: 195 (1977) (Referenced on page 30.)

[25] L. N. Hand, *Experimental investigation of pion electroproduction*. Phys. Rev. **129**: 1834 (1963) (Referenced on page 32.)

[26] K. Abe, T. Akagi, P. L. Anthony, *et al.*, (E143 Collaboration), *Measurements of the proton and deuteron spin structure functions g_1 and g_2*. Phys. Rev. D **58**: 112003 (1998) (Referenced on pages 33 and 44.)

[27] J. Soffer and O. V. Teryaev, *Positivity constraints and flavor dependence of higher twists*. Phys. Lett. B **490**: 106 (2000) (Referenced on page 34.)

[28] D. Drechsel, S. S. Kamalov, and L. Tiator, *Gerasimov-Drell-Hearn sum rule and related integrals*. Phys. Rev. D **63**: 114010 (2001) (Referenced on pages 34 and 59.)

[29] K. V. Dharmawardane, *Spin structure functions of the deuteron measured with CLAS in and above the resonance region*. Ph.D. thesis, Old Dominion University (2004) (Referenced on page 34.)

[30] P. L. Anthony, R. G. Arnold, T. Averett, *et al.*, (E-155 Collaboration), *Measurements of the Q^2-dependence of the proton and neutron spin structure functions g_1^p and g_1^n*. Phys. Lett. B **493**: 19 (2000) (Referenced on pages 36 and 45.)

[31] L. W. Whitlow, S. Rock, A. Bodek, *et al.*, *A precise extraction of $R = \sigma_L/\sigma_T$ from a global analysis of the SLAC deep inelastic $e-p$ and $e-d$ scattering cross sections.* Phys. Lett. B **250**: 193 (1990) (Referenced on pages 35 and 207.)

[32] W. Melnitchouk, R. Ent, and C. E. Keppel, *Quark-hadron duality in electron scattering.* Phys. Rep. **406**: 127 (2005) , arXiv:hep-ph/0101224v1 (Referenced on pages 35, 36, and 52.)

[33] J. Pumplin, D. R. Stump, J. Huston, *et al.*, *New generation of parton distributions with uncertainties from global QCD analysis.* J. High Energy Phys. **07**: 012 (2002) (Referenced on page 37.)

[34] W. Melnitchouk and A. W. Thomas, *Neutron/proton structure function ratio at large x.* Phys. Lett. B **377**: 11 (1996) (Referenced on pages 38 and 39.)

[35] H. Abramowicz, G. Hansl-Kozanecki, J. May, *et al.*, (CDHS collaboration), *Measurement of neutrino and antineutrino structure functions in hydrogen and iron.* Z. Physik C **25**: 29 (1984) (Referenced on page 39.)

[36] X. Zheng, *Flavor decomposition of polarized quark distributions from E99-117 g_1^n/F_1^n data.* Technical report, JLab Hall A E99-117 (2004), http://hallaweb.jlab.org/physics/experiments/he3/A1n/ana/memo19_deltaq.pdf (Referenced on page 38.)

[37] H. Avakian, S. J. Brodsky, A. Deur, *et al.*, *Effect of orbital angular momentum on valence-quark helicity distributions.* Phys. Rev. Lett. **99**: 082001 (2007) (Referenced on pages 40, 50, and 51.)

[38] E. Leader, A. V. Sidorov, and D. B. Stamenov, *NLO QCD analysis of polarized deep inelastic scattering.* Int. J. Mod. Phys. A **13**: 5573 (1998) (Referenced on pages 40, 49, and 50.)

[39] A. Airapetian, N. Akopov, Z. Akopov, *et al.*, (HERMES collaboration), *Quark helicity distributions in the nucleon for up, down, and strange quarks from semi-inclusive deep-inelastic scattering.* Phys. Rev. D **71**: 012003 (2005) (Referenced on pages 40 and 45.)

[40] K. Abe, T. Akagi, B. D. Anderson, *et al.*, (E154 Collaboration), *Next-to-leading-order QCD analysis of polarized deep inelastic scattering data.* Phys. Lett. B **405**: 180 (1997) (Referenced on page 40.)

[41] X. Zheng, K. Aniol, D. S. Armstrong, *et al.*, (E99-117 collaboration), *Precision measurement of the neutron spin asymmetries and spin-dependent structure functions in the valence quark region.* Phys. Rev. C **70**: 065207 (2004) (Referenced on pages 40, 46, 55, 59, 191, 213, 217, and 218.)

[42] K. V. Dharmawardane, S. E. Kuhn, P. Bosted, *et al.*, (CLAS collaboration), *Measurement of the $x-$ and Q^2- dependence of the asymmetry A_1 on the nucleon.* Phys. Lett. B **641**: 11 (2006) (Referenced on pages 40, 46, and 53.)

[43] T. Gehrmann, R. G. Roberts, and M. R. Whalley, *A compilation of structure functions in deep inelastic scattering.* J. Phys. G **25**: A1 (1999) , http://durpdg.dur.ac.uk/hepdata/online/f2/structindex.html (Referenced on page 41.)

[44] D. Adams, B. Adeva, E. Arik, *et al.*, (Spin Muon Collaboration), *Spin structure of the proton from polarized inclusive deep-inelastic muon-proton scattering.* Phys. Rev. D **56**: 5330 (1997) (Referenced on page 41.)

[45] A. Abragam, *Principles of Nuclear Magnetism*. International Series of Monographs on Physics, Oxford Science Publications (1961) (Referenced on pages 41 and 80.)

[46] D. Adams, B. Adeva, E. Arik, *et al.*, (Spin Muon Collaboration), *The polarized double cell target of the SMC*. Nucl. Inst. & Meth. in Phys. Res. A **437**: 23 (1999) (Referenced on page 44.)

[47] B. Adeva, T. Akdogan, E. Arik, *et al.*, (Spin Muon Collaboration), *Spin asymmetries A_1 and structure functions g_1 of the proton and deuteron from polarized high energy muon scattering*. Phys. Rev. D **58**: 112001 (1998) (Referenced on page 44.)

[48] P. Abbon, E. Albrecht, V. Y. Alexakhin, *et al.*, (COMPASS Collaboration), *The COMPASS experiment at CERN*. Nucl. Inst. & Meth. in Phys. Res. A **577**: 455 (2007) (Referenced on page 44.)

[49] V. Y. Alexakhin, Y. Alexandrov, G. D. Alexeev, *et al.*, (COMPASS Collaboration), *The deuteron spin-dependent structure function g_1^d and its first moment*. Phys. Lett. B **647**: 8 (2007) (Referenced on page 44.)

[50] M. G. Alekseev, V. Y. Alexakhin, Y. Alexandrov, *et al.*, (COMPASS Collaboration), *The spin-dependent structure function of the proton g_1^p and a test of the Bjorken sum rule*. Phys. Lett. B **690**: 466 (2010) (Referenced on page 44.)

[51] P. L. Anthony, R. G. Arnold, H. R. Band, *et al.*, (E142 Collaboration), *Deep inelastic scattering of polarized electrons by polarized ^{3}he and the study of the neutron spin structure*. Phys. Rev. D **54** (11): 6620 (1996) (Referenced on pages 44 and 213.)

[52] K. Abe, T. Akagi, B. D. Anderson, *et al.*, (E154 Collaboration), *Precision determination of the neutron spin structure function g_1^n*. Phys. Rev. Lett. **79**: 26 (1997) (Referenced on page 45.)

[53] P. L. Anthony, R. G. Arnold, T. Averett, *et al.*, (E155 Collaboration), *Measurement of the deuteron spin structure function $g_1^d(x)$ for $1\ (GeV/c)^2 < Q^2 < 40\ (GeV/c)^2$*. Phys. Lett. B **463**: 339 (1999) (Referenced on page 45.)

[54] A. A. Sokolov and I. N. Ternov, *On polarization and spin effects in the theory of synchrotron radiation*. Sov. Phys. Dokl. **8**: 1203 (1964) (Referenced on page 45.)

[55] B. A. Mecking, G. Adamas, S. Ahmad, *et al.*, (CLAS Collaboration), *The CEBAF large acceptance spectrometer (CLAS)*. Nucl. Inst. & Meth. in Phys. Res. A **503**: 513 (2003) (Referenced on page 46.)

[56] C. D. Keith, M. Anghinolfi, M. Battaglieri, *et al.*, *A polarized target for the CLAS detector*. Nucl. Inst. & Meth. in Phys. Res. A **501**: 327 (2003) (Referenced on page 46.)

[57] (CLAS Collaboration), *CLAS Physics Database*. http://depni.sinp.msu.ru/cgi-bin/jlab/db.cgi (Referenced on page 46.)

[58] R. Fatemi, A. V. Skabelin, V. D. Burkert, *et al.*, (CLAS Collaboration), *Measurement of the proton spin structure function $g_1(x, Q^2)$ for Q^2 from 0.15 to 1.6 GeV^2 with CLAS*. Phys. Rev. Lett. **91**: 222002 (2003) (Referenced on page 46.)

[59] G. Franklin, S. Riordan, D. Seymour, *et al.*, *Measurement of neutron spin asymmetry A_1^n in the valence quark region using 8.8 GeV and 6.6 GeV beam energies and BigBite spectrometer in Hall A*. Proposal for Jefferson Lab PAC 30 (2006), spokespersons: G. Cates, N. Liyanage, G. Rosner, B. Wojtsekhowski and X. Zheng (Referenced on page 46.)

[60] S. Zhou, X. Li, H. Gao, *et al.*, *Measurement of neutron spin asymmetry A_1^n in the valence quark region using an 11 GeV beam and a polarized ^{3}He target in Hall C.* Proposal for Jefferson Lab PAC 36 (2010), spokespersons: G. Cates, J.-P. Chen, Z. E. Meziani, and X. Zheng (Referenced on pages 46 and 53.)

[61] R. P. Feynman, M. Kislinger, and F. Ravndal, *Current matrix elements from a relativistic quark model.* Phys. Rev. D **3**: 2706 (1971) (Referenced on page 46.)

[62] F. E. Close, *On the transformation between current and constituent quarks and consequences for polarised electroproduction structure functions.* Nucl. Phys. B **80**: 269 (1974) (Referenced on pages 46 and 47.)

[63] A. Bodek, M. Breidenbach, D. L. Dubin, *et al.*, *Comparisons of deep-inelastic $e-p$ and $e-n$ cross sections.* Phys. Rev. Lett. **30**: 1087 (1973) (Referenced on page 47.)

[64] J. S. Poucher, M. Breidenbach, R. Ditzler, *et al.*, *High-energy single-arm inelastic $e-p$ and $e-d$ scattering at 6 and 10°.* Phys. Rev. Lett. **32**: 118 (1974) (Referenced on page 47.)

[65] E. M. Riordan, A. Bodek, M. Breidenbach, *et al.*, *Extraction of $R = \sigma_L/sigma_T$ from deep inelastic $e-p$ and $e-d$ cross sections.* Phys. Rev. Lett. **33**: 561 (1974) (Referenced on page 47.)

[66] F. E. Close, *νw_2 at small ω' and resonance form factors in a quark model with broken SU(6).* Phys. Lett. B **43**: 422 (1973) (Referenced on page 48.)

[67] R. Carlitz, *SU(6) symmetry breaking effects in deep inelastic scattering.* Phys. Lett. B **58**: 345 (1975) (Referenced on page 48.)

[68] A. D. Rújula, H. Georgi, and S. L. Glashow, *Hadron masses in a gauge theory.* Phys. Rev. D **12**: 147 (1975) (Referenced on page 48.)

[69] N. Isgur, G. Karl, and R. Koniuk, *Violations of SU(6) selection rules from quark hyperfine interactions.* Phys. Rev. Lett. **41**: 1269 (1978) , see erratum in Phys. Rev. Lett. **45**: 1738 (1980) (Referenced on page 48.)

[70] N. Isgur, *Valence quark spin distribution functions.* Phys. Rev. D **59**: 034013 (1999) (Referenced on pages 48 and 49.)

[71] X. Zheng, private communication (Referenced on pages 49, 50, 52, 55, and 56.)

[72] G. Farrar and D. R. Jackson, *Pion and nucleon structure functions near $x = 1$.* Phys. Rev. Lett. **35**: 1416 (1975) (Referenced on page 49.)

[73] G. Farrar, *Testing QCD.* Phys. Lett. B **70**: 346 (1977) (Referenced on page 49.)

[74] S. J. Brodsky, M. Burkardt, and I. Schmidt, *QCD constraints on the shape of polarized quark and gluon distributions.* Nucl. Phys. B **441**: 197 (1995) (Referenced on pages 49 and 50.)

[75] E. Leader, A. V. Sidorov, and D. B. Stamenov, *Some remarks on methods of QCD analysis of polarized DIS data.* Phys. Rev. D **80**: 054026 (2009) (Referenced on page 50.)

[76] E. Leader, A. V. Sidorov, and D. B. Stamenov, *Impact of CLAS and COMPASS data on polarized parton densities and higher twist.* Phys. Rev. D **75**: 074027 (2007) (Referenced on pages 50 and 51.)

[77] D. Stamenov, private communication (Referenced on pages 50 and 51.)

[78] E. Leader, A. V. Sidorov, and D. B. Stamenov, *Determination of polarized parton densities from a QCD analysis of inclusive and semi-inclusive deep inelastic scattering data*. Phys. Rev. D **82**: 114018 (2010) (Referenced on page 50.)

[79] M. Arneodo, A. Arvidson, B. Badelek, *et al.*, (NMC Collaboration), *Measurement of the proton and the deuteron structure functions, F_2^p and F_2^d*. Phys. Lett. B **364**: 107 (Referenced on page 50.)

[80] K. Abe, T. Akagi, P. L. Anthony, *et al.*, (E143 Collaboration), *Measurements of $R = \sigma_L/\sigma_T$ for $0.03 < x < 0.1$ and fit to world data*. Phys. Lett. B **452**: 194 (1999) (Referenced on pages 50, 207, 208, and 209.)

[81] C. Bourrely, F. Buccella, G. Miele, *et al.*, *Fermi-Dirac distributions for quark partons*. Z. Physik C **62**: 431 (1994) (Referenced on page 51.)

[82] J. Soffer, *New developments in the statistical approach of parton distributions*. J. Phys. Conf. Ser. **53**: 458 (2006) (Referenced on pages 51 and 52.)

[83] C. Bourrely, J. Soffer, and F. Buccella, *A statistical approach for polarized parton distributions*. Eur. Phys. J. C **23**: 487 (2002) (Referenced on pages 51 and 52.)

[84] J. Cleymans, I. Dadić, and J. Joubert, *Structure functions of the nucleon in a statistical model*. Z. Physik C **64**: 275 (1994) (Referenced on page 52.)

[85] R. S. Bhalerao, *Statistical model for the nucleon structure functions*. Phys. Lett. B **380**: 1 (1996) , see erratum in Phys. Lett. B **387**: 881 (1996) (Referenced on page 52.)

[86] R. S. Bhalerao, N. G. Kelkar, and B. Ram, *Model for polarized and unpolarized parton density functions in the nucleon*. Phys. Lett. B **476**: 285 (2000) (Referenced on page 52.)

[87] E. D. Bloom and F. J. Gilman, *Scaling, duality, and the behavior of resonances in inelastic electron-proton scattering*. Phys. Rev. Lett. **25**: 1140 (1970) (Referenced on page 52.)

[88] E. D. Bloom and F. J. Gilman, *Scaling and the behavior of nucleon resonances in inelastic electron-nucleon scattering*. Phys. Rev. D **4**: 2901 (1971) (Referenced on pages 52 and 53.)

[89] I. Niculescu, C. S. Armstrong, J. Arrington, *et al.*, *Evidence for valencelike quark-hadron duality*. Phys. Rev. Lett. **85**: 1182 (2000) (Referenced on page 53.)

[90] A. Airapetian, N. Akopov, Z. Akopov, *et al.*, (HERMES collaboration), *Evidence for quark-hadron duality in the proton spin asymmetry A_1*. Phys. Rev. Lett. **90**: 092002 (2003) (Referenced on page 53.)

[91] P. E. Bosted, K. V. Dharmawardane, G. E. Dodge, *et al.*, (CLAS collaboration), *Quark-hadron duality in spin structure functions g_1^p and g_1^d*. Phys. Rev. C **75**: 035203 (2007) (Referenced on page 53.)

[92] P. Solvignon, N. Liyanage, J.-P. Chen, *et al.*, (Jefferson Lab E01-012 collaboration), *Quark-hadron duality in neutron (^{3}He) spin structure*. Phys. Rev. Lett. **101**: 182502 (2008) (Referenced on page 53.)

[93] W. Melnitchouk, *Local duality predictions for $x \sim 1$ structure functions*. Phys. Rev. Lett. **86**: 35 (2001) , see erratum in Phys. Rev. Lett. **93**: 199901 (2001) (Referenced on pages 53 and 54.)

[94] W. Melnitchouk, private communication (Referenced on page 54.)

[95] A. D. Rújula, H. Georgi, and H. D. Politzer, *Demythification of electroproduction local duality and precocious scaling*. Ann. Phys. (NY) **103**: 315 (1977) (Referenced on page 53.)

[96] F. E. Close and W. Melnitchouk, *Symmetry breaking and quark-hadron duality in structure functions*. Phys. Rev. C **68**: 035210 (2003) (Referenced on page 53.)

[97] D. I. Diakonov and V. Y. Petrov, *Nucleons as chiral solitons*. In M. Shifman, editor, *At the Frontier of Particle Physics: Handbook of QCD*, World Scientific (2001) (Referenced on pages 54 and 55.)

[98] E. Guadagnini, *Baryons as solitons and mass formulae*. Nucl. Phys. B **236**: 35 (1984) (Referenced on page 54.)

[99] Y. Nambu and G. Jona-Lasinio, *Dynamical model of elementary particles based on an analogy with superconductivity. I.* Phys. Rev. **122**: 345 (1961) (Referenced on page 54.)

[100] Y. Nambu and G. Jona-Lasinio, *Dynamical model of elementary particles based on an analogy with superconductivity. II.* Phys. Rev. **124**: 246 (1961) (Referenced on page 54.)

[101] H. Weigel, L. Gamberg, and H. Reinhardt, *Polarized nucleon structure functions within a chiral soliton model*. Phys. Rev. D **55**: 6910 (1997) (Referenced on pages 54 and 55.)

[102] H. Weigel, L. Gamberg, and H. Reinhardt, *Nucleon structure functions from a chiral soliton*. Phys. Lett. B **399**: 287 (1997) (Referenced on pages 54 and 55.)

[103] O. Schröder, H. Reinhardt, and H. Weigel, *Nucleon structure functions in the three-flavor NJL soliton model*. Nucl. Phys. A **651**: 174 (1999) (Referenced on pages 54 and 55.)

[104] M. Wakamatsu, *Light-flavor sea-quark distributions in the nucleon in the SU(3) chiral quark soliton model. I. Phenomenological predictions*. Phys. Rev. D **67**: 034005 (2003) (Referenced on page 55.)

[105] M. Wakamatsu, *Light-flavor sea-quark distributions in the nucleon in the SU(3) chiral quark soliton model. II. Theoretical formalism*. Phys. Rev. D **67**: 034006 (2003) (Referenced on page 55.)

[106] N. I. Kochelev, *Instantons and polarized structure functions*. Phys. Rev. D **57**: 5539 (1998) (Referenced on page 55.)

[107] C. Boros and A. W. Thomas, *Parton distributions for the octet and decuplet baryons*. Phys. Rev. D **60**: 074017 (1999) (Referenced on pages 56 and 57.)

[108] A. Chodos, R. L. Jaffe, K. Johnson, *et al.*, *New extended model of hadrons*. Phys. Rev. D **9**: 3471 (1974) (Referenced on page 56.)

[109] A. W. Schreiber, A. I. Signal, and A. W. Thomas, *Structure functions in the bag model*. Phys. Rev. D **44**: 2653 (1991) (Referenced on page 56.)

[110] X. Song and J. S. McCarthy, *Model calculation of nucleon structure functions*. Phys. Rev. D **49**: 3169 (1994) (Referenced on page 56.)

[111] S. Théberge, A. W. Thomas, and G. A. Miller, *Pionic corrections to the MIT bag model: The (3,3) resonance*. Phys. Rev. D **22**: 2838 (1980) (Referenced on page 56.)

[112] A. W. Thomas, *Chiral symmetry and the bag model: A new starting point for nuclear physics*. Adv. Nucl. Phys. **13**: 1 (1984) (Referenced on page 56.)

[113] A. W. Schreiber, P. J. Mulders, A. I. Signal, *et al.*, *Pion cloud of the nucleon and its effect on deep-inelastic structure*. Phys. Rev. D **45**: 3069 (1992) (Referenced on page 56.)

[114] A. W. Thomas, *The spin of the proton*. Prog. Nucl. Part. Phys. **61**: 219 (2008) (Referenced on page 56.)

[115] F. E. Close and A. W. Thomas, *The spin and flavor dependence of parton distibution functions*. Phys. Lett. B **212**: 227 (1988) (Referenced on page 57.)

[116] F. M. Steffens, H. Holtmann, and A. W. Thomas, *Mesonic corrections to the shape of quark distributions*. Phys. Lett. B **358**: 139 (1995) (Referenced on page 57.)

[117] B. W. Filippone and X. Ji, *The spin structure of the nucleon*. Adv. Phys. Part. Nucl. **26**: 1 (2001) (Referenced on pages 59 and 60.)

[118] M. Göckeler, R. Horsley, D. Pleiter, *et al.*, *Investigation of the second moment of the nucleon's g_1 and g_2 structure functions in two-flavor lattice QCD*. Phys. Rev. D **72**: 054507 (2005) (Referenced on pages 59 and 60.)

[119] M. Amarian, L. Auerbach, T. Averett, *et al.*, (E94-010 collaboration), *Q^2 evolution of the neutron spin structure moments using a ^{3}He target*. Phys. Rev. Lett. **92**: 022301 (2004) (Referenced on page 59.)

[120] P. L. Anthony, R. G. Arnold, T. Averett, *et al.*, (E155 Collaboration), *Measurement of the proton and deuteron spin structure functions g_2 and asymmetry A_2*. Phys. Lett. B **458**: 529 (1999) (Referenced on page 59.)

[121] C. W. Kao, T. Spitzenberg, and M. Vanderhaeghen, *Burkhardt-Cottingham sum rule and forward spin polarizabilities in heavy baryon chiral perturbation theory*. Phys. Rev. D **67**: 016001 (2003) (Referenced on page 59.)

[122] X. Zheng, P. Bertin, J.-P. Chen, *et al.*, *Precision measurement of the neutron d_2: Towards the electric χ_e and magnetic χ_b color polarizabilities*. Proposal for Jefferson Lab PAC 29 (2005), spokespersons: Seonho Choi, X. Jiang, Z.-E. Meziani, and B. Sawatzky. (Referenced on pages 59, 60, and 86.)

[123] Z.-E. Meziani, W. Melnitchouk, J. P. Chen, *et al.*, *Higher twists and color polarizabilities in the neutron*. Phys. Lett. B **613**: 148 (2005) (Referenced on page 59.)

[124] M. Burkardt, *The g_2 structure function*. Spin Structure at Low Q^2 Workshop, Jefferson Lab (2009), arXiv: hep-ph/0905.4079v1 (Referenced on pages 59 and 60.)

[125] E. Stein, P. Górnicki, L. Mankiewicz, *et al.*, *QCD sum rule calculation of twist-3 contributions to polarized nucleon structure functions*. Phys. Lett. B **343**: 369 (1995) (Referenced on page 60.)

[126] M. Wakamatsu, *Polarized structure function $g_2(x)$ in the chiral quark soliton model*. Phys. Lett. B **487**: 118 (2000) (Referenced on page 60.)

[127] F. W. Bissey, A. W. Thomas, and I. R. Afnan, *Structure functions for the three-nucleon system*. Phys. Rev. C **64**: 024004 (2001) (Referenced on pages 61 and 75.)

[128] *The Big Family of experiments: Readiness review document* (2007), http://hallaweb.jlab.org/experiment/BigFamily/Document/bigfamily.pdf (Referenced on page 62.)

[129] *Jefferson Lab Picture Exchange*. http://www1.jlab.org/ul/jpix/ (Referenced on page 64.)

[130] C. W. Leemann, D. R. Douglas, and G. A. Krafft, *The continuous electron beam accelarator facility: CEBAF at the Jefferson Laboratory*. Annu. Rev. Nucl. Part. Sci. **51**: 413 (2001) (Referenced on pages 61, 62, 63, and 67.)

[131] D. T. Pierce and F. Meier, *Photoemission of spin-polarized electrons from GaAs*. Phys. Rev. B **13**: 5484 (1976) (Referenced on page 62.)

[132] R. Alley, H. Aoyagi, J. Clendenin, *et al.*, *The Stanford linear accelerator polarized electron source*. Nucl. Inst. & Meth. in Phys. Res. A **365**: 1 (Referenced on pages 62 and 65.)

[133] T. Maruyama, E. L. Garwin, R. Prepost, *et al.*, *Observation of strain-enhanced electron-spin polarization in photoemission from InGaAs*. Phys. Rev. Lett. **66**: 2376 (1991) (Referenced on page 64.)

[134] T. Maruyama, D.-A. Luh, A. Brachmann, *et al.*, *Systematic study of polarized electron emission from strained GaAs/GaAsP superlattice photocathodes*. Appl. Phys. Lett. **85**: 2640 (2004) (Referenced on page 65.)

[135] J. Grames, *Polarized electron sources at JLab*. Lecture for Hampton University Graduate Studies at Jefferson Lab (2008), http://www.jlab.org/accel/inj_group/docs/2008/HUGS08_Grames.pdf (Referenced on page 65.)

[136] J. Hansknecht and M. Poelker, *Synchronous photoinjection using a frequency-doubled gain-switched fiber-coupled seed laser and ErYb-doped fiber amplifier*. Phys. Rev. Spec. Top. Accel. Beams **9**: 063501 (2006) (Referenced on page 65.)

[137] R. L. Sutherland, *Handbook of Nonlinear Optics*. 2nd edition, CRC Press (2003) (Referenced on page 65.)

[138] C. K. Sinclair, P. A. Adderley, B. M. Dunham, *et al.*, *Development of a high average current polarized electron source with long cathode operational lifetime*. Phys. Rev. Spec. Top. Accel. Beams **10**: 023501 (2007) (Referenced on page 66.)

[139] J. M. Grames, C. K. Sinclair, J. Mitchell, *et al.*, *Unique electron polarimeter analyzing power comparison and precision spin-based energy measurement*. Phys. Rev. Spec. Top. Accel. Beams **7**: 042802 (2004) , see erratum in Phys. Rev. Spec. Top. Accel. Beams **13**: 069901 (2010) (Referenced on pages 66, 106, and 192.)

[140] J. Alcorn, B. D. Anderson, K. A. Aniol, *et al.*, (Hall A Collaboration), *Basic instrumentation for Hall A at Jefferson Lab*. Nucl. Inst. & Meth. in Phys. Res. A **522**: 294 (2004) (Referenced on pages 68, 70, 72, 75, 94, 95, and 107.)

[141] *JLab Hall A general operations manual*. Technical report, Hall A collaboration (2010), http://hallaweb.jlab.org/news/minutes/OSP/osp.pdf (Referenced on pages 67, 80, 83, 85, and 104.)

[142] M. Pitt, *Helicity control requests from the G^0 experiment*. Technical report, G^0 Collaboration, Jefferson Lab (2001), http://www.jlab.org/ rom/g0helicity.pdf (Referenced on page 67.)

[143] C. Hyde-Wright, L. Todor, and G. Laveissiere, *Beam position studies for e93050*. Technical Report TN-01-001, JLAB (2001) (Referenced on pages 69, 72, and 73.)

[144] S. Riordan, *Measurements of the electric form factor of the neutron at Q^2 = 1.7 and 3.5 GeV^2*. Ph.D. thesis, Carnegie Mellon University (2008) (Referenced on pages 69, 90, 151, 156, 157, 158, 174, 193, and 194.)

[145] R. Kazimi, B. Dunham, G. A. Krafft, *et al.*, *Precision intercomparison of beam current monitors at CEBAF*. In L. Gennari, editor, *Proceedings of the 1995 Particle Accelerator Conference and International Conference on High-Energy Accelerators*, volume 4, 2610–2612, IEEE Operations Center (1995) (Referenced on page 70.)

[146] V. Sulkosky, private communication (Referenced on page 72.)

[147] J. J. LeRose, *Hall A HRS calculated first-order optical properties* (1999), http://hallaweb.jlab.org/news/minutes/fo_matrix.html (Referenced on page 73.)

[148] G. Franklin, private communication (Referenced on pages 73, 137, 162, and 192.)

[149] M. G. Tiefenback and D. Douglas, *Proposal for a beam profile monitor using a static wire pickup*. Technical Report TN92-061, JLab (1992) (Referenced on page 74.)

[150] D. Marchand, *Calculation of Radiative Corrections for Virtual Compton Scattering, and Absolute Electron Beam Measurement at Jefferson Lab (Hall A) by a Magnetic Method: The Arc Project [in French]*. Ph.D. thesis, Université Blaise Pascal (1998) (Referenced on page 75.)

[151] C. Dutta, *Measurement of single-target spin asymmetries in the electroproduction of negative pions in the semi-inclusive deep inelastic reaction* $n\uparrow(e,e'\pi^+)X$ *on a transversely polarized* ^{3}*He target*. Ph.D. thesis, University of Kentucky (2010) (Referenced on pages 75, 78, 79, 80, 81, 83, 84, and 96.)

[152] I. Kominis, *Measurement of the neutron (*^{3}*He) spin structure at low* Q^2 *and the extended Gerasimov-Drell-Hearn sum rule*. Ph.D. thesis, Princeton University (2001) (Referenced on pages 76, 77, and 147.)

[153] A. S. Kolarkar, *Precision measurements of the neutron electric form factor at high momentum transfers*. Ph.D. thesis, University of Kentucky (2008) (Referenced on pages 77, 78, 79, and 82.)

[154] M. E. Wagshul and T. E. Chupp, *Laser optical pumping of high-density Rb in polarized* ^{3}*He targets*. Phys. Rev. A **49**: 3854 (1994) (Referenced on page 77.)

[155] W. Happer, *Optical pumping*. Rev. Mod. Phys. **44**: 169 (1972) (Referenced on page 77.)

[156] E. Babcock, I. Nelson, S. Kadlecek, *et al.*, *Hybrid spin-exchange optical pumping of* ^{3}*He*. Phys. Rev. Lett. **91**: 123003 (2003) (Referenced on page 77.)

[157] T. G. Walker and W. Happer, *Spin-exchange optical pumping of noble-gas nuclei*. Rev. Mod. Phys. **69**: 629 (1997) (Referenced on page 77.)

[158] N. R. Newbury, A. S. Barton, P. Bogorad, *et al.*, *Polarization-dependent frequency shifts from Rb-*^{3}*He collisions*. Phys. Rev. A **48**: 558 (1993) (Referenced on page 77.)

[159] T. G. Walker, J. H. Thywissen, and W. Happer, *Spin-rotation interaction of alkali-metal-He-atom pairs*. Phys. Rev. A **56**: 2090 (1997) (Referenced on page 78.)

[160] A. B. Baranga, S. Appelt, M. V. Romalis, *et al.*, *Polarization of* ^{3}*He by spin exchange with optically pumped Rb and K vapors*. Phys. Rev. Lett. **80**: 2801 (1998) (Referenced on page 78.)

[161] K. Allada, *Measurement of single spin asymmetries in semi-inclusive deep inelastic scattering reaction* $n^\uparrow(e,e'\pi^+)X$ *at Jefferson Lab*. Ph.D. thesis, University of Kentucky (2010) (Referenced on pages 78, 86, 87, 90, 92, 93, 94, 96, 97, 103, 169, 170, and 182.)

[162] T. E. Chupp, R. A. Loveman, A. K. Thompson, *et al.*, *Tests of a high density polarized ^3He target for electron scattering*. Phys. Rev. C **45**: 915 (1992) (Referenced on page 79.)

[163] W. Lorenzon, T. R. Gentile, and R. D. McKeown, *NMR calibration of optical measurement of nuclear polarization in ^3He*. Phys. Rev. A **47**: 468 (1993) (Referenced on pages 80, 81, and 82.)

[164] S. R. Schaefer, G. D. Cates, T.-R. Chien, *et al.*, *Frequency shifts of the magnetic-resonance spectrum of mixtures of nuclear spin-polarized noble gases and vapors of spin-polarized alkali-metal atoms*. Phys. Rev. A **39**: 5613 (1989) (Referenced on page 82.)

[165] K. Kramer, X. Zong, R. Lu, *et al.*, *A high-pressure polarized ^3He gas target for the High Intensity Gamma Source (HIγS) facility at Duke Free Electron Laser Laboratory*. Nucl. Inst. & Meth. in Phys. Res. A **582**: 318 (2007) (Referenced on page 82.)

[166] *Transversity Photo Diary*. http://hallaweb.jlab.org/wiki/index.php/Transversity/Photo_Diary (Referenced on pages 84, 87, and 159.)

[167] L. El Fassi, *Geometry of ^3He, reference and water cells*. Technical report, JLab Hall A E06-014 (2009), http://www.jlab.org/∼elfassi/d2n/wall_thick/cells_geometry.pdf (Referenced on pages 84, 85, and 86.)

[168] A. Afanasev, P. Bosted, A. Camsonne, *et al.*, *$\vec{e}-^2H$ Parity Violating Deep Inelastic Scattering (PVDIS) at CEBAF 6 GeV*. Proposal for Jefferson Lab PAC 33 (2007), spokespersons: R. Michaels, P.E. Reimer and X.-C. Zheng (Referenced on pages 85 and 144.)

[169] D. J. J. de Lange, J. J. M. Steijger, H. de Vries, *et al.*, *A large acceptance spectrometer for the internal target facility at NIKHEF*. Nucl. Inst. & Meth. in Phys. Res. A **406**: 182 (1998) (Referenced on page 86.)

[170] X. Qian, *Measurement of single target-spin asymmetry in semi-inclusive $n^\uparrow(e,e'\pi^\pm)$ reaction on a transversely polarized ^3He target*. Ph.D. thesis, Duke University (2010) (Referenced on pages 88, 89, 95, 151, 154, 157, 158, 161, 176, 178, 179, and 202.)

[171] B. Sawatzky, *Hall A technical note for the BigBite Čerenkov detector*. Technical report, JLab Hall A (in press) (Referenced on pages 90, 92, and 164.)

[172] D. H. Perkins, *Introduction to High Energy Physics*. 4th edition, Cambridge University Press (2000) (Referenced on page 91.)

[173] B. Sawatzky, *Design notes and cost breakdown for the BigBite Čerenkov detector*. Technical report, Temple University (2007), http://www.jlab.org/ brads/d2n/cerenkov/review_cerenkov_d2.pdf (Referenced on page 92.)

[174] R. Winston, *Light collection within the framework of geometrical optics*. J. Opt. Soc. Am. **60**: 245 (1970) (Referenced on page 92.)

[175] B. Wojtsekhowski, private communication (Referenced on page 93.)

[176] R. W.-M. Chan, *Construction and characterization of multi-wire drift chambers*. Master's thesis, University of Virginia (2005) (Referenced on page 94.)

[177] G. Bathow, E. Freytag, M. Köbberling, *et al.*, *Measurements of the longitudinal and lateral development of electromagnetic cascades in lead, copper and aluminum at 6 GeV*. Nucl. Phys. B **20**: 592 (1970) (Referenced on page 94.)

[178] D. Green, *The Physics of Particle Detectors*. Cambridge University Press (2000) (Referenced on page 94.)

[179] L. M. Mikhailov and Z. S. Aref'eva, *Tables for the design of lead glass shielding for a "broad beam" of gamma rays*. Atomic Energy **12**: 58 (1962) (Referenced on page 94.)

[180] D. Flay, *LHRS particle identification analysis*. Technical report, JLab Hall A E06-014 (2010), http://www.jlab.org/∼flay/thesis/tech_notes/eff_note.pdf (Referenced on page 95.)

[181] D. Flay, *LHRS trigger efficiency for good electrons analysis*. Technical report, JLab Hall A E06-014 (2010), http://www.jlab.org/∼flay/thesis/tech_notes/trig_note.pdf (Referenced on page 97.)

[182] R. Michaels, *Hall A HRS trigger* (2003), http://hallaweb.jlab.org/equipment/daq/trigger.html (Referenced on page 98.)

[183] B. Sawatzky, private communication (Referenced on pages 99 and 100.)

[184] K. Allada, private communication (Referenced on page 102.)

[185] *VME International Trade Association*. http://www.vita.com/specifications.html (Referenced on page 101.)

[186] W. A. W. III, J. Chen, G. Heyes, *et al.*, *CODA: A scalable, distributed data acquisition system*. IEEE Trans. Nucl. Sci. **41**: 61 (1994) (Referenced on page 101.)

[187] V. Gyurjyan, C. Timmer, D. Abbott, *et al.*, *Jefferson Lab data acquisition run control system*. In A. Aimar, J. Harvey, and N. Knoors, editors, *Proceedings of the Computing in High Energy Physics and Nuclear Physics 2004 Conference*, volume 1, 151, CERN-2005-002 (2005) (Referenced on page 102.)

[188] S. A. Lewis, *Overview of the Experimental Physics and Industrial Control System: EPICS*. Technical report, Lawrence Berkeley National Laboratory (1998), http://www.epics.org/overview.pdf (Referenced on page 102.)

[189] R. Brun and F. Rademakers, *ROOT - an object oriented data analysis framework*. Nucl. Inst. & Meth. in Phys. Res. A **389**: 81 (1997) , see also http://root.cern.ch (Referenced on page 103.)

[190] *Hall A Analyzer*. http://hallaweb.jlab.org/podd/ (Referenced on page 104.)

[191] D. J. Maraziotis, W. Chen, D. Dutta, *et al.*, *Measurement of a single target-spin asymmetry in semi-inclusive $n^{\uparrow}(e,e'\pi^{-})$ reaction on a transversely polarized ^{3}He target*. Proposal for Jefferson Lab PAC 29, spokespersons: J.-P. Cheng, X. Jiang, and J.-C. Peng (Referenced on page 104.)

[192] C. K. Sinclair, *Electron beam polarimetry*. Technical Report 98-04, JLAB-ACC (1998) (Referenced on page 106.)

[193] M. O. Muether, *Strange quark contributions to nucleon electric and magnetic form factors from parity-violating electron scattering asymmetries in the backward angle G^0 experiment*. Ph.D. thesis, University of Illinois at Urbana-Champaign (2010) (Referenced on page 106.)

[194] A. A. Kresnin and L. N. Rozentsveig, *Polarization effects in the scattering of electrons and positrons by electrons*. Sov. Phys. JETP **5**: 288 (1957) (Referenced on page 107.)

[195] A. V. Glamazdin, V. G. Gorbenko, L. G. Levchuk, *et al.*, *Electron beam Møller polarimeter at JLAB Hall A*. Fiz. B **8**: 91 (1999) , hep-ex/9912063 (Referenced on page 107.)

[196] A. H. Compton, *A quantum theory of the scattering of X-rays by light elements*. Phys. Rev. **21**: 483 (1923) (Referenced on page 108.)

[197] O. Klein and Y. Nishina, *Über die Streuung von Strahlung durch freie Elektronen nach der neuen relativistischen Quantendynamik von Dirac*. Z. Physik **52**: 853 (1929) (Referenced on page 108.)

[198] F. W. Lipps and H. A. Tolhoek, *Polarization phenomena of electrons and photons. I: General method and application to Compton scattering*. Physica **20**: 85 (1954) (Referenced on page 108.)

[199] F. W. Lipps and H. A. Tolhoek, *Polarization phenomena of electrons and photons. II: Results for Compton scattering*. Physica **20**: 395 (1954) (Referenced on page 108.)

[200] S. Gasiorowicz, *Elementary Particle Physics*. John Wiley and Sons, Inc. (1966) (Referenced on page 109.)

[201] C. Y. Prescott, *Spin-dependent Compton scattering for use in analyzing electron beam polarizations*. Technical Report TN-73-1, SLAC (1973) (Referenced on page 109.)

[202] M. Woods, (SLD collaboration), *The scanning Compton polarimeter for the SLD experiment*. In *The Workshop on High Energy Polarimeters at NIKHEF*, volume SLAC-PUB-7319, SLAC (1996) (Referenced on page 109.)

[203] D. P. Barber, H.-D. Bremer, M. Böge, *et al.*, *The HERA polarimeter and the first observation of electron spin at HERA*. Nucl. Inst. & Meth. in Phys. Res. A **329**: 79 (1993) (Referenced on page 109.)

[204] M. Beckmann, A. Borissov, S. Brauksiepe, *et al.*, *The longitudinal polarimeter at HERA*. Nucl. Inst. & Meth. in Phys. Res. A **479**: 334 (2002) (Referenced on page 109.)

[205] I. Passchier, D. W. Higinbotham, C. W. de Jager, *et al.*, *A Compton backscattering polarimeter for measuring longitudinal electron polarization*. Nucl. Inst. & Meth. in Phys. Res. A **414**: 446 (1998) (Referenced on page 109.)

[206] A. Denner and S. Dittmaier, *Complete $o(\alpha)$ QED corrections to polarized Compton scattering*. Nucl. Phys. B **540**: 58 (1999) (Referenced on page 109.)

[207] A. Lath, *A precise measurement of the left-right cross section asymmetry in Z boson production*. Ph.D. thesis, Massachusetts Institute of Technology (1994) (Referenced on pages 109, 111, and 113.)

[208] J. D. Jackson, *Classical Electrodynamics*. 3rd edition, John Wiley and Sons, Inc., New York (1999) (Referenced on pages 111 and 172.)

[209] R. C. King, *A precise measurement of the left-right asymmetry of Z boson production at the SLAC linear collider*. Ph.D. thesis, Stanford University (1994) (Referenced on page 113.)

[210] G. Bardin, C. Cavata, D. Neyret, *et al.*, *Conceptual design report of a Compton polarimeter for CEBAF Hall A*. Technical Report 96-14, DAPNIA-SPhN (1996) (Referenced on pages 114 and 115.)

[211] S. Nanda and D. Lhuillier, *Conceptual design report for Hall A Compton polarimeter upgrade*. Technical report, JLab Hall A (2004), http://hallaweb.jlab.org/parity/prex/compton_upgrade.pdf (Referenced on pages 115 and 116.)

[212] K. A. Aniol, M. B. Epstein, D. J. Margaziotis, *et al.*, *A clean measurement of the neutron skin of ^{208}Pb through parity violating electron scattering*. Proposal for Jefferson Lab PAC 29 (2005), spokespersons: R. Michaels, P. A. Souder, and G. M. Urciuoli (Referenced on page 115.)

[213] S. Escoffier, *Precision measurement of the polarization of the TJNAF electron beam via Compton polarimetry, for the G_E^p and $N-\Delta$ experiments [in French]*. Ph.D. thesis, Université Paris 7-Denis Diderot (2001) (Referenced on pages 117 and 120.)

[214] M. Baylac, *Measurement of the polarization of the electron beam at Jefferson Laboratory via the Compton effect, for the HAPPEX experiment to measure parity violation in elastic electron-proton scattering [in French]*. Ph.D. thesis, Université Claude Bernard-Lyon 1 (2000) (Referenced on pages 117, 120, 121, and 122.)

[215] R. W. P. Drever, J. L. Hall, F. V. Kowalski, *et al.*, *Laser phase and frequency stabilization using an optical resonator*. Appl. Phys. B **31**: 97 (1983) (Referenced on page 117.)

[216] E. D. Black, *An introduction to Pound-Drever-Hall laser frequency stabilization*. Amer. J. Phys. **69**: 79 (2001) (Referenced on page 117.)

[217] J. P. Jorda, E. Burtin, C. Cavata, *et al.*, *A Fabry-Pérot cavity for Compton polarimetry*. Nucl. Inst. & Meth. in Phys. Res. A **412**: 1 (1997) (Referenced on pages 118 and 119.)

[218] R. A. Boyd, J. L. Bliss, and K. G. Libbrecht, *Teaching physics with 670-nm diode lasers – experiments with Fabry-Perot cavities*. Amer. J. Phys. **64**: 1109 (1996) (Referenced on page 118.)

[219] N. Falletto, *Study, conception and realization of a Fabry-Perot cavity for the Compton polarimeter at TJNAF [in French]*. Ph.D. thesis, Université Joseph Fourier-Grenoble 1 (1999) (Referenced on page 119.)

[220] D. Neyret, T. Pussieux, T. Auger, *et al.*, *A photon calorimeter using lead tungstate crystals for the CEBAF Hall A Compton polarimeter*. Nucl. Inst. & Meth. in Phys. Res. A **443**: 231 (2000) (Referenced on page 122.)

[221] S. Escoffier, P. Y. Bertin, M. Brossard, *et al.*, *Accurate measurement of the electron beam polarization in JLab Hall A using Compton polarimetry*. Nucl. Inst. & Meth. in Phys. Res. A **551**: 563 (2005) (Referenced on page 123.)

[222] G. W. Miller, *Parity violation in forward angle elastic electron-proton scattering*. Ph.D. thesis, Princeton University (2001) (Referenced on pages 123, 130, and 194.)

[223] G. Franklin and R. Michaels, *Integrating FADCs*. Technical report, JLab Hall A (HAPPEX Collaboration) (2007) (Referenced on page 125.)

[224] K. A. Aniol, D. J. Margaziotis, F. Bataru, *et al.*, *A measurement of nucleon strange form factors at high Q^2*. Proposal for Jefferson Lab PAC 29 (2005), spokespersons: P. A. Souder and K. D. Paschke (Referenced on pages 128 and 130.)

[225] R. Michaels and B. Moffit, *Parity DAQ for charge asymmetry feedback*. http://hallaweb.jlab.org/experiment/HAPPEX/HAPPEXII/paritydaq/parity_daq.html (Referenced on pages 129 and 193.)

[226] K. Paschke, private communication (Referenced on page 131.)

[227] S. Agostinelli, J. Allison, K. Amako, *et al.*, *G4 – a simulation toolkit*. Nucl. Inst. & Meth. in Phys. Res. A **506**: 250 (2003) (Referenced on page 131.)

[228] J. Allison, K. Amako, J. Apostolakis, *et al.*, *Geant4 developments and applications*. IEEE Trans. Nucl. Sci. **53**: 270 (2006) (Referenced on page 131.)

[229] H. R. Weller, M. W. Ahmed, H. Gao, *et al.*, *Research opportunities at the upgraded HIγS facility*. Prog. Nucl. Part. Phys. **62**: 257 (2009) (Referenced on page 131.)

[230] C. Sun, Y. K. Wu, G. Rusev, *et al.*, *End-to-end spectrum reconstruction method for analyzing Compton gamma-ray beams*. Nucl. Inst. & Meth. in Phys. Res. A **605**: 312 (2009) (Referenced on page 132.)

[231] M. Friend, private communication (Referenced on pages 133, 134, 136, 137, 138, 142, and 144.)

[232] *University of Virginia helium-3 target lab report* (2009), http://galileo.phys.virginia.edu/research/groups/spinphysics/transversity/transcells.html (Referenced on page 147.)

[233] Y. Zhang, *Target analysis for E06-014*. http://jlab.org/∼yawei/d2n/targ_ana.html (Referenced on pages 147 and 148.)

[234] K. Kramer, *A search for higher twist effects in the neutron spin structure function* $g_2^n(x, Q^2)$. Ph.D. thesis, College of William and Mary (2003) (Referenced on page 147.)

[235] Y. Zhang, private communication (Referenced on pages 147 and 150.)

[236] N. J. Stone, *Table of nuclear magnetic dipole and electric quadrupole moments*. At. Data. Nucl. Data Tables **90**: 75 (2005) (Referenced on page 148.)

[237] J. Singh, *A primer on using atom-light interactions to study spin-exchange optical pumping polarized* ^{3}*He target cells*. Technical report, JLab (2009), http://www.jlab.org/∼singhj/docs/jfarrotv2002.pdf (Referenced on page 148.)

[238] E. Babcock, I. A. Nelson, S. Kadlecek, *et al.*, ^{3}*He polarization-dependent EPR frequency shifts of alkali-metal-*^{3}*He pairs*. Phys. Rev. A **71**: 013414 (2005) (Referenced on page 148.)

[239] Y. Zhang, *Electron paramagnetic resonance (EPR) project summary*. Technical report, Hall A Collaboration (2011), http://www.jlab.org/∼yawei/weeklymeeting/110209/epr.pdf (Referenced on pages 148 and 149.)

[240] M. Posik, private communication (Referenced on pages 151, 152, 153, 161, 164, 171, 184, and 192.)

[241] M. Dell'Orso and L. Ristori, *A highly parallel algorithm for track finding*. Nucl. Inst. & Meth. in Phys. Res. A **287**: 436 (1990) (Referenced on pages 152 and 154.)

[242] R. Mankel, *Pattern recognition and event reconstruction in particle physics experiments*. Rep. Prog. Phys. **67**: 553 (2004) (Referenced on page 154.)

[243] M. Posik, *BigBite T2 trigger*. Technical report, Temple University (2010) (Referenced on page 164.)

[244] V. Mamyan, private communication (Referenced on page 172.)

[245] J. Huang, private communication (Referenced on page 193.)

[246] Y. Qiang, private communication (Referenced on page 194.)

[247] J. Dahlberg, *BigBite detector package survey*. Technical Report A1219, Jefferson Lab Alignment Group (2009), http://www.jlab.org/accel/survalign/documents/dthalla/A1219.pdf (Referenced on page 202.)

[248] L. W. Whitlow, *Deep inelastic structure functions from electron scattering on hydrogen, deuterium, and iron at 0.6 $GeV^2 \leq Q^2 \leq$ 30.0 GeV^2*. Ph.D. thesis, Stanford University (1990), SLAC Report 357 (Referenced on page 207.)

[249] M. Arneodo, A. Arvidson, B. Badelek, *et al.*, (NMC Collaboration), *The Q^2 dependence of the structure function ratio F_2^{Sn}/F_2^C and the difference $R^{Sn} - R^C$ in deep inelastic muon scattering*. Nucl. Phys. B **481**: 23 (1996) (Referenced on page 207.)

[250] L. H. Tao, L. Andivahis, P. L. Anthony, *et al.*, (E140X Collaboration), *Precision measurement of $R = \sigma_L/\sigma_T$ on hydrogen, deuterium, and beryllium targets in deep inelastic electron scattering*. Z. Physik C **483**: 387 (1996) (Referenced on page 207.)

[251] F. Bissey, V. Guzey, M. Strikman, *et al.*, *Complete analysis of spin structure function g_1 of He-3*. Phys. Rev. C **65**: 064317 (2002) (Referenced on page 218.)

[252] S. A. Kulagin and W. Melnitchouk, *Spin structure functions of ^3He at finite Q^2*. Phys. Rev. C **78**: 065203 (Referenced on page 218.)

[253] W. Bertozzi, O. Gayou, S. Gilad, *et al.*, *Measurement of A_x and A_z asymmetries in the quasi-elastic $^3\vec{\mathrm{He}}(\vec{e}, e'd)$ reaction*. Proposal for Jefferson Lab PAC 28 (2005), spokespersons: S. Gilad, D. W. Higinbotham, W. Korsch, B. E. Norum, and S. Širca (Referenced on page 218.)